

Design, installation and commissioning of new read-out electronics for HADES ECAL and diamond detectors for T0-reconstruction and beam diagnostics

Rost, Adrian
(2020)

DOI (TUprints): <https://doi.org/10.25534/tuprints-00012235>

Lizenz:



CC-BY-NC-ND 4.0 International - Creative Commons, Attribution Non-commercial, No-derivatives

Publikationstyp: Ph.D. Thesis

Fachbereich: 05 Department of Physics

Quelle des Originals: <https://tuprints.ulb.tu-darmstadt.de/12235>

Design, installation and commissioning of new read-out electronics for HADES ECAL and diamond detectors for T0-reconstruction and beam diagnostics

Design, Installation und Inbetriebnahme einer neuen Ausleseelektronik für HADES ECAL und Diamant-Detektoren für die T0-Rekonstruktion und Strahldiagnose

Zur Erlangung des Grades eines Doktors der Naturwissenschaften (Dr. rer. nat.)

genehmigte Dissertation von Adrian Rost, M.Sc. aus Frankfurt am Main

Tag der Einreichung: 11.02.2020, Tag der Prüfung: 29.04.2020

Darmstadt 2020 – D 17

1. Gutachten: Prof. Dr. Tetyana Galatyuk

2. Gutachten: Jun.-Prof. Dr. Florian Hug



TECHNISCHE
UNIVERSITÄT
DARMSTADT

Fachbereich Physik
Institut für Kernphysik
AG Galatyuk (ViP-QM)

Design, installation and commissioning of new read-out electronics for HADES ECAL and diamond detectors for T0-reconstruction and beam diagnostics

Design, Installation und Inbetriebnahme einer neuen Ausleseelektronik für HADES ECAL und Diamant-Detektoren für die T0-Rekonstruktion und Strahldiagnose

Genehmigte Dissertation von Adrian Rost, M.Sc. aus Frankfurt am Main

1. Gutachten: Prof. Dr. Tetyana Galatyuk

2. Gutachten: Jun.-Prof. Dr. Florian Hug

Tag der Einreichung: 11.02.2020

Tag der Prüfung: 29.04.2020

Darmstadt – D 17

Bitte zitieren Sie dieses Dokument als:

URN: urn:nbn:de:tuda-tuprints-122352

URL: <http://tuprints.ulb.tu-darmstadt.de/12235>

Dieses Dokument wird bereitgestellt von tuprints,

E-Publishing-Service der TU Darmstadt

<http://tuprints.ulb.tu-darmstadt.de>

tuprints@ulb.tu-darmstadt.de



Die Veröffentlichung steht unter folgender Creative-Commons-Lizenz:

Attribution-NonCommercial-NoDerivatives 4.0 International (CC BY-NC-ND 4.0)

<https://creativecommons.org/licenses/by-nc-nd/4.0/>

Erklärung zur Dissertation

Hiermit versichere ich, die vorliegende Dissertation ohne Hilfe Dritter nur mit den angegebenen Quellen und Hilfsmitteln angefertigt zu haben. Alle Stellen, die aus Quellen entnommen wurden, sind als solche kenntlich gemacht. Diese Arbeit hat in gleicher oder ähnlicher Form noch keiner Prüfungsbehörde vorgelegen.

Darmstadt, den 14. September 2020

(Adrian Rost)



Abstract

This work deals with the design, installation and commissioning of the front-end electronics for the newly installed HADES electromagnetic calorimeter (ECAL) detector at GSI Helmholtzzentrum für Schwerionenforschung GmbH in Darmstadt. A Charge-to-Digital-Converter (QDC) and Time-to-Digital-Converter (TDC) based on a commercial FPGA (Field Programmable Gate Array) technology is used to read out 978 Photomultiplier tubes (PMT) of the ECAL. The charge measurement of the detector signals is based on a modified time-over-threshold (TOT) measuring method. In the context of this work the second generation of the PaDiWa-AMPS front-end board for the TRB3 (General Purpose Trigger and Readout Board - generation 3) was designed, tested in the laboratory and integrated into the HADES data acquisition infrastructure. The front-end achieves a time measurement precision of $\sigma_t = 16$ ps. The relative charge measurement precision for signal amplitudes above 1 V is below 0.5 %. A successful operation of the read-out system was shown during a four week physics production beam time with an 1.58A GeV Ag beam.

A similar read-out concept is used to read out diamond based beam detectors in the HADES experiment. Those detectors are used as a trigger and for the T0 determination in the HADES time-of-flight measuring system, which is important for the particle identification. Beside this, they are used for online beam monitoring purposes. The requirement for the time precision of the sensors is about 50 ps. Currently the read-out system is adapted to new Ultra-Fast Silicon Detector (UFSD) technology which might replace the diamond detectors in the HADES experiment in the future. A UFSD prototype detector has been tested successfully with a proton beam. Furthermore, it is planned to use this technology as a diagnostic instrument for Energy Recovery Linac (ERL) operations of the electron accelerator S-DALINAC at TU Darmstadt in future.

For further research and development of beam detectors a permanent multi-purpose detector test set-up was installed at the S-DALINAC. It allows tests of detectors with an electron beam with an energy up to 130 MeV and beam currents up to 20 μ A. The set-up has been successfully commissioned and offers optimal conditions for future tests for research and development of beam detectors with a beam of minimum ionizing particles.



Zusammenfassung

Diese Arbeit befasst sich mit dem Design, der Installation und der Inbetriebnahme der Ausleseelektronik für das neu installierte elektromagnetische Kalorimeter im HADES-Experiment am GSI Helmholtzzentrum für Schwerionenforschung GmbH in Darmstadt. Zum Auslesen von 978 Photomultiplier (PMT) des ECAL-Detektors wird ein Charge-to-Digital-Converter (QDC) und Time-to-Digital-Converter (TDC) basierend auf der kommerziellen Field Programmable Gate Array (FPGA) Technologie verwendet. Die Ladungsmessung der Detektorsignale basiert auf einem modifizierten Time-over-Threshold (TOT) Messverfahren. Im Rahmen dieser Arbeit wurde die zweite Generation des PaDiWa-AMPS Front-End-Boards für das TRB3 (General Purpose Trigger and Readout Board - Generation 3) entworfen, im Labor getestet und in die HADES-Datenerfassungs-Infrastruktur (DAQ) integriert. Das Front-End erreicht eine Zeitmesspräzision von $\sigma_t = 16$ ps. Die relative Ladungsmessgenauigkeit für Signalamplituden über 1 V liegt unter 0.5%. Ein erfolgreicher Betrieb des Auslesesystems wurde während einer vierwöchigen physikalischen Produktionsstrahlzeit mit einem Ag Strahl mit einer Energie von 1.58A GeV gezeigt.

Ein ähnliches Auslesekonzept wird für das Auslesen von diamantbasierten Strahldetektoren im HADES-Experiment verwendet. Diese Detektoren werden als Trigger und für die T0-Bestimmung im HADES-Flugzeitmesssystem verwendet, welches für die Identifizierung der Teilchen wichtig ist. Daneben werden sie für eine Online-Strahldiagnose eingesetzt. Die Anforderungen an die Zeitgenauigkeit der Sensoren liegen bei etwa 50 ps. Derzeit wird das Auslesesystem an die neue Ultra-Fast Silicon Detector (UFSD) Technologie adaptiert, welche in Zukunft die Diamantdetektoren im HADES-Experiment ersetzen könnten. Ein erster UFSD Prototyp-Detektor wurde mit einem Protonenstrahl erfolgreich getestet. Es ist geplant, diese Technologie in Zukunft als Diagnoseinstrument für den Energy Recovery Linac (ERL) Betrieb des Elektronenbeschleunigers S-DALINAC der TU Darmstadt einzusetzen.

Für die weitere Forschung und Entwicklung von Strahldetektoren wurde am S-DALINAC ein permanenter Mehrzweck-Detektor-Testaufbau installiert. Er ermöglicht Tests von Detektoren mit einem Elektronenstrahl mit einer Energie bis zu 130 MeV und einem Strahlstrom bis zu 20 μ A. Der Aufbau wurde erfolgreich in Betrieb genommen und bietet in Zukunft optimale Bedingungen um Tests für die Forschung und Entwicklung von Strahldetektoren mit einem Strahl aus minimal ionisierenden Teilchen durchzuführen.



Contents

1. Introduction	1
1.1. Exploration of strongly interacting matter in the laboratory	1
1.2. HADES physics program at SIS18 at GSI	3
1.3. HADES set-up	4
1.4. Motivation of this thesis	13
2. Calorimetry in HADES	15
2.1. Motivation for the possibility of an energy measurement in HADES	15
2.2. Basics of calorimetry in high energy physics	16
2.2.1. Working principle of a lead glass calorimeter	17
2.2.2. Photon detection with a photo-multiplier tube	18
2.2.3. Energy resolution of a calorimeter	19
2.3. The HADES electromagnetic calorimeter upgrade project	21
2.3.1. Lead glass calorimeter modules	22
2.3.2. Read-out requirements	22
3. FPGA based charge and time measurement principle for ECAL	25
3.1. Charge and time measurement method	25
3.2. General Purpose Trigger and Read-Out (TRB) platform	28
3.3. PaDiWa-AMPS2 front-end board for the TRB3 platform	28
3.4. Production of the second version of the PaDiWa-AMPS front-end board	30
3.4.1. SPICE model of the PaDiWa-AMPS2 board	30
4. Integration of the read-out electronics into the ECAL detector	33
4.1. ECAL support frame and module installation	33
4.2. Read-out electronics and network infrastructure inside ECAL	34
4.3. Read-out electronics installation and naming conventions	34
4.4. Low and high voltage distribution system	35
4.5. Integration of the read-out electronics into the HADES software structure	38
5. Characterization and commissioning of the ECAL read-out electronics	39
5.1. Characterization of the PaDiWa-AMPS2 board in the laboratory	39
5.1.1. Time measurement precision	39
5.1.2. Charge measurement precision	40
5.1.3. Dynamic measurement range and threshold settings	41
5.1.4. Rate capability	42
5.1.5. Power consumption and heat emission	43
5.1.6. Delay adjustment of the DISCHARGE signal	45
5.2. Commissioning of the read-out electronics in the ECAL detector	45
5.2.1. Slow control and DAQ-operator tools	46
5.2.2. Threshold settings	47
5.2.3. Commissioning with LASER signals, cosmic muons and test-beam	48
5.3. Performance issues and solutions	52
5.3.1. Cross-talk and alternative charge measurement method	52
5.3.2. SLOW channel failure	55
5.3.3. Electromagnetic shielding of PMTs and quality testing	55

6. Read-out electronics performance during the HADES Ag+Ag run	59
6.1. Stability of the read-out electronics	59
6.2. Verification of the "overshoot" charge measurement method	59
6.3. Time and energy calibration in ECAL	61
6.4. Reconstruction of the neutral pion decay	62
7. Beam diagnostics and T0 reconstruction in HADES	65
7.1. Aspects of diamond detectors	65
7.1.1. Diamond material properties	65
7.1.2. Working principle of diamond detectors	66
7.1.3. Charge collection efficiency	68
7.2. T0 reconstruction and beam diagnostics during the HADES Ag+Ag run	68
7.2.1. Diamond detectors, read-out and online monitoring system	69
7.2.2. Beam profile and position measurement	71
7.2.3. Spill profile, time structure and quality factor	71
7.2.4. Precision of the reaction time (T0) reconstruction	73
7.3. Research and development of Ultra-Fast Silicon Detectors for HADES	74
7.3.1. Working principle of Ultra-Fast Silicon Detectors	74
7.3.2. Performance study with proton beam at the COSY facility	76
8. Multi-purpose detector test set-up at the S-DALINAC	79
8.1. S-DALINAC in Energy Recovery Linac mode	79
8.2. Aspects of beam dynamics	83
8.2.1. Dipole magnet	83
8.2.2. Quadrupole magnet	85
8.2.3. Linear beam dynamics	86
8.2.4. Beam profile	90
8.2.5. Beam dispersion	90
8.3. Construction of a multi-purpose detector test set-up at the S-DALINAC	91
8.3.1. Beam transport simulations	92
8.3.2. Dipole magnets, quadrupole magnets and power supplies	93
8.3.3. Vacuum chamber	94
8.3.4. Exit window	96
8.3.5. Test set-up	97
8.3.6. Beam dump	97
8.4. Installation and alignment of beam elements	99
8.5. Commissioning of the detector test set-up	100
9. Summary and outlook	105
A. Appendix	107
A.1. Technical drawings	107
A.2. Schematics	120
A.3. Magnet currents during the beam commissioning at S-DALINAC	123
A.4. Beam dynamic simulation to the beam dump in vacuum	123
A.5. PaDiWa-AMPS2 delay adjustment values	124

List of Figures

1.1	Evolution of a heavy ion collision	2
1.2	The conjectured QCD phase diagram of strong-interaction matter	3
1.3	HADES cylindrical panorama composite	4
1.4	Reconstructed e^+e^- invariant mass distribution from Au + Au collisions measured by the HADES collaboration	5
1.5	Transverse section view of the HADES detector layout	6
1.6	Arrangement of the Start-Target-Veto System and photography of the target	6
1.7	Schematic drawing of an MDC chamber and schematic drawing of a MDC drift cell	7
1.8	Correlation between the specific energy loss in MDC and the momentum measured with the RPC	8
1.9	Visualization of the time-of-flight measurement system in HADES	8
1.10	HADES multi-gap RPC cell layout and schematic drawing of an RPC sector	9
1.11	Particle separation in the HADES detector using information of time-of flight and momentum	10
1.12	Schematic drawing of the RICH detector and picture of the RICH detector looking into beam direction	11
1.13	Typical response pattern of the RICH photon detection plane in a Ag+Ag heavy ion collision	11
1.14	Computer animation of the ECAL detector	12
1.15	Simplified HADES DAQ system	12
1.16	Interaction rates achieved by existing and planned heavy-ion experiments as a function of center-of-mass energy	13
2.1	Excess radiation as a function of center-of-mass beam energy and simulation of multiplicities for different beam energies of the π^0 , η , and ω mesons	15
2.2	Energy measured by ECAL vs. momentum \times charge for Ag+Ag at 1.58A GeV beam data	16
2.3	Idealized electromagnetic shower production in a calorimeter and electromagnetic shower simulation for a 20 GeV e^- in a HADES ECAL lead glass module	18
2.4	Working principle of a Photomultiplier Tube (PMT)	19
2.5	Energy resolution of a HADES ECAL module	20
2.6	Technical drawing of the ECAL detector	21
2.7	Photography of the HADES set-up	21
2.8	Schematic drawing of an ECAL module	22
2.9	Raw signals of an ECAL module containing a 3-inch Hamamatsu R6091 PMT	23
2.10	Raw signals of an ECAL module containing a 1.5-inch EMI 9903KB PMT	23
3.1	Simplified read-out scheme of the HADES ECAL detector	25
3.2	Simplified time and charge measurement principle	26
3.3	Signal discrimination via the LVDS input buffer	27
3.4	Schematics of the PaDiWa-AMPS2 board	27
3.5	Typical signal shapes on the PaDiWa-AMPS2	28
3.6	Photography of the TRB3 and TRB3sc boards	29
3.7	Photography of the PaDiWa-AMPS2 board	30
3.8	Top layer view of the new PaDiWa-AMPS2 PCB layout	31
3.9	LTspice model of the PaDiWa-AMPS2 circuit	32

3.10	LTspice simulation, comparing FAST and SLOW signals of the obsolete BFS520 transistor with its replacement BFU550W	32
4.1	Cylindrical panorama composite of ECAL	33
4.2	Front view of the ECAL mainframe	34
4.3	Read-out scheme of the HADES ECAL detector	35
4.4	CAD drawing of the infrastructure in the ECAL mainframe	36
4.5	Description of two standard 19-inch racks housing ECAL infrastructure	36
4.6	ECAL module grouping scheme	37
4.7	Location of the TRB3sc boards in the ECAL mainframe	37
4.8	Side view into sector number 5	38
5.1	Laboratory test set-up for the characterization of the PaDiWa-AMPS2 prototype.	39
5.2	Laboratory set-up for the time precision determination and distribution of the measured time difference of the two FAST leading edges	40
5.3	Measured Q2ToT for different input pulse charges	41
5.4	Relative charge measurement precision.	42
5.5	Illustration of time-walk and jitter effects of a discriminated signal pulse	43
5.6	Multi-peak structure visible in the Q2ToT time-over-threshold measurement	43
5.7	Saturation of the SLOW signal	44
5.8	Rate capability of the read-out electronics.	44
5.9	Temperature measurement with an infrared camera.	45
5.10	Schematic drawing of the DISCHARGE signal delay inside the FPGA	46
5.11	Visualization of the delayed DISCHARGE signal	46
5.12	Central monitoring tool in HADES.	47
5.13	ECAL monitoring tool which shows the FAST signal rate in s^{-1} which is displayed for each module	48
5.14	Relative position of the baselines for FAST and SLOW channels	49
5.15	Noise width of the baseline for FAST and SLOW channels	49
5.16	Schematic picture of the ECAL LASER system	50
5.17	Oscilloscope reference measurement of the signal-pulse-area (\sim charge) distribution of an ECAL module which is equipped with a 3-inch PMT obtained with LASER light.	50
5.18	PaDiWA-AMPS2 input channels number 5 and 7 show a non-physical gap at measured Q2ToT of about 65 ns.	52
5.19	Cross-talk between DISCHARGE signal and SLOW signal.	53
5.20	Explanation of the "overshoot" SLOW measurement method	54
5.21	Q2ToT measurement precision for the overshoot method	54
5.22	High amplitude noise signal and oddly shaped wide PMT signals	56
5.23	Active electrostatic shielding of a PMT	57
5.24	Module calibration procedure	58
5.25	Difference of the new HV settings to the previous HV settings	58
6.1	HADES run statistic for the March 2019 Ag+Ag 1.58A GeV production beam time.	59
6.2	Configuration of the ECAL detector during the Ag beam time in March 2019	60
6.3	Verification of the overshoot charge measurement method	60
6.4	Time walk correction	61
6.5	Connection of measured Q2ToT and signal amplitude	62
6.6	Energy calibration of the measured Q2ToT with the help of electrons	63
6.7	Reconstruction of the neutral pion decay	63
6.8	Dielectron invariant mass distribution reconstructed in Ag+Ag collisions at 1.58A GeV	64

7.1	Stopping power $-\left\langle \frac{dE}{dx} \right\rangle$ for positive muons in copper as a function of $\beta\gamma = p/Mc$. . .	67
7.2	Mean energy loss of electrons/positrons in diamond and Si.	67
7.3	Working principle of a diamond detector	68
7.4	Close-up photography of the CVD diamond sensors in HADES.	69
7.5	HADES diamond detector system mounted on a PCB plates.	70
7.6	Read-out scheme of the HADES diamond detector	70
7.7	Online beam monitoring system	71
7.8	Beam profile measurement in x - and y -direction	72
7.9	Particle fluence on the HADES diamond detector	72
7.10	Macro- and micro-spill time structure measured by the scCVD diamond sensor	73
7.11	Quality factor of the Ag beam	73
7.12	Working principle of a Low-gain avalanche detector.	75
7.13	Close-up picture of the prototype UFSD sensor for HADES	75
7.14	Read-out scheme of the UFSD prototype detector.	76
7.15	UFSD telescope set-up used for a beam time at the COSY facility.	76
7.16	Time difference between the first and the second sensor using the NINO and PaDiWa discriminators.	77
8.1	Cylindrical panorama composite of the S-DALINAC main hall	79
8.2	Principle of a once recirculating ERL operation applied to the S-DALINAC	80
8.3	S-DALINAC: main accelerator hall.	81
8.4	S-DALINAC: extraction beamline	82
8.5	H-yoke dipole magnet	84
8.6	Magnetic flux density of a magnet as a function of the location	85
8.7	Focusing effects in a sector magnet and definition of the edge angles	85
8.8	Cross section view of a quadrupole magnet	86
8.9	Illustration of the moving coordinate system.	87
8.10	Two dimension phase space ellipse in the x - x' -plane	88
8.11	Gaussian density distribution of a beam profile.	90
8.12	Visualization of the transverse dispersion	91
8.13	Overview plan of the detector test set-up at the S-DALINAC.	91
8.14	Beam dynamics calculations for the NEPTUN beamline using the original lattice	93
8.15	Beam dynamics calculations for the NEPTUN beamline with an additional pair of quadrupoles added.	93
8.16	Beam dynamics calculations from the main linac extraction to the detector test set-up	94
8.17	Beam dynamics calculations of the beam dispersion from the main linac extraction to the detector test set-up	94
8.18	Schematic drawing and photograph of the support structure for the dipole magnet	95
8.19	Vacuum chamber of the twice recirculating S-DALINAC	96
8.20	Reconstruction of the original deflecting angles and construction of new deflecting angles and design of a new vacuum chamber	96
8.21	Exit window made of aluminum	97
8.22	Side and top view of the detector test set-up.	98
8.23	Example of a set-up for silicon and diamond detector tests	98
8.24	Schematic view of the beam dump	99
8.25	Alignment of quadrupoles in the E5-"kleine Halle" area	100
8.26	Vertical alignment of the vacuum chamber and two quadrupoles.	101
8.27	Commissioning of the new detector test set-up.	101
8.28	Camera picture of the E5T2 target.	102
8.29	Projection of the E5T2 target picture on the horizontal and vertical axis.	102

8.30	Camera picture of the E5R1 target103
8.31	Projection of the E5R1 target picture on the horizontal and vertical axis.103
A.1	Technical drawing: PaDiWa-AMPS2 mounting bracket for ECAL107
A.2	Technical drawing: Fully assembled dipole magnet support structure108
A.3	Technical drawing: Dipole magnet support structure: Base frame109
A.4	Technical drawing: Dipole magnet support structure: Top plate110
A.5	Technical drawing: Dipole magnet support structure: Adjustment bracket111
A.6	Technical drawing: Dipole magnet support structure: Fully assembled top plate.112
A.7	Technical drawing: Vacuum chamber for the dipole magnet.113
A.8	Technical drawing: Dipole magnet and vacuum chamber.114
A.9	Technical drawing: Vacuum chamber for the dipole magnet - part 1115
A.10	Technical drawing: Vacuum chamber for the dipole magnet - part 2116
A.11	Technical drawing: Aluminum exit window117
A.12	Technical drawing: Beam tube holder - upper part118
A.13	Technical drawing: Beam tube holder - lower part119
A.14	Schematics: Analog part of the first channel of the PaDiWa-AMPS2 front-end board120
A.15	Schematics: Analog part of the first channel of the PaDiWa-AMPS1 front-end board121
A.16	Schematics: 5V-distribution board.122
A.17	Beam dynamics calculations from the main linac extraction to the beam dump of the detector test set-up.123
A.18	PaDiWa-AMPS2 delay adjustment values124

List of Tables

3.1. Summary of some key facts of the TRB3 platform	29
5.1. Minimal FAST thresholds values from which cross-talk occurs in adjacent FAST channels .	55
7.1. Material properties of diamond and Si	66
8.1. S-DALINAC beam parameters at the detector test set-up	80
8.2. Parameters used for the X-BEAM beam transport simulations	92
8.3. Physical parameters of the dipole magnet	95
A.1. Magnet current set values in order to focus the beam on the E5T2 target	123
A.2. Magnet current set values in order to focus the beam on the E5R1 target	123



1 Introduction

Particle accelerators play an important role in a wide range of scientific discoveries and industrial applications. The interest in accelerating particles can be dated back to a remarkable experiment which was conducted by Ernest Rutherford [1] at the beginning of the 20th century. He demonstrated that the atom has a structure which consists of a heavy positively charged *nucleus*, surrounded by negatively charged *electrons*. Further experiments, using particle accelerators, revealed *protons* and *neutrons* as constituents of the nucleus. Today it is assumed that the basic building blocks of the *nucleons* (protons and neutrons) are so-called *quarks*.

Accelerators can be divided into two basic classes: *electrostatic* and *electrodynamic accelerators*. Electrostatic accelerators use static electric fields to accelerate particles. The achievable kinetic energy for particles in these devices is determined by the accelerating voltage, which is limited by electrical breakdown. Electrodynamic accelerators use changing electromagnetic fields to accelerate particles. This type of accelerator allows the particles to pass through the same accelerating field multiple times. The output energy is therefore not limited by the strength of the accelerating field.

A *linear particle accelerator* (linac) is a type of particle accelerator which allows to accelerate charged subatomic particles or ions to a high speed by subjecting them to a series of oscillating electric potentials along a linear beamline. Linacs have many applications: they generate X-rays and high energy electrons for medical purposes in radiation therapy, serve as particle injectors for higher-energy accelerators, and are used directly to achieve the highest kinetic energy for light particles (electrons and positrons) for particle physics.

Circulation accelerators are particle accelerators in which the charged particles repeatedly follow an approximately spiral or circular path. The advantage is that the particles can use the same acceleration paths again and again. A circular accelerator is therefore more economical and, for high final energies, more space-saving than a comparable linac. The disadvantage is that at sufficiently high speed the particles emit synchrotron radiation because of the necessary deflection, and thus lose energy.

A kind of "green" accelerator is the *Energy Recovery Linac* (ERL). In this type of accelerator a beam is accelerated by passing an accelerating cavity. Afterwards the beam is sent back through the same cavity, but this time decelerating. The beam's energy is captured and made available for new particles to be accelerated. This technique allows to achieve brighter beams, which would have required too much energy in a conventional accelerator.

Worldwide there are more than 30,000 [2] accelerators in operation. A large fraction is used for medical purposes. For example the irradiation with strongly interacting hadrons, such as protons or carbon nuclei, allows a more precise energy input than conventional tumor therapy. Thus, the surrounding tissue is less damaged and a large part of the dose is delivered into the tumor.

Only few hundred accelerators in the world serve research. Nevertheless, they play a major role in material science and fundamental research, e.g. structure of nuclei, the nature of nuclear forces, properties of nuclei not found in nature and to create and investigate strongly interacting matter in the laboratory.

1.1 Exploration of strongly interacting matter in the laboratory

Particle accelerators in combination with particle detectors provide an experimental access in order to study matter under conditions as it exists a few microseconds after the *Big Bang* (13.8 billion years ago [3]), or matter created in astrophysical processes like neutron star mergers [4], which take place hundreds of light years away from us.

In order to produce matter under extreme conditions of temperature, density, isospin, in the laboratory, particles are accelerated to almost the speed of light in a particle accelerator and afterwards brought to collision. A schematic evolution of a heavy-ion collision is shown in Fig. 1.1. The collision can be divided into various steps. In the first step, nucleon-nucleon interactions with a high energy transfer occur. If the energy-density is high enough, a *quark-gluon-plasma* may be created. This state of matter

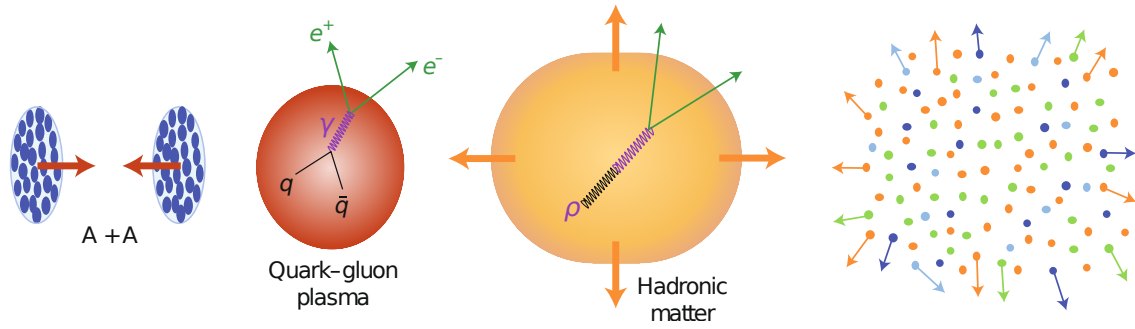


Figure 1.1.: Evolution of a heavy ion collision. Two Lorentz-contracted nuclei $A + A$ collide and form a *fireball* of strongly interacting matter. Important steps are the formation of a quark–gluon plasma, and hot and dense hadronic matter before freeze out of the system. In all steps dileptons (e^+e^- pairs) are created via virtual photons γ from quark-antiquark ($q\bar{q}$) annihilations or ρ -meson decays. They do not undergo strong interactions and therefore provide an ideal probe for the microscopic properties, e.g. temperature and density of the dense and hot medium which is created in the collision. (Taken from [5])

is thought to consist of asymptotically free strong-interacting quarks and gluons which are ordinarily confined by color confinement inside atomic nuclei or other hadrons. Due to the expansion, temperature and density of the system will decrease with time. This stage of the collision is often called *hot and dense hadronic phase*. The last step of the collision can be separated into a *chemical freeze-out*, where inelastic scatterings stop, and a *kinetic freeze-out*, when elastic collisions terminate and thus individual particle momenta remain constant.

Strongly interacting matter at extreme conditions can be investigated by the measurement of different observables, e.g. fluctuations of overall conserved quantities, correlations, flavor production or dileptons. *Dileptons* (e^+e^- or $\mu^+\mu^-$ pairs) are created in all steps of the heavy-ion collision via the decay of *virtual photons* γ^* (e.g. from quark-antiquark ($q\bar{q}$) annihilation or ρ -meson decays). Dileptons are interesting since they do not undergo strong interactions and therefore provide an ideal probe for the microscopic properties of the dense and hot medium which is created in the collision.

Of particular interest are the light vector mesons ρ , ω and ϕ which have the same quantum numbers as virtual photons ($J^P = 1^-$), with the ρ meson playing a particular role. The ρ meson has a very short life time ($\tau_\rho \approx 1$ fm) and thus decays into a e^+e^- pair inside the fireball ($\tau_{\text{fireball}} \approx 10$ fm). The light vector mesons decay mainly in a hadronic channel, but with a very small probability they can decay into an e^+e^- pair. This is a very rare process. For example, the branching ratio of a ρ meson into e^+e^- is $4.72 \cdot 10^{-5}$ [6].

Since dileptons are rare probes, a high interaction-rate detector with a high acceptance and low material budget is needed. The detector should be able to operate at high read-out frequencies in order to obtain a large statistic, which is essential for later data analysis. All this requirements are fulfilled by the HADES detector which will be introduced in the following Sections 1.2 and 1.3.

In addition to the study of the microscopic structure of matter, the study of its various forms is a major research field. The *quantum chromodynamics* (QCD) *phase diagram* describes the behavior of nuclear matter as a function of *temperature* T and the *net-baryon density* or *baryochemical potential* μ_B , which is a measure of the difference between the number of particles and antiparticles in a system. The phase diagram of quark matter is up to now not well known, either experimentally or theoretically.

Up to now *lattice-QCD* (lQCD) calculations are the only known theoretical method which addresses the thermodynamics of quarks and gluons for vanishing baryochemical potential ($\mu_B = 0$). The theory predicts the restoration of *chiral symmetry* and *deconfinement* via a crossover at the *critical temperature* of $T_c = 156 \pm 1.5$ MeV [7].

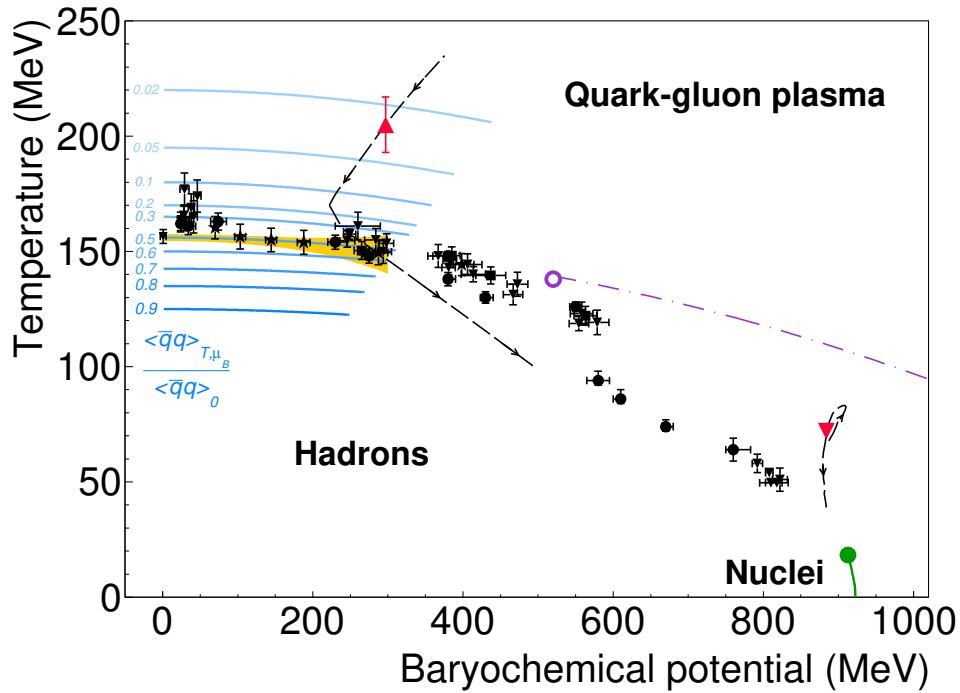


Figure 1.2.: The conjectured QCD phase diagram of strong-interaction matter. The black symbols are experimental data points. The expectation values of the chiral condensate relative to the vacuum as constrained by QCD are depicted as blue curves. The yellow band is the crossover region. The dotted–dashed purple curve shows the conjectured first-order phase transition, which terminates in a second-order QCD critical point (open purple circle). The red upright triangle displays the temperature deduced from the dimuon invariant-mass spectrum measured by the NA60 Collaboration [11], while the red inverted triangle is the result of the HADES Collaboration, reported in [12]. The two black dashed curves indicate the corresponding predicted evolution of the fireball parameters. The solid green curve marks the first-order liquid–gas phase transition in nuclear matter, terminating in the critical end point (green circle). (Taken from [12])

For larger net-baryon densities and lower temperatures, QCD inspired *effective field theories* predict a structure of the QCD phase diagram. A first order phase transition into a deconfined phase which terminates in a second order *critical point* (CP) or exotic phases like *quarkyonic matter* are predicted [8] and remains to be addressed experimentally.

The QCD phase diagram can be probed experimentally with heavy-ion collisions by varying the collision energy and geometry [9]. The freeze-out parameters (T , μ_B) can be extracted from statistical model fits [10] to the final hadron abundances. The conjectured phase diagram of QCD matter is shown in Fig. 1.2. Up to now the location of the onset of a deconfined phase and the CP is not detected, which hides still a large discovery potential.

1.2 HADES physics program at SIS18 at GSI

The *High Acceptance DiElectron Spectrometer* (HADES) [13] is in operation at *GSI Helmholtzzentrum für Schwerionenforschung GmbH* in Darmstadt since 1994. The spectrometer has been designed as a fixed target experiment at the SIS18 (heavy ion synchrotron, 18 Tm rigidity). The physics program of the HADES collaboration is focused on beam energies between 1A GeV for heavy-ions and 3.5 GeV for proton beams in order to study the properties of baryon rich matter ($\mu_B \approx 700$ MeV) at moderate temperatures ($T \leq 70$ MeV). The main topics are the mechanism of strangeness production, the emissivity

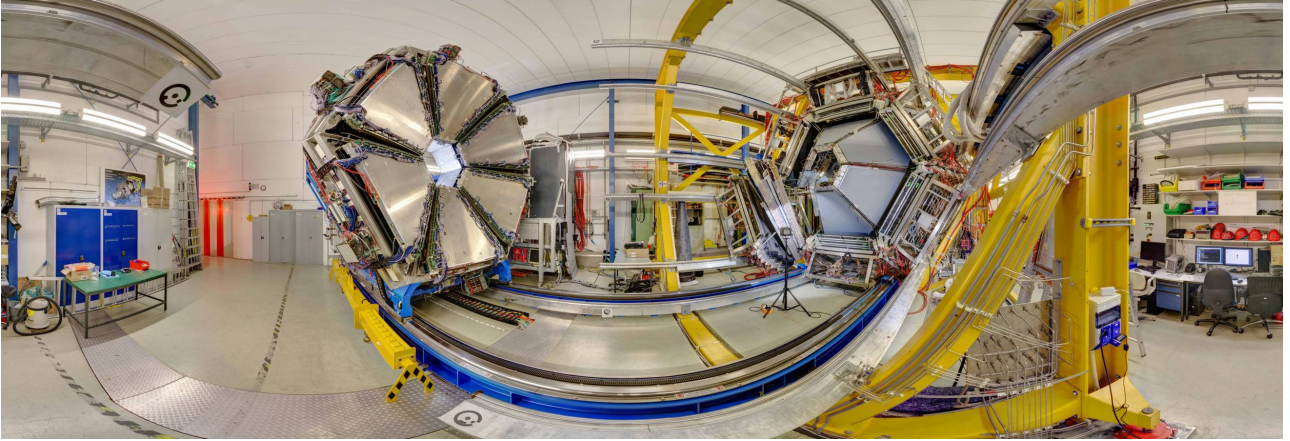


Figure 1.3.: Cylindrical panorama composite of the HADES experimental cave at *GSI Helmholtzzentrum für Schwerionenforschung GmbH* in Darmstadt. On the left side one can see the ECAL and RPC detectors which are mounted on a rail system and parked in service position. On the right side a yellow colored main frame and the back planes of MDC and TOF detectors are visible. Almost each subsystem of HADES is segmented into six trapezoidal sectors. (Picture taken in February 2019)

of resonance matter and the role of baryonic resonances herein. In Fig. 1.3 a panoramic picture of the HADES experiment is shown.

Up to now, HADES conducted several measurement campaigns, e.g. proton on H_2 and Nb targets, deuteron on H_2 , C on C, Ar on KCl, Au on Au, Ag on Ag. Au+Au at 1.25A GeV, the highest energy for heavy-ions available at SIS18, is the heaviest system measured so far. The possibility to carry out experiments with HADES using a secondary pion beam, e.g. π^- beam on C and PE [14], is unique. Those experiments provide a chance to study the coupling of virtual photons to baryonic resonances by means of the reaction $\pi N \rightarrow R \rightarrow e^+e^-N$. Besides that, one could study one- and two- pion production channels, strangeness (K^\pm, K_S^0, ϕ) production in π -nucleus reactions, as well as hyperon production.

The HADES collaboration is currently continuing its physics program at SIS18 in the view of *FAIR Phase 0*. This is an intermediate forefront research program at GSI with improved beam quality and FAIR detectors. At future SIS100 (heavy ion synchrotron, 100 Tm rigidity), which will be in operation at *Facility for Antiproton and Ion Research* (FAIR), the HADES spectrometer will be part of the *Compressed Baryonic Matter* (CBM) experiment [15]. It is planned to move the set-up in front of the CBM detector system in order to continue the physics program especially at collision energies up to 29 GeV for elementary and 4.5A GeV for medium-heavy systems. The CBM experiment will be able to measure heavy systems at maximal energies up to 12A GeV.

One of the recent highlights from HADES is the measurement of thermal radiation from baryon-rich matter. A reconstructed e^+e^- invariant mass distribution from Au+Au collisions is shown in Fig. 1.4. The HADES experiment reconstructed thermal dilepton radiation in collisions of heavy-ions at energy of 1.23A GeV [12]. In this so-called *low-mass region* the spectrum consists of overlapping contributions from different sources. Unfortunately, Dalitz decays mostly from, $\pi^0 \rightarrow e^+e^-\gamma$ and $\eta \rightarrow e^+e^-\gamma$ are contributing to a physics background that complicates the determination of the thermal dilepton yield. A newly installed *electromagnetic calorimeter* (ECAL), which will be introduced in Chapter 2, will play an important role in future measurement campaigns. The ECAL will allow to study via photon measurements π^0 , η and will provide a better electron-to-pion separation for large momenta.

1.3 HADES set-up

The HADES set-up covers polar angles from 18° up to 85° and nearly the full azimuthal angular range. The identification of electrons, pions, kaons, protons and light nuclei is possible by means of time-of-

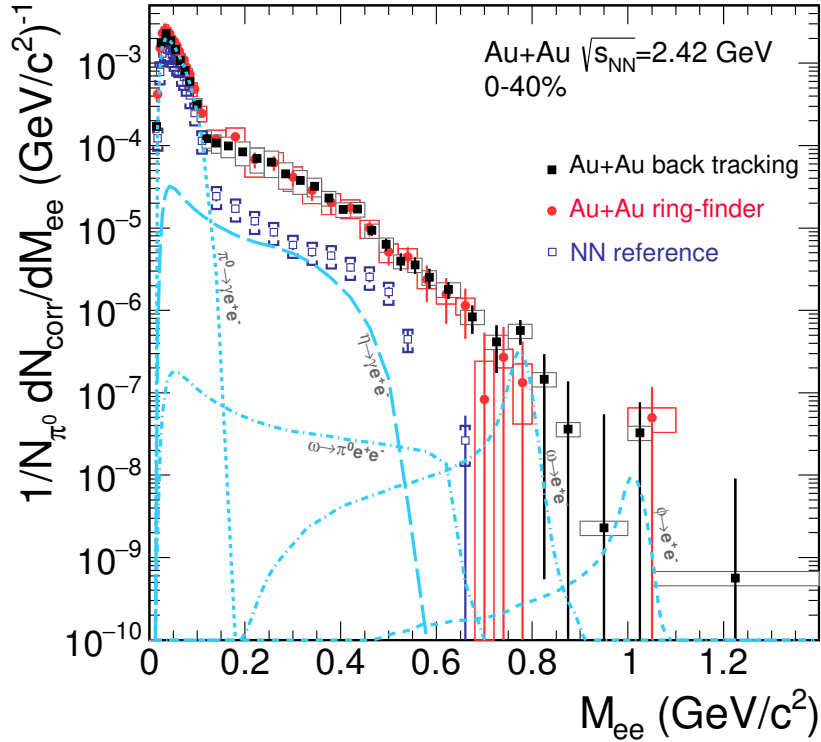


Figure 1.4.: Reconstructed e^+e^- invariant mass distribution from Au + Au collisions measured by the HADES collaboration. Back tracking and ring-finder analysis strategies are compared to the NN reference spectrum. The blue curves represent the π^0 , η and ω Dalitz components, as well as ω and ϕ direct decays after decoupling from the fireball. (Taken from [12])

flight, particle tracking, momentum and energy loss measurements. Most detector subsystems of the HADES consist of six trapezoidal sectors which are arranged in a hexagon. A transverse section view of the detector layout is shown in Fig. 1.5. The main components are the *Ring Imaging Cherenkov* (RICH) detector for electron and positron identification. A tracking system consisting of four planes of *Mini Drift Chambers* (MDC), two located in front of and two behind a superconducting magnet. A time-of-flight system consisting of the Start-Target-Veto System, a *Resistive Plate Chamber* (RPC) and a scintillator based *Time-of-Flight Wall* (TOF). An energy measurement can be performed with an *electromagnetic calorimeter* (ECAL). A *Forward Hodoscope Wall* is used for the event plane reconstruction and centrality determination. The high performance *Data Acquisition System* (DAQ), which deals with about 100 000 individual front-end channels, reaches event rates up to 100 kHz for p+p and 20 kHz for Au+Au collision systems. The data writing capability is up to 400 MBytes/s.

During the last years its subsystems have been continuously improved and upgraded. Recently the ECAL was installed and the photon detection plane of the RICH detector was upgraded. In the following each subsystem will be described shortly.

Start-Target-Veto system

The *start-veto* detector system [17, 18] in the HADES experiment consists of two sensors made of *Chemical Vapor Deposition* (CVD) diamond material. The first sensor, a *single-crystal Chemical Vapor Deposition* (scCVD) diamond based sensor, is located about 2 cm in front of the target. This detector is used to determine the *reaction time* (T0) with a precision of about 50 ps. Besides this, it is used for beam diagnostic purposes. A second *poly-crystal Chemical Vapor Deposition* (pcCVD) based sensor is located 70 cm behind the target with the task to *veto* beam particles which show no interaction in the target. The detectors are aligned with the beam axis and the beam is focused on the target. In order to reduce photon conversion

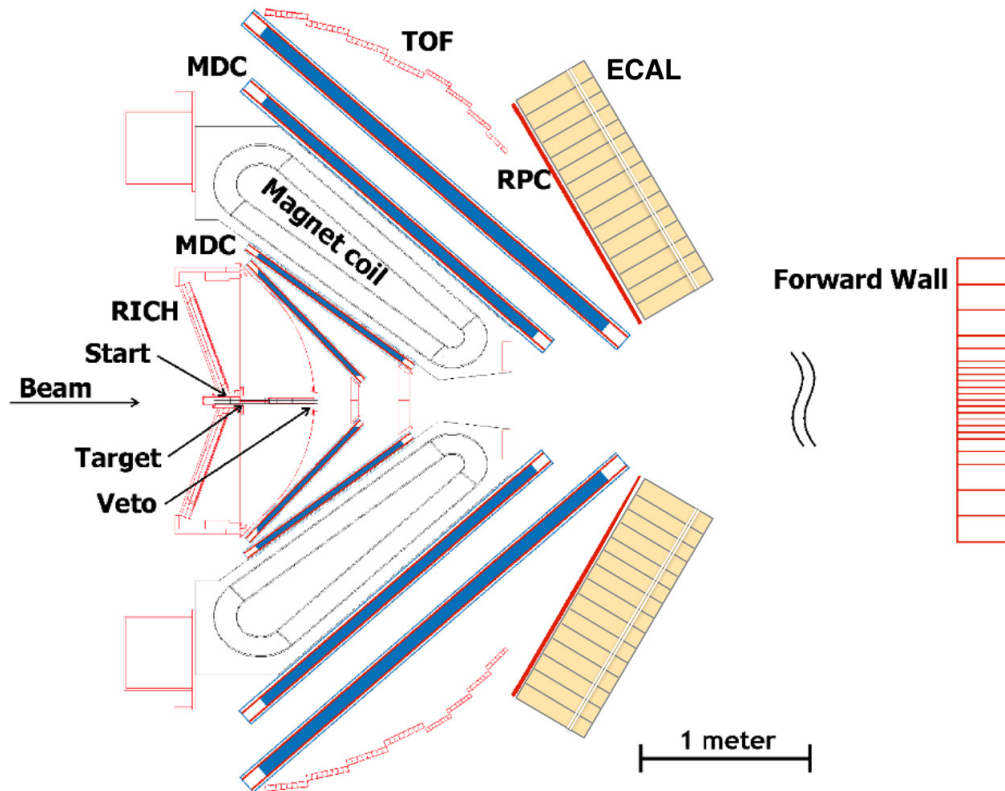


Figure 1.5.: Transverse section view of the HADES detector layout. The beam hits a segmented target which is surrounded by the RICH detector used for electron/positron identification. The magnet spectrometer consists of two double layers of drift chambers in front of and behind a toroidal magnetic field region. A time-of-flight measurement is possible with a scintillator based TOF detector and an RPC detector. Energy measurement is possible with the ECAL detector. A *Forward Hodoscope Wall* is used in order to determine the centrality and the reaction plane of the heavy ion collisions. (Taken from [16])

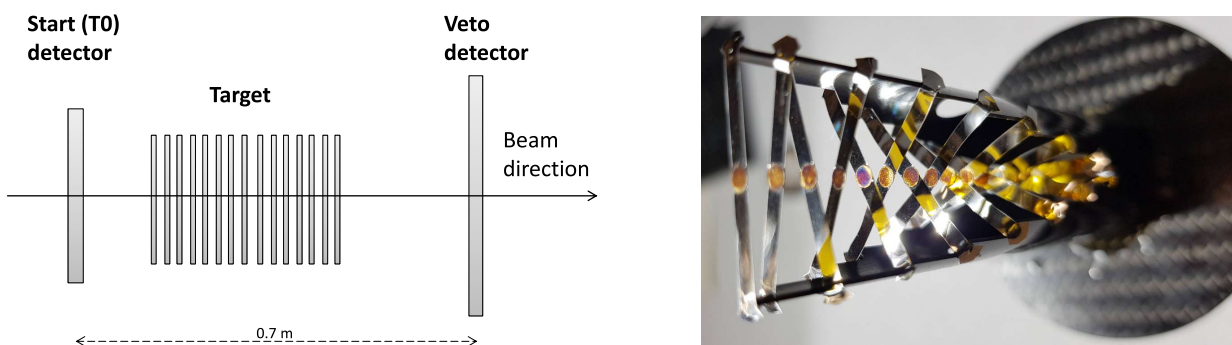


Figure 1.6.: Left: Arrangement of the Start-Target-Veto System. Right: Photography of the fifteen times segmented Ag target which was used during the HADES Ag+Ag production beam.

in the target region, the target consists of 15 silver foils which are glued on kapton foils. The target foils are held in place with the help of a carbon fiber structure which is placed inside the RICH detector. The arrangement of the diamond detectors and the target is shown in Fig. 1.6. A more detailed description of the diamond sensors and its read-out system will be given in Section 7.2.1.

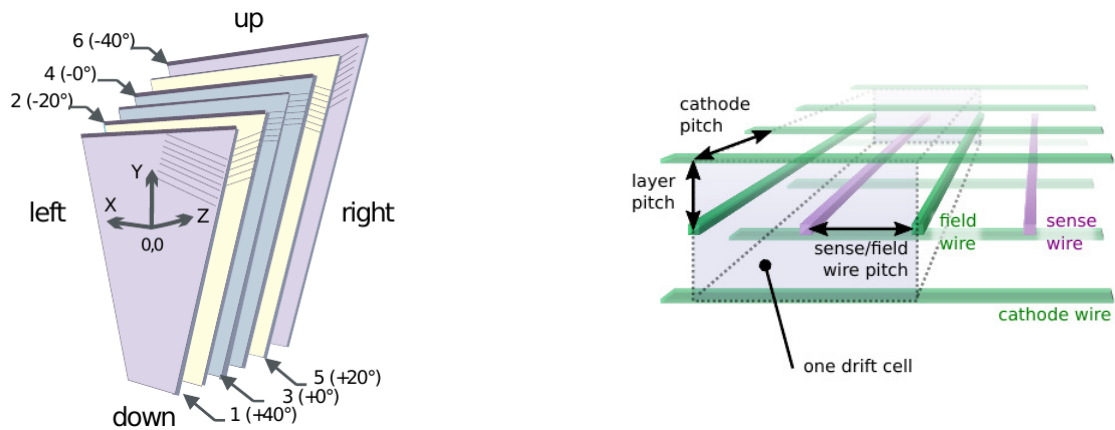


Figure 1.7.: **Left:** A MDC chamber is made out of six layers of drift cells. The different inclinations of sense and field wires in the layers are shown. All cathode wires are aligned in y -direction and are not shown. (Taken from [13]) **Right:** The definition of the MDC drift cell, defined by a sense wire which is delimited by field wires and cathode wires. (Taken from [20])

Particle tracking system

The tracking of charged particles is realized by four planes of *Mini Drift Chambers* (MDCs) [19]. Two planes are placed in front of and two behind a superconducting magnet (see Fig. 1.5). This system allows the tracking of charged particles and their momentum reconstruction by measuring the deflection angle of particles traversing the magnetic field. It is also possible to identify charged particles by energy loss measurements inside the chambers. The magnet consists of six superconducting NbTi coils. A toroidal magnetic field is generated with a gradient from 3.6 T at the coil surface to 0.8 T in the center of HADES. Polar angles between 18° and 85° are covered by the system. Each plane consists of six chambers. A chamber is composed out of six layers of drift cells. A single drift cell consists of two layers of cathode wires. Two field wires, which are made of Al with a thickness of $100\ \mu\text{m}$, are under high voltage and therefore provide an electrical field. A gold plated tungsten sense wire with a thickness of $20\ \mu\text{m}$ is used as an anode in between the field wires. The field and sense wire planes have an orientation of 0° , 20° and 40° in relation to the normal on the symmetry axis of the module. In Fig. 1.7 a schematic drawing of an MDC chamber is shown and the definition of the drift cell is given. Depending on the MDC type, a mixture of argon and CO_2 (70% : 30%) or a mixture of argon and isobutane (84% : 16%) is used as counting gas. A traversing charged particle ionizes the counting gas. Consequently, electrons are accelerated towards the sense wires. Close to the wires an avalanche is created because of the high electric field gradient. In total, about 30 000 channels have to be read out. Currently, the read-out electronics is planned to be upgraded [20] in order to archive a higher rate capability besides improving the reliability.

With the help of the momentum, which can be reconstructed by the tracking system and an dE/dx energy loss measurement, particles in the HADES detector can be identified. An example is shown in Fig. 1.8.

Time-of-flight measurement system

The *time-of-flight* (ToF) measurement is realized by three detectors. A diamond based beam-detector (start detector), which is located in front of the target, is used in order to determine the start time of a reaction in the target. A scintillator based *Time of Flight Wall* (for polar angles $44^\circ < \Theta < 88^\circ$) and *Resistive Plate Chambers* (for polar angles $18^\circ < \Theta < 45^\circ$), which are both located about 3 m upstream of the target, are measuring the arrival time of charged particles. The time-of-flight measurement principle in HADES is schematically visualized in Fig. 1.9.

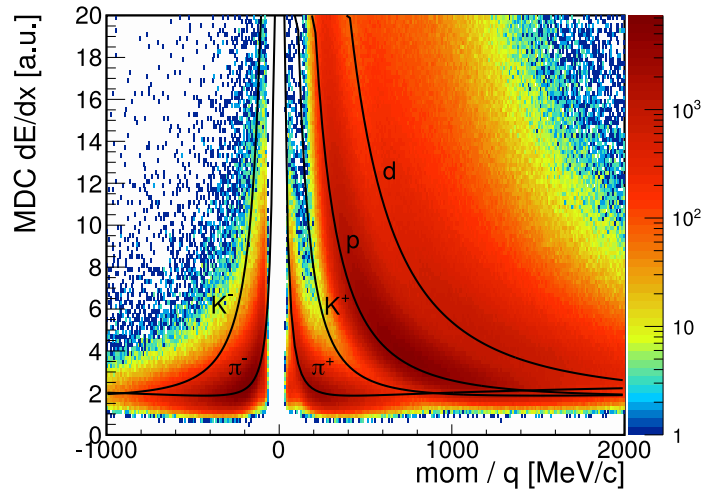


Figure 1.8.: Correlation between the specific energy loss in MDC and the momentum measured with the RPC which can be used for particle separation. Theoretical particles curves are indicated in black. Electrons, pions, protons, kaons and also heavy fragments (i.e. deuterium) are separated. (Taken from [21])

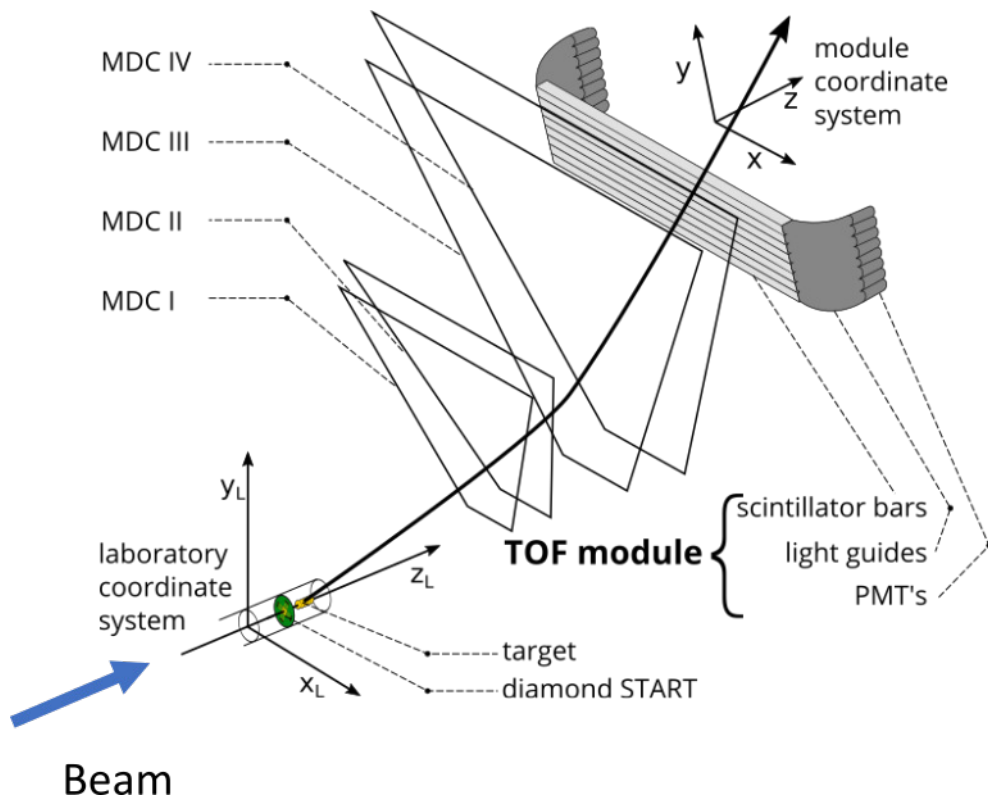


Figure 1.9.: Visualization of the time-of-flight measurement system in HADES using a diamond based Start detector and the TOF and RPC (not shown) detectors. The TOF detector consists of plastic scintillators which are read out by PMTs on both sides. The flight path can be reconstructed by the MDC tracking system. (Taken from [22])

Each sector of the *Time-of-Flight Wall* (TOF) [23] detector consists of 48 plastic scintillation rods which are arranged in sets of eight modules, enclosed in a carbon fiber case. The cross section is $20 \times 20 \text{ mm}^2$ for the innermost 192 rods and $30 \times 30 \text{ mm}^2$ for the 192 outermost rods. The rod length varies from 1 m to 2 m, respectively, from smaller to larger polar angles. Each rod is made of Bicron BC408 plastic

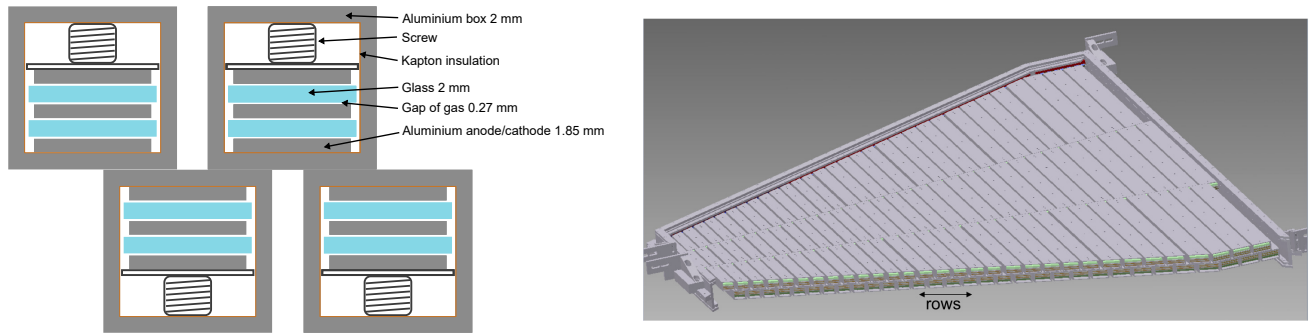


Figure 1.10.: Left: Schematic drawing of the HADES multi-gap RPC cell layout. The cells are aligned in two overlapping rows. (Taken from [25]) Right: Schematic drawing of a RPC sector. The cells have smaller sizes at smaller polar angles and fill the trapezoidal support frame. (Taken from [26])

scintillator material. Both ends of the rod are glued to a light guide which is bent by 70° with respect to the rod itself and coupled to a *photo multiplier tube* (PMT). Charged particles traversing the plastic scintillator are generating scintillation light. The rod itself is used to guide the scintillation light to both ends of the rod, where the PMTs are located. From the arrival time of the PMT signal a position information can be obtained. The system also provides a trigger signal for the HADES data acquisition. The time resolution of the detector is 150 ps. Additional information provided by the TOF detector is the specific energy loss which can be derived from the signal amplitude.

Each sector of the *Resistive Plate Chamber* (RPC) [24] detector consists of 1116 cells with different dimensions. A schematic drawing of a sector and the cell structure are shown in Fig. 1.10. A cell is made of a sandwich of three aluminum and two glass electrodes which carry a potential of 5 kV. The cell is enclosed by an aluminum box which is filled with a gas mixture of SF_6 and $\text{C}_2\text{H}_2\text{F}_4$. A charged particle traversing the detector will ionize the gas atoms along its track. Due to the external electric field an avalanche will be created which leads to a discharge of the electrodes. Due to the high resistivity of the electrodes, the electric field close to the discharge will be switched off. This prevents a full discharge of the electrodes and other parts of the detector are still fully operational. This technology enables a high time precision in combination with a high rate capability. The time precision which can be achieved with the HADES RPC is 70 ps [24].

The combination of the time-of-flight measurement with momentum determination, provided by the tracking system, and, in addition, energy-loss measurement permits to perform efficient particle identification. An example of particle velocity vs. momentum times polarity is shown in Fig. 1.11. Different particle species can be separated.

Electron identification

A *Ring Imaging CHerenkov* (RICH) detector [28] is used in order to identify electrons and positrons. A schematic drawing which illustrates the working principle is shown in Fig. 1.12 (left). The physical process which is used in the RICH detector is the *Cherenkov effect*. A charged particle traversing the C_4F_{10} radiator gas with a velocity faster than the phase velocity of light in that medium is emitting *Cherenkov photons* in a Mach cone. The *Cherenkov cone* is reflected by a spherical ultraviolet mirror which is made out of 18 pieces. This configuration allows full azimuth coverage of 360° . Due to the mirror diameter of 145 cm, theta angles between 18° and 85° are covered. Ring images are focused on the *photon detection plane*. Recently, the photon detection system was upgraded utilizing *multi anode photomultiplier tubes* (MAPMTs) which are read out by newly developed read-out electronics [29]. Figure 1.12 (right) shows the front side of the RICH providing an inside into the new read-out system which consists of 1100 read-out boards which are directly connected to the MAPDs. A typical response pattern of the RICH photon detection plane in a Ag+Ag heavy ion collision is shown in Fig. 1.13.

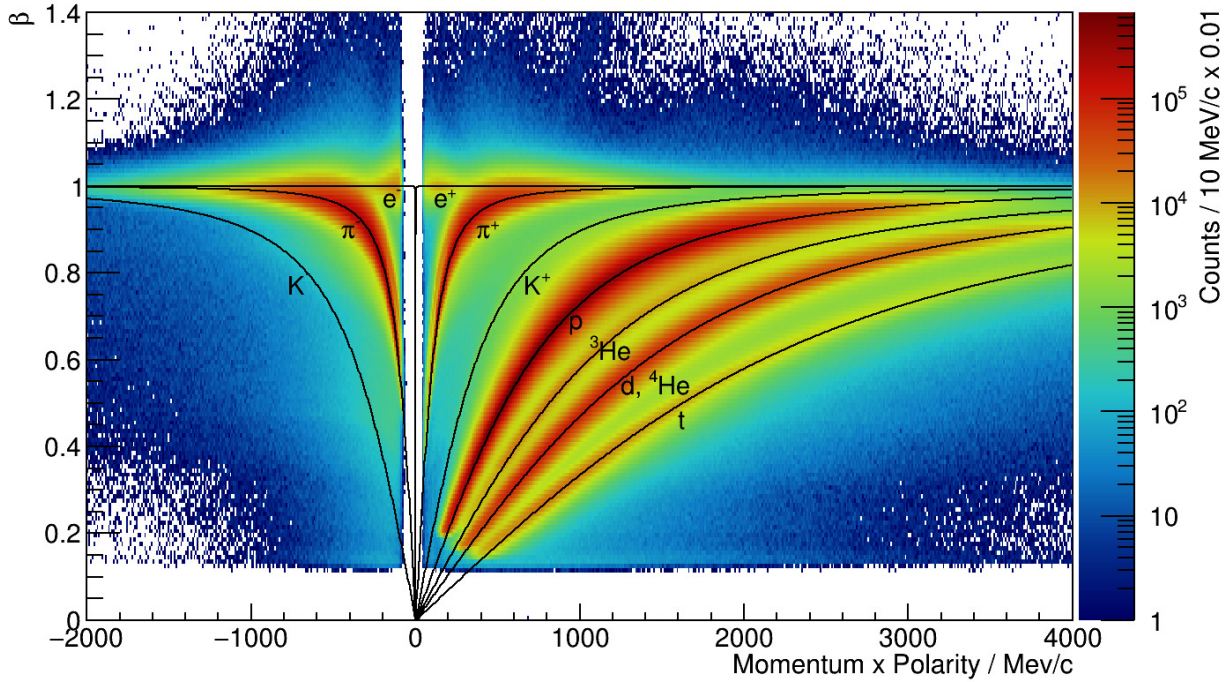


Figure 1.11.: Particle separation in the HADES detector for a Ag+Ag (1.23A GeV) collision system, using the velocity information of time-of flight system and the momentum and charge information obtained by the tracking system. Besides electrons, pions, protons and also heavy fragments (e.g. K^+ , ${}^3\text{He}$, deuterium and tritium) are visible. (Taken from [27])

Energy measurement and photon detection

In 2018, HADES was extended by an *Electromagnetic CALorimeter (ECAL)* [32, 33] which now enables an energy measurement. It replaces the *Pre-Shower* [34] detector and covers almost full azimuths and polar angles from 12° to 45° . The detector consists of 978 lead glass modules which are arranged in six sectors. The spatial arrangement of the glass modules and the support structure are shown in Fig. 1.14. Since the ECAL upgrade project is a main part of this work a detailed description will be given in section 2.3.

Data acquisition and slow control

All sub-detectors of the HADES spectrometer are connected to a common *Data Acquisition (DAQ)* network [35]. In order to simplify development, integration and maintenance it is based on a common network structure which consists of two main parts. One part is an *Field Programmable Gate Array (FPGA)* based custom network, the so-called *TrbNet* [36] network, which utilizes high bandwidth optical fibers. This network consists of three channels which are used for triggering, data transport and slow control. The second part is based on a commercial Gigabit Ethernet infrastructure in order to transport the data to the server farm for storage.

In Fig. 1.15 the simplified structure of the HADES DAQ network is shown. All HADES detectors own a dedicated *front-end electronics (FEE)* which is connected to the DAQ network. The TrbNet network can be divided into three virtual channels. The first channel is used for the distribution of the *first level (LVL1)* trigger signal which is distributed by the *Central Trigger System (CTS)* [38] and controls the read-out process of all data collecting front-ends. Once the trigger information packet is transmitted, the channel remains blocked until all front-end endpoints have returned a busy-release packet. After a trigger cycle is completed, the CTS has to instruct all front-end endpoints to send their data. This is done in a second TrbNet channel. The event data is requested from the CTS and transferred via Ethernet to a cluster of event builder servers. Here, up to 16 event building processes receive the data and save

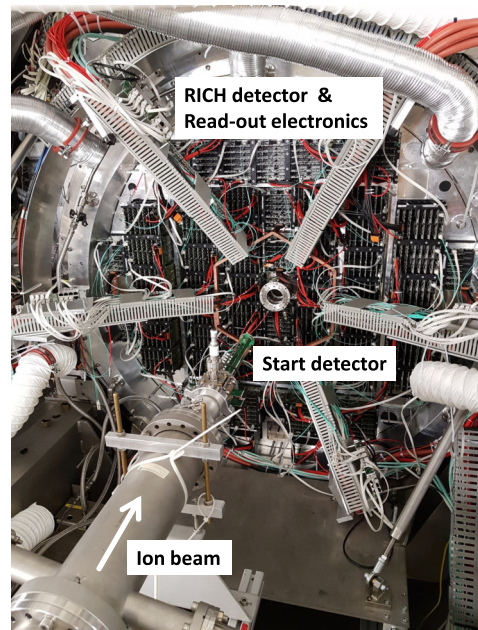
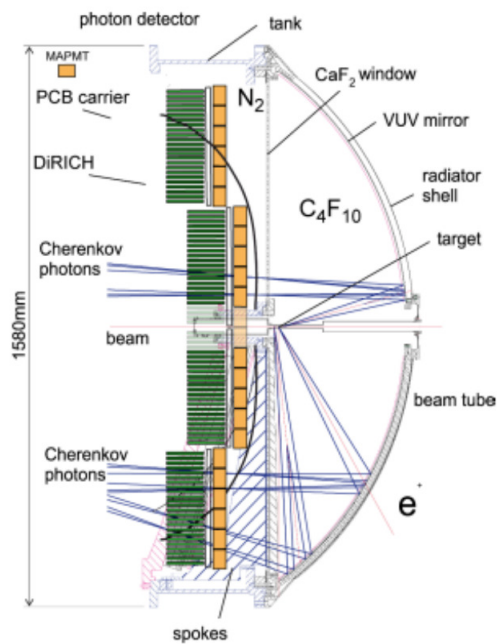


Figure 1.12.: Left: Schematic drawing of the RICH detector. The *Cherenkov cone* of an electron (the same holds for positrons) is focused by a spherical mirror on the photon detection system which is based on *multi-anode photo-multiplier tubes* (MAPMTs). (Taken from [30]) Right: The back side of the RICH detector provides an inside into the new read-out system which consist of 150 DiRICH-Boards. The beam pipe is currently opened and the diamond based Start detector, which is mounted on a green PCB, is visible.

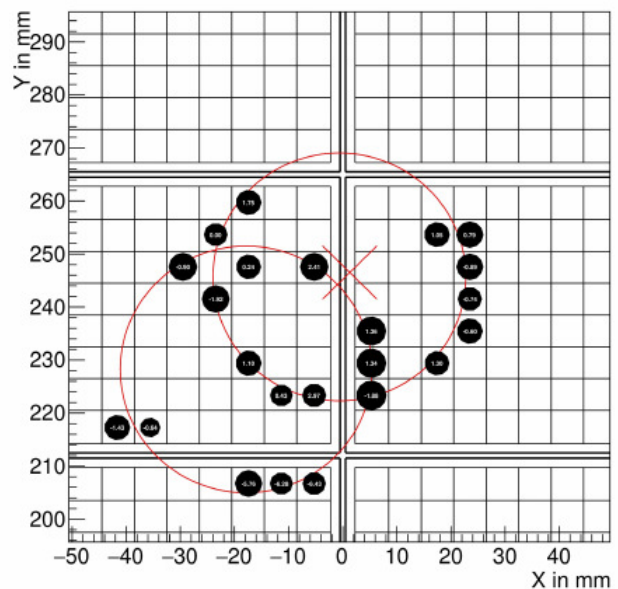
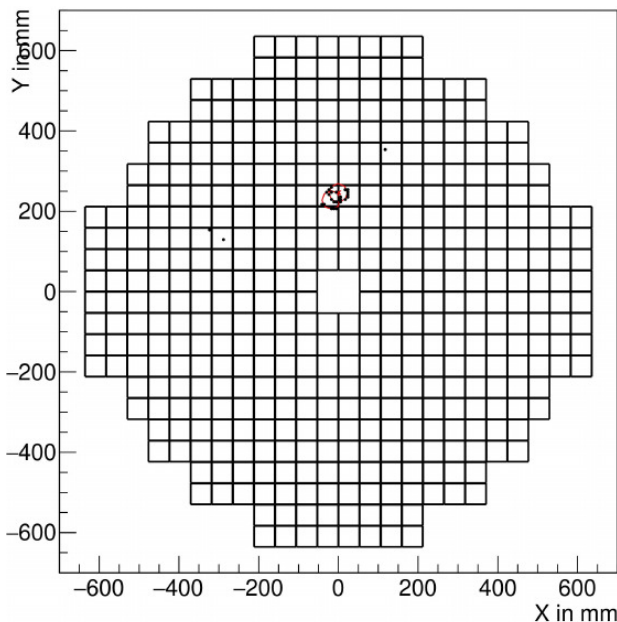


Figure 1.13.: Left: Typical response pattern of the RICH photon detection plane in a Ag+Ag heavy ion collision. Each square corresponds to a MAPMT. Two possible ring candidates are visible in the upper part of the detection plane. Right: Enlarged view of the ring candidates. (Taken from [31])

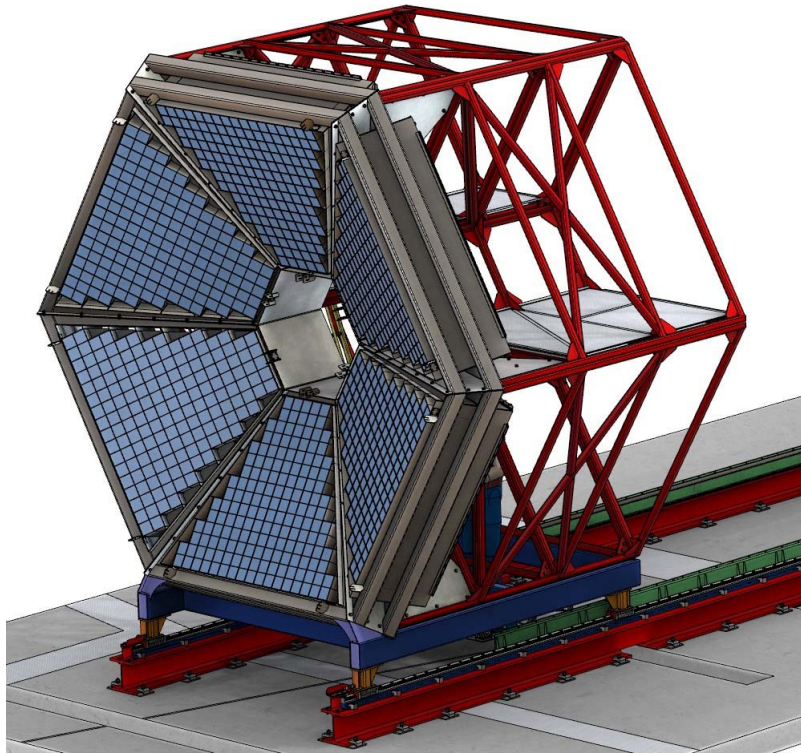


Figure 1.14.: Computer animation of the ECAL detector consisting of 978 lead glass modules which are arranged in six sectors. (Taken from [26])

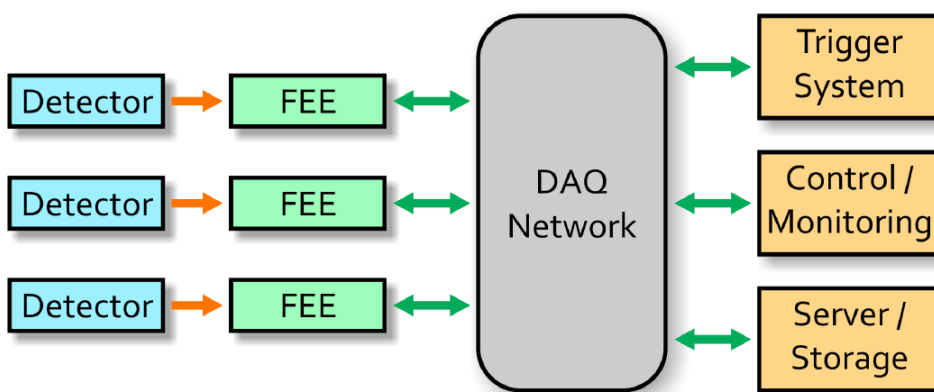


Figure 1.15.: Simplified HADES DAQ system. Detector signals are processed in the front-end electronics which are connected to the HADES DAQ network (TrbNet) consisting of three parts. (Taken from [37])

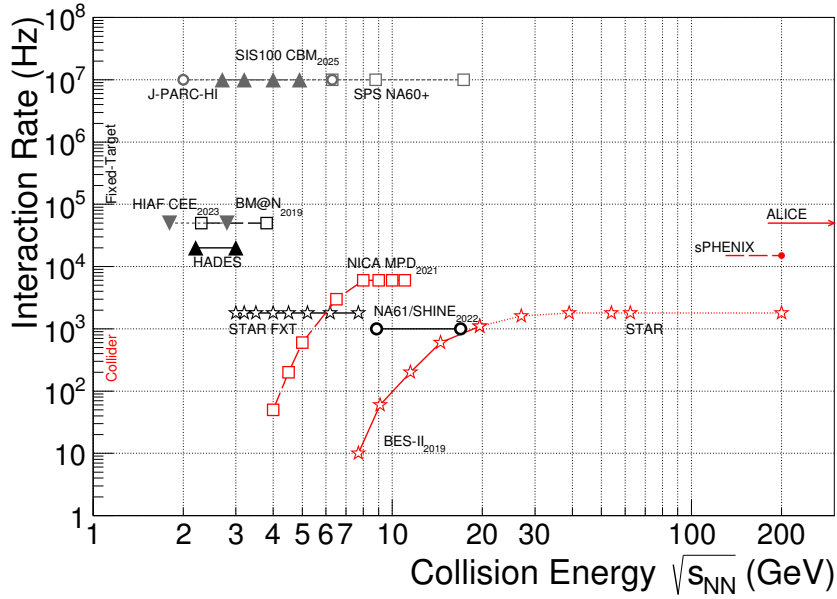


Figure 1.16.: Interaction rates achieved by existing and planned heavy-ion experiments as a function of center-of-mass energy $\sqrt{s_{NN}}$. Experiments in collider mode are shown in red, fixed target experiments are shown in black and gray. (Taken from [9])

the raw event files to hard disks and to a tape archive. The event building software is based on the *Data Acquisition Backbone Core* (DABC) framework [39, 40]. A third channel of the TRBNet is used for controlling and monitoring of the different detectors and front-end boards. The TRB3 platform, which will be introduced in Chapter 3, is fully compatible with the TrbNet network since it is already in use by the HADES experiment which makes it well implementable to integrate new read-out electronics based on the TRB3 family.

During a four week long physics production beam time with an Ag beam of 1.58A GeV on an Ag target in 2019, the HADES DAQ system was recording with a trigger rate of about 10 kHz resulting in a data rate of 150 MB s⁻¹. In total 360 TB of data have been recorded to hard disks. It is planned to upgrade the DAQ system in order to increase the trigger rate to about 100 kHz in the near future. An overview of interaction rates achieved by existing and planned heavy-ion experiments as a function of center-of-mass energy is shown in Fig. 1.16.

1.4 Motivation of this thesis

In the context of this work, the read-out system of the recently installed HADES *electromagnetic calorimeter* (ECAL) was designed, installed and commissioned. A successful operation of the new detector has been shown during a four week physics production beam time with a 1.58A GeV Ag beam. Furthermore, this work deals with diamond based beam detectors since they are used in HADES with a read-out concept similar to the one of ECAL. Beyond this, for future research and development of new beam detectors and their read-out electronics, a permanent test set-up has been designed and installed at the S-DALINAC electron accelerator.

In Chapter 2 the HADES ECAL upgrade will be introduced and basic concepts of calorimetry in high energy physics will be given. The signal generation in ECAL will be used as an example of a homogeneous lead glass calorimeter. Afterwards, the requirements to the read-out electronics will be given. In Chapter 3 the read-out scheme of the HADES ECAL will be depicted in detail. The charge measurement of the detector signals is based on a modified time-over-threshold measuring method, implemented in the PaDiWa-AMPS front-end board for the TRB3 platform. Chapter 4 gives technical details of the ECAL construction in the HADES cave. Beside the read-out electronics installation in the ECAL detector their

integration into the HADES data acquisition system will be shown. Chapter 5 deals with a full characterization of the read-out electronics in the laboratory which was necessary before a mass scale production of about 150 boards. The commissioning of the ECAL systems was done by LASER signals, cosmic muons and a Ag test beam. Issues which have been encountered during the commissioning and their solutions will be addressed. In Chapter 6 the performance of the ECAL read-out electronics, during a four week physics production beam time, will be shown. The energy calibration process will be explained and first analysis results, like the reconstruction of the $\pi^0 \rightarrow \gamma + \gamma$ decay, will be presented. In Chapter 7 diamond based beam detectors which are used for T0 determination for the HADES time-of-flight system will be introduced. Their read-out concept is similar to ECAL. The beam detectors were proven to be useful during beam focusing and the monitoring of its quality during the beam time. At the end of the section, new *Ultra-Fast Silicon Detector* (UFSD) technology, will be introduced. In Chapter 8 a permanent detector test set-up, which was installed at the S-DALINAC electron accelerator of TU Darmstadt, will be introduced. The set-up allows beam tests with a 130 MeV electron beam. The installation provides ideal conditions to perform research and development of various detectors using minimum ionizing particles.

2 Calorimetry in HADES

Recently HADES has been upgraded by an *Electromagnetic CALorimeter (ECAL)* [32] which allows energy measurement and the direct detection of photons. In this section the HADES ECAL upgrade will be introduced. Afterwards an introduction into calorimetry will be given. A strong focus will be on the electromagnetic lead glass calorimeter type since it is used in HADES.

2.1 Motivation for the possibility of an energy measurement in HADES

An addition of ECAL in the HADES set-up will allow a direct photon measurement. This opens the possibility to reconstruct the decay channels of $\pi^0 \rightarrow \gamma\gamma$ and $\eta \rightarrow \gamma\gamma$ which are important to understand the theoretical foundations which were introduced in Section 1.1. In addition, the ω vector mesons can now be reconstructed via the decay channel $\omega \rightarrow \pi^0\gamma \rightarrow \gamma\gamma\gamma$.

In order to extract the dilepton excess yield, a measurement of π^0 , η and ω is important. The excess yield as a function of the center-of-mass collision energy is shown in Fig. 2.1 (left). In the energy regime $2 \text{ GeV} \leq \sqrt{s_{NN}} \leq 10 \text{ GeV}$ no measurement data exists. In addition, the η and ω production is not measured in this energy regime. A simulation of the excitation functions of the π^0 , η , and ω mesons is shown in Fig. 2.1 (right). Since the HADES detector is (and will be, in combination with the CBM experiment) operating in the above mentioned energy regime, the collaborations can make an important contribution to the understanding of the behavior of the excess yield.

A reconstruction of π^0 and η in HADES without ECAL is not trivial. So far the so-called *photon conversion method* [21] was used. A direct photon measurement with ECAL will significantly facilitate their identification and increase the precision of the measurement.

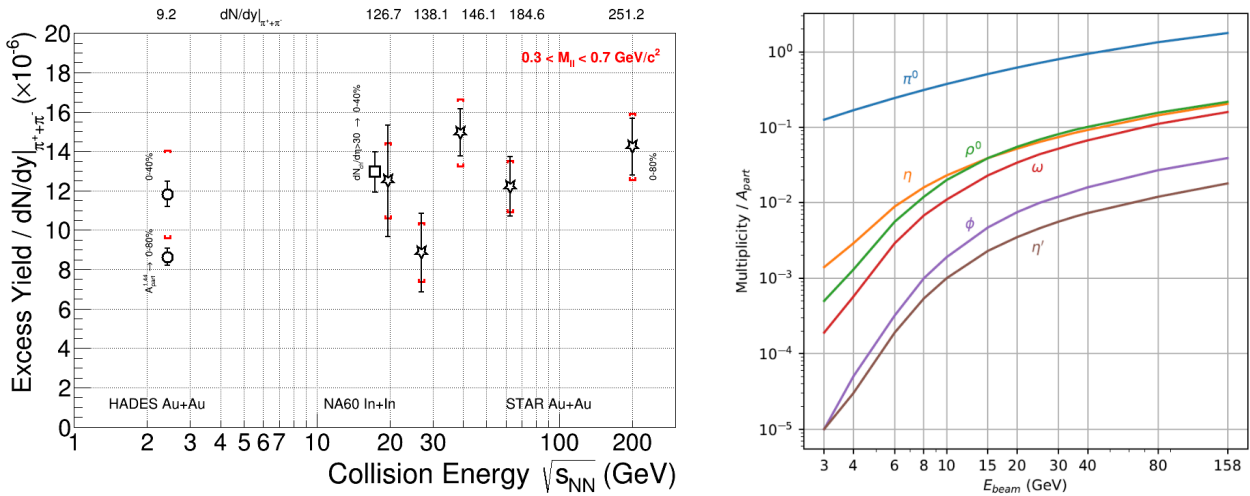


Figure 2.1.: Left: Excess radiation as a function of center-of-mass beam energy. In the energy regime between 2.5 GeV and 10.5 GeV no data exists. (Taken from [41]) Right: Simulation of multiplicities for different beam energies of the π^0 , η , and ω mesons. The particles follow excitation functions that are shown as colored lines. (Taken from [42])

Furthermore, an ECAL detector would be essential for the understanding of the hyperon structure. The importance of the hyperon radiative decays for the understanding of hyperon structure has already been theoretically motivated in the mid-eighties, but only little experimental progress has been achieved in the last thirty years. The hyperon structure can be probed by measurements of the electromagnetic transition form factors in space-like and time-like regions. Dalitz decays of hyperons, in this context, play an important role since they probe an important mass region $-4M^2 \leq -Q^2 \leq 0$ and allow to study the evolution of the hyperon electromagnetic transition form factors from the space-like to the time-like

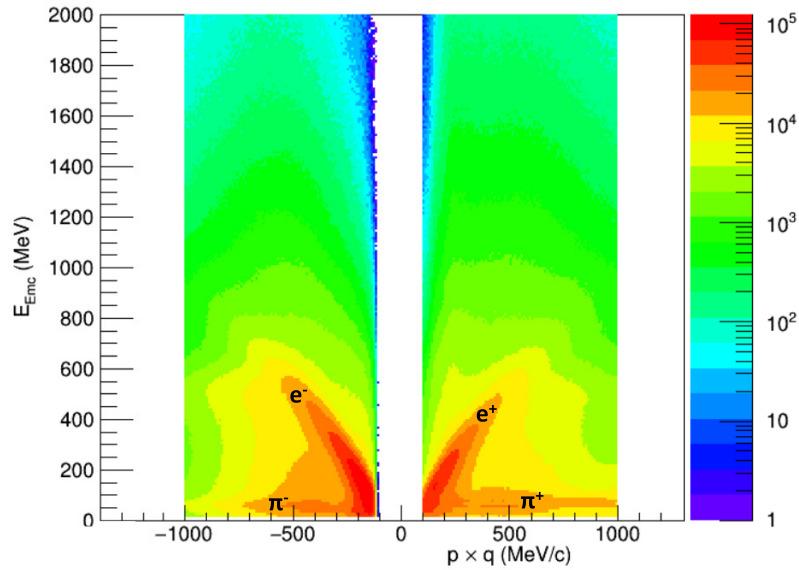


Figure 2.2.: Energy measured by ECAL vs. momentum \times charge for Ag+Ag at 1.58A GeV beam data. Pions deposit a constant energy in an ECAL regardless of their momentum. Electrons, on the other hand, show a linear energy deposition. This fact can be used to separate electrons from pions at momenta $p < 400$ MeV/c. (Taken from [43])

region. A special interest is on the decays of the Σ -baryon via the radiative decay $\Sigma^0 \rightarrow \Lambda^0 \gamma$ and the Dalitz decay $\Sigma^0 \rightarrow \Lambda^0 \gamma^* \rightarrow \Lambda^0 e^+ e^-$ channels. Both, Dalitz decay of hyperons and their radiative decay could be reconstructed with HADES. The real photon can be reconstructed by a direct measurement with the ECAL. This program has a novel character due to the unique combination of a broad range of beams provided by GSI/FAIR with universal detection capabilities of HADES.

An additional advantage of ECAL will be the improvement of the electron/pion separation at large momenta. As shown in Fig. 1.11 for momenta $p > 400$ MeV/c electrons and pions lie on one line and cannot, or only with difficulty, be distinguished. Pions deposit a constant energy in an ECAL regardless of their momentum. Electrons, on the other hand, show a linear energy deposition. This fact can be used to distinguish between the two particles. The electron/pion separation is demonstrated in Fig. 2.2 for Ag+Ag at 1.58A GeV beam data.

2.2 Basics of calorimetry in high energy physics

The word calorimeter is derived from the Latin word *calor*, meaning heat and the Greek word *metron*, meaning measure. A calorimeter is a device used for calorimetry, e.g. for measuring the heat of chemical reactions or physical changes as well as heat capacity. In particle physics, a calorimeter is a detector which is used to determine the kinetic energy of particles. Calorimeters are differentiated by their interaction with particles. *Electromagnetic calorimeters* are able to detect particles by their interaction with the material via the electromagnetic force (e.g. electrons, photons) and *hadronic calorimeters* are suited for particles interacting via the strong force (hadrons: e.g. protons, pions, kaons, neutrons). The basic principle in both types is to stop an incoming particle in an absorber material and measure the deposited energy. This is the reason why they are typically located in the outer shell of a detector system, e.g. behind tracking detectors. From a technical point of view, calorimeters can be divided into two types. On the one hand, there are *homogeneous calorimeters* where energy absorption and detection are combined in the same material. On the other hand, there are *sampling calorimeters* where absorber and detection media are separated in different materials. Those types are so-called *sandwich calorimeters* as they form a sandwich of repeating absorber and detection material. In both calorimeter

types the energy measurement is based on the detection of *scintillation light* (e.g. scintillator crystals), on the measurement of *ionization* (e.g. liquid noble gases) or *Cherenkov radiation* (e.g. lead glass). Regardless on the detection material the produced signal is proportional to the deposited energy of the incoming particle. Consequently, the energy of a particle can be determined by measuring one of the three measurable variables: *scintillation*, *ionization* or *Cherenkov radiation*.

2.2.1 Working principle of a lead glass calorimeter

In the following, the signal generation and the read-out of electromagnetic lead glass calorimeters will be discussed since this type is used in HADES. The sensitive material which is used there is a lead glass block with the dimensions of 92 mm × 92 mm × 420 mm. A detailed description of the detector module will be given in Section 2.3.1.

For example, a photon which enters the lead glass block with an energy greater than 1 MeV has a high probability to interact with the material via pair production. This effect occurs in presence of an atomic nucleus where the energy of photons can be converted into an electron–positron pair:



The produced electron–positron pair will again interact with the material mainly via the *Bremsstrahlung* process which creates high energetic photons. Those photons can produce electron–positron pairs again, hence an electromagnetic shower is developing, consisting mainly of electrons, positrons and gamma photons. Simplified, one can assume that the number of shower particles in a depth $t = x/X_0$, which is normalized to the radiation lengths X_0 , is [44]:

$$N(t) = 2^t. \quad (2.2)$$

In Fig. 2.3 an idealized and a simulated electromagnetic shower development in lead glass is shown. The mean energy of each particle at the depth t , can be calculated by [44]

$$E(t) = E_0 \cdot 2^{-t}. \quad (2.3)$$

The shower process continues until the particle’s energies fall below a critical energy $E_0/N = E_C$. At these energies, Compton scattering and photoelectric effects for photons, and ionization for electrons, dominate. The shower maximum is reached when $E_C = E_0 \cdot 2^{-t_{max}}$ is fulfilled for the critical energy, thus [44]:

$$t_{max} = \frac{\ln(E_0/E_C)}{\ln(2)}. \quad (2.4)$$

High energy electrons (> 10 MeV) lose energy mainly by *Bremsstrahlung* and high energy photons by pair-production. A more general description of the interaction of charged particles with matter can be provided by the *Bethe-Bloch* equation which will be introduced in Section 7.1.1.

The radiation length X_0 describes the characteristic amount of matter which is traversed for these related interactions. It is the mean distance over which a high-energy electron loses all but $1/e$ of its energy by *Bremsstrahlung*, and $7/9$ of the mean free path for pair production by a high-energy photon [45]. Since the radiation length is characteristic for both the energy loss of charged particles and photons, it defines a length scale for electromagnetic showers. This is particularly important for choosing the right radiator length during the construction of calorimeters. In order to measure the particle’s full energy, the module length has to be chosen accordingly in order to keep the full shower inside the radiator. If the particle enters the radiator close to the edge, the shower will extend to the neighboring module. In this case, the summation of energies in all involved modules, a so-called *cluster*, has to be taken into account in order to reconstruct the full energy of the incoming particle.

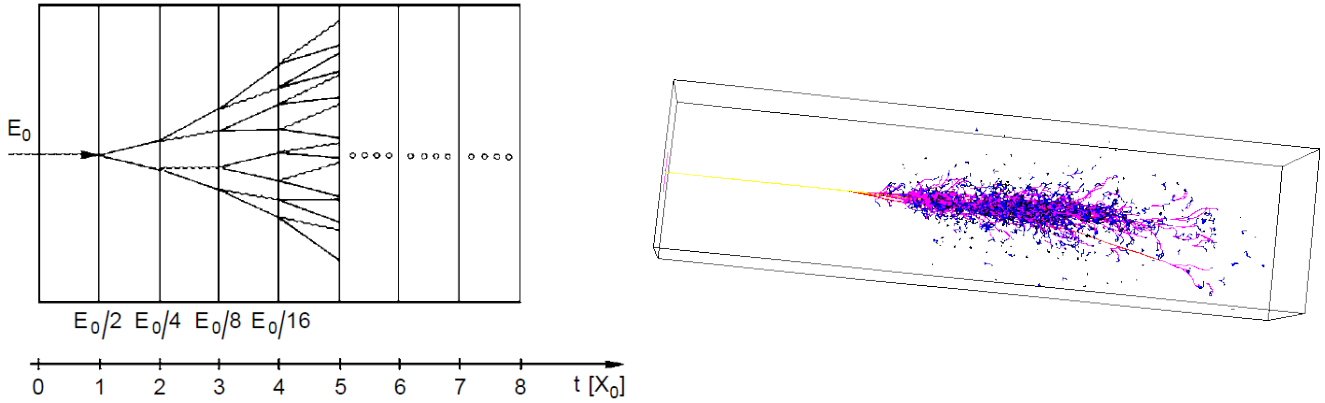


Figure 2.3.: **Left:** Idealized electromagnetic shower production in a calorimeter. The waved lines are photons and the continuous lines are electron tracks. The material length t is given in radiation length units X_0 . (Taken from [44]) **Right:** Simulation of an electromagnetic shower for a 20 GeV photon in a lead glass module as it will be used in the HADES ECAL detector. Straight yellow lines are photons, blue and magenta curved lines are electrons and positrons, respectively. (Taken from [46])

In order to detect the created shower particles, different measurement techniques for electrons/positrons and photons would be necessary. This is difficult to realize technically. Therefore, a further effect is exploited, namely the *Cherenkov* effect. Charged particles, which are created in the shower process, may travel through the lead glass at a speed greater than the phase velocity v of light in that medium which can be calculated from the index of refraction n and the speed of light in vacuum c :

$$v = \frac{c}{n}. \quad (2.5)$$

Those particles will emit an electromagnetic radiation, so-called *Cherenkov radiation*. It will be emitted in the direction of a cone which is similar to a Mach cone in analogy with the sonic boom of a supersonic aircraft. The radiation cone can be described by

$$\cos(\theta) = \frac{1}{n\beta}, \quad (2.6)$$

where θ is half of the opening angle of the cone and $\beta = v/c$ the beta factor. For example, a cosmic muon with the velocity $\beta \approx 1$ traversing a lead glass module with an refraction index of $n = 1.708$ will emit *Cherenkov light* in a Mach cone with a half opening angle of $\theta = 54^\circ$.

The frequency spectrum of *Cherenkov* radiation in lead glass has its maximum in the visible blue and near ultraviolet light. The *Cherenkov* radiation threshold energy for electrons in lead glass $T_C^E \approx 120$ keV [44] is low, implying that the total number of *Cherenkov* photons is approximately proportional to the total track length of all charged particles which are produced within the shower. Therefore, the number of *Cherenkov* photons is proportional to the deposited energy [44]. Thus, an energy measurement of a particle can be reduced to the detection of *Cherenkov* photons, which is technically well realizable.

2.2.2 Photon detection with a photo-multiplier tube

Since decades the *photo-multiplier tube* (PMT) is used for photon detection. The advantages of PMTs are large sensing areas, fast response and excellent timing performance. Beside this, they provide high gain

along with low electronic noise. A disadvantage is the high price and the required high voltage supply. A PMT is able to detect photons with wavelengths from an ultraviolet spectrum up to near infrared and converts them into a measurable electrical signal. A schematic view of a PMT is shown in Fig. 2.4. It consists of an evacuated glass tube with a light sensitive photocathode behind the face-plate. The photocathode is usually made of deposited photoemissive semiconductors or consists of alkali metals with very low work functions. An incoming photon hitting the photocathode will be transferred into an electron via the external *photoelectric effect*. The maximum kinetic energy $E_{K,max}$ of the ejected electron is given by

$$E_{K,max} = hf - W, \quad (2.7)$$

where h is the Planck constant and f the frequency of the incident photon. The term W is the work function which gives the minimum energy required to remove an electron from the surface of the metal. Afterward, the ejected electron is accelerated by the electrical field of the focusing electrode towards the first dynode of the electron multiplier. In the surface of the dynode more electrons are generated through secondary emission. Several stages of dynodes, which have a positive high voltage applied in order to accelerate the electrons to the next dynode, follow. In this way, the number of electrons grows from dynode to dynode resulting in the multiplication of electrons typically by six orders of magnitude which finally reach the anode. At the anode an electrical signal can be measured.

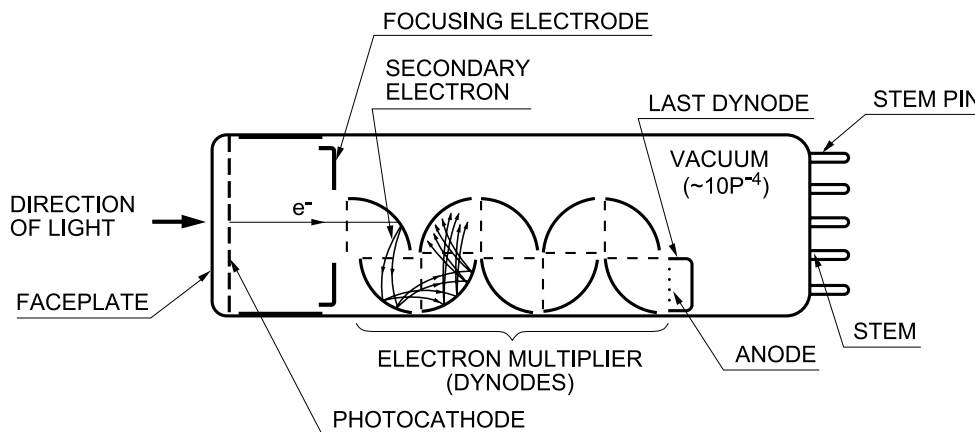


Figure 2.4.: Working principle of a linear focused Photomultiplier Tube (PMT). The two phenomena fundamental to the operation of a PMT are photo emission on the photocathode and secondary electron emission at the dynodes. (Taken from [47])

A PMT attached to a lead glass module allows to detect the produced *Cherenkov* photons. The signal charge is proportional to the number of photons hitting the photocathode. Consequently, the signal charge is proportional to the energy which is deposited in the lead glass module.

The performance of a PMT can be affected by magnetic fields because the trajectories of the electrons could be bent out of the multiplication region. The effect can be reduced by shielding the region using a material with high magnetic permeability, so-called *Mu-metal*. Also electrostatic fields can influence the PMT in a negative way. This effect will be explained in Section 5.3.3 in more detail and effective countermeasures will be presented.

2.2.3 Energy resolution of a calorimeter

The energy resolution of a lead glass calorimeter can be determined by sending gamma photons with known energy into a lead glass module and measuring the signal charge of the PMT. One gets a distribution of measured charges which can be transferred into energy by a calibration. The width of the distribution characterizes the resolution. In approximation a *Gaussian* distribution can be used to de-

scribe the measured data and its standard deviation σ can be used to characterize the resolution. In this work the resolution is defined by

$$\sigma_E = \frac{\sigma}{\mu} \cdot 100[\%], \quad (2.8)$$

with the standard deviation σ and the mean value μ of a *Gaussian* distribution which was fitted to the measurement data.

In general the energy resolution of a calorimeter is defined by [44]:

$$\left(\frac{\sigma_E}{E}\right) = \left(\frac{a}{\sqrt{E}}\right) \cdot \left(\frac{b}{E}\right) \cdot (c), \quad (2.9)$$

where a characterizes the photo-electron statistic (stochastic term), b characterizes the noise of the readout electronic and c characterizes the possible uncertainty in the calibration. In Fig. 2.5 the energy resolution of a HADES ECAL module for different photon energies is shown. The measurement [48] has been conducted at the *Mainzer Mikrotron* (MAMI) facility in Mainz. Among others, the ECAL read-out electronics PaDiWa has been compared with a CAEN flash ADC reference measurement (GSI MA8000 shaper and CAEN ADC) for an ECAL module containing a 3-inch PMT. For this configuration an energy resolution of

$$\frac{\sigma_E}{E} = \frac{5.5\%}{\sqrt{E[\text{GeV}]}} \quad (2.10)$$

was determined by the reference measurement. In the ECAL detector 1.5-inch PMTs will be used as well. With this PMT type the resolution is

$$\frac{\sigma_E}{E} = \frac{5.8\%}{\sqrt{E[\text{GeV}]}} \quad (2.11)$$

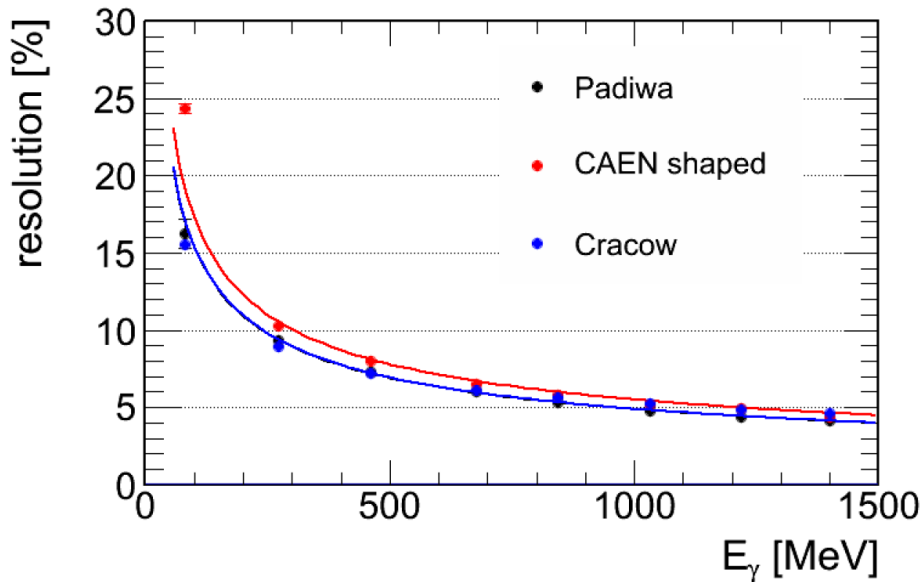


Figure 2.5.: Energy resolution of a HADES ECAL module with a 3-inch PMT which was irradiated with different photon energies. Among others, the ECAL read-out electronics PaDiWa was compared with a CAEN flash ADC reference measurements (GSI MA8000 shaper and CAEN ADC) [48].

2.3 The HADES electromagnetic calorimeter upgrade project

The HADES electromagnetic calorimeter detector consists of 978 lead glass modules which are arranged in six sectors. Each module has a weight of approximately 16 kg which leads to an overall mass of more than 15 t. The support structure is mounted on a rail system in order to allow moving the detector into a service position. The mechanical construction is used to support the modules of the calorimeter and the RPC detectors which will be mounted on its front side. A technical drawing of ECAL is shown in Fig. 2.6. A photograph of the current set-up of the HADES experiment is shown in Fig. 2.7. In the following the module structure will be explained in detail and the requirements for the read-out electronics will be given.

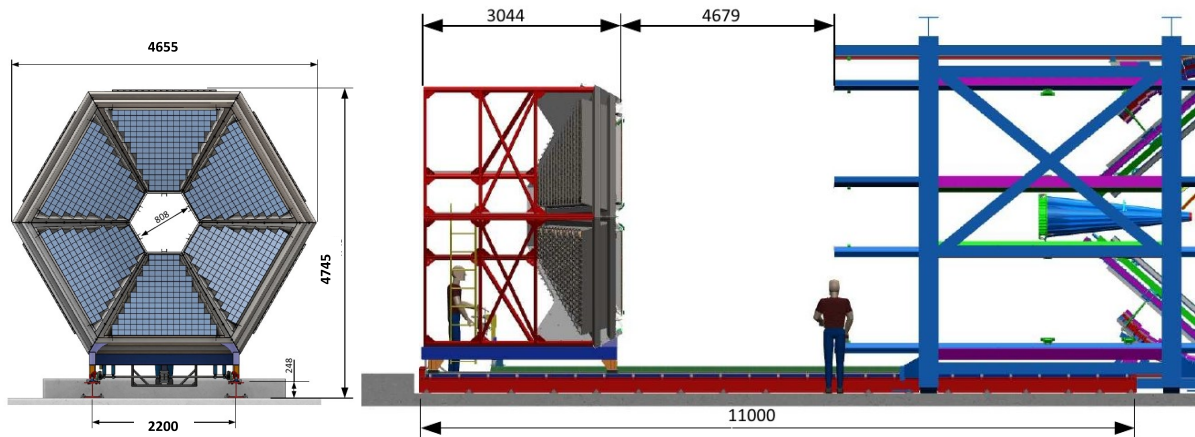


Figure 2.6.: Technical drawing of the ECAL detector consisting of 978 lead glass modules which are arranged in six sectors. The detector is mounted on a rail system in order to have easy access during service. The dimensions are given in mm. (Taken from [32])

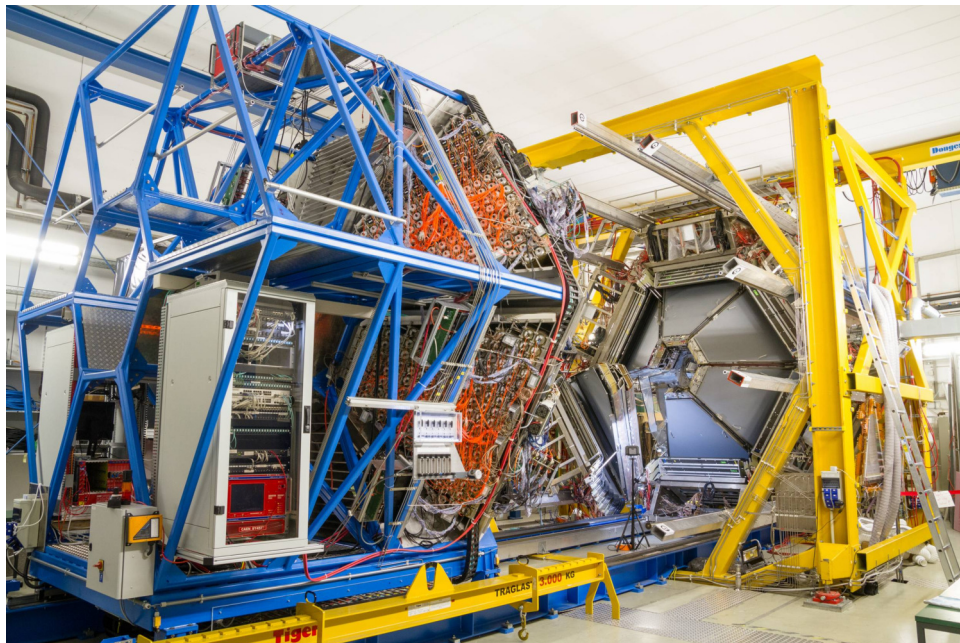


Figure 2.7.: The HADES set-up at *GSI Helmholtzzentrum für Schwerionenforschung GmbH* in Darmstadt while it is extended to a service position. The new ECAL detector is mounted on a blue movable support structure. (Picture taken in January 2019)

2.3.1 Lead glass calorimeter modules

Each of the 978 HADES ECAL modules consist of a lead glass (Corning CEREN 25) radiator obtained on loan from the OPAL End-Cap calorimeter at CERN [49, 50]. The glass has a density of $\rho = 4.06 \text{ g cm}^{-3}$, a refraction index of $n = 1.708$ (for photons with a wavelength of 410 nm) and a radiation length of $X_0 = 2.51 \text{ cm}$. All radiators have the same dimensions of $92 \text{ mm} \times 92 \text{ mm} \times 420 \text{ mm}$, where the length is equivalent to 16.7 radiation lengths. A brass box with a wall thickness of 0.45 mm is used as housing for the radiator, the PMT and its high voltage divider. The PMT is attached to one side of the lead glass radiator via optical grease (Rhodorsil Paste No. 7). Two types of photo-multiplier tubes are in use, recycled 1.5-inch EMI 9903KB from the WA80 experiment at CERN [51] and new 3-inch Hamamatsu R6091, which both have a comparable performance (see Section 2.2.3). All sides of the glass block are mirror polished and wrapped into white paper (TYVEK 1060B) in order to reduce lateral escape of photons. An optical fiber is coupled to the glass block, having a standard *Lampert Connector* (LC). This allows to send external light from a LED or a LASER system into the module, which then can be used for calibration and monitoring purposes. A schematic drawing of an ECAL module is shown in Fig. 2.8.

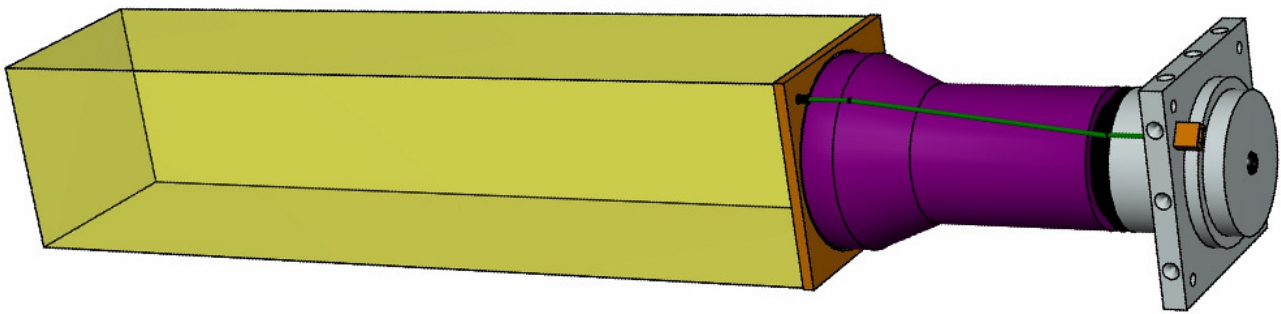


Figure 2.8.: Schematic drawing of an ECAL lead glass calorimeter module. The lead glass block (shown in yellow) with the dimensions of $92 \text{ mm} \times 92 \text{ mm} \times 420 \text{ mm}$ is coupled to a 3-inch Hamamatsu R6091 photo-multiplier tube (shown in magenta). The optical fiber (shown in green) allows to send LED or LASER light into the module which can be used for testing or calibration purposes. The module is surrounded by a 0.45 mm thick brass box (not shown).

2.3.2 Read-out requirements

A read-out electronic which is able to provide a precise arrival time and charge measurement of the PMT pulses is required. Typical pulse shapes of 1.5-inch EMI 9903KB and the 3-inch Hamamatsu R6091 PMTs, generated with blue LASER light, which was coupled into the lead glass, are shown in Fig. 2.9 and 2.10. The signal shape of the PMTs generated by LED light is very similar to the shape obtained from cosmic muons or gamma beams. Therefore, it can be used as a useful tool for the evaluation of detector modules and the read-out electronics. The PMT pulses have a full rise-time of about 2.5 ns and a full fall-time of about 50 ns. A dynamic measurement range of signal amplitudes from 5 mV - 5000 mV has to be covered with an accuracy of 5 mV. A time precision of at least 500 ps is required [32]. The expected hit rate is in the order of 10 kHz per channel. Beside this, the read-out system should be technically feasible to integrate into the existing HADES read-out scheme.



Figure 2.9.: Raw signals of an ECAL module containing a 3-inch Hamamatsu R6091 PMT. The signals are generated by LASER light, which is coupled into the lead glass.

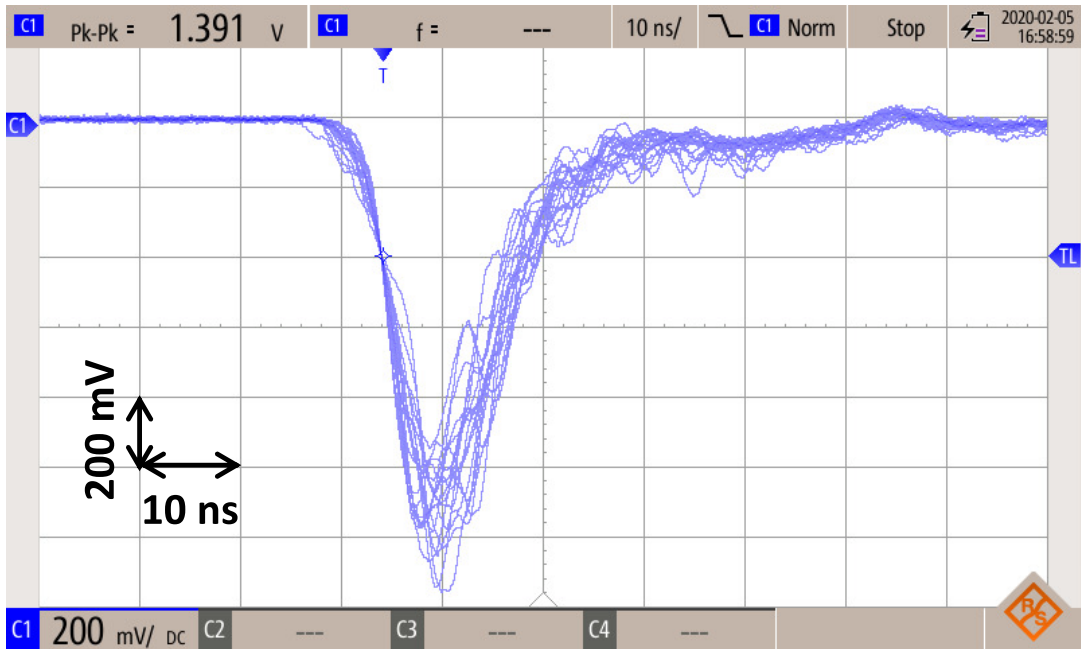


Figure 2.10.: Raw signals of an ECAL module containing a 1.5-inch EMI 9903KB PMT. The signals are generated by LASER light, which is coupled into the lead glass.



3 FPGA based charge and time measurement principle for ECAL

The simplified read-out scheme of the HADES ECAL detector is shown in Fig. 3.1. Signals from photo-multiplier tubes are processed in the PaDiWa-AMPS [52] front-end board for the TRB3 [53] platform. Remarkable is that the charge and time measurement is based on commercially available *Field Programmable Gate Arrays* (FPGAs), which make it possible to digitize many channels using low cost tools. On the front-end board the arrival time and pulse charge, which is proportional to the deposited energy in the ECAL module, is measured via a modified time-over-threshold method. The TRB3 platform carries out the needed high precision time-to-digital conversion and concentrates the data, which is sent to the HADES data acquisition system when a read-out is requested by the HADES physics trigger. The HADES data acquisition system is based on the custom network structure TRBNet containing three channels for trigger, data and slow-control.

In the following the PaDiWa-AMPS front-end board for the TRB3 platform will be introduced. The charge and time measurement method will be explained in detail. The evaluation of the PaDiWa-AMPS2 board and finally the installation and commissioning inside the ECAL detector will be covered in Chapters 4 and 5.

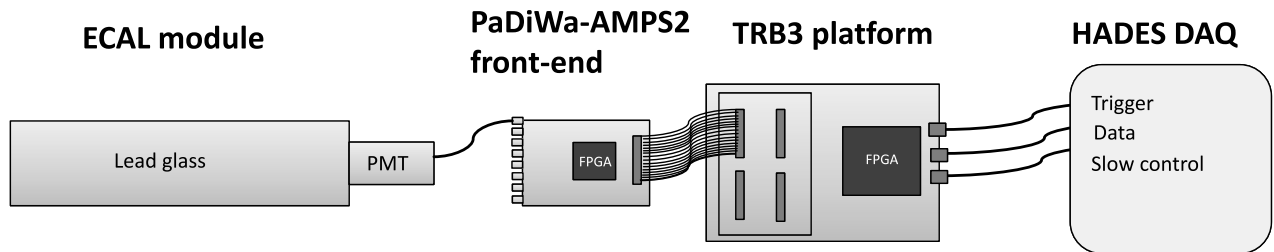


Figure 3.1.: Simplified read-out scheme of the HADES ECAL detector. Photo-multiplier tube signals are digitized in the PaDiWa-AMPS front-end board via a modified time-over-threshold method. The TRB3 platform is used for the needed time-to-digital conversion. A connection to the HADES DAQ is realized via the custom network structure TRBNet which contains three channels for trigger, data and slow-control.

3.1 Charge and time measurement method

As shown in Section 2.2 the energy of a particle, which is deposited in lead glass, is proportional to the signal charge of the PMT signal. The charge therefore has to be measured with a high accuracy. A standard *time-over-threshold* (ToT) discriminator cannot be used to cover the expected dynamic range. A saturation of the discriminated signal width for pulses with high amplitude will start rather soon, which makes it especially difficult to distinguish signals with high amplitudes. To avoid this problem the charge measurement method is based on a modified Wilkinson-ADC [54] circuit where the charge of the PMT pulse is encoded in the width of a digital pulse via a so-called *charge-to-time-over-threshold* (Q2ToT)¹ conversion system.

The simplified measurement principle allows to determine the arrival time and the charge of detector pulses and is shown in Fig. 3.2. The analog part and the FPGA based discriminator are realized on the PaDiWa-AMPS2 front-end board. The needed FPGA based *Time-to-Digital-Converters* (TDCs) are implemented on the TRB3 board. In the analog part, the input signal is linearly amplified and split into a FAST and SLOW component. The so-called *FAST signal* is sent directly to the discriminator, which is implemented with the help of an FPGA. The leading edge of the discriminated FAST-signal contains

¹ In the following Q2ToT is also abbreviated as ToT in some places. In general the ToT of the so-called SLOW channel has the same meaning as Q2ToT.

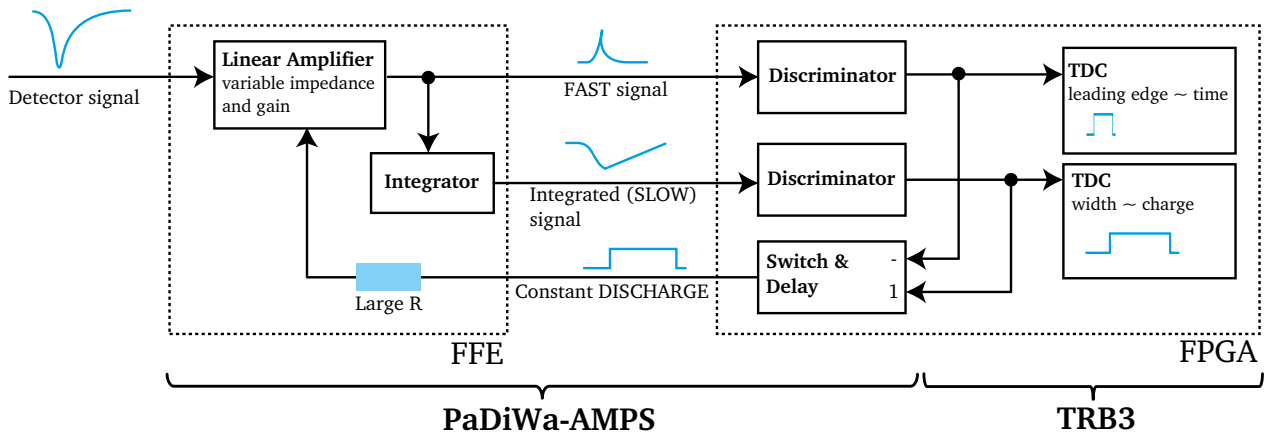


Figure 3.2.: After attenuation/amplification, the input signal is split into a FAST component, containing the arrival time and a SLOW component, which contains the charge information. The FAST signal is discriminated with the help of an FPGA. Afterwards, a TDC implemented in a second FPGA is used to measure its leading edge which contains the arrival time information. The SLOW signal is integrated by a capacitor and discharged by a discriminator driven current source. The SLOW signal is also discriminated in an FPGA and its time-over-threshold, representing the charge, is measured by an FPGA-TDC.

the arrival time information of the PMT pulse. The SLOW component is integrated with the help of a capacitor. Inside the FPGA a logical AND gate between the leading edge of the SLOW and a delayed FAST leading edge is used to start a constant discharging signal. This so-called *DISCHARGE* signal is fed back into the analog part and ensures a constant discharge of the integrated capacitor. When the trailing edge of the SLOW signal reaches the threshold, the DISCHARGE signal is switched off. The resulting so-called *SLOW signal* is sent to the FPGA for discrimination. This signal is proportional to the input charge (see 5.3), thereby the charge is encoded in the width of the discriminated SLOW signal.

In summary, one can say that the energy deposited inside an ECAL module is proportional to a charge measurement of a PMT pulse. For that the charge measurement is converted into a width measurement, which is encoded in the width of the SLOW signal. The width can be calculated from the *leading* (LE) and *trailing edge* (TE) measurement of the SLOW signal:

$$\text{Energy} \propto \text{Charge} \propto Q2ToT = TE_{\text{SLOW}} - LE_{\text{SLOW}}. \quad (3.1)$$

Both the discriminated FAST and SLOW signals are sent via *Low Voltage Differential Signaling* (LVDS) to the TRB3 platform which implements precise (8 ps RMS) [55] FPGA based TDCs and data acquisition functionality.

The signal discrimination [56] on the PaDiWa family is realized with the help of an FPGA. Its *Low Voltage Differential Signaling* (LVDS) input buffers are used as a comparator. For that, the analog FAST and SLOW signals, generated in the analog part of the PaDiWa-AMPS board, are sent to the input buffers of the FPGA and compared to a reference voltage. The signal discrimination scheme is visualized in Fig. 3.3. The discrimination threshold can be set by varying the reference voltage of the input buffer. The reference voltage, often also called threshold voltage, is generated via a *Digital-to-Analog Converter* (DAC) implemented with the help of *Pulse Density Modulation* (PDM) which is generated inside the FPGA. A low pass filter is used to filter out the edges in order to get a constant reference voltage. Discriminated signals are processed in the FPGA and sent to the FPGA output buffers. The arrival time and the charge information of the detector input pulse is then encoded in the digital LVDS output pulse.

In Fig. 3.4 the electronic schematic of the analog electronics part is shown for the first physical input channel of the PaDiWa-AMPS2 board. The input impedance is matched to the 50 Ω impedance of the PMTs coax cable used in ECAL. The electronics scheme has been optimized for pulse shapes generated

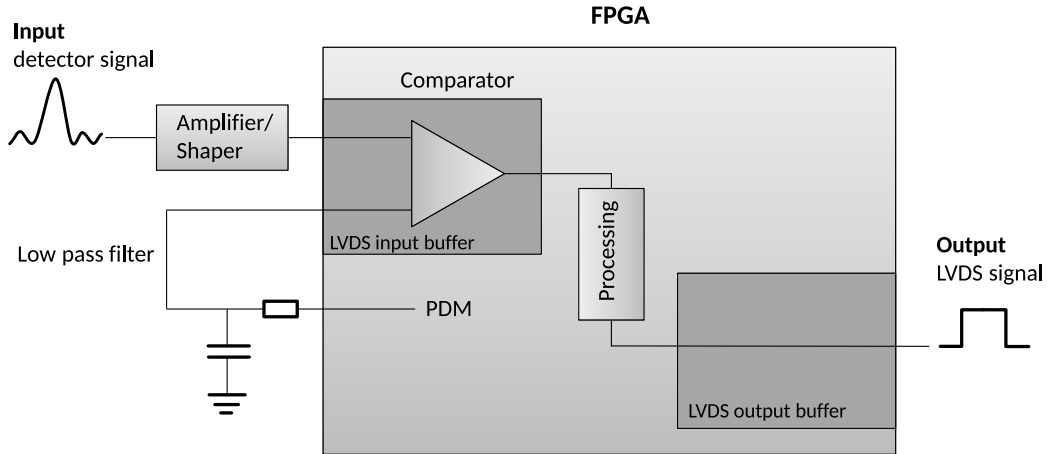


Figure 3.3.: Scheme of the signal discrimination via the LVDS input buffers. Discrimination threshold can be set to the input signals by an *Digital-to-Analog-Converter (DAC)* using *Pulse Density Modulation (PDM)* in combination with a low pass filter.

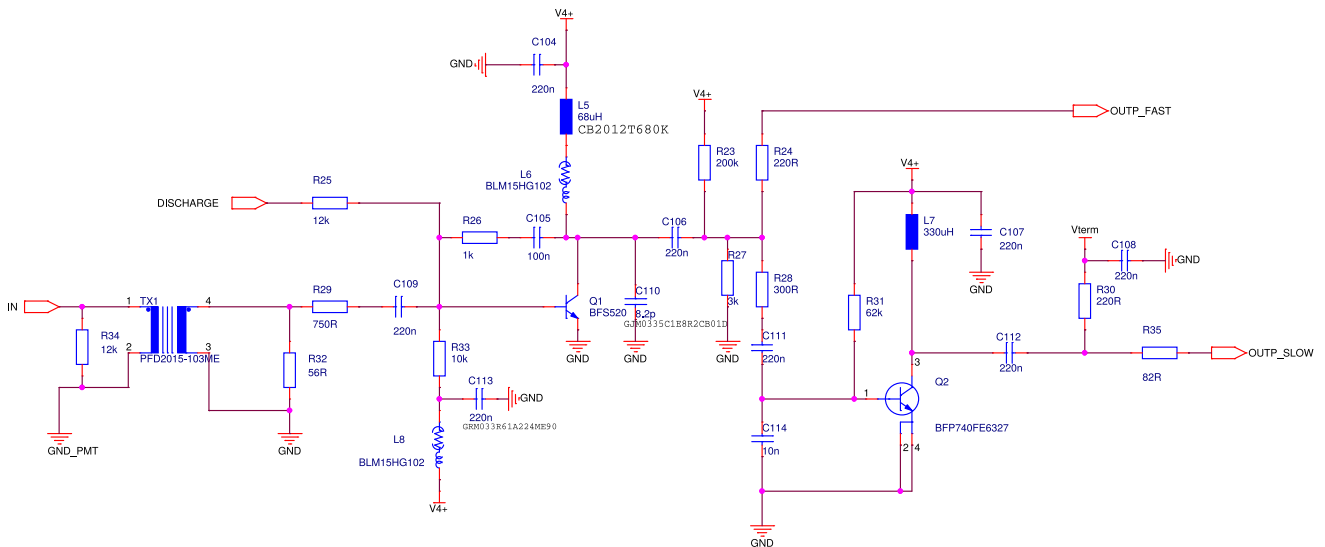


Figure 3.4.: Schematics of the analog stage of the PaDiWa-AMPS2 board. A transformer (TX1) was added in order to decouple the input ground from the board ground.

by the HADES ECAL detector. The simple circuit design allows to adjust the electronics to different signal shapes. In order to improve the signal-to-noise ratio a transformer was added in the second version of the front-end board which decouples the input ground from the board ground and therefore improves the signal to noise ratio. After the first amplification stage, using a BFS520 transistor (Q1) in an emitter-circuit, the signal is split into a FAST and SLOW component. The FAST signal is sent to the FPGA for discrimination (OUTP_FAST). The SLOW component is integrated with the help of a 10 nF capacitor (C114). The BFP740 transistor (Q2) is used to amplify the voltage at the integration capacitor. Since ECAL PMTs generate signal amplitudes in the order of several hundreds of millivolts, the amplitude gain for ECAL is almost 1 VV^{-1} . The DISCHARGE signal, which is generated inside the FPGA, is fed back to the circuit. The integration capacitor is thus discharged by a constant current source which results in a linear voltage drop at the capacitor. The SLOW signal is afterwards sent to the FPGA for discrimination (OUTP_SLOW). Typical analog signals of FAST, SLOW and DISCHARGE, probed with an oscilloscope, are shown in Fig. 3.5.

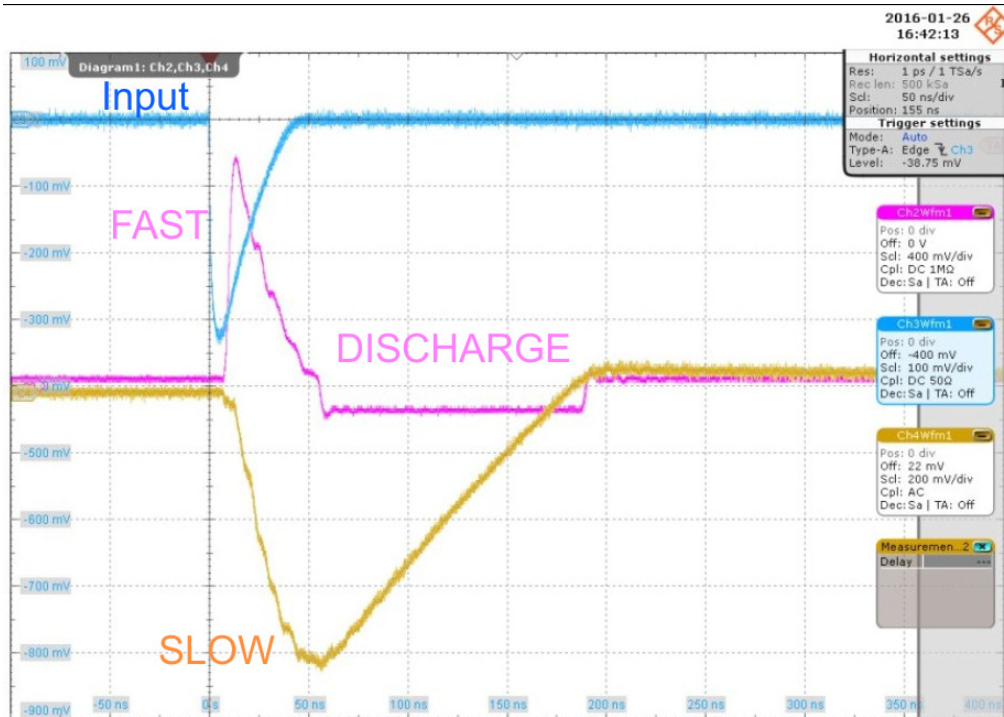


Figure 3.5.: Typical signal shapes measured on the PaDiWa-AMPS2 board with an oscilloscope. The input signal (blue), the resulting FAST (magenta) and SLOW (yellow) signals are shown. The DISCHARGE signal is visible in the FAST signal.

3.2 General Purpose Trigger and Read-Out (TRB) platform

The HADES ECAL read-out system is based on the *General Purpose Trigger and Read-Out Platform* (TRB3) [53, 57]. The abbreviation TRB3, of the read-out platform which is available in the third generation, has different meanings: *TDC-Readout-Board*, *Triggered-Readout-Board* and *Triggerless-Readout-Board*. This underpins the flexibility of the platform. The TRB3 platform was initially developed for the needs of the HADES experiment, but its flexibility already attracted other experiments and applications all over the globe. A large variety of front-end boards is available, e.g. the PaDiWa discriminator family. The newest variation is the TRB3 board which implements up to 260 multi-hit *Time-to-Digital-Converter* (TDC) channels. The TDCs are implemented via the tapped delay line method [58, 59] inside four FPGAs. This allows single edge and *time-over-threshold* (ToT) measurements, with a time precision of 8 ps RMS [55]. In a fifth FPGA a *central trigger system* (CTS) [38] and *data acquisition* (DAQ) functionality is implemented. In table 3.1 the key facts of the TRB3 board are summarized. The board is applicable as a standalone system and also in large systems with many TRB3 boards. A comprehensive software package is available which includes configuration, read-out and online analysis software [60, 39]. Slow control communication with front-end boards, e.g. threshold setting is implemented via a *Serial Peripheral Interface* (SPI). In the ECAL detector the crate compatible version TRB3sc [57] is used. This version is fully compatible with the TRB3 board and is equipped with 48 TDC channels implemented in a single FPGA which allows to read-out three PaDiWa-AMPS boards in parallel. The TRB3 front-end board and its crate compatible version TRB3sc are shown in Fig. 3.6.

3.3 PaDiWa-AMPS2 front-end board for the TRB3 platform

A new front-end board for the TRB3 platform was specially developed for the read-out requirements of the HADES ECAL. In the context of this work the second version of the so-called *PaDiWa-AMPS* [52]

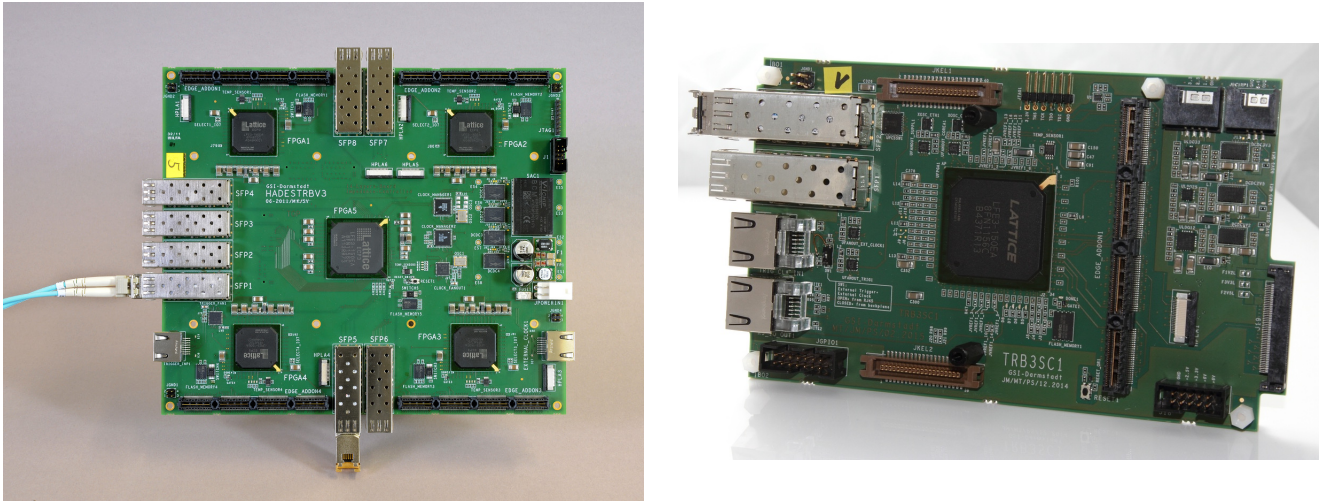


Figure 3.6.: **Left:** The successor board of the TRB family is the TRB3 board which implements 260 FPGA-TDC channels and data acquisition functionality. **Right:** The smaller crate capable version TRB3sc, which is used in the HADES ECAL detector, implements 48 FPGA-TDC channels. (Pictures by G. Otto, GSI)

Key	Facts
Supply voltage	48 V (40-50 V), galvanically isolated on board
Power supply current	0.5 A minimum without AddOns
GbE-connectivity	max. 95 MBytes/s transfer per link
GbE-slow-control	up to 400 registers/transfer, speed depends on GbE latency
Connectivity	max. 8 SFPs, each 2GBit/s on board. 4 AddON boards
Max. read-out trigger rate	about 300 kHz
Max. hit rate	50 MHz (burst of 63 hits)
TDC channels	260 (multi-hit single edge detection)
Time precision	<20 ps
Minimum pulse width	<500 ps

Table 3.1.: Summary of some key facts of the TRB3 platform [57].

board was designed, manufactured, tested and finally installed in the ECAL detector. A successful operation has been shown during a HADES production beam time in March 2019.

The PaDiWa [61] board was originally developed as a discriminator front-end board for the PANDA DIRC [62] detector. This front-end board was modified and redesigned to implement a charge measurement. The front-end board was developed according to the *Keep it small and simple* (KISS) principle. The analog part is based on discrete electronics while signal discrimination and digital processing is implemented with the help of a commercially available *Field Programmable Gate Array* (FPGA). It is therefore possible to adjust the electronics easily to different signal shapes. A photograph of the PaDiWa-AMPS2 front-end board is shown in Fig. 3.7. The board has outer dimensions of 87 mm × 52 mm and is equipped with eight *micro-miniature coaxial* (MMCX) connectors, allowing to read-out eight PMTs in parallel. For each physical input an analog electronics part is used in order to prepare the PMT signals for discrimination. The measurement principle (see also Section 3.1) is to integrate the signals and to encode the charge in the width of a digital pulse via a modified time-over-threshold method. The discrimination of the signals is implemented with the help of a Lattice MachXO3 FPGA. Afterwards, the discriminated signals are sent via a 40-pin differential signal flat cable to a TRB3 board for further processing.

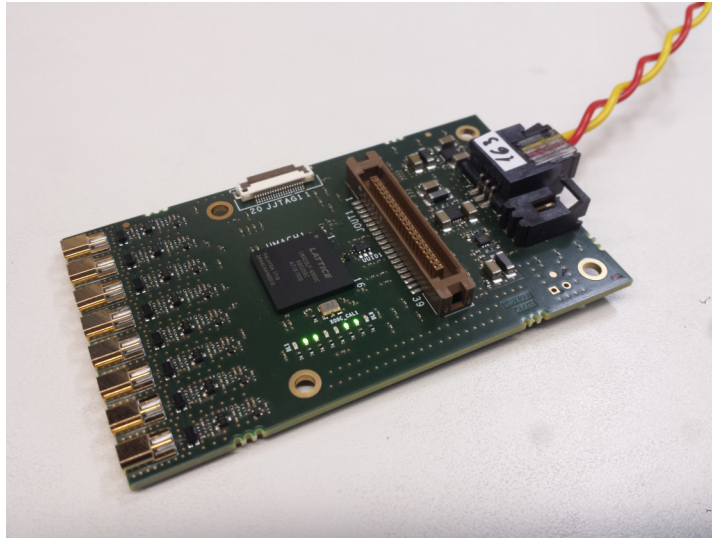


Figure 3.7.: The PaDiWa-AMPS2 discriminator front end board for the TRB3 platform which is used in the HADES ECAL detector. Eight PMT signals can be read-out paralelly. A charge measurement is implemented via a modified time-over-threshold method.

3.4 Production of the second version of the PaDiWa-AMPS front-end board

In 2017 a prototype of the second version of the PaDiWa-AMPS [63] board was designed and manufactured. The first prototype PaDiWa-AMPS1 was already systemically investigated. It was demonstrated in the laboratory [64] and with test-beam [48] that it is possible to read-out the HADES ECAL modules with good performance. For the mass production of the required boards for the ECAL its layout was reworked in order to fix several bugs and add new features. A significant change in the new version is the use of a newer generation of FPGA (Lattice MachXO3) in order to provide more resources for future firmware developments. The MMCX connectors have been exchanged for edge mountable types which are mechanically more stable and three times cheaper. The imperial package size was reduced from 0402 to 0201 which allows more space for an optimized placement of the components on the *printed circuit board* (PCB). A *High-Density-Interconnect-PCB* with eight layers and *micro-via technology* allows complex routing. For example, signal layers are now shielded by ground layers in order to increase the signal to background ratio. Also, the routing of signals lines was optimized to improve the signal timing. The upper layer of the new PaDiWa-AMPS2 layout is shown in Fig. 3.8. In total, 150 boards have been manufactured and assembled at the *GSI Department for Experiment Electronics*.

3.4.1 SPICE model of the PaDiWa-AMPS2 board

For the simulation of analog, digital and mixed electrical circuits the *Simulation Program with Integrated Circuit Emphasis* (SPICE) [66] software can be used. The algorithm searches for approximate solutions for the system describing differential equations. Their relationship is determined by the circuit topology and transferred to the simulator by means of a net list describing the components and their connections. The components are described by models which are partly physically oriented, but can also be completely abstract. In the latter case, a subsystem is described only by inputs/outputs and linking equations, instead of consisting of single components. This leads to a fast and accurate simulation result.

In this work the LTspice [67] software for circuit simulation from the former semiconductor manufacturer Linear Technology (since 2017: Analog Devices) was used. Several analog components and idealized digital gates are provided in the libraries. Since the software is based on SPICE, models from other sources can be easily adopted and used. The PaDiWa-AMPS1 circuitry was fully modeled [68] using this software. In the context of this work the simulation was adopted in order to simulate features of the new PaDiWa-AMPS2 board. The analog part is modeled including the SPICE models of the transistors.

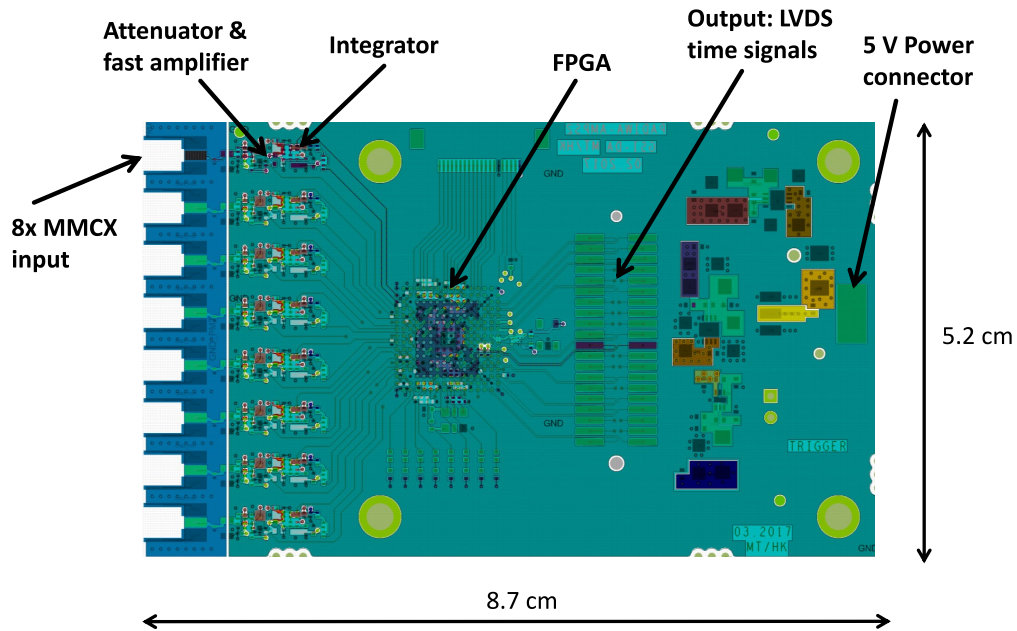


Figure 3.8.: Top layer view of the new PaDiWa-AMPS2 PCB layout [65]. By reducing the package size to 0201 more space for the placement of components and routing is available. This allowed for signal timing optimizations.

The discriminator and the logic of the DISCHARGE signal generation is emulated with the help of replacement circuits. Signals of PMTs (triangular pulses) with different amplitudes can be injected into the input and all signals (e.g. FAST, SLOW and DISCHARGE) can be probed. The simulation results have been proven by laboratory measurements to be close to the expected behavior. The LTspice model is described in Fig. 3.9.

The LTspice model was used in several steps during the design and the optimization of the analog circuit in order to match it to PMT signals of the ECAL. For example, during the manufacturing of the PaDiWa-AMPS2 board it was used to adopt a replacement transistor in the first amplification stage to the schematics. The BFS520 transistor (see Q1 in Appendix A.15), which was used in the PaDiWa-AMPS1 board, is no longer in production and replaced by the BFU55W transistor. Its effect on the analog signals was simulated and studied. Among others, the signal shapes of the FAST and SLOW signals were examined more closely. A comparison of the simulated FAST and SLOW signals for both transistor types are shown in Fig 3.10. They show a similar behavior and theretofore an adjustment of the schematics was not necessary in order to use the replacement transistor. Nevertheless, before installation of the boards into the ECAL detector, a detailed performance investigation was done and will be discussed in Section 5.1.

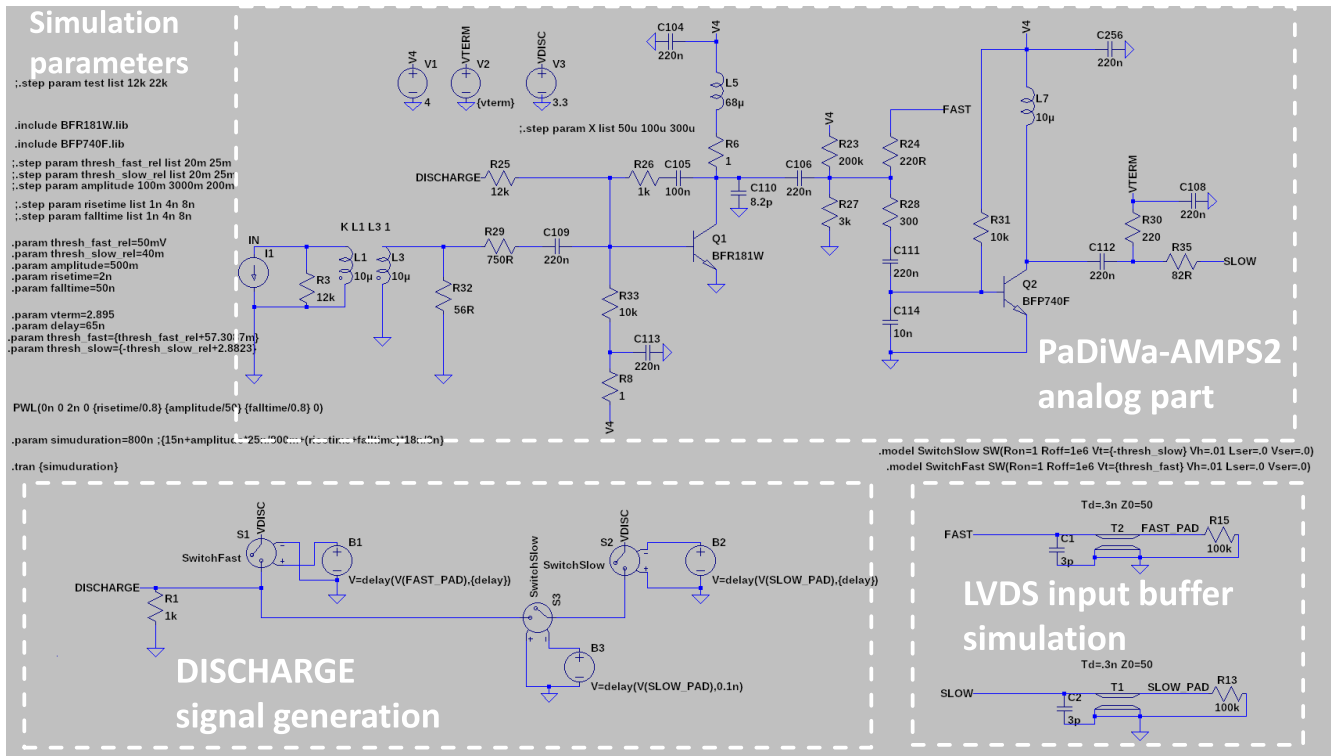


Figure 3.9.: LTspice model of the PaDiWa-AMPS2 circuit which is based on [68]. In the upper part, the analog electronic part is modeled. In the lower left, the generation of the DISCHARGE signal is modeled. In the lower right, the LVDS input buffers are simulated.

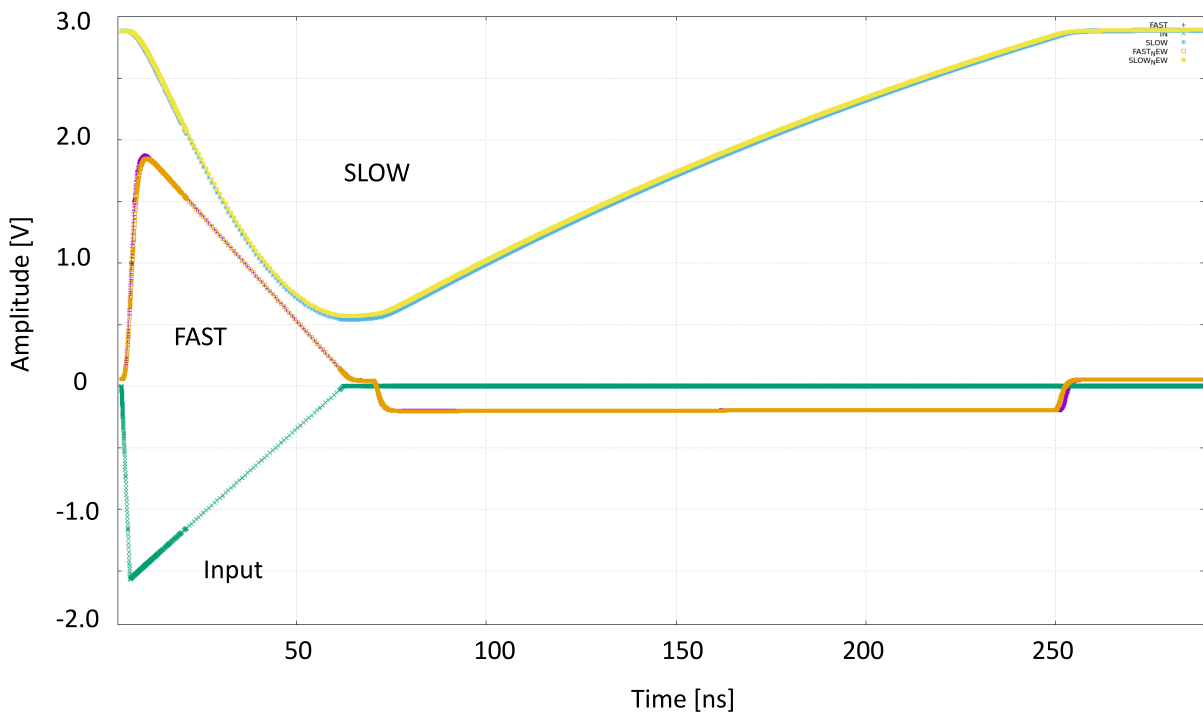


Figure 3.10.: LTspice simulation, comparing FAST and SLOW signals of the obsolete BFS520 transistor with its replacement BFU550W. The input signal for the simulation is shown in green. FAST and SLOW signals are shown for both transistor types and have only very slight deviations from each other.

4 Integration of the read-out electronics into the ECAL detector

The ECAL mainframe has been installed inside the HADES cave in 2017. Until the beginning of 2018 four sectors have been filled with detector modules and equipped with read-out hardware afterwards. In Fig. 4.1 a panoramic photography shows an inside view of the ECAL detector. Three of the four fully equipped sectors are visible from its back side.

Within the scope of this work, the read-out electronics was installed inside ECAL. This includes the installation of infrastructure for the data acquisition, the laying of several kilometers of cables and the installation and commissioning of network and read-out equipment. In this section the integration process will be described. The read-out structure is shown in more detail and naming conventions of the individual components are given.

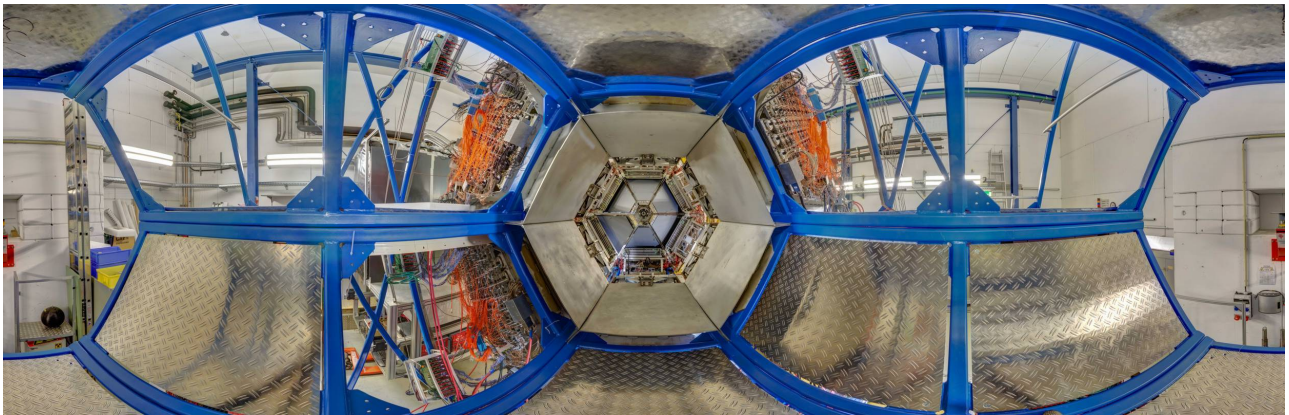


Figure 4.1.: Cylindrical panorama composite sitting inside the ECAL detector. In the central hole one can see the back side of HADES with TOF detector and the back-most layers of the MDC. Three fully equipped ECAL sectors are visible which illustrate the high degree of cabling (brownish: signal and high voltage cables, orange: optical fibers). (Picture taken in February 2019)

4.1 ECAL support frame and module installation

The installation of the ECAL support frame in the HADES cave took place in August 2017. In Fig. 4.2 (left) the support frame after installation in the cave is shown. In the picture the numbering convention of the six sectors is indicated. Lead glass modules have been inserted from the front side. Each module is fixed with four screws on holding rods. During laboratory tests it was found out that the brass box of the modules is not fully light tight. Therefore the front side of each sector is covered with black PVC foil. Black silicone is used to close possible light leakages on the back side of the modules. So far, four sectors have been equipped with detector modules. The upper two sectors number 2 and 6 are equipped with modules containing new 3-inch Hamamatsu R6091 PMTs. The lower two sectors number 3 and 5 are equipped with 1.5-inch EMI 9903KB PMTs. A fifth sector is planned to be equipped until the beginning of 2020 and the last sector will follow in the end of 2020. Those sectors will be equipped with 3-inch Hamamatsu R6091 PMTs. It is also intended to upgrade sectors number 3 and 5 with 3-inch PMTs in the near future. The ECAL support structure is also used to mount the RPC detector (see Fig. 1.5) which is attached on the front-side of the detector. In future, parts of a new forward tracking system [69] will be mounted in the central hole of the support structure. They will allow tracking of particles in polar angles between 0° and 7° which is currently not covered by HADES. All three sub detectors, ECAL, RPC and the future forward tracking system, share the same infrastructure. It has been taken care to create as many synergies as possible. For example, devices are shared between the detectors, e.g. power supplies and the network infrastructure.

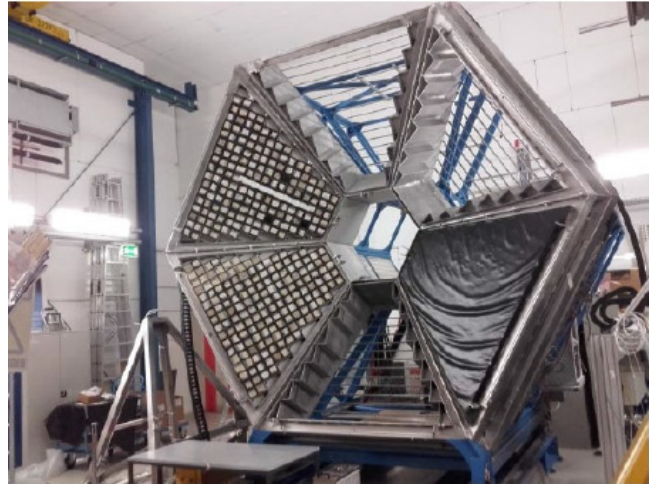
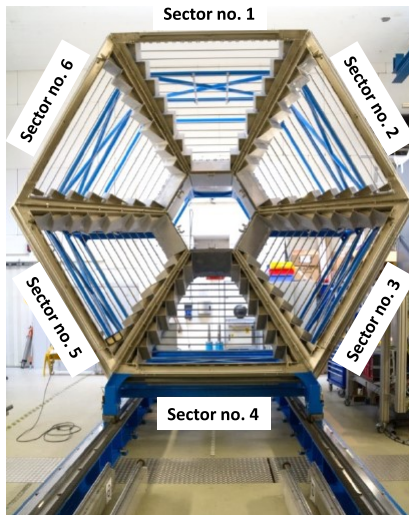


Figure 4.2.: **Left:** Front view (facing into beam direction) of the ECAL mainframe mounted on a rail system which allows moving it to a service position. The numbering of the sectors is indicated. (Picture taken in August 2017) **Right:** Three sectors filled with modules. One sector is already covered with a light-tight black PVC foil in order to seal the modules from external light. (Picture taken in January 2018)

4.2 Read-out electronics and network infrastructure inside ECAL

In Fig. 4.3 the read-out scheme inside the ECAL detectors is shown in detail. Up to eight PMTs are connected to one PaDiWa-AMPS2 front-end board. A TRB3sc TDC board, which is located in a small crate, is used to read out three PaDiWa-AMPS2 boards. In total, six TRB3sc crates are evenly distributed in the detector in order to keep read-out cables as short as possible. Inside the crate seven TRB3sc TDC boards are connected via a backplane with a TRB3sc master board. This board is used for the communication with the HADES DAQ. It receives the trigger information and the reference time from the HADES DAQ via an Ethernet connection. The data requested by the HADES DAQ is also delivered via Ethernet connection. Control data is sent and received in both directions via an optical link.

It is possible to send photons, generated by a LASER system, into each ECAL module which can be used for monitoring and calibration purposes. Each sector is equipped with its own LASER system. Each system contains a LASER diode and an optical micro lens system which couples the LASER diode to 196 optical fibers. The control of each LASER system is realized with a pulser add-on board [70] for the TRB3 platform. This allows the control and configuration of the LASER system via TRB3 software which allows to switch on the LASER system during spill brakes. More details about the LASER system will be given in Section 5.2.3.

In order to house the network infrastructure and power supplies two standard 19-inch network racks with 32 height units (Tritron RMA-32-A68-CAX-A1) have been mounted in the rear part of the ECAL support frame. The mounting position was chosen to allow access from both sides. The racks house the low and high voltage powers supplies, network equipment and the hardware for the trigger and reference time distribution. Cables are guided through cable chains which are mounted on the support rails of the ECAL mainframe. The position of the racks is shown in Fig. 4.4. The installed equipment inside the two racks is shown in Fig. 4.5.

4.3 Read-out electronics installation and naming conventions

In the following, an overview of the read-out electronics integration in the sectors and the naming convention will be given. Each module is equipped with two coax cables, a high voltage and a signal cable. Both cables have a length of approximately 1.5 m. In order to guide the cables of each module

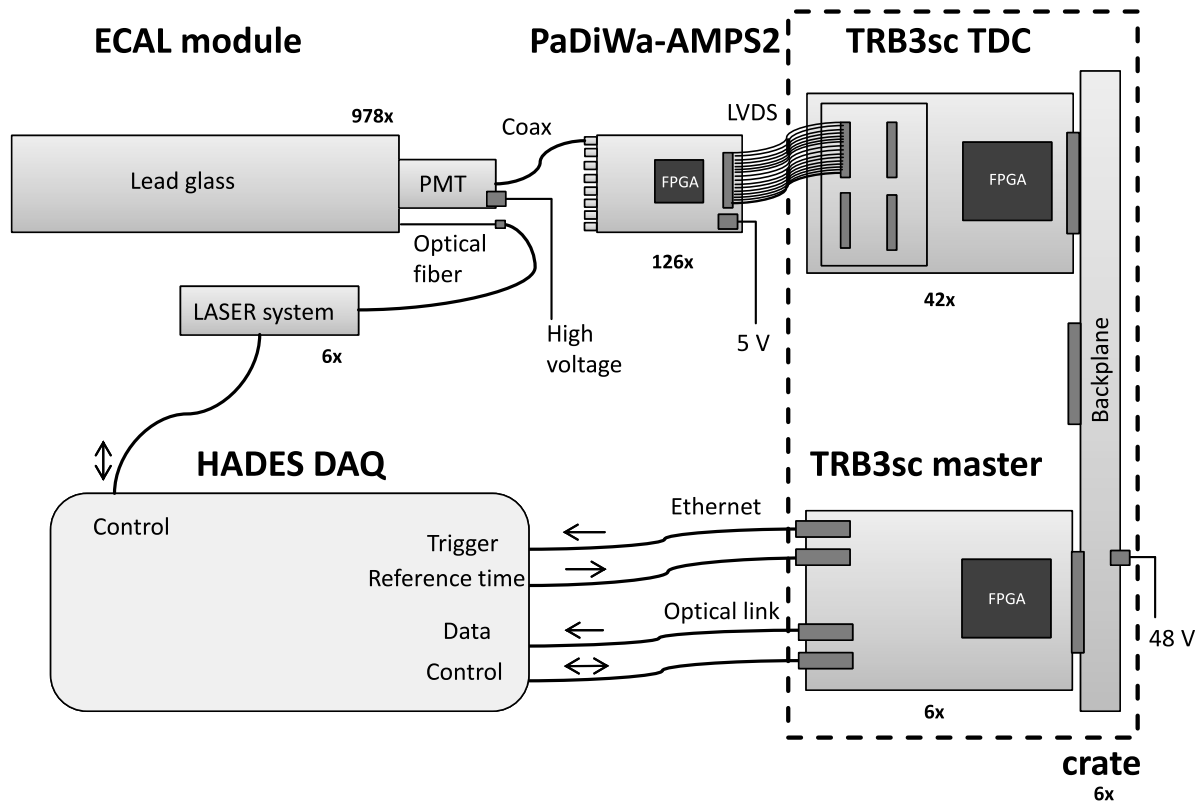


Figure 4.3.: Read-out scheme of the HADES ECAL detector including the number of installed elements. PMT signals are digitized in the PaDiWa-AMPS2 front-end board for the TRB3 platform. The TRB3sc crate compatible version is in use. The read-out is triggered by the HADES DAQ and data is sent to it. Control communication is sent in a separate line.

to the read-out electronics and high voltage distribution boxes the grouping scheme shown in Fig. 4.6 is used. The 163 modules of each sector are divided into seven groups. Each group consists of three subgroups containing eight modules, respectively. The signal and high voltage cables of each of the seven groups are guided to the edge of the detector, where the HV distribution boxes are located. Close to the HV distribution box, a mounting frame is installed, each containing three PaDiWa-AMPS2 boards. The mounting frame was designed in order to allow passive ventilation between the boards and to give easy access to them in case of a failure. A technical drawing of the mounting frame can be found in Appendix A.1.

Each of the three PaDiWa-AMPS2 boards, which are mounted inside the mounting frame, is connected via 1 m (a few with 1.5 m) long 40-pin LVDS flat cables to one TRB3sc TDC board. Those boards are mounted in six crates which are evenly distributed in the detector. Each crate contains a master TRB3sc and seven TRB3sc TDC boards. The schematic drawing in Fig. 4.7 shows the crate location in the ECAL mainframe and the addresses of the boards. Each crate contains a master board with the address 8A0X and seven TDC boards addressed 60XY, where X is the number of the corresponding sector and Y the board number, both counting from 0. All read-out elements described are indicated in Fig. 4.8, which gives a side view into sector number 5.

4.4 Low and high voltage distribution system

A *low voltage* (LV) distribution is needed for the six TRB3sc crates and the 126 PaDiWa-AMPS boards. Beside this a *high voltage* (HV) distribution is needed for each detector module. In Fig. 4.4 the routing for the HV cables is visualized too. The required high voltage is provided by three CAEN SY4527 crates which are equipped with 14 modules (CAEN 1535N and CAEN 7495N). With each module 24 PMTs can

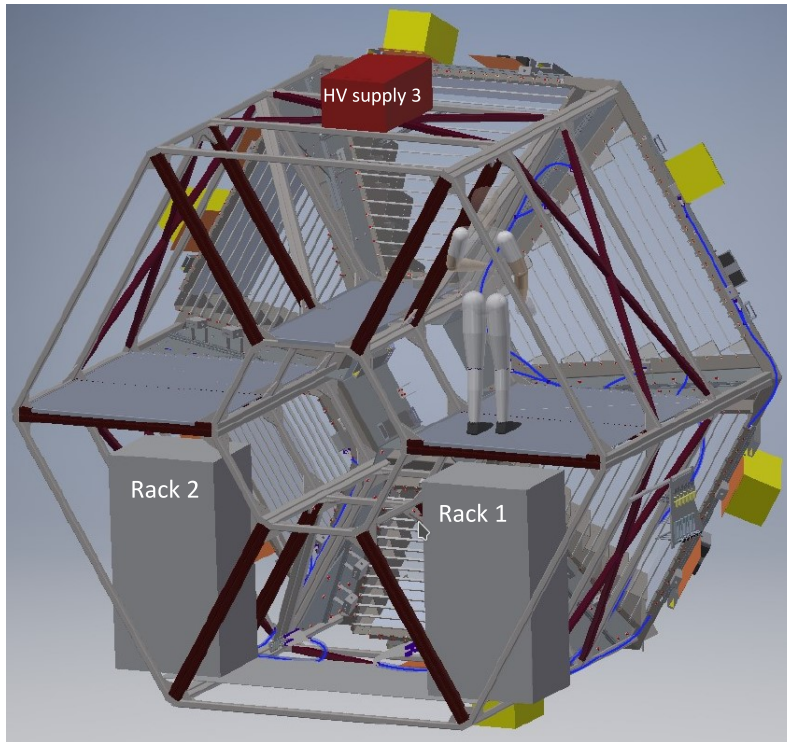


Figure 4.4.: CAD drawing of the infrastructure in the ECAL mainframe. Two 19-inch racks house the network infrastructure, low and high voltage power supplies. A third HV power supply (red box) is mounted on the top side. The routing of high and low voltage cables is shown in blue. The yellow boxes are the read-out boards of the RPC detector. The hole in the middle is kept free since forward tracking detectors will be installed there in future.

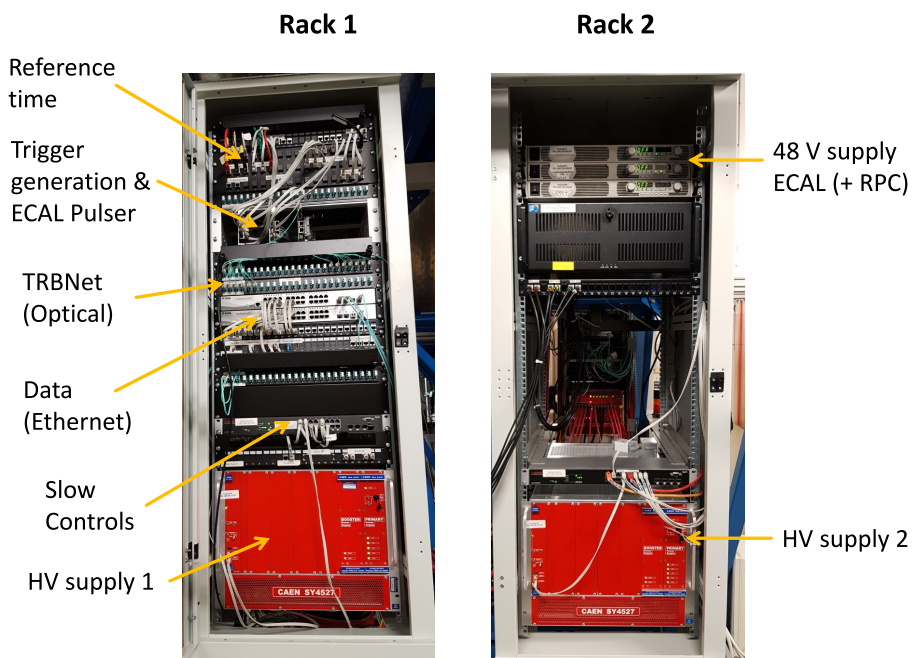


Figure 4.5.: Description of the interior of two standard 19-inch racks which are mounted in the ECAL main-frame. They house the low voltage and high voltage powers supplies, network hubs, the trigger and the reference time distribution.

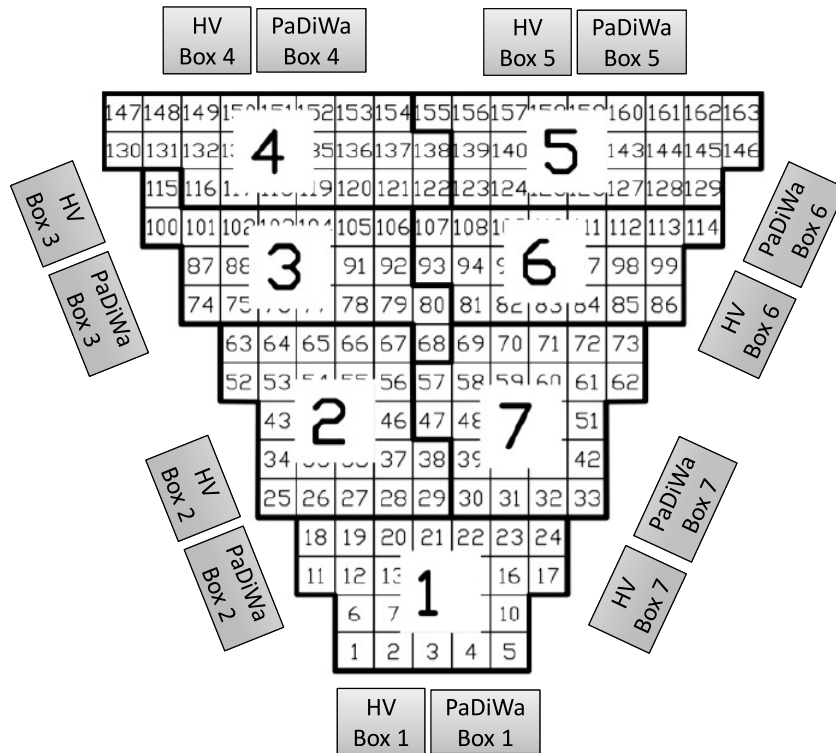


Figure 4.6.: ECAL module grouping scheme, facing to the back side of a sector. The 163 modules in an ECAL sector are arranged in seven groups. Each group is divided into three subgroups containing eight modules, respectively.

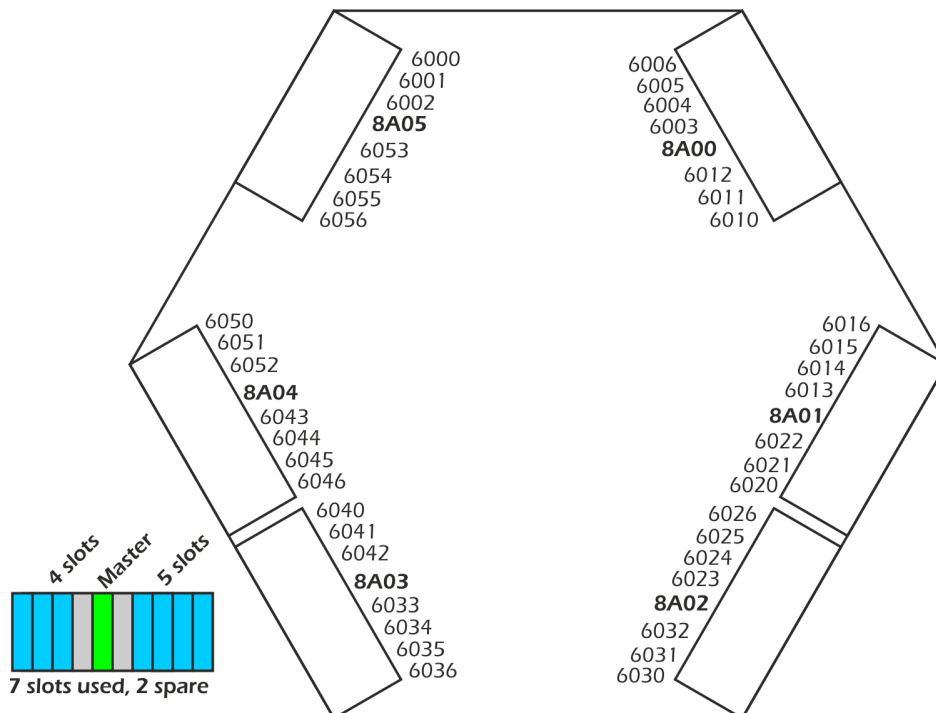


Figure 4.7.: Location of the TRB3sc boards, facing the beam direction. The boards are mounted in six crates. Each crate contains a master board 8A0X and nine TDC boards 60XY, where X is the sector number and Y the board number counting from 0. (Taken from [71])

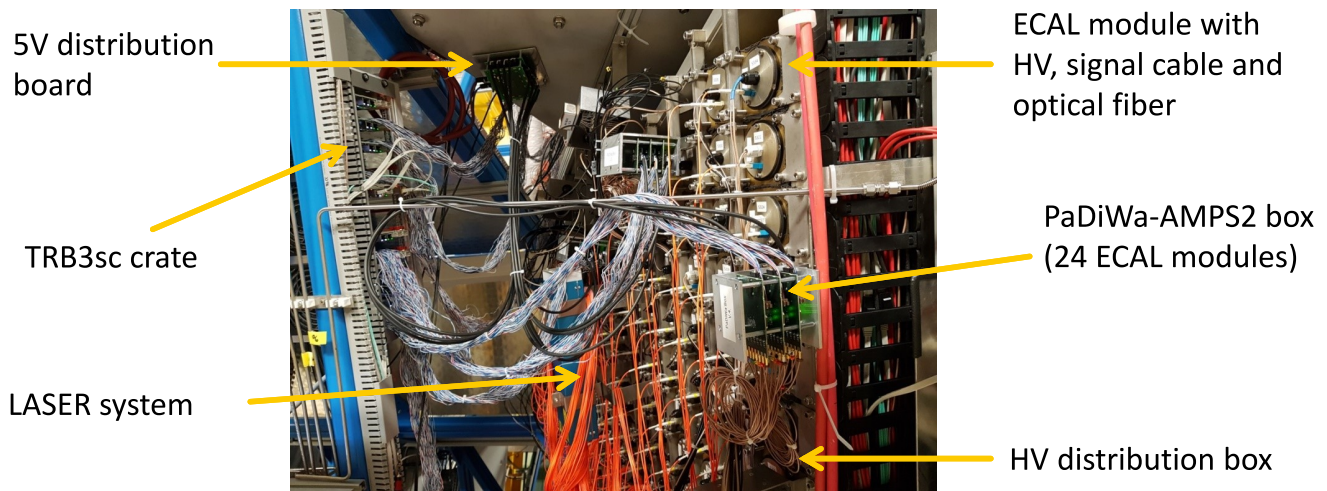


Figure 4.8.: Side view into sector number 5. The main read-out parts are marked.

be powered. A HV crate is located in each of the two racks, a third one is mounted on top of the ECAL. Since the low voltage power supplies are located close to the HV devices, they follow the same cable routing to the sectors.

The PaDiWA-AMPS front-end board needs a voltage of 5 V and a current of about 700 mA which results in a power consumption of 3.5 W per board. For that, three power supplies (Rohde&Schwarz HMP4040) are used. Each one is equipped with four output channels. One channel is connected to 12 PaDiWa boards resulting in a power consumption of 42 W per channel. In order to keep the cable losses low 6 mm² cables are used since long distances with lengths up to 10 m have to be overcome. The energy loss for a 10 m long 6 mm² cable with an operating voltage of 5 V is 0.7 W. A voltage drop of 0.4 V is expected for the same cable which can both be compensated by the power supplies. The cables are routed to the sectors in the same way as the HV cables. At the sector the cable is connected to a distribution board which allows to connect up to twelve PaDiWa-AMPS2 boards. The schematics of the distribution board can be found in Appendix A.16.

The six TRB3sc crates need a 48 V low voltage power supply with a total power of about 300 W. The power supply is located in rack number 2. Cables with a cross-sectional area of 4 mm² are in use. All power supplies can be controlled remotely which is useful to perform a power-cycle of the read-out electronics in case of a problem during beam time.

4.5 Integration of the read-out electronics into the HADES software structure

After installation of the ECAL read-out electronics, the hardware was integrated into the HADES software structure. The module naming conventions have been shown in Fig. 4.6. A *look-up table* (LUT) was created which allows an assignment of the TDC address and channel to the corresponding ECAL module. The table contains the TRB3 address, the TDC channel number, a FAST or SLOW channel flag and the corresponding module number which results in about 2000 entries.

5 Characterization and commissioning of the ECAL read-out electronics

The performance of the read-out electronic was systematically studied in the laboratory before installation into the ECAL detector. The evaluation of the PaDiWa-AMPS2 prototype before the final batch fabrication of 150 boards at GSI was important. For this a SPICE simulation is available and laboratory tests have been conducted in order to characterize the charge and time measurement precision. Furthermore, this chapter deals with the commissioning of the entire read-out system of the ECAL detector. The threshold setting procedure for the discriminators and the commissioning of the detector and read-out system with LED signals, cosmic muons and test-beam will be shown. In the end, issues which have been encountered during commissioning are addressed and their solutions will be presented.

5.1 Characterization of the PaDiWa-AMPS2 board in the laboratory

Before installation of the PaDiWa-AMPS2 board into the ECAL detector its performance was investigated in the laboratory. A typical set-up is shown in Fig. 5.1. The PaDiWa-AMPS2 board is connected to a TRB3 board in a stand-alone set-up. A laboratory pulse generator is used in order to generate signals similar to PMT pulses. Analog and digital signals can be probed on the PCB with the help of an oscilloscope. A standard *personal computer* (PC), equipped with the read-out software DABC [39] and Go4 [60], allows a data analysis in real-time. For example ROOT [72] based analysis macros can be executed in real-time which is very useful in a laboratory environment.

In the following, the measurements, which have been conducted in order to evaluate important parameters like time and charge precision, will be presented.

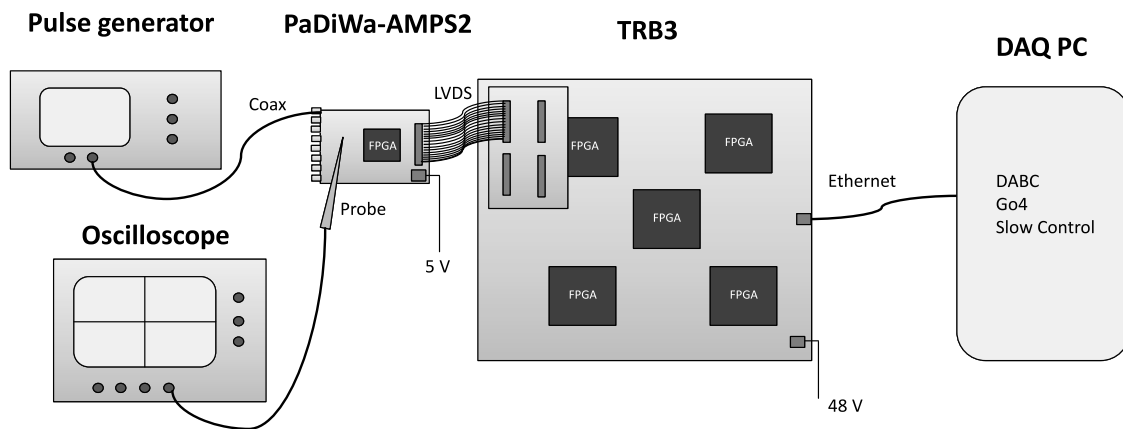


Figure 5.1.: Laboratory test set-up for the characterization of the PaDiWa-AMPS2 prototype. Test signals, generated by a laboratory pulse generator, are injected to the PaDiWa-AMPS2 board which is connected to a TRB3 board. A DAQ PC with ROOT based analysis software is used to investigate the performance of the system.

5.1.1 Time measurement precision

An important performance parameter is the time precision of the full read-out chain. It can be characterized by the width of a distribution which one gets from a repeated time measurement. In order to determine the time precision of the PaDiWa-AMPS2 board, a PMT shaped signal with a rising edge of 5 ns and a falling edge of 50 ns and an amplitude of 1.5 V was generated by the laboratory pulse generator. The measurement set-up is shown in Fig. 5.2 (left). The pulse generator signals were split and sent into two different input channels. As described in Chapter 3, the FAST channel is used for the determination of the arrival time, where the time information is encoded in the leading edge of the discriminated FAST

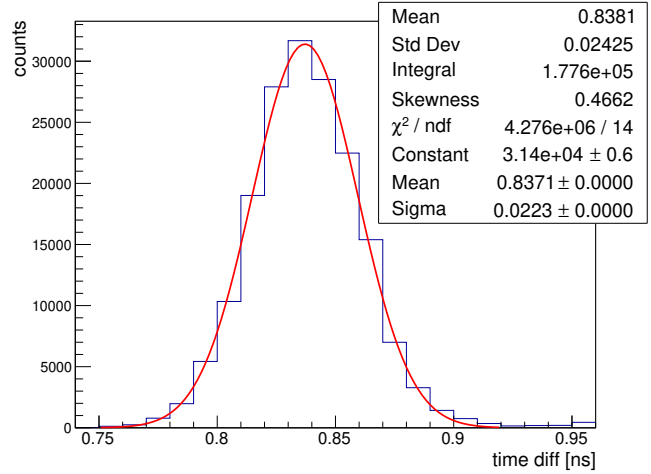
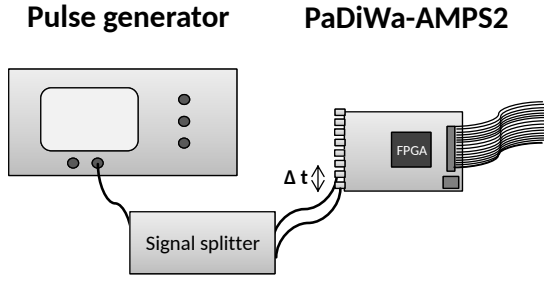


Figure 5.2.: Left: Laboratory set-up for the time precision determination. Right: Distribution of the measured time difference of the two FAST leading edges with a fitted *Gaussian distribution*.

signal. The distribution of the measured time difference of the two leading FAST edges is shown in Fig. 5.2 (right). The measurement precision is characterized by the sigma value $\sigma_{\text{ch1,ch2}} = 22.3 \text{ ps}$ of a fitted *Gaussian distribution*. By taking into account that both channels have the same contribution to the time precision, the precision of a single channel can be estimated with:

$$\sigma_{\text{ch1}} = \frac{\sigma_{\text{ch1,ch2}}}{\sqrt{2}} = 15.8 \text{ ps}. \quad (5.1)$$

The achieved precision exceeds by far the required precision for ECAL, which is about 300 ps.

5.1.2 Charge measurement precision

Another important performance parameter is the precision of the charge measurement method. For the evaluation PMT shaped pulses (rise time: 5 ns, fall time: 50 ns) were generated by a laboratory pulse generator. The amplitude was varied in order to get different pulse charges. The signals have been injected into the PaDiWa-AMPS2 board and the resulting Q2ToT was extracted in a ROOT analysis. The Q2ToT distributions have been fitted with *Gaussian* functions. The fitting parameters for the mean value μ_{Q2ToT} and the standard deviation σ_{Q2ToT} are used to characterize the charge and its precision. Thereby the relative measurement precision is then defined by:

$$\Delta\text{Q2ToT} = \frac{\sigma_{\text{Q2ToT}}}{\mu_{\text{Q2ToT}}} \cdot 100\%. \quad (5.2)$$

In Fig. 5.3 the measured Q2ToT for different input pulse charges is shown. The charges correspond to pulse amplitudes between 50 mV and 2500 mV. Besides a comparison with the PaDiWa-AMPS1 board, the PaDiWa-AMPS2 prototype is compared with a version containing a galvanic isolation of the input signal ground. Since a galvanic isolation could potentially deteriorate the signal shape in a negative way a careful investigation was needed. It has been shown that the version with a transformer shows a different slope for the measured Q2ToT values. Nevertheless, its course still shows no saturation. Also, its non-linear behavior will not influence the charge measurement in ECAL, since the full system will be calibrated offline.

For each Q2ToT measurement the standard deviation σ_{Q2ToT} was extracted from a *Gaussian* fit and the relative charge measurement precision was calculated by equation 5.2. The result is shown in Fig. 5.4. The results obtained with the PaDiWa-AMPS front-ends are compared with a reference charge mea-

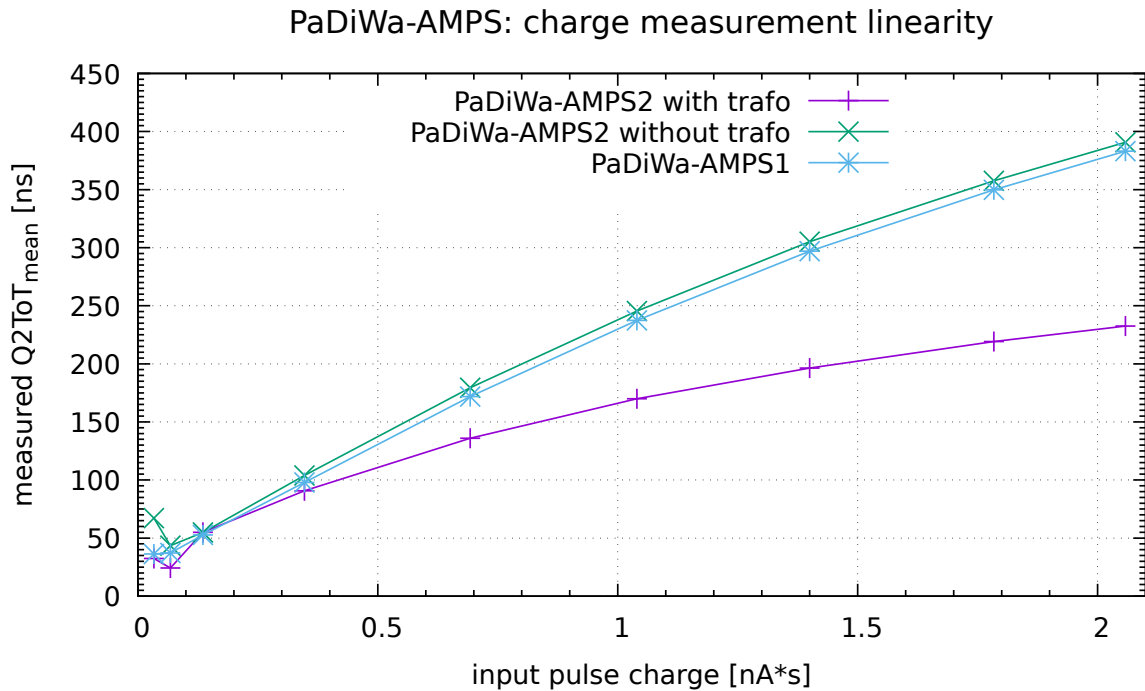


Figure 5.3.: Measured Q2ToT for different input pulse charges. The PaDiWa-AMPS2 board with and without galvanic isolation is compared with the PaDiWa-AMPS1 prototype.

surement, performed with an oscilloscope. For signal charges above 0.5 nAs (signal amplitude above 300 mV) the relative precision is below 0.5 %. The best precision was obtained with the PaDiWa-AMPS2 board containing the transformer.

Every threshold triggered discriminator is affected by a *time-walk effect*. The effect is illustrated in Fig. 5.5. Signals with different amplitudes reach the voltage value of the threshold at different times. The effect is especially pronounced for signals with small amplitudes where the arrival time is shifted to later times, therefore falsifying the time measurement. This effect has to be taken into account and corrected. An offline time-walk correction for the ECAL data will be applied on an event-by-event basis. A detailed description of the calibration process of ECAL will be shown in Chapter 6.

A time-over-threshold measurement is typically very sensitive for noise frequencies in the range of the measured time-over-threshold. In this case a *jitter* (see also Fig. 5.5) on the input signal and especially low frequency noise on the signal could distort the measured time-over-threshold by superimposed interference. This is typically indicated by a multi-peak structure in the time-over-threshold distribution [74]. In the PaDiWa-AMPS1 prototype this effect was very pronounced and visible in almost all Q2ToT distributions. An example of such a structure is shown in Fig. 5.6. In the PaDiWa-AMPS2 board these structures are not present any longer. The improvement can be explained by the transformer in the input stage which improves the signal-to-noise ratio, e.g. by the elimination of ground loops.

5.1.3 Dynamic measurement range and threshold settings

Another important property of the read-out electronic is its dynamic measurement range. It is defined by the ratio of the largest and smallest measurable signal amplitude. In order to achieve the highest possible dynamic range the proper threshold settings are important. The FAST threshold should be very close to baseline to achieve the best time precision since the signal rise is steepest here. A value of 50 mV above the baseline has proven to be an optimal value. The threshold for the SLOW signal is more challenging due to its high sensitivity to low frequency noise. It is difficult to measure the charge of signals with amplitudes below 40 mV using the proposed measurement concept. This is due to noise in the SLOW

PaDiWa-AMPS: relative charge precision

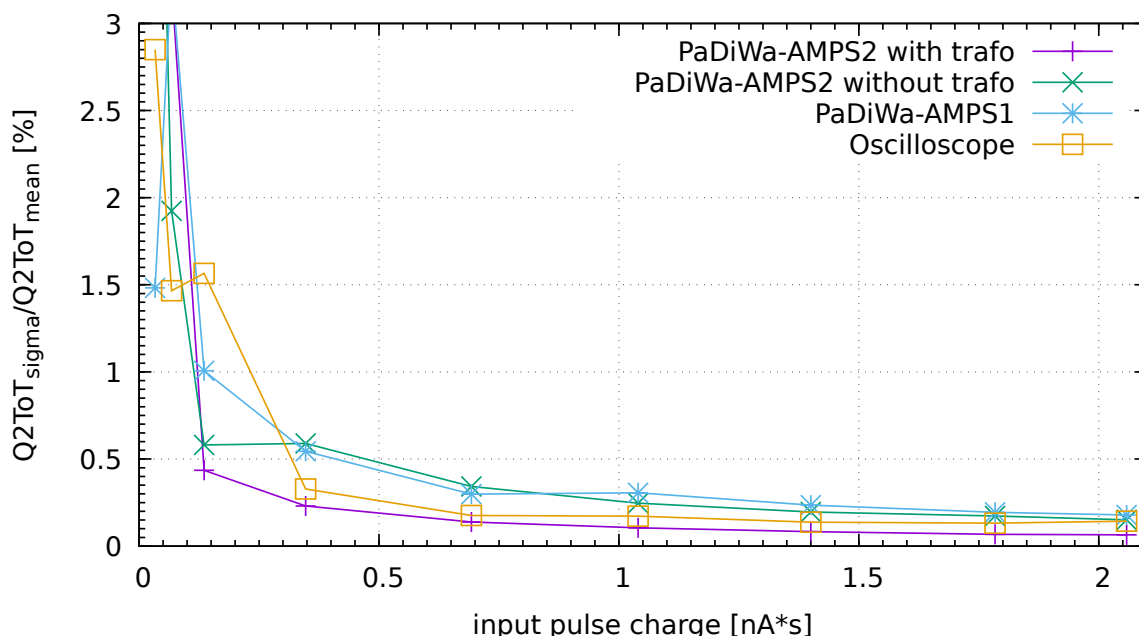


Figure 5.4.: Relative charge measurement precision for the input charge. The PaDiWa-AMPS2 board, with and without galvanic isolation, is compared with the PaDiWa-AMPS1 prototype and a oscilloscope measurement.

channels which make a threshold setting below this value difficult. In the SLOW channel a value of about 50 mV is prudent.

At input amplitudes above 3 V the SLOW signal starts to saturate. This is due to the fact that it reaches the reference voltage which prevents a further rise of the signal. This behavior is shown in Fig. 5.7. Since the SLOW signals are still increasing in their width, by increasing amplitude of the input signal, the measuring method also works with large input amplitudes (or larger charges). Even so, the charge measurement principle has been proven to work with signals amplitudes up to 10 V which results in a dynamic measurement range of 250, where input amplitudes between 40 mV and at least up to 10 V can be measured.

5.1.4 Rate capability

The rate capability of the read-out electronics is limited to about 100 kHz. This limitation is due to a signal overshoot, followed by an undershoot which both are present in the SLOW signal. The oscilloscope picture in Fig. 5.20 shows the overshoot and undershoot. Together, they have a natural decay time in the order of about 10 μ s. A subsequent signal pulse will be influenced by the overshoot and undershoot in the SLOW signal in case they are not fully decayed. Consequently, because of the fixed discriminator threshold voltage, a smaller width of the signal will be measured. For the PaDiWa-AMPS1 prototype there was an attempt to reduce the overshoot [64] by tuning the inductance L5 (see the PaDiWa-AMPS2 schematics in 3.4 and the PaDiWa-AMPS1 schematics in Appendix. A.15), however, only an active baseline restorer will be able to eliminate this effect fully.

A new front-end board for the TRB platform is currently under development [75]. The new measurement technique is specially designed for the measurement of signal pulses and is by default equipped with an active baseline restorer. The board is fully compatible with the TRB platform. A first prototype will soon be tested for the compatibility with ECAL signals.

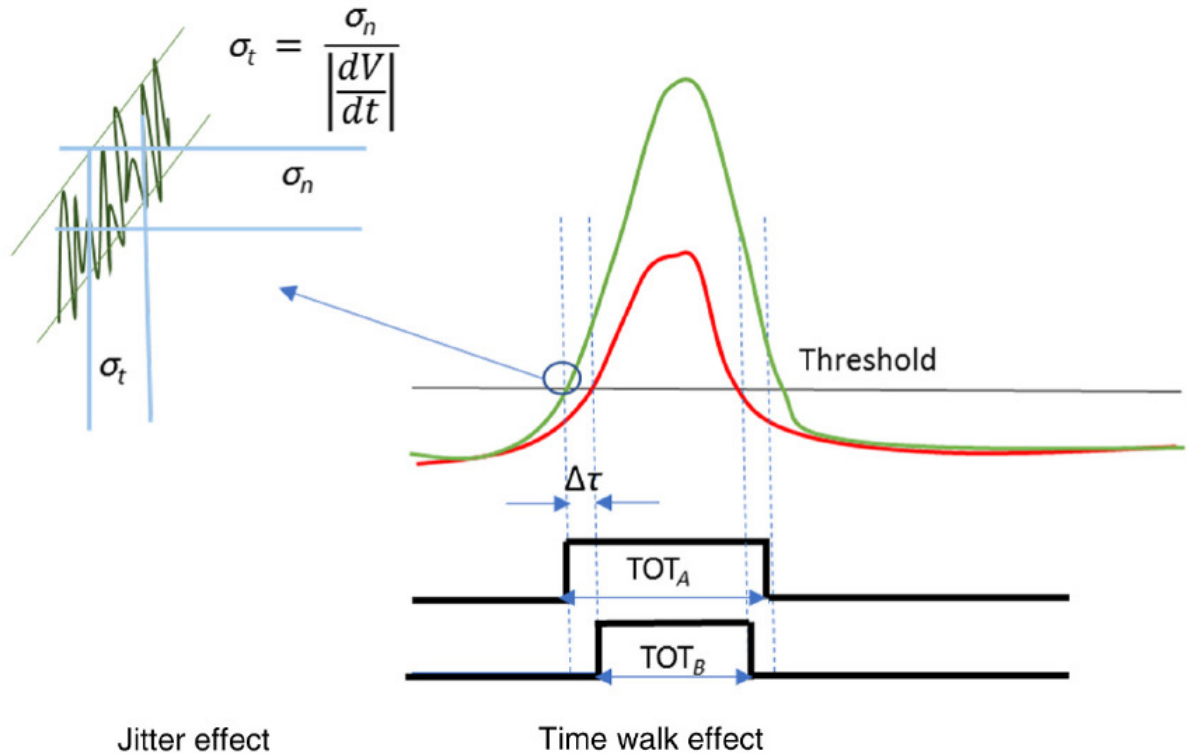


Figure 5.5.: Illustration of *time-walk* and *jitter* effects of a discriminated signal pulse. The time-walk effect is due to the fact that voltage values of the threshold are reached at different times which are due to the physics of signal formation. This effect is especially pronounced for signals with small amplitudes. An additional noise jitter added to the signal causes small amplitude variations which deteriorates the time measurement precision. (Taken from [73])

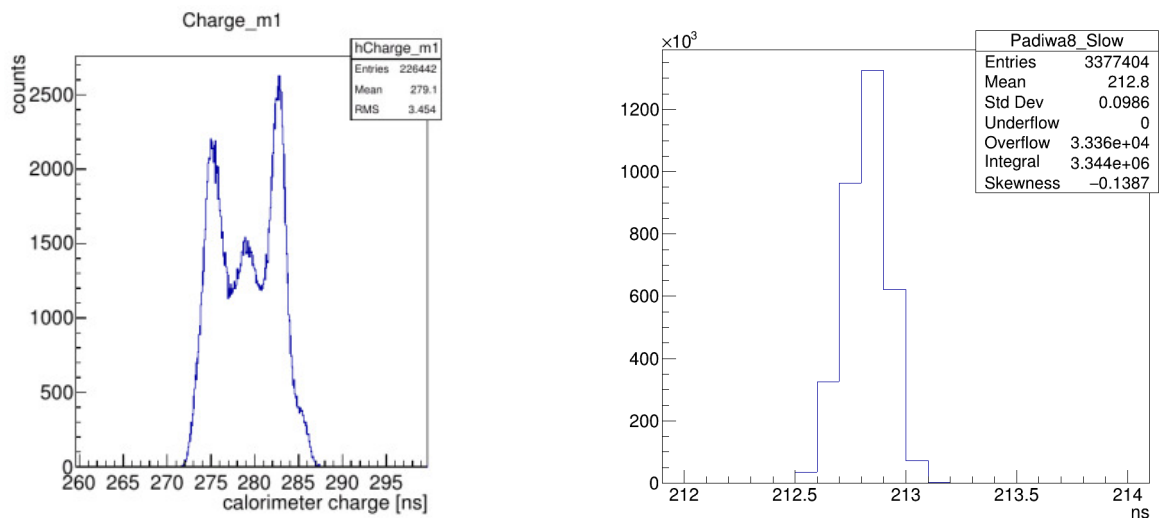


Figure 5.6.: **Left:** Multi-peak structure visible in the Q2ToT time-over-threshold measurement of the PaDiWa-AMPS1 prototype board. **Right:** In the new PaDiWa-AMPS2 board, which is equipped with a transformer in the input stage, the multi-peak structure is not present any longer.

5.1.5 Power consumption and heat emission

The total power consumption of the PaDiWa-AMPS2 board is about 3.5 W. In Fig. 5.9 a thermal camera picture of the board is shown. Hot spots (see yellow spots in Fig. 5.9) are the transistors of the first atten-

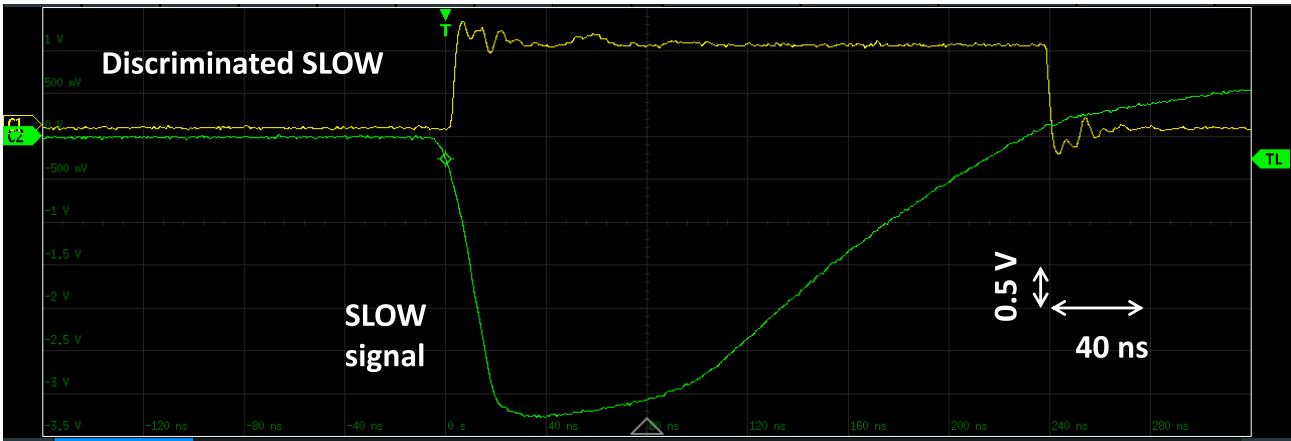


Figure 5.7.: A saturation of the SLOW signal is visible for input signal with an amplitude above 3 V. The analog SLOW signal for a 5 V input signal is shown in green, the corresponding discriminated SLOW signal is shown in yellow.

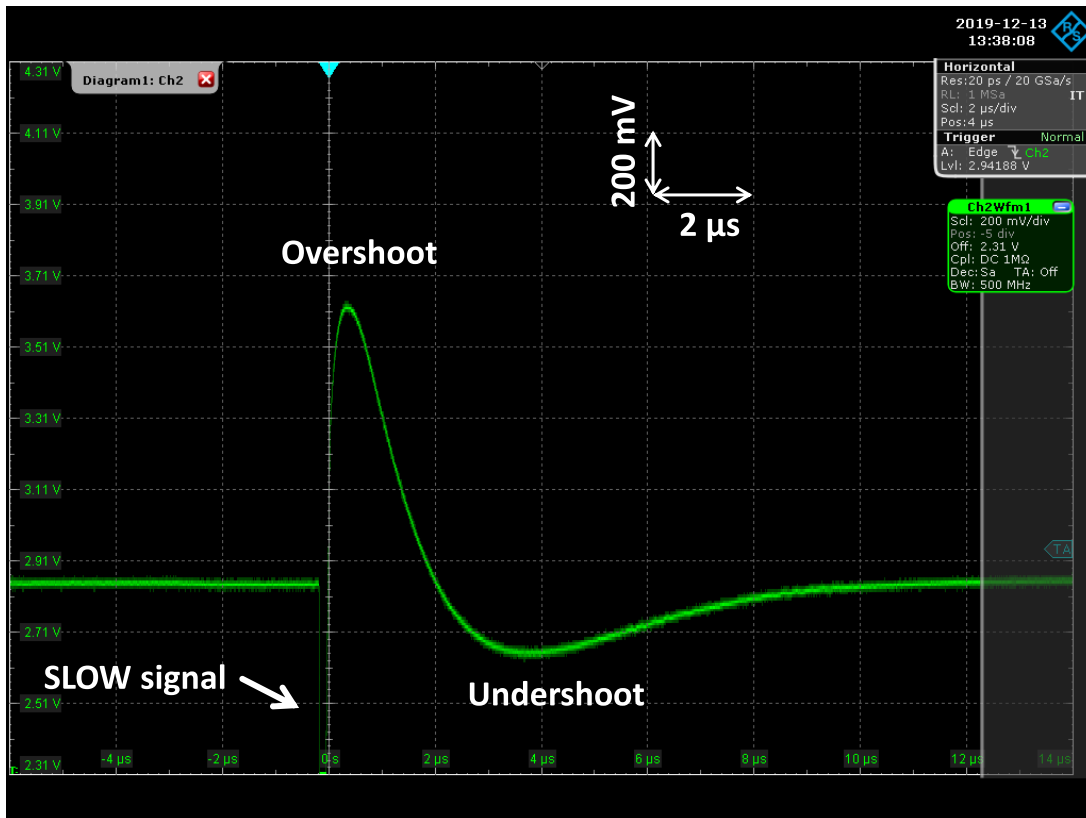


Figure 5.8.: The SLOW signal contains an overshoot, followed by an undershoot. Both have a total decay time of about $10\ \mu\text{s}$ which limits the rate capability of the read-out electronics to about 100 kHz.

uation stage, the FPGA and the *Low-Drop-Out regulators* (LDOs) for the power supply. The temperature of the hot spots can reach up to $50\ ^\circ\text{C}$. Since the boards are not densely arranged in the ECAL detector an external cooling will not be necessary. It is known that temperature changes can influence the signal run times inside an FPGA. Since the HADES cave is actively air-conditioned large temperature variations, which could potentially harm the functionality of the PaDiWa-AMPS2 board, are not expected.

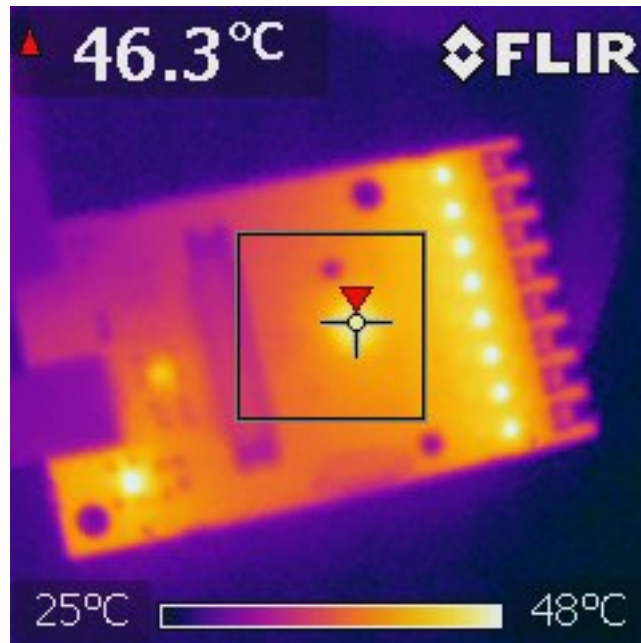


Figure 5.9.: Temperature measurement with an infrared camera. Hot spots (yellow spots) are the eight transistors of the first attenuation stage, the FPGA and the Low-dropout regulators (LDO) which are placed in the lower left region.

5.1.6 Delay adjustment of the DISCHARGE signal

Within the framework of a mini-research project [76] the internal delay of the DISCHARGE signal has been investigated. As described in Section 3.1, this signal is used to discharge the integration capacitor in a controlled way. This capacitor should ideally be discharged when the input pulse is fully integrated. This depends on the width of the input pulse. An adjustment for the start of the DISCHARGE signal is needed to allow to adopt the measurement principle to a large variety of pulse shapes.

The DISCHARGE signal is generated from a logical AND between the leading edge of the FAST and the leading edge of the SLOW signal. The same signal is switched off when the trailing edge of the SLOW signal is detected. Signals, which are routed inside the FPGA need a specific time to pass through the electronic switches along its route. This causes a delay of the signal, which can be used to delay the DISCHARGE signal. In order to generate the delay, the DISCHARGE signal is sent back and forth between two banks which are located on the edges of the FPGA. The arrangement of the banks is schematically shown in Fig. 5.10. With the help of a multiplexer it is possible to select the number of times the signal is routed between the banks A and B. The multiplexer allows a selection of time delays in 64 steps. The obtained time delay for the chosen step number is shown in Appendix A.18. Delays can be generated between 10 ns and 200 ns with a step size of about 2 ns. In practice, a delay value of 20 ns is used in order to match the used ECAL PMTs signal shapes (see Fig. 2.9 and Fig. 2.10). The adoption process of the DISCHARGE signal to an input signal is shown in Fig. 5.11.

5.2 Commissioning of the read-out electronics in the ECAL detector

In this section the most important DAQ-Operator tools will be introduced. The threshold adjustment and setting procedure will be described. After this, the performance of the ECAL for LASER, cosmic muons and an Ag-test beam will be given. In the end, issues which have been encountered during the commissioning and their solutions will be presented.

After the installation of the read-out electronics and the DAQ infrastructure, the ECAL detector was put into operation. It had to be ensured that all individual components function properly and the performance of the whole system had to be evaluated. In order to test the full read-out system, test signals

FPGA

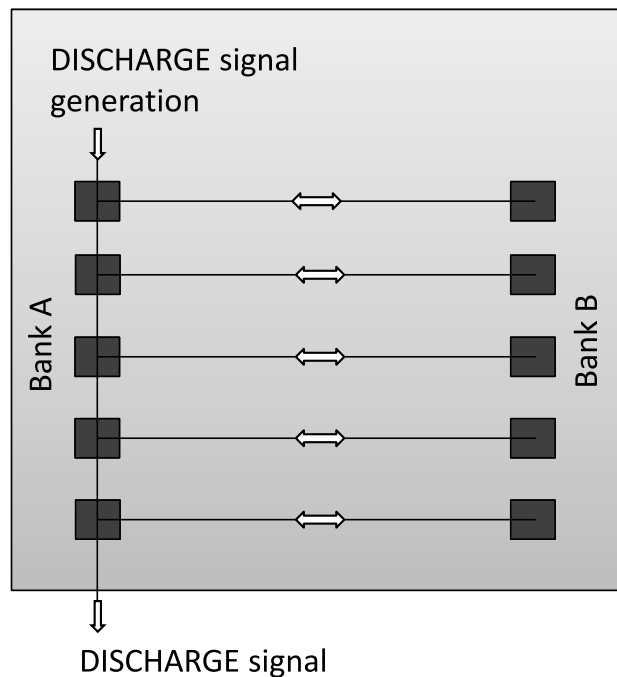


Figure 5.10.: Schematic drawing of the DISCHARGE signal delay inside the FPGA. The DISCHARGE signal is delayed by routing it back and forth between the banks A and B.

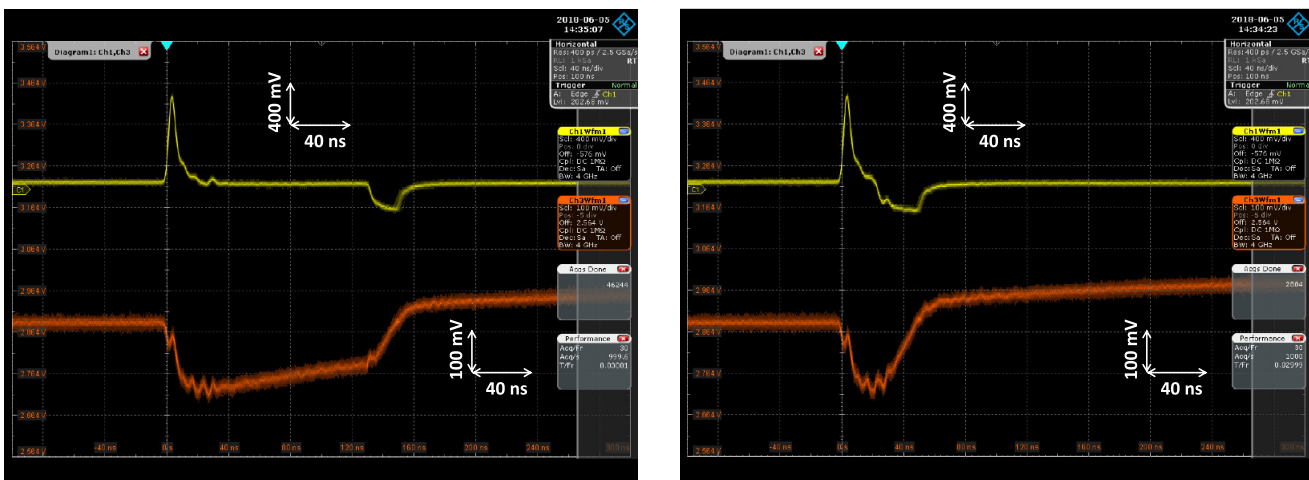


Figure 5.11.: Left: The FAST signal including the DISCHARGE signal is shown in yellow. The SLOW signal is shown in orange. In this situation the DISCHARGE delay is too large. Right: In this situation the DISCHARGE is adjusted to the width of the input signal width which is equivalent to the width of the FAST signal.

have been generated by the ECAL LASER system, or cosmic muons have been used. An important part of the commissioning phase was the threshold settings for almost 2000 FAST and SLOW channels. Furthermore, tools had to be developed to visualize the proper functioning of the detector during beam time.

5.2.1 Slow control and DAQ-operator tools

For the detector monitoring during a four weeks long beam time, the necessary visualization tools were developed. They visualize the proper function of the detector and its read-out electronics. The monitor-



Figure 5.12.: The central monitoring tool in HADES is the *tactical overview* which visualizes the current status of the sub detectors and the DAQ-system using a simple color code. The most important parts for the ECAL operator are marked, e.g. the indication that all TRB3sc and PaDiWa-AMPS2 boards are addressable, the temperature of the boards and the state of the high-voltage system.

ing scripts are based on *Dmon tools* [37] which are available in the comprehensive software package for the TRB3 platform. They allow reading and visualizing, e.g. registers from the TrbNet and *Experimental Physics and Industrial Control System* (EPICS), variables can be displayed in graphs and tables. A big advantage of the system is that all information is accessible from any web browser, including mobile devices. The central monitoring tool in HADES is the *tactical overview* which visualizes the current status of the sub-detectors and the DAQ-system using a simple color code. An example is shown in Fig. 5.12 where the most important parts for the ECAL operation are marked. In addition, scripts allowing a power-cycling of the ECAL front-end boards in case of a failure have been added in the form of buttons to the main DAQ control computer.

A very useful monitoring tool was developed in collaboration with the RICH detector group [77], since the RICH detector uses also the TRB3 platform. This tool allows to display the TDC-scaler values of the FAST and SLOW channels for every ECAL module in a web browser. Besides the SLOW and FAST channel hit rates, the current threshold value can be displayed for each module. In Fig. 5.13 the configuration of the ECAL detector during a test beam is shown. It is noticeable that modules especially in sector number 3 and 6 are affected by high rates above 10 kHz which is due to missing electrostatic shielding of the PMTs. A detailed explanation will follow in Section 5.3.3.

5.2.2 Threshold settings

A key task during the commissioning was the threshold setting for almost 2000 FAST and SLOW channels. Especially the thresholds for the SLOW channels must be very close to the baseline in order to obtain the largest possible dynamic range. Problems may occur if the threshold is set too low which might result in picking up of baseline noise. In the worst case scenario, this could lead to an oscillation of the

Min: Max: 10000 Send bgr fast

last update: Mon, 03 Dec 2018 - 00:44:45

ECal rate fast chan

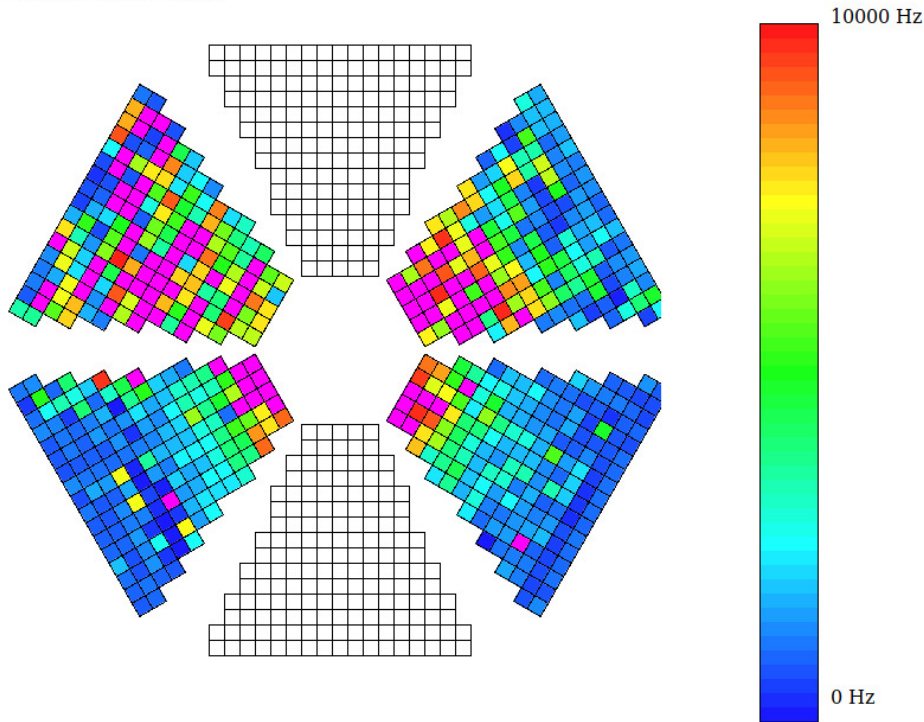


Figure 5.13.: The color code shows the FAST signal rate in s^{-1} which is displayed for each module, facing into beam direction. Magenta colored modules show rates above 10 kHz which is due to the "Max: 10000" filtering.

channels which makes it temporally unusable. In such a case, the threshold has to be set to a higher value in order to stop the oscillations. Afterward, the threshold can be set back to the nominal value. The threshold setting has already been discussed in Section 5.1.3. Since a different noise situation prevails after installation in the HADES cave, the optimal values must be determined again. The experience in the laboratory showed that the absolute values of the baselines and thresholds are stable. Thus, one set of thresholds can be used for a complete beam-time which is typically in the order of several weeks.

The thresholds in the ECAL detector can be set automatically via a software [78] which was originally developed for the HADES RICH detector and adopted to the needs of ECAL. The software runs an automatic routine in order to find baselines and noise widths for every channel. The threshold value can afterwards be set relative to the baseline. In Fig. 5.14 the relative position of the SLOW channels (even TDC-numbers) are shown for three PaDiWa-AMPS2 boards which are connected to the same TRB3sc board. The baseline width for the FAST (odd TDC-numbers) and SLOW channels (even TDC-numbers) are shown in Fig. 5.15. On average, the base-lines of the FAST channels have a width of about 2 mV, the SLOW channels of about 2.5 mV. After extensive testing, a relative FAST threshold of 40 mV and 50 mV in the SLOW channel was found to be the best compromise between high dynamic measurement range and noise reduction.

5.2.3 Commissioning with LASER signals, cosmic muons and test-beam

Every module in ECAL is equipped with an optical fiber in order to allow to send external light into the lead glass. Each sector is equipped with its own LASER system which allows to do a fast calibration before the runs and during the beam times. It can also be used for performance monitoring of every single ECAL module. The system consist of a LASER diode (PL 450B, emission wavelength: 450 nm) and

2D Rate vs. Threshold of 6045

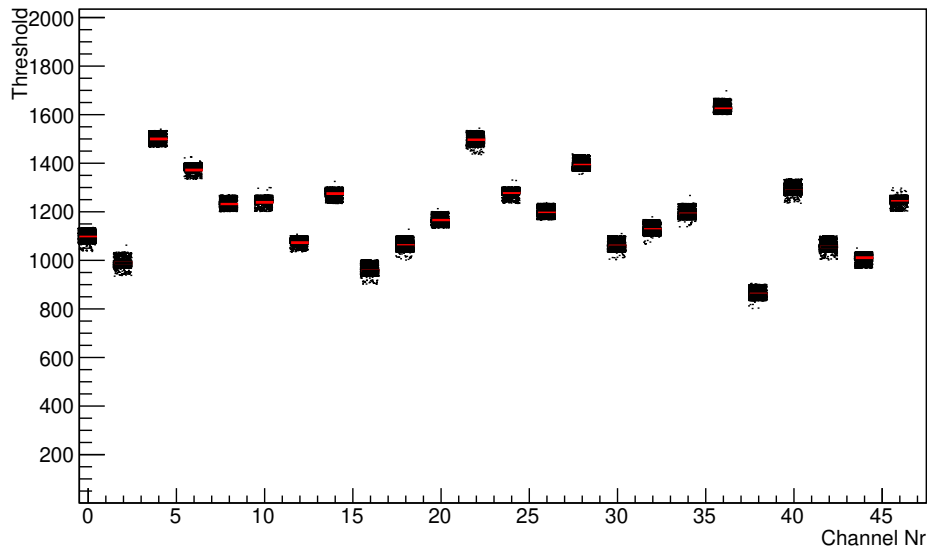


Figure 5.14.: Relative position of the baselines for FAST (even channel number) and SLOW (odd channel number) channels for three PaDiWa-AMPS2 boards which are connected to the same TRB3sc board.

Noisewidthhistogram of 6045

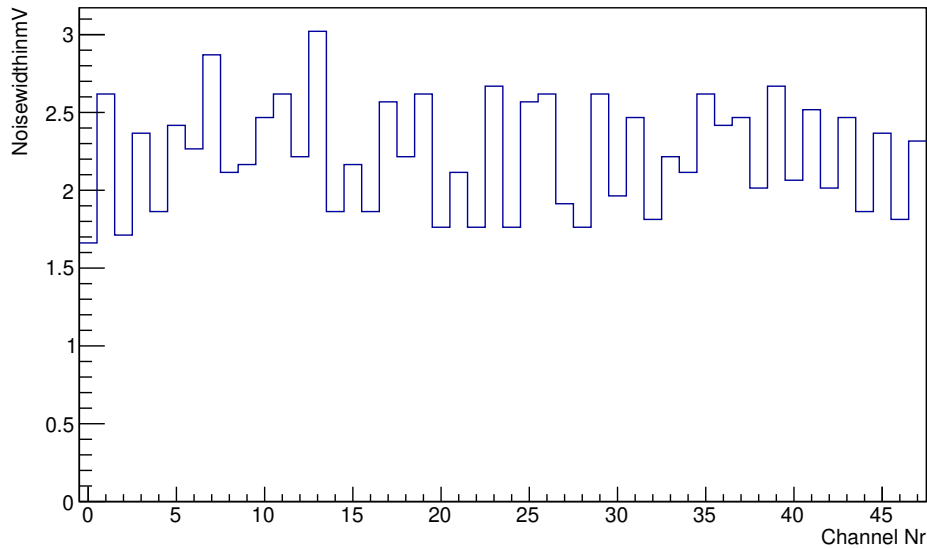


Figure 5.15.: Noise width of the baseline for FAST (even channel number) and SLOW (odd channel number) channels for three PaDiWa-AMPS2 boards which are connected to the same TRB3sc board.

a lens system which distributes the light into 196 fibers. The intensity variation of each fiber is below 15%. The LASER system is controlled by a special pulser add-on board [70] for the TRB3 family which allows remote operation. A schematic picture of the LASER system is shown in Fig. 5.16.

During the commissioning of ECAL, the LASER system was used as an useful tool in order to test the full read-out chain from threshold settings up to data storage and finally to debug the ECAL software. In addition, the LASER system can be used to characterize the measurement precision of the read-out system. In Fig. 5.17 the charge measurement distribution of an ECAL module, which is equipped with

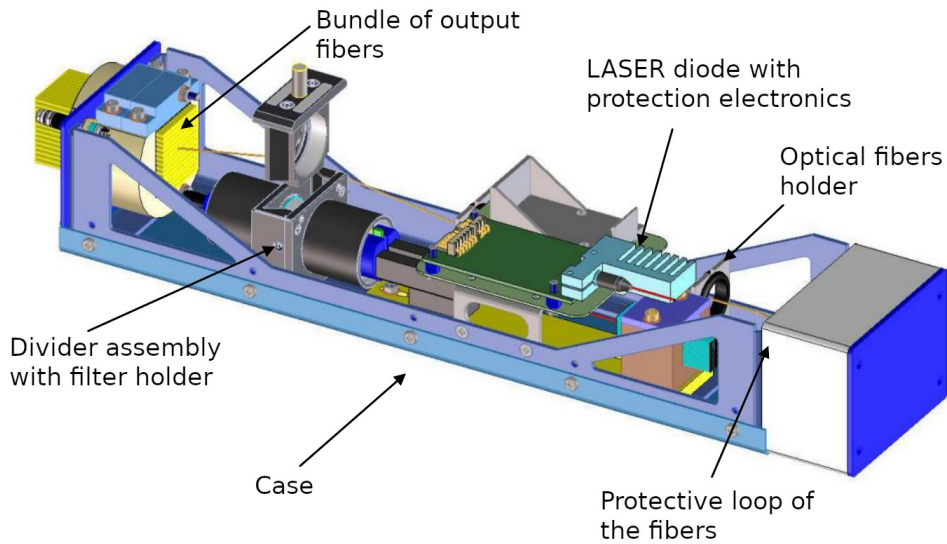


Figure 5.16.: Schematic picture of the ECAL LASER system which distributes the light of a LASER diode over 196 fibers. (Taken from [79])

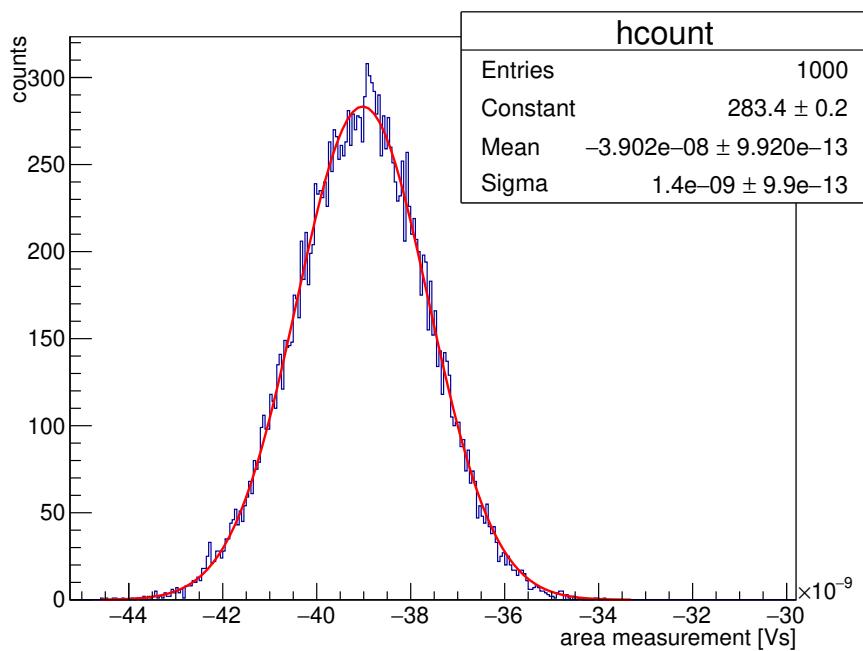


Figure 5.17.: Oscilloscope reference measurement of the signal-pulse-area (\sim charge) distribution of an ECAL module which is equipped with a 3-inch PMT obtained with LASER light. The relative measurement precision is $\sigma/\text{mean} = 3.6\%$.

a 3-inch PMT, is shown for LASER light. The measurement was done using an oscilloscope in order to obtain a reference measurement of the pulse area (\sim charge) distribution. The relative measurement precision is $\sigma/\text{mean} = 3.6\%$. This represents the lower limit of the energy resolution of an ECAL module for LASER light.

Another method in order to test the performance of the read-out system is the usage of cosmic muons. They are created indirectly as decay products of collisions of cosmic rays with particles of the Earth's atmosphere. At ground level the average muon energy is about 4 GeV [6]. The muons follow an angular

distribution proportional to $\cos^2 \theta$. The signal response of an ECAL module to a cosmic muon, which traverses the entire length of the module, is equivalent to the response of a photon with an energy of 580 MeV [48]. A cosmic muon, which crosses the module laterally, generates a signal which is equivalent to a 100 MeV photon. This value is important for cosmic muon measurements in ECAL, since the modules are located nearly horizontally. Cosmic muons also play an important role for the energy calibration process which will be explained in detail in Section 6.3. In order to achieve a large statistic cosmic muon measurements are usually running for several days.

In December 2018 the ECAL detector was commissioned using an Ag beam. A beam with an energy of 1.58A GeV has been provided by the SIS18 accelerator of GSI. The main purpose of the test beam was the commissioning of new detector systems like the HADES RICH and the ECAL detector. The test beam allowed to test the full read-out chain including data unpacking and analysis.

5.3 Performance issues and solutions

During the commissioning and after the analysis of the test-beam data several issues have been identified. In this section, the main issues which are related to the read-out electronics will be summarized. Even if not every issue was solved completely, a fix was found to guarantee a safe data taking during the production beam-time. An important part in this section is the introduction of an alternative charge measurement method in the SLOW channels.

5.3.1 Cross-talk and alternative charge measurement method

In 25 % of the modules the analysis of the test-beam data showed a nonphysical gap at measured Q2ToT at about 65 ns. An example of an affected module is shown in Fig. 5.18. On closer inspection it has been discovered that the behavior is only visible in the data of modules which are connected to the PaDiWa-AMPS2 input channels number 5 and 7.

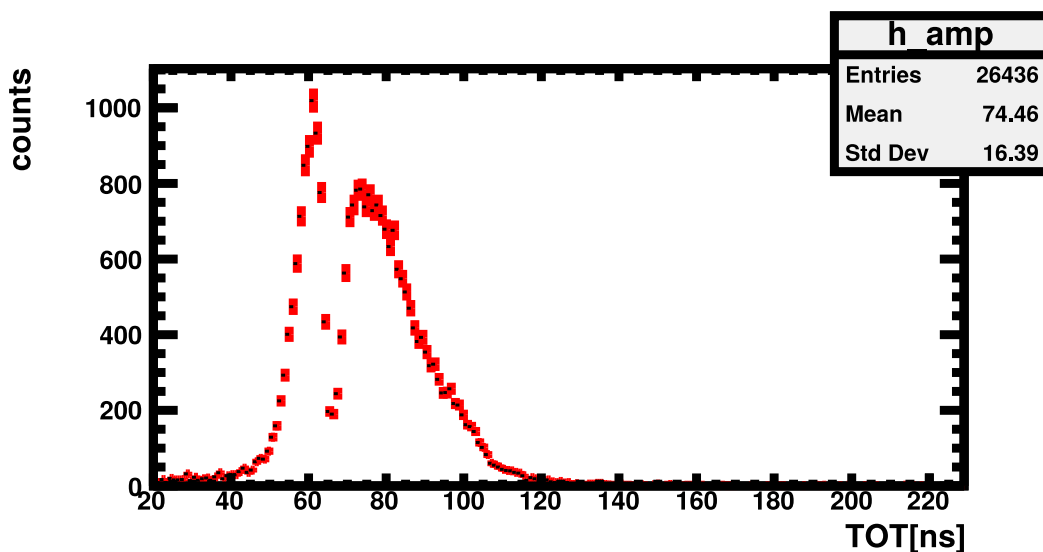


Figure 5.18.: The PaDiWa-AMPS2 input channels number 5 and 7 show a nonphysical gap at measured Q2ToT of about 65 ns [80].

A more detailed examination in the laboratory showed a cross-talk between the DISCHARGE signal which couples into the falling edge of the SLOW signal. The effect is visualized in Fig. 5.19. When the DISCHARGE signal is switched on or off, a wiggle is visible in the SLOW signal. This effect is especially pronounced in the PaDiWa-AMPS2 input channels number 5 and 7. For signals with certain amplitude it can happen that the wiggle is exactly at the level of the discriminator threshold voltage. In this case, either the smaller or the larger Q2ToT value will be detected by the TDCs which results in a gap in the measured Q2ToT spectra. This problem was not discovered in the laboratory because only single pulses with a defined amplitude were used. However, a continuous amplitude spectrum of data was generated during the beam test.

The first approach in order to eliminate this behavior was to change the driver strength of the LVDS outputs of the FPGA which drive the DISCHARGE signal. By doing so, the amplitude of the cross-talk signal was substantially reduced. Furthermore, a mistake was suspected on the PCB-layout which may be caused by a faulty signal line routing. However, in close inspection, no error was detected. No qualitative differences have been found between channels number 5 and 7 in the layout of the PaDiWa-AMPS2 board.

Since the problem could not be solved completely, an alternative charge-measurement method was considered. This new method is based on the measurement of the overshoot in the SLOW signal (also see Section 5.1.4). The measurement principle is shown in Fig. 5.20. In the standard procedure, a negative

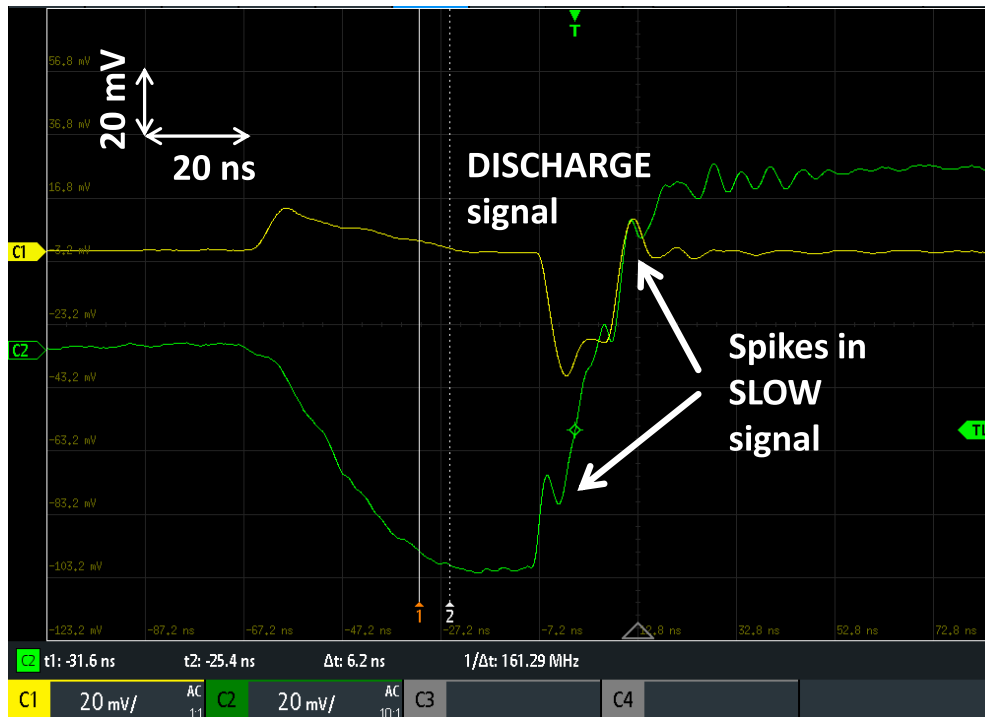


Figure 5.19.: The gap in the Q2ToT spectra is caused by cross-talk. The FAST signal including the DISCHARGE signal is shown in yellow. The corresponding SLOW signal is shown in green. At the time when the DISCHARGE signal is switched on and off, a wiggle is visible in the SLOW signal. In case the wiggle is crossing the threshold, two different Q2ToT values have been measured.

threshold is set to the SLOW channel in order to discriminate the negative part of the SLOW signal. But one can also set the threshold to a positive value in order to discriminate the overshoot of the SLOW signal. This has the advantage that the disturbance caused by the much later switch off of the DISCHARGE signal is thereby reduced to an amplitude that is far away from the threshold and thus no longer has any influence on the time-over-threshold measurement. Since the original charge was also discharged with the DISCHARGE signal, the time-over-threshold signal is still proportional (with an offset) to the input charge of the input signal and therefore can be used for the Q2ToT measurement. In the following, this method is called "*overshoot*" charge measuring method. It can easily be implemented without any changes in the PCB and FPGA firmware. Only the thresholds in the SLOW channels have to be set to positive values.

In order to evaluate the "overshoot" charge measurement method for compatibility with the PMT signals, tests have been performed. The measurement precision and the dynamic range were investigated more closely. The measured $Q2ToT_{overshoot}$ for different signals generated by the LASER system are shown in Fig. 5.21 (left). The behavior is similar to the standard measurement method. The "overshoot" method results in typical $Q2ToT_{overshoot}$ between 200 ns and 1200 ns in comparison of 50 ns to 200 ns with the standard measurement method. The "overshoot" charge measurement precision is shown in Fig. 5.21 (right). For large signals the precision is mainly limited by the photon statistics inside the lead-glass which is in the order of 3.6 % (see Fig.5.17). In the laboratory it was proven that the $Q2ToT_{overshoot}$ measurement precision for laboratory pulser signal amplitudes for input amplitude above 300 mV is below 0.5 %. For example, a signal with an amplitude of 4.65 V can be measured with a relative precision of 0.22 %. It could thus be proven that the alternative charge measurement method meets the ECAL read-out requirements.

New threshold settings for the SLOW channels are needed to realize the "overshoot" measurement method. A big advantage of this method is that the SLOW threshold is not required to be set close

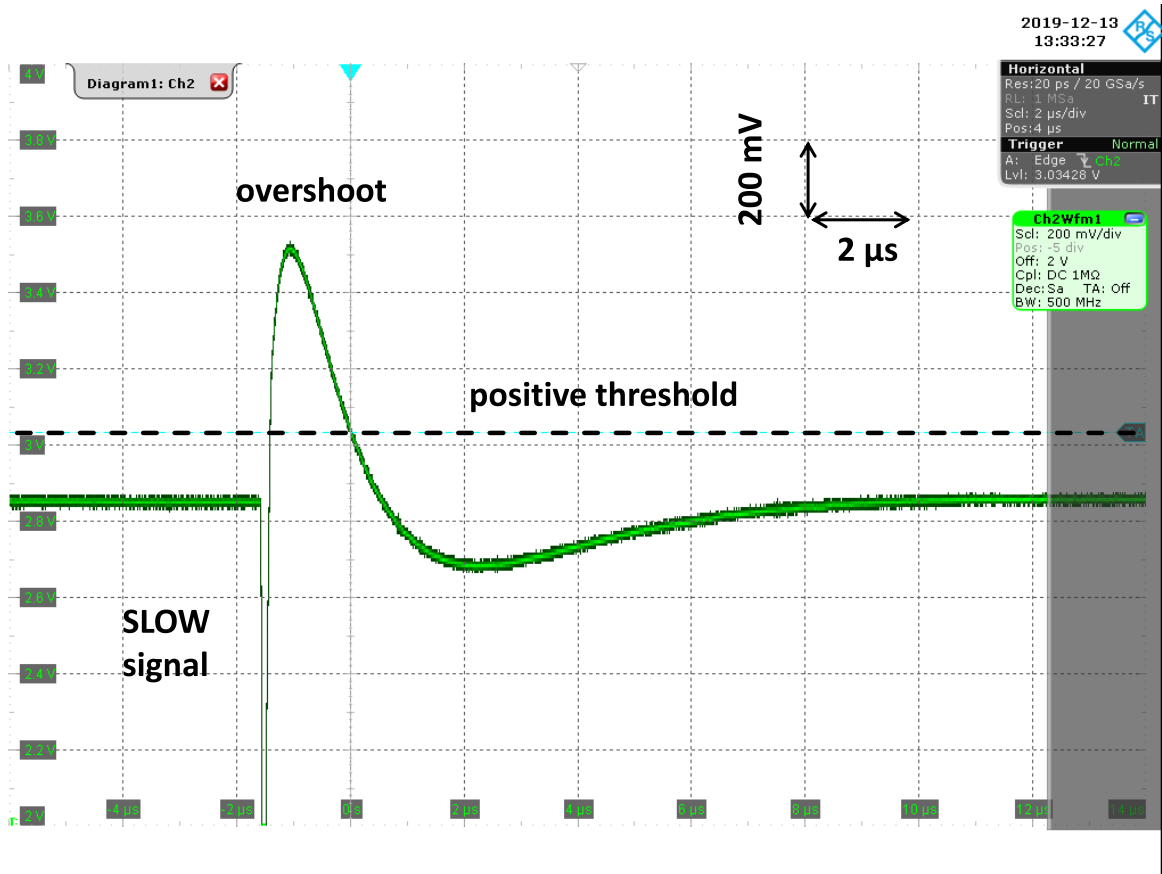


Figure 5.20.: Overshoot and undershoot in the SLOW signal. The width of the overshoot is proportional to the input charge. By setting the SLOW thresholds on the overshoot it can be used as alternative charge measurement method.

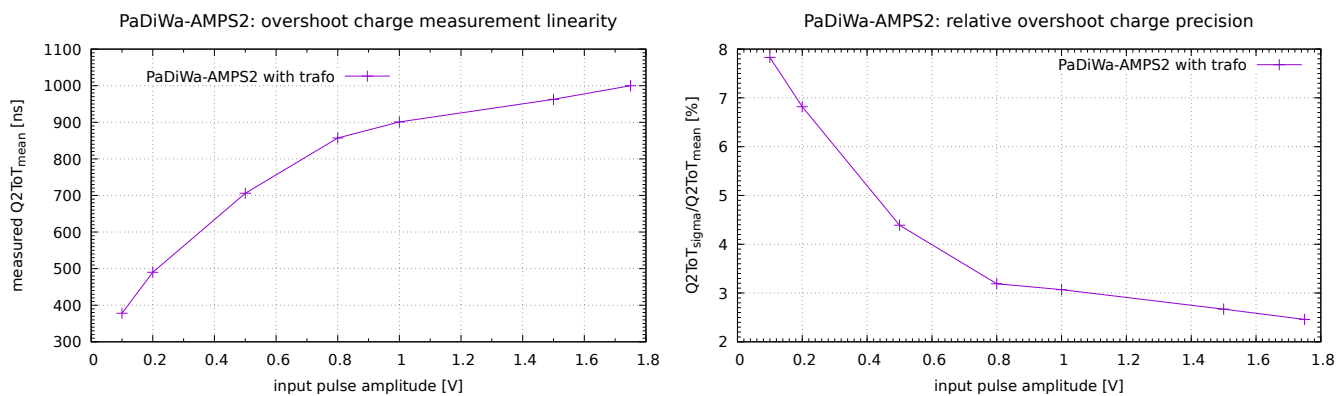


Figure 5.21.: Left: With the overshoot method measured Q2ToT for different input pulse charges. Right: Q2ToT measurement precision for the overshoot method.

to the baseline any longer in order to cover the largest possible dynamical measurement range. Even a small signal is generating an overshoot with amplitude of several hundred millivolts. It has been found that a SLOW threshold of 200 mV can be used to measure PMT signals with amplitudes from 50 mV up to at least 5 V.

For the generation of an overshoot in the SLOW signal the DISCHARGE signal, which is generated by the FAST signal and the SLOW signal leading edges, must always be present. Therefore, the threshold

setting of the FAST signal is also important in order to cover a large charge measuring range in the SLOW channel. The FAST threshold must remain as close to the baseline as possible.

During the investigation of the minimal possible FAST threshold setting, a cross-talk was observed in adjacent FAST channels. The minimal thresholds from which cross-talk occurs in adjacent FAST channels are summarized in Table 5.1. In most channels a cross-talk is visible for thresholds below 20 mV, but channel number 1 shows cross-talk already at 40 mV. In order to simplify the threshold settings and to make sure that no cross-talk occurs in the FAST channels, a minimum threshold of 40 mV is recommended to be set in all ECAL FAST channels.

Table 5.1.: Minimal FAST thresholds values from which cross-talk occurs in adjacent FAST channels.

input	minimum threshold	note
ch1	40 mV	cross-talk in ch2
ch2	20 mV	no cross-talk
ch3	20 mV	no cross-talk
ch4	20 mV	no cross-talk
ch5	20 mV	no cross-talk
ch6	20 mV	no cross-talk
ch7	20 mV	cross-talk in ch8
ch8	10 mV	no cross-talk

5.3.2 SLOW channel failure

During the test beam time it was observed that several SLOW channels failed and did not provide data any longer. Modules close to the beam axis were affected the most. Since the hit-rate is higher in those modules, the problem can be assumed to be rate dependent. The same effect was observed during the investigation of the FAST thresholds. By going down to FAST thresholds below 20 mV in PaDiWa-AMPS2 input channels numbers 2-6 and 8, an unstable behavior was observed in all SLOW channels. In this case suddenly no signals were visible in the SLOW channels. The effect is also caused by high hit rates in the FAST channels since base-line noise is picked up.

A closer investigation showed high rates might cause the FPGA to no longer generate the DISCHARGE signal. Why this happens remains unclear and is still under investigation. However, a detailed analysis of the FPGA source codes uncovered no problems. The problem has been solved temporarily by setting the threshold of the SLOW signal to a high value and then resetting it to the nominal values. Therefore, a script [81] is running in the background of the HADES DAQ system which monitors the state of the SLOW channels, and, if necessary, performs a threshold reset procedure in order to activate affected SLOW channels.

5.3.3 Electromagnetic shielding of PMTs and quality testing

During the commissioning of sectors number 2 and 6, which are equipped with new 3-inch Hamamatsu PMTs, an unexpected behavior was observed in almost all modules. As shown in Fig. 5.13, the upper two sectors showed a higher rate than sectors number 3 and 5 which are equipped with 1.5-inch PMTs. Besides this, an unstable behavior of the HADES DAQ system was observed during the ramp-up of high voltages in ECAL. This could lead to a failure of the ECAL read-out electronics, which afterwards needed to be restarted in order to work again. The first explanation was related to electromagnetic discharges which are generated by the PMTs or its high voltage dividers during ramping of high voltage. By looking more closely at the PMT signals with an oscilloscope, unexpected signal shapes were observed. Those signals showed high amplitudes up to 50 V and oddly shaped wide signals in combination with an unexpected high signal rate. Examples of such signals are shown in Fig. 5.22.

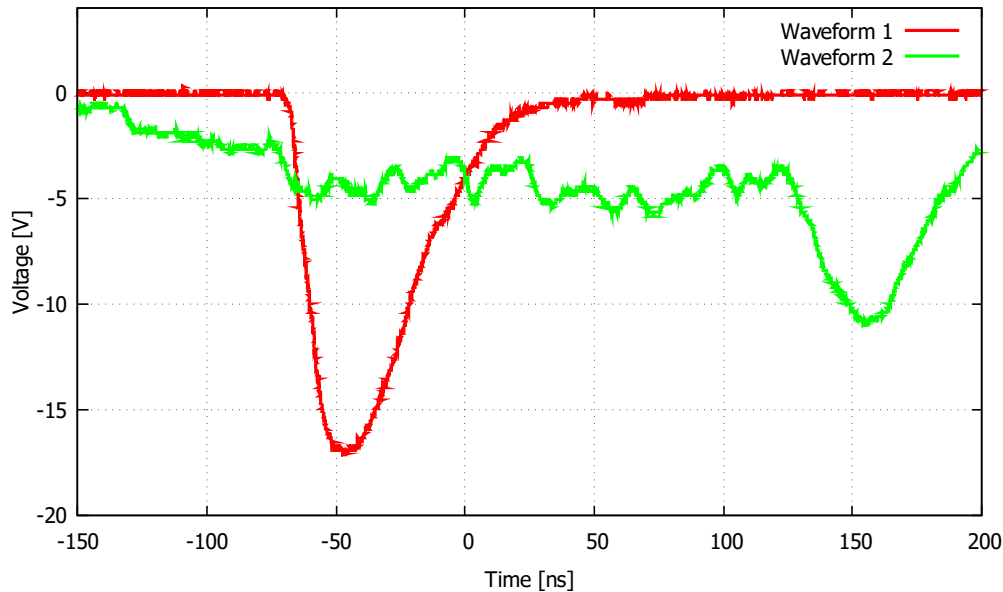


Figure 5.22.: High amplitude noise signal (red) and oddly shaped wide (green) PMT signals.

In order to find the reason of the problem, an affected module was fully disassembled and reassembled piece by piece afterwards. During reassembling, the PMT signals were monitored in each intermediate step. In this way, it was found that the problem is related to the position of the magnetic shielding which surrounds the PMT [82]. It may happen that the shielding is not placed straight and parts of the shielding come very close to, or even touch, the region of the photo-cathode. The inner surface of the bulb, near the cathode of the PMT, is aluminum-coated and maintained on the cathode potential. If the outside of the bulb has a large potential difference with respect to the cathode, scintillation may occur in the glass between the two surfaces [47]. The scintillation light is reflected into the photo-cathode which cause an increase in the dark current.

In order to solve the issue, an active shielding has to be applied to the PMT. A treatment technique, which is effective in reducing the noise increase caused by the surrounding electric potential, is called *HA treatment* [47]. For this, the outer shell of the PMT is maintained on the same potential as the photo-cathode. This can be done by painting the glass with conductive paint which is connected to the cathode pin of the high voltage divider. Afterwards an insulating protective cover is applied for safety and to prevent discharges. The treatment layers are schematically shown in Fig. 5.23 (left).

A similar treatment was developed and successfully tested for the 3-inch ECAL PMTs. A treated PMT is shown in Fig. 5.23 (right). The cathode pin is connected to the conductive graphite paint which is attached in the region of the photo-cathode. Afterwards, the whole PMT is covered with black paint. The photo cathode is additionally protected by a piece of shrinkable tube. In addition, the inner layer of the magnetic shielding is protected by *Kapton* foil. With this treatment, the electromagnetic influence of the PMT has been fully eliminated and a stable operation during several days was proven.

The treatment needs to be applied to all ECAL 3-inch PMTs in ECAL. Since the PMTs cannot be removed from the modules in the measurement position, ECAL sectors number 2 and 6 where disassembled after the beam time in March 2018. In the detector laboratory of GSI all modules have been opened and the PMTs were treated with the active electrostatic shielding.

After reassembling, the modules had to be tested in order to proof the functionality and to re-calibrate the high voltage settings. The test procedure consisted of two parts. In a first step the PMT is operated at its nominal high voltage settings and the raw signals of the PMT are observed with an oscilloscope for several minutes. For this test, the trigger threshold needs to be set to 100 mV in order to evaluate the signal rates. A typical signal rate is usually in the order of a few Hertz which is mainly caused by cosmic

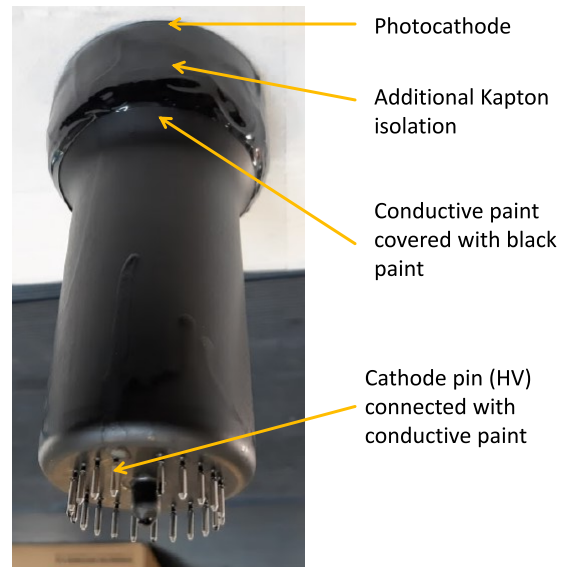
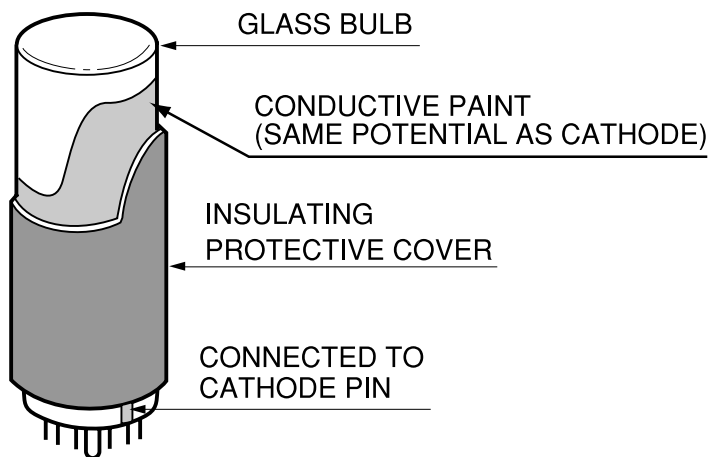


Figure 5.23.: **Left:** Active electrostatic shielding of a PMT which is called *HA treatment*. For that the PMT is painted with conductive paint which is connected to the same potential as the cathode. (Taken from [47]) **Right:** Photography of a treated 3-inch PMT of the ECAL detector.

particles. After this test, the trigger threshold is set to 500 mV in order to detect signals with amplitudes above 5 V which are not present at all on a normal functioning PMT.

If the check of the raw signal is passed, a calibrated LED light pulse is injected into the module. The LED signal is calibrated with the help of cosmic muons. The calibration procedure is illustrated in Fig. 5.24. The signal amplitude for cosmic muons is measured with an oscilloscope for a reference module. The trigger signal is realized via a coincidence from two plastic scintillator detectors which are placed above and below the module. The high voltage of the PMT is adjusted in order to achieve signal amplitudes of 1.5 V. After the the calibration with cosmic muons, an LED light pulse is injected into the same module. The amplitude of the signal, which drives the LED, is then tuned in order to achieve a signal amplitude of 1.5 V without changing the high voltage settings. For that the pulse generator is used in pulse mode with typical signal repetition rate of 1 kHz. The rise and fall times of the signal is 5 ns with a width of 15 ns. The calibrated LED set-up can then be used to perform a efficiently high voltage calibration of every module.

All modules of sector number 2 and 6 have been tested with the procedure mentioned above. The main goal was to identify modules which still show high signal rates and amplitudes. Besides this, all modules have been re-calibrated with the help of a calibrated LED signal. In Fig. 5.25 the difference of the new HV settings to the previous HV settings, which have been used during the Ag beam time in March 2019, are shown. The new values are approximately 50 V above the values, which were used during the beam time. The deviations can be explained by the fact that the calibration was carried out with only one reference module and, in contrast to the previous calibration, a new LED diode was used. Nevertheless, a deviation of a few volts is not critical, because each module in ECAL will be finally calibrated with beam data (see Section 6.3). The test also ensured that no problematic modules are going to be installed in the ECAL.

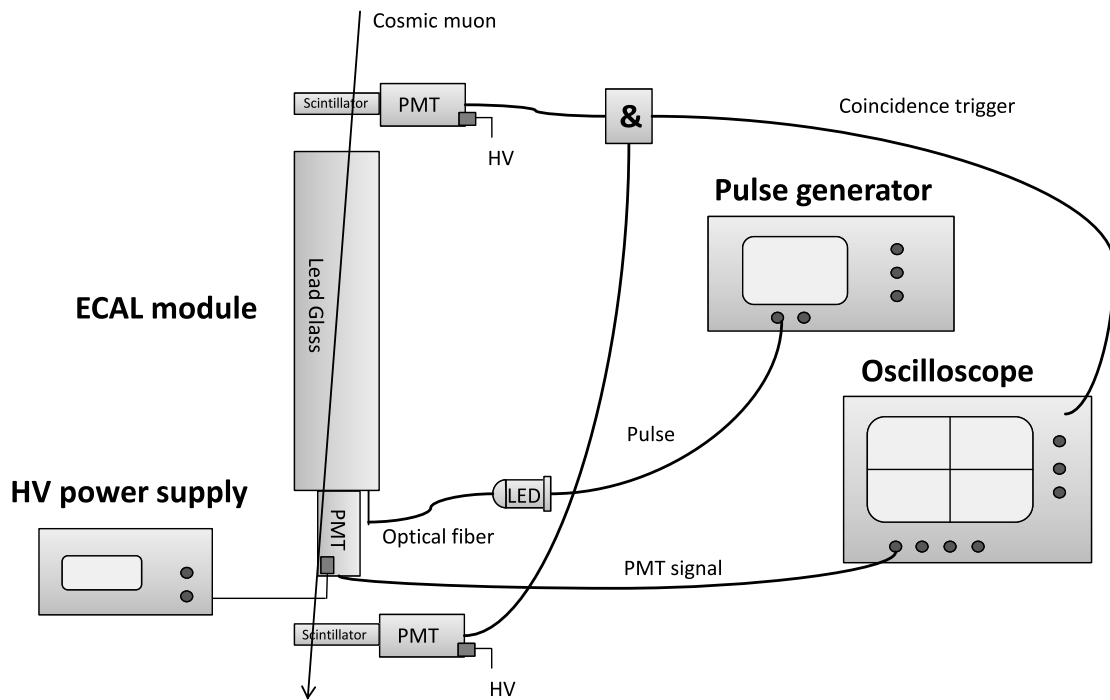


Figure 5.24.: Module calibration procedure. The LED diode is calibrated with a reference module in a cosmic muon set-up. The calibrated LED signal can be used to tune the high voltage of ECAL modules efficiently.

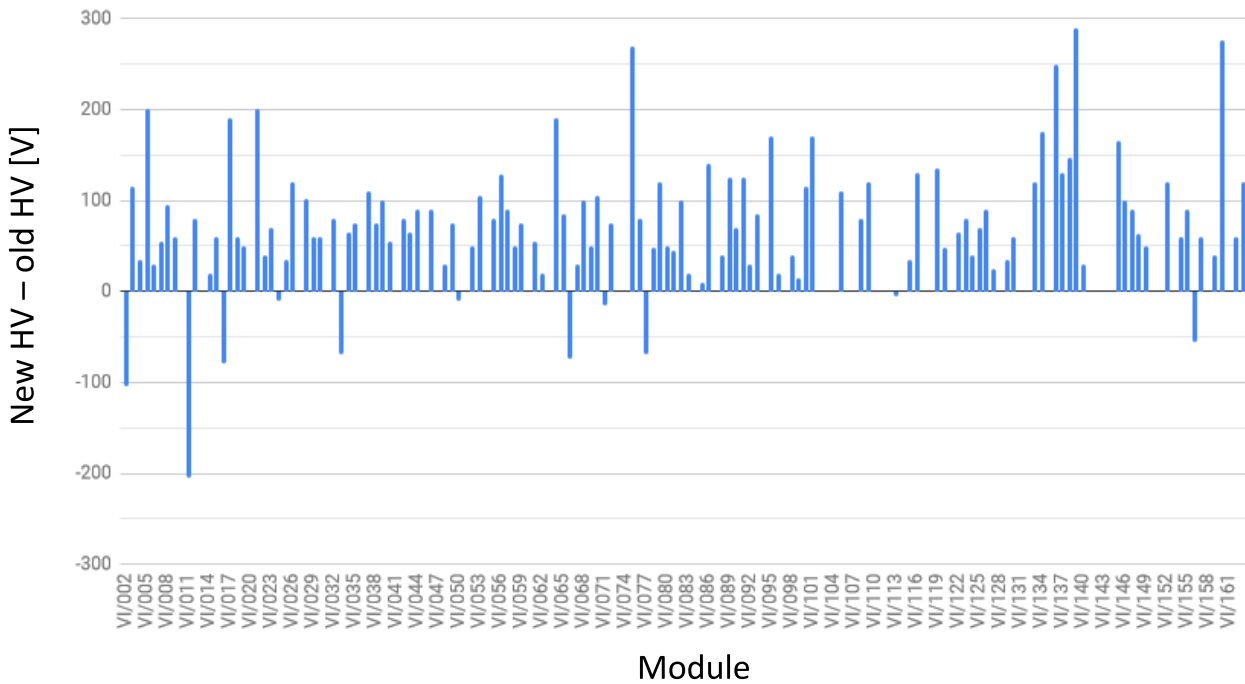


Figure 5.25.: Difference of the new HV settings to the previous HV settings which have been used during the Ag beam time in March 2019 for sector number 6.

6 Read-out electronics performance during the HADES Ag+Ag run

In March 2019 HADES carried out a four week long physics production beam time using a beam of accelerated Ag ions impinging on a stack of Au foils (Ag+Ag at 1.58A GeV, $\sqrt{s_{NN}} = 2.55$ GeV). In total, 15.3×10^9 events have been recorded which resulted in a total collected data of 359.23 TB. In Fig. 6.1, the run statistic is shown for the full-beam time. In terms of the number of events recorded, the beam time was a success. But also the first online analysis shows the very good quality of the recorded data. In this section, the performance of the ECAL detector, with particular focus on its read-out system, will be shown. At the end, first analysis results will be presented, e.g. the reconstruction of the $\pi^0 \rightarrow \gamma\gamma$ decays with photons detected in ECAL.

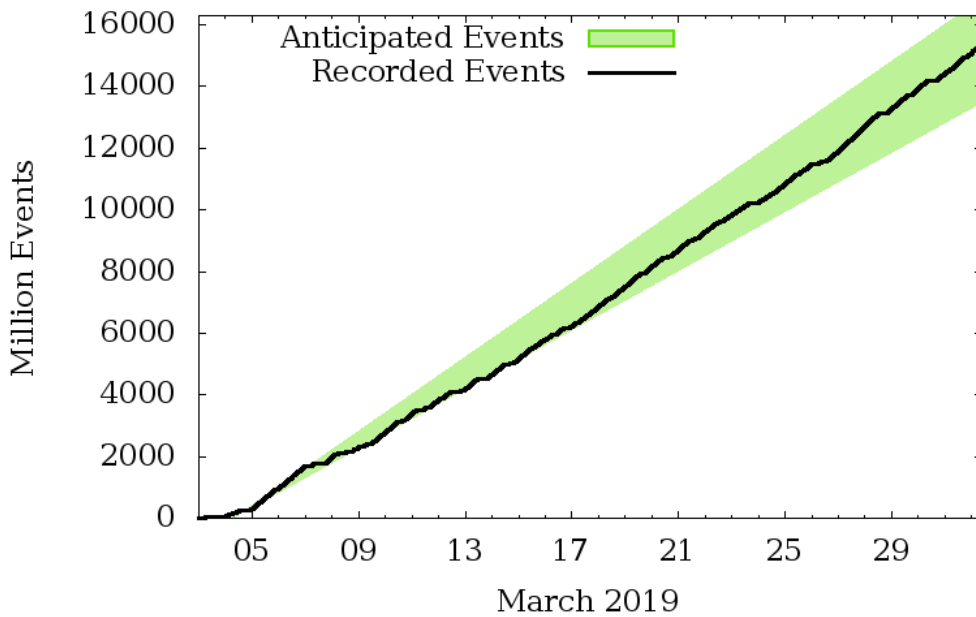


Figure 6.1.: The HADES run statistic for the March 2019 Ag+Ag 1.58A GeV production beam time [83].

6.1 Stability of the read-out electronics

The configuration of the ECAL detector during the beam time is shown in Fig 6.2. The sectors number 4 and 5, which are equipped with 1.5-inch EMI PMTs, were fully operational. Sectors number 2 and 6, which are equipped with 3-inch Hamamatsu PMTs, were only partially operational, because of missing electromagnetic shielding (see Section 5.3.3). It was tried to switch on as many modules as possible while keeping the stability of the DAQ within a reasonable frame. Unfortunately, sector number 6 needed to be switched off almost completely, only two outer rows of modules, which are equipped with 1.5-inch EMI PMT, stayed switched on. In the last days of the beam time, five modules with 3-inch PMT which were treated with a first prototype of electromagnetic shielding have been installed in the first row of sector number 1 for testing purposes. Those modules remained connected to the electronics in sector 6. Besides this, free channels of the ECAL electronics were used to read out a prototype of a quartz crystal based *forward hodoscope* [84].

6.2 Verification of the "overshoot" charge measurement method

An important task during the first days of the beam time was the evaluation of the overshoot measurement method with beam data. The quality of data was constantly checked during the runs. The Q2ToT

Min: Max: 10000 Send bgr slow

ECal rate slow chan

last update: Wed, 27 Mar 2019 - 13:28:36

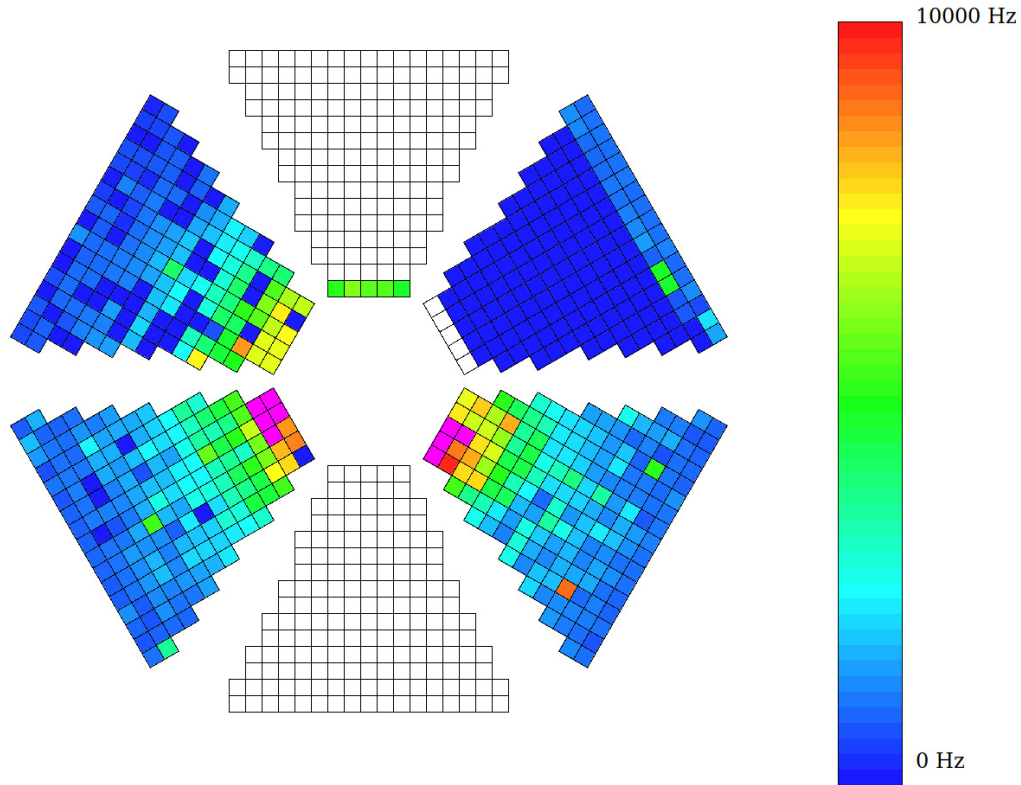


Figure 6.2.: Configuration of the ECAL detector during the Ag beam time in March 2019. White fields indicate where no modules were installed, dark blue fields indicate modules which are switched off. Five modules with an electromagnetic shielding prototype have been installed for testing purposes in sector number 1.

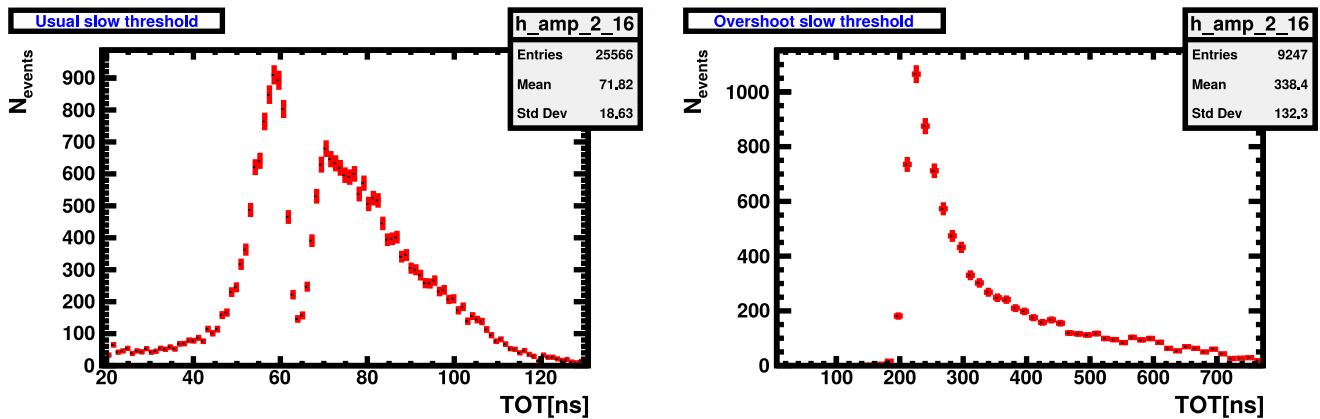


Figure 6.3.: Left: Test beam Q2ToT spectra recorded during the test beam in December 2017. The original SLOW signal measurement method shows an unexpected gap in the spectra at around 65 ns. Right: Verification of the Q2ToT spectra in the beginning of the Ag beam time in March 2019. As expected from measurements in the laboratory, the gap vanishes completely [80].

distribution for both measurement methods is compared in Fig. 6.3 for two identical channels. As expected from laboratory measurements, the gap vanishes completely. For the complete beam time, the thresholds have been set to 40 mV in all FAST channels and to 200 mV in all SLOW channels.

6.3 Time and energy calibration in ECAL

The discrimination method used in ECAL inevitably produces a walk-effect which must be corrected offline. Besides this, time delays in each channel differ and also have to be corrected. In addition, the non-linearity of the charge measurement method must be corrected and a calibration of the measured Q2ToT to the energy is essential. In the following, the calibration process will be described briefly.

Time delays in the channels are mainly caused by variations in the length of the read-out cables. Those shifts have been corrected [85] using test beam data from December 2017. During this test, the HADES was measuring without a magnetic field which resulted in straight particle trajectories. It can be assumed that all paths from the interaction point to the modules have roughly the same length. The time-of-flight of photons and relativistic electrons from the interaction point to ECAL is known to be about 8 ns which can be used for calibration. By subtracting the offset in each individual channel, the measured time is equalized to the real time of flight.

A walk correction has to be applied to every channel. As shown in Fig. 5.5 time shifts occur because of different signal amplitudes. Especially the arrival times of particles which generate a small signal in the ECAL module are deferred to later times. This effect can be corrected with the help of the RPC detector since this detector is mounted about 10 cm in front of the ECAL modules. Charged particles which hit the RPC detector can therefore be assumed to be registered in an ECAL module, which is placed behind it, at the same time. A Q2ToT spectrum for an ECAL module before and after calibration is shown in Fig. 6.4.

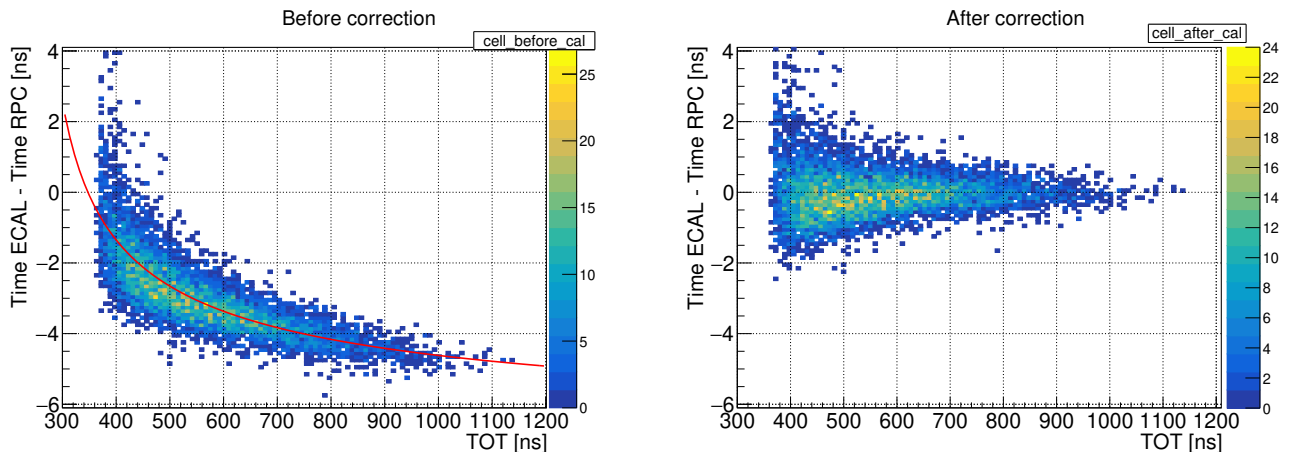


Figure 6.4.: Left: Time-walk effect which is strongly pronounced for small Q2ToT times. Right: After a time-walk correction all signals, independent from the measured Q2ToT, have the same arrival time in ECAL (and RPC) [86].

An important task is the energy calibration of each individual module, which is currently ongoing [86]. The current status will be shown in the following. A calibration curve which links the measured Q2ToT with a signal amplitude is shown in Fig. 6.5. This curve was generated by using LASER signals, varying their amplitude and measuring the Q2ToT. As expected (see also Section 5.1.2) the behavior is not linear. Nevertheless, with this information one still cannot deduce the associated energy.

Electrons are the best candidates for an energy calibration of ECAL. They generate signals in the ECAL module which are identical to those of photons with the same energy. In contrast to photons, electrons are registered by all detectors in HADES and their trajectories can be reconstructed using information from tracking and time-of-flight systems. Hence their momentum can be determined, and from this their energy can be derived. Assignments of fired ECAL modules and electron tracks, with known energy, can be done with the help of the RPC detector which is placed close to ECAL. In Fig. 6.6 (left) an example

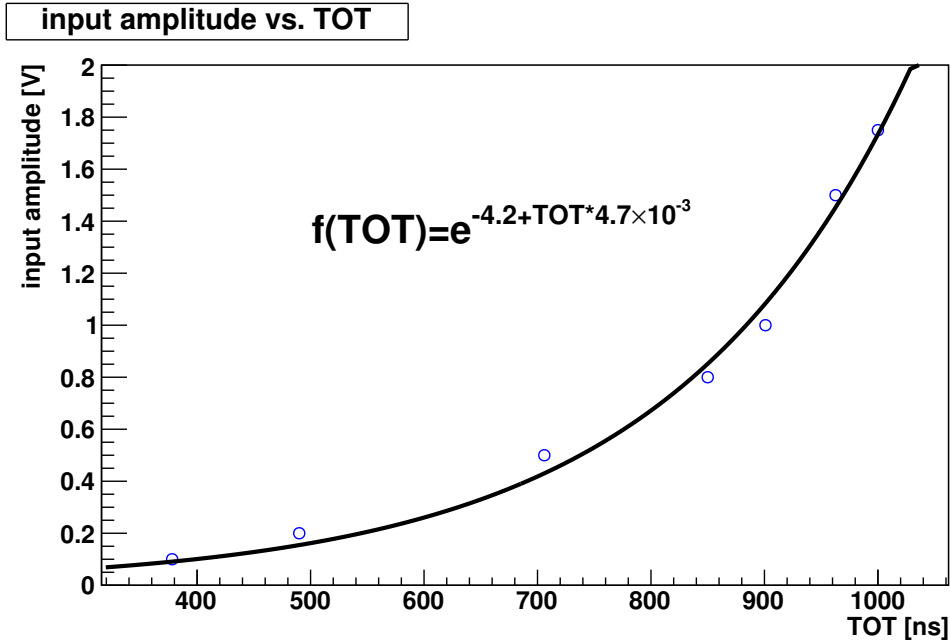


Figure 6.5.: Connection of measured Q2ToT and signal amplitude, where the signals were generated by the LASER system.

of the assignment between electron energy and the corresponding Q2ToT is shown for one module. The connection of Q2ToT and energy can be described with the calibration equation:

$$E = \exp([0] + \log(\text{ToT}) \cdot [1] + \log(\text{ToT}) \cdot \log(\text{ToT}) \cdot [2]) + [3], \quad (6.1)$$

with the fit parameters $[0] = 16.82 \pm 0.42$, $[1] = -5.23 \pm 0.42$, $[2] = 0.53 \pm 0.42$ and $[3] = -36.37 \pm 0.42$. The width of the band, which is shown in Fig. 6.6 (left), can be used to characterize the energy resolution of the ECAL detector. Each energy bin can be projected onto the y -axis and fitted by a *Gaussian distribution*. The resulting sigma value is divided by energy in order to characterize the energy resolution (see also 2.2.3). The energy resolution for each measured electron energy is shown in Fig. 6.6 (right). Currently an energy resolution of $\frac{\sigma_E}{E} = \frac{6.6\%}{\sqrt{E[\text{GeV}]}}$ is achieved. However, it is expected that the energy resolution of ECAL will be improved with an improved calibration of the detector.

6.4 Reconstruction of the neutral pion decay

As mentioned in Section 2.1, the additional calorimeter in the HADES set-up allows to measure real photons directly. This opens the possibility to identify the light neutral pseudo-scalar mesons, e.g. π^0 and η , via their decay into two photons (diphoton). The decay channel $\pi^0 \rightarrow \gamma + \gamma$ has been successfully reconstructed using data from the HADES Ag+Ag 1.58A GeV beam time [86].

In Fig. 6.7 a preliminary invariant mass distribution is shown. All possible combinations of the identified photons (black histogram), the mixed-event combinatorial background (blue histogram) and the signal after background subtraction (red histogram) are indicated. A clear π^0 peak is visible on top of the combinatorial background. The analysis was done, using data from sector number 2 only. The invariant mass distribution of the diphotons has been reconstructed by taking into account all possible combinations of the identified photons. The combinatorial background has been obtained via the mixed event method, where all combinations of two photons from different events are included. The combinatorial background has then been normalized to the measured one outside the meson peaks. In order to improve the π_0 reconstruction, only photons with energy $E_\gamma > 400$ MeV and with $0.9 < \beta_\gamma < 1.2$ were used for both, signal and background reconstruction. Besides this, there should be no hit in the RPC detector,

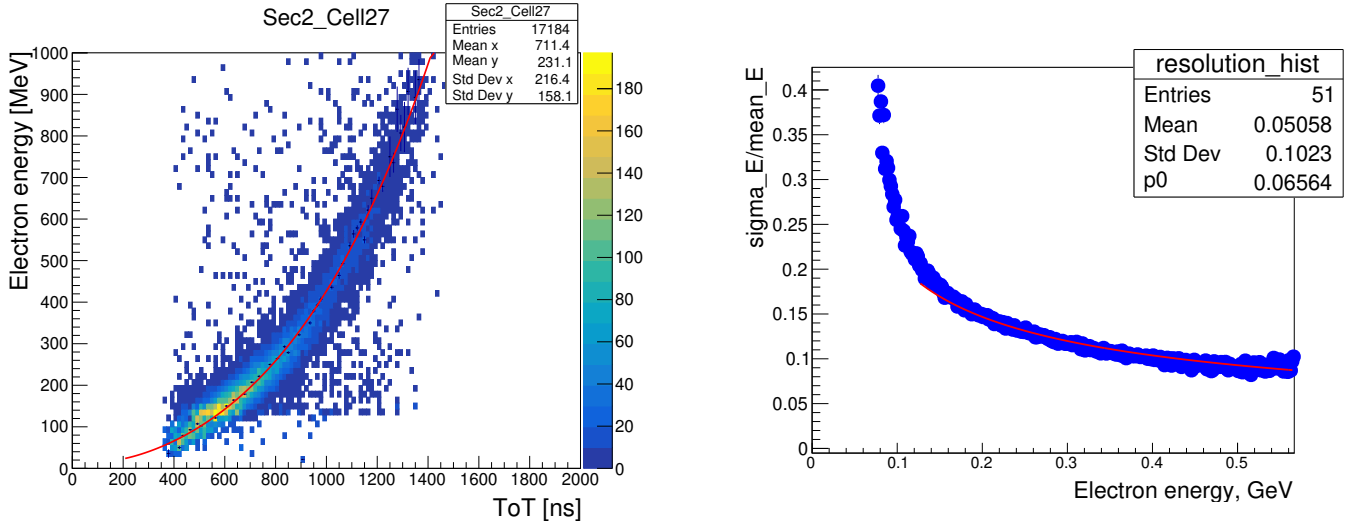


Figure 6.6.: Left: Energy calibration of the measured Q2ToT with the help of electrons since their energy can be reconstructed with by the HADES tracking-system [86]. Right: Currently an energy resolution of $\frac{\sigma_E}{E} = \frac{6.6\%}{\sqrt{E[\text{GeV}]}}$ is achieved [86].

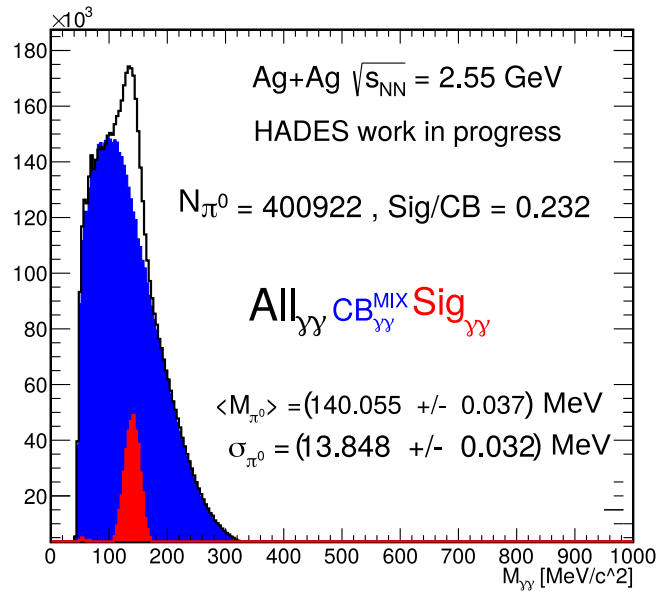


Figure 6.7.: Diphoton invariant mass spectra reconstructed in Ag+Ag collisions at 1.58A GeV. All possible combinations of the identified photons (black histogram), the mixed-event combinatorial background (blue histogram) and the signal after background subtraction (red histogram) are shown. A clear π^0 peak is visible on top of the combinatorial background [86].

since this detector is not sensitive to photons. A *Gaussian* fit of the signal peak (red distribution) delivers a mass of $\langle M_{\pi^0} \rangle = 140.06 \text{ MeV}/c^2$ with a resolution of $\sigma_{\pi^0} = 13.8 \text{ MeV}/c^2$. The mass of the π^0 is already close to the PDG value of $134.98 \text{ MeV}/c^2$ [6].

With ECAL it is also possible to reconstruct the $\pi^0 \rightarrow \gamma + e^+ + e^-$ decay channel. For that, an important ingredient is the electron pair. A preliminary invariant-mass distribution of electron pairs reconstructed in Ag+Ag collisions at 1.58A GeV is shown in Fig. 6.8. The analysis includes a full event reconstruction and electron identification after applying background rejection cuts, together with a cocktail of all signal sources. The main source of random combinations is a mix of incompletely detected pairs from π^0 -Dalitz decays or external conversion of photons in the detector and target materials. An additional cut

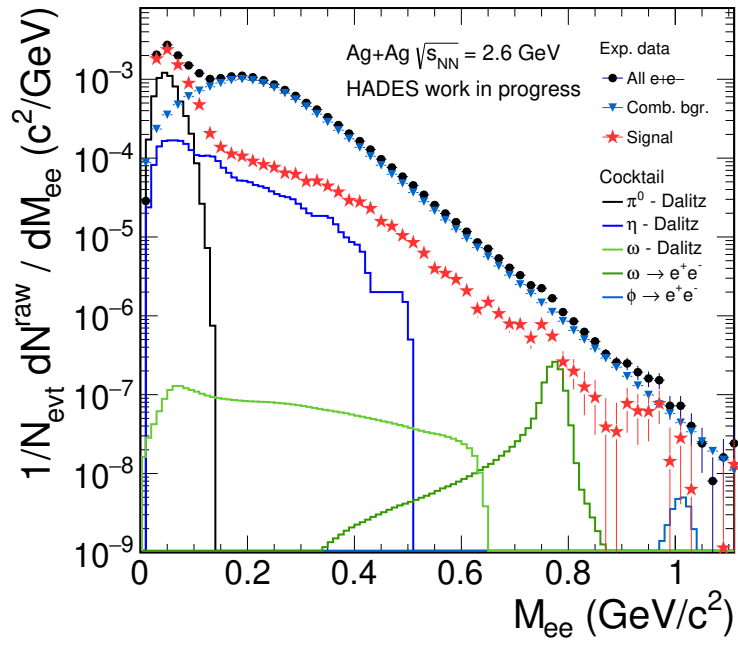


Figure 6.8.: Dielectron invariant mass distribution reconstructed in Ag+Ag collisions at 1.58A GeV. Sources of e^+e^- are shown in different colors. The combinatorial background is subtracted from all e^+e^- contributions leading to the signal [87].

on the energy measured by ECAL will improve the lepton identification. This should further improve the statistics, especially at high invariant masses $M > 1 \text{ GeV}/c^2$.

7 Beam diagnostics and T0 reconstruction in HADES

In this chapter, an overview of beam detectors used in the HADES experiment will be given. In the beginning, diamond based detectors, which are used for the T0 reconstruction and beam monitoring, will be introduced and their performance during the HADES Ag+Ag run will be shown. In the end, the research and development status of new *Ultra-Fast Silicon Detector* (UFSD) technology will be given. For future investigations of beam detectors, a test set-up at the electron accelerator of TU Darmstadt has been constructed which will be described in Chapter 8.

7.1 Aspects of diamond detectors

The name *diamond* is derived from the ancient Greek word *adámas*, meaning *proper; unalterable, unbreakable, untamed*. In fact, diamond material possesses outstanding properties, e.g. its supreme hardness, high thermal conductivity, as well as extraordinary semiconductor properties which have attracted scientific and technological interest for decades. In the following, diamond based beam detectors will be described. After an introduction into important aspects of artificial diamond material, the beam detectors of the HADES experiment will be introduced. Their performance for beam monitoring and T0 reconstruction during the Ag+Ag production beam time follows afterwards.

7.1.1 Diamond material properties

Artificial diamond material can be produced using the *high-pressure-high-temperature* (HPHT) technique or by using the *chemical vapor deposition* (CVD) process [88]. Diamond material produced with the HPHT is not suitable for detectors due to the large number of impurities in the material. Diamonds produced by the CVD process have less impurities and a smaller defect density. The CVD process is based on the deposition of atomic carbon onto a substrate within a gaseous atmosphere. The technique allows to grow *poly-crystalline* (pcCVD) and *single-crystalline* (scCVD) diamonds. The pcCVD diamond grows in a random orientation with a wafer size in the order of several cm. The more expensive scCVD diamonds are grown on a single crystal diamond resulting in typical wafer sizes of several mm. Both pcCVD and scCVD diamonds types can be used for particle detection, but scCVD diamonds show better performance, e.g. higher charge collection efficiency which results in a better energy resolution.

The material properties of diamond have many advantages for particle detectors in comparison to conventional *silicon* (Si) material. The main properties and their advantages and disadvantages for diamond detector operation are summarized in Table 7.1. Diamond is a radiation-hard material and therefore can be used in regions with high radiation which makes diamond detectors very attractive for various applications in the field of particle accelerators. The high band gap in diamond in combination with negligible temperature dependence allows to operate them at room temperature without additional cooling. The high carrier mobilities in diamond results in a very fast charge collection which is of advantage for timing applications and to handle high particle rates. The only major disadvantage of diamond is the significantly higher energy which is needed to create an electron-hole-pair. This fact results in smaller electrical signals compared to silicon material. Nevertheless, in Section 7.3 a new detector technology which is based on Si material will be introduced. Outstanding timing properties can be achieved due to a special doping of the material.

Energy loss in diamond material

The mean energy loss per unit length $-\left\langle\frac{dE}{dx}\right\rangle$ (or *stopping power*) of a charged particle in a given material can be described by the *Bethe-Bloch equation* [6]:

$$-\left\langle\frac{dE}{dx}\right\rangle = Kz^2\frac{Z}{A}\frac{1}{\beta^2}\left[\frac{1}{2}\ln\left(\frac{2m_e c^2\beta^2\gamma^2 W_{\max}}{I^2}\right) - \beta^2 - \frac{\delta(\beta\gamma)}{2}\right], \quad (7.1)$$

Table 7.1.: Material properties of diamond and Si and their advantages (+) and disadvantages (-) for diamond detector operation. Values taken from [89].

Symbol	Property	Diamond	Si	Unit	Diamond detector property
Z	Atomic number	6	14		
ρ	Density	3.51	2.33	g cm^{-3}	
κ	Thermal conductivity	2000	150	$\text{W K}^{-1} \text{m}^{-1}$	+ heat dissipation
E_g	Band gap	5.47	1.12	eV	+ room temp. operation
μ_e	Electron mobility	1800-4500	1350	$\text{cm}^2 \text{V}^{-1} \text{s}^{-1}$	+ fast signal
μ_h	Hole mobility	1200-3500	480	$\text{cm}^2 \text{V}^{-1} \text{s}^{-1}$	+ fast signal
E_{eh}	Energy to create e-h pair	11.6-16	3.6	eV	- lower signal amplitude
q_p	Mean MIP ionization	36	108	$e \mu\text{m}^{-1}$	
E_{dp}	Displacement energy	43	13-20	eV	+ radiation hardness

with the coefficient $K = 4\pi N_a r_r^2 m_e c^2$ where N_a is the Avogadro's number, r_r the classical electron radius, m_e the electron mass and c the speed of light in vacuum. Furthermore, z is the charge number of the incident particle, Z the atomic number of the absorber, A the atomic mass of the absorber, $\gamma = 1/\sqrt{1-\beta^2}$ is the Lorentz factor with $\beta = v/c$, I the mean excitation energy and $\delta(\beta\gamma)$ the density effect correction to the ionization energy loss. The maximum possible energy transfer W_{\max} to an electron in a single collision can be calculated for an incident particle with the mass M by [6]

$$W_{\max} = \frac{2m_e c^2 \beta^2 \gamma^2}{1 + 2\gamma m_e/M + (m_e/M)^2}. \quad (7.2)$$

The energy loss mainly depends on the particle's charge and $\beta\gamma = p/Mc$ which is just a function of its velocity v . By normalizing the energy loss to the material mass-density, the energy loss of all materials are in the same order of magnitude and follow the same dependence on $\beta\gamma$. As an example, the dependence of the energy loss on $\beta\gamma$ of muons in copper is shown in Fig. 7.1. At $\beta\gamma \approx 3$ the energy loss is at its minimum where all charged particles become so-called *minimum ionizing particles* (MIPs). Those particles will produce the smallest signal charge in a particle detector and are therefore often used as a benchmark during the development of a new detector.

In Fig. 7.2 the energy loss of electrons/positrons is shown for diamond and Si. At energies below 1 MeV the loss is dominated by the ionization effect. At large energies the energy loss is dominated by the *Bremsstrahlung* effect, where the electron/positron emits photons due to the interaction with atomic nuclei. The energy from where the *Bremsstrahlung* effect dominates the ionization can be estimated by [89]

$$E_c = \frac{600 \text{ MeV}}{Z}. \quad (7.3)$$

Hence, the critical energy for diamonds is at 100 MeV, while it is at 43 MeV for Si. The minimum energy loss which corresponds to the loss of a MIP is 1.6 eV in diamond and 1.3 eV in Si.

For future research and development of beam detectors, a test set-up has been constructed at the electron accelerator of TU Darmstadt. A detailed description of the set-up will follow in Chapter 8. The accelerator can deliver energies up to 130 MeV ($\beta\gamma = 254$) which is ideal in order to study the behavior of detectors and read-out electronics using particles in the MIPs regime.

7.1.2 Working principle of diamond detectors

In Fig. 7.3 the working principle of a diamond based particle detector is shown. The diamond material is typically a few hundred microns thick. Electrodes are attached on both sides in order to form an ohmic contact. The electrodes can be realized as stripes or in a pixel configuration which allows to get a

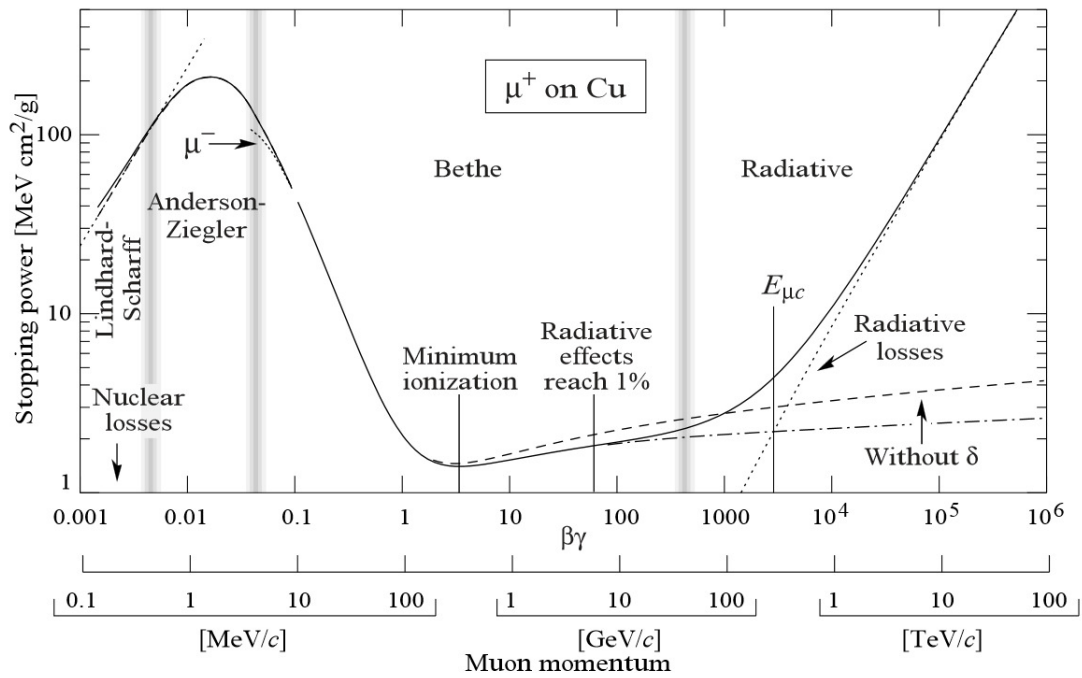


Figure 7.1.: The stopping power $-\langle \frac{dE}{dx} \rangle$ for positive muons in copper as a function of $\beta\gamma = p/Mc$. (Taken from [90])

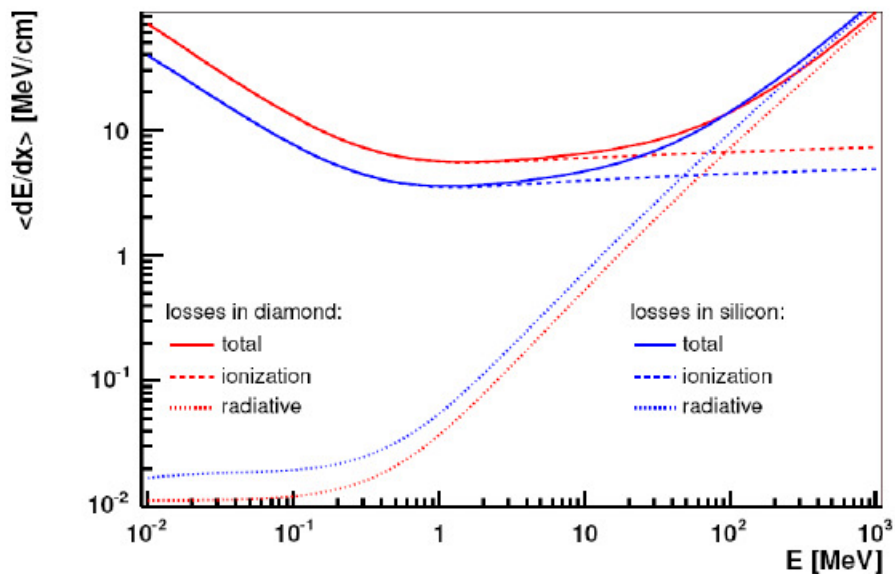


Figure 7.2.: Mean energy loss of electrons/positrons in diamond and Si. Dashed curves show the loss due to ionization, dotted curves the energy loss due to *Bremsstrahlung* while the solid lines show the total energy loss. (Taken from [89])

position information. Because there is no pn-junction, the polarity of the electric field is irrelevant. The applied voltage is typically around $2 \text{ V } \mu\text{m}^{-1}$. Initially, all free carriers inside the material are drained by the applied electric field and there is no charge movement. Exceptions are thermally excited electron-hole pairs which will immediately drift to the electrodes. When a charged particle is traversing the diamond material, atoms in the crystal lattice along the track are ionized which promotes electrons into the conduction band and leaves holes in the valence band. In case of a MIP which is traversing the

detector perpendicularly, the number of generated pairs can be calculated from the bulk thickness d and the mean MIP ionization $q_p = 36 e \mu\text{m}^{-1}$ by

$$Q_{pairs} = q_p d. \quad (7.4)$$

The electrons will move towards the positive electrode while the holes will drift in the opposite direction towards the negative electrode. Because of the movement, a charge will be induced in the electrodes which can be measured by a charge sensitive amplifier. For signal generation it is irrelevant whether the charges will finally reach the electrodes, only their path contributes to the final signal integral [91]. Since the duration of the signal depends only on the length of the charge generation process, a thin sensor produces a faster signal. But on the other hand, a thin sensor has a smaller sensitive volume and therefore produces a smaller signal [91]. In addition, due to trapping and recombination, because of defects or impurities in the diamond material, many charge carriers will not reach the electrodes. The resulting small electric signal charges require special emphasis in the signal post processing, e.g. signal amplification and digitization.

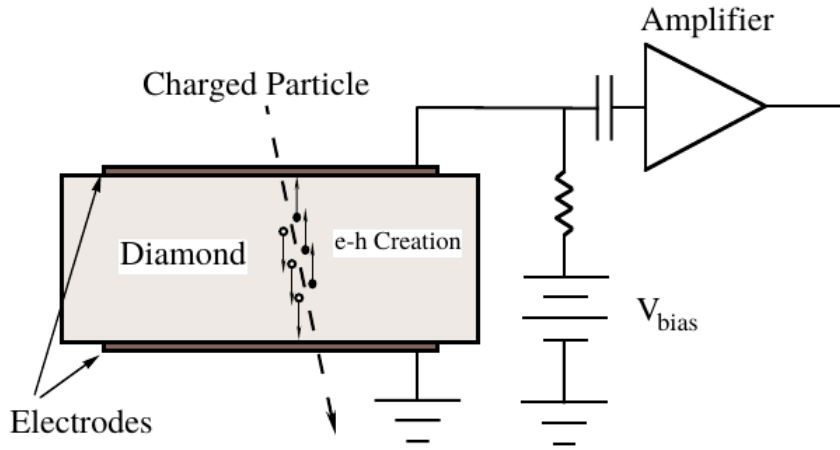


Figure 7.3.: Working principle of a diamond detector. (Taken from [92])

7.1.3 Charge collection efficiency

An important parameter in order to characterize a diamond sensor, with a thickness d , is its *charge collection efficiency* (CCE). It is defined from the ratio of collected charge measured at the electrode Q_{coll} and the produced charge inside the bulk due to ionization [93]:

$$CCE = \frac{Q_{coll}}{Q_{pairs}} = \frac{Q_e}{36 e \mu\text{m}^{-1} \cdot d}. \quad (7.5)$$

The produced charge Q_{pairs} can be calculated with equation 7.4. Besides the CCE, the *charge collection distance* (CCD) is used which represents the average drift length of the electron and is given by

$$CCD = CCE \cdot d. \quad (7.6)$$

7.2 T0 reconstruction and beam diagnostics during the HADES Ag+Ag run

During the the HADES Ag+Ag physics production beam time in March 2019, two diamond based detectors have been used for T0 reconstruction. Moreover, a second independent read-out system allowed an

online beam monitoring. In the following, a detailed description of the sensors, the read-out system and their performance will be given.

7.2.1 Diamond detectors, read-out and online monitoring system

The main detector [18, 17, 94], which is used in HADES in order to construct the *reaction time* (T_0), and also provides beam quality monitoring, is made of scCVD diamond material. A similar detector [17] has been already used for a $^{197}\text{Au}^{69+}$ beam, with a kinetic energy of 1.23A GeV and currents up to 10^7 ions/s. The detector has an active area of $4.7\text{ mm} \times 4.7\text{ mm}$. A thickness of $70\text{ }\mu\text{m}$ is chosen in order to reduce the nuclear interaction probability of the beam ions in the detector material. The diamond material is metallized with a 50 nm Cr layer which is covered by a 150 nm Au layer. The metallization is arranged in 16 strips (each $300\text{ }\mu\text{m}$ wide) which is rotated by 90° on the other side. This configuration allows beam profile measurements in x - and y -directions. The sensor is able to deliver a time precision $<100\text{ ps RMS}$ and allows to handle rates up to 10^7 particles/channel.

A second diamond based veto detector is located behind the target (see also Fig. 1.6). It is made of pcCVD material with the dimensions of $8\text{ mm} \times 8\text{ mm}$ and thickness of $107\text{ }\mu\text{m}$. A boxed shaped metallization is chosen in order to allow fragment identification. This allows to exclude events without a reaction in the target from the HADES trigger generation. A close-up picture of both sensors can be found in Fig. 7.4.

Both diamond sensors are glued to a *Printed Circuit Board* (PCB) which serves as holder and provides electrical connections to the read-out electronics. The read-out segments of the diamond sensors are bonded with aluminum wires to the conducting traces on the PCB. An additional mechanical holding structure is used to install the detector system close to the target inside the beam tube. It consists of four PCB rods which serve as a mechanical holder including signal lines for the sensor read-out. The full detector assembly is shown in Fig. 7.5.

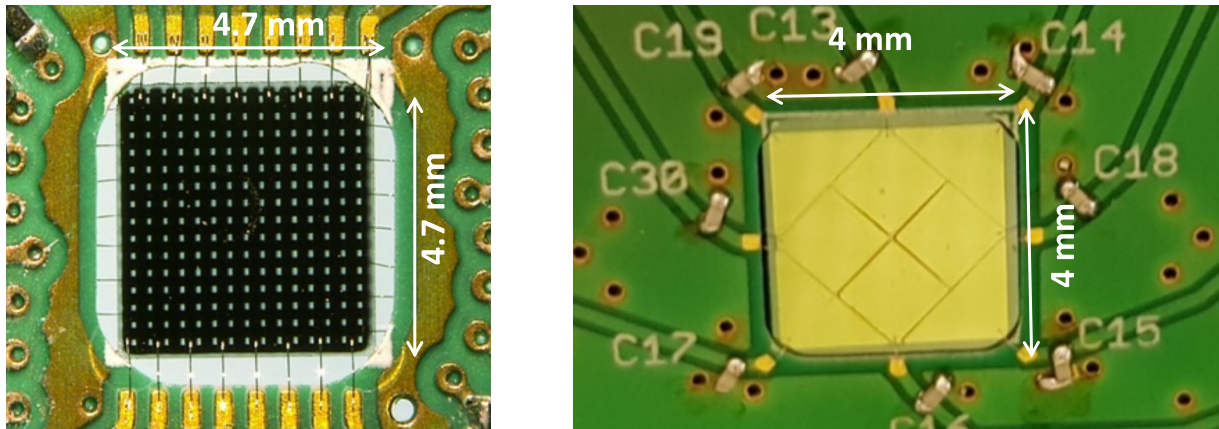


Figure 7.4.: **Left:** Close-up photography of the scCVD diamond based sensor. The metallization is arranged in 16 strips (each $300\text{ }\mu\text{m}$ wide) which allows beam profile measurements. **Right:** Close-up photography of the pcCVD diamond based veto detector. A boxed shaped metallization was chosen in order to allow fragment identification [95].

The diamond detector read-out scheme, as it was used during the Ag beam time in March 2019, is schematically shown in Fig. 7.6. Signals from the sensor are amplified and discriminated afterward. The signal discrimination is based on the NINO [96] chip which also has a fan-out functionality. In order to prevent a possible influence on the T_0 measurement, which is very important for HADES, two independent TRB3 based read-out systems are used. One TRB3 board is included in the standard HADES DAQ system and used to measure the T_0 time of the reaction in the target. A second independent TRB3 system in combination with the *Data Acquisition Backbone Core* (DABC) [39] framework is used to allow to extract online beam monitoring [18] information from the same sensor data.

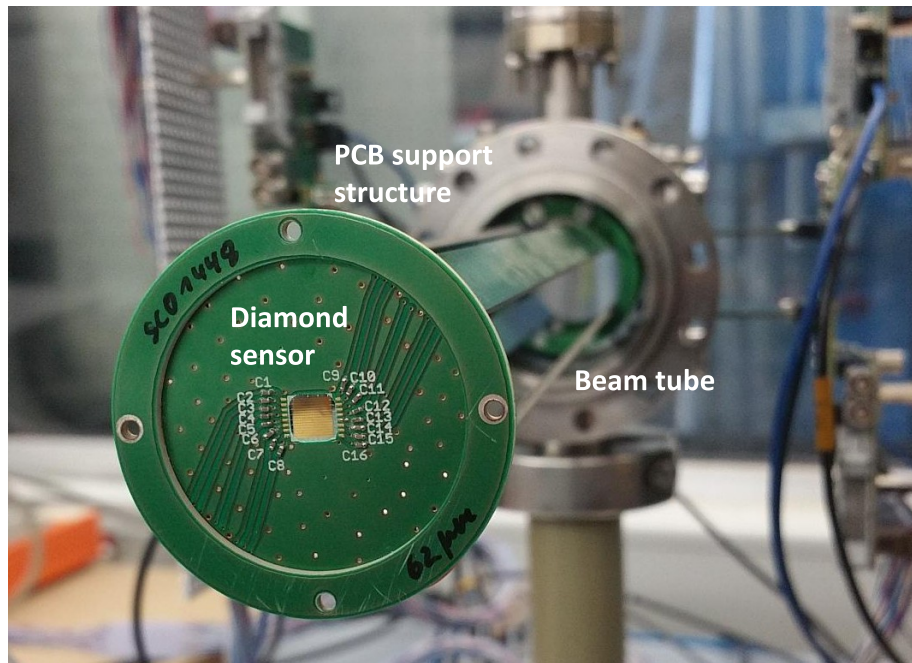


Figure 7.5.: The diamond detector system mounted in the HADES beam tube. The diamond sensor is mounted on PCB plates and the read-out electrodes are bonded to the PCB traces using aluminum wires.

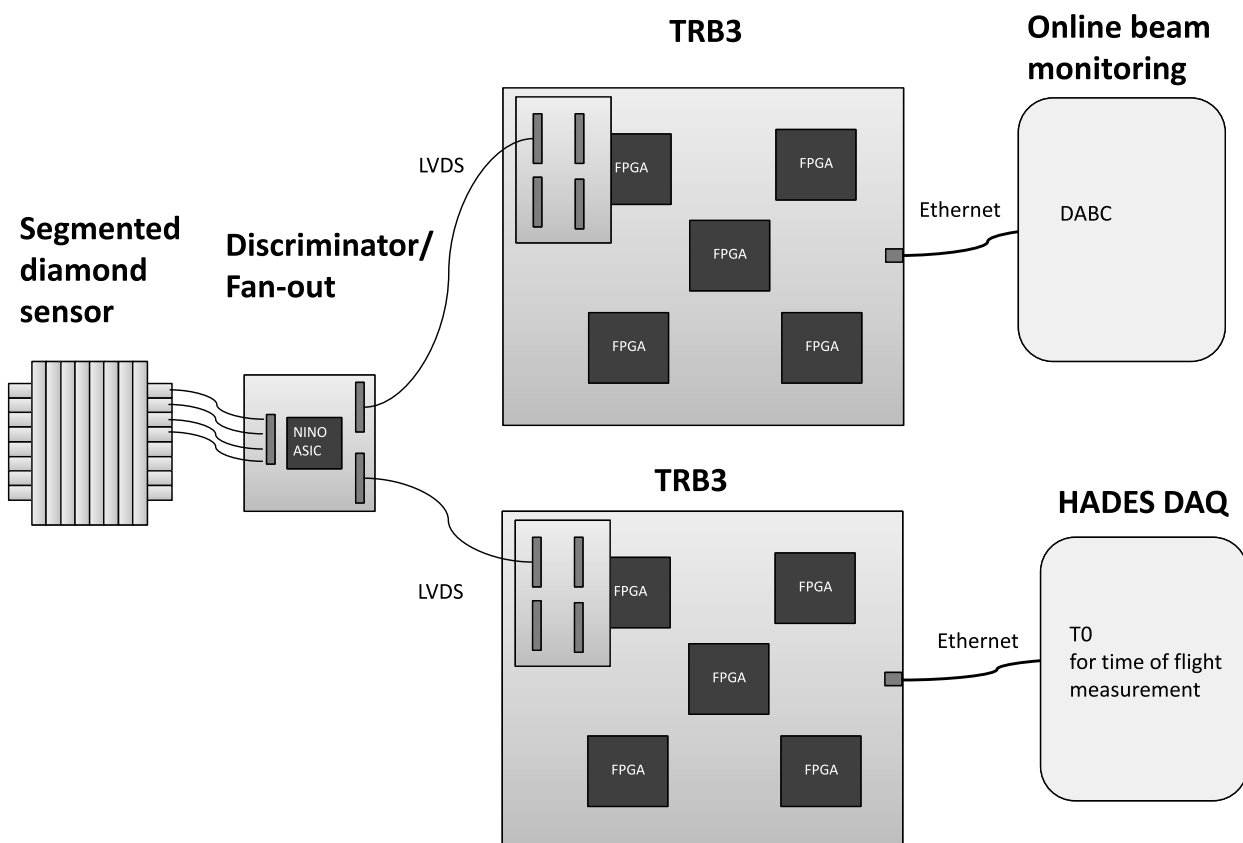


Figure 7.6.: Read-out scheme of the HADES diamond detector. Signal discrimination is based on the NINO chip which also implements a fan-out functionality. Two independent TRB3 based read-out systems are used.

The DABC software [39] is used to collect the data from the TRB3 boards, performs the needed online time calibrations, and allows to apply an online data analysis. The results of the data processing in form of histograms are provided to the DABC web server for visualization. Trend plots showing the beam position in x - and y -direction can be used for online beam monitoring purposes. In addition, the time structure of the beam and the beam intensity can be visualized. Those plots can be rendered as a live display in any web browser. They provide a very useful tool for the accelerator operators during beam adjustment and they allow a long-term evaluation of the beam stability which is crucial for an efficient data recording in HADES. An example of such a live display, showing important beam properties, can be found in Fig. 7.7.

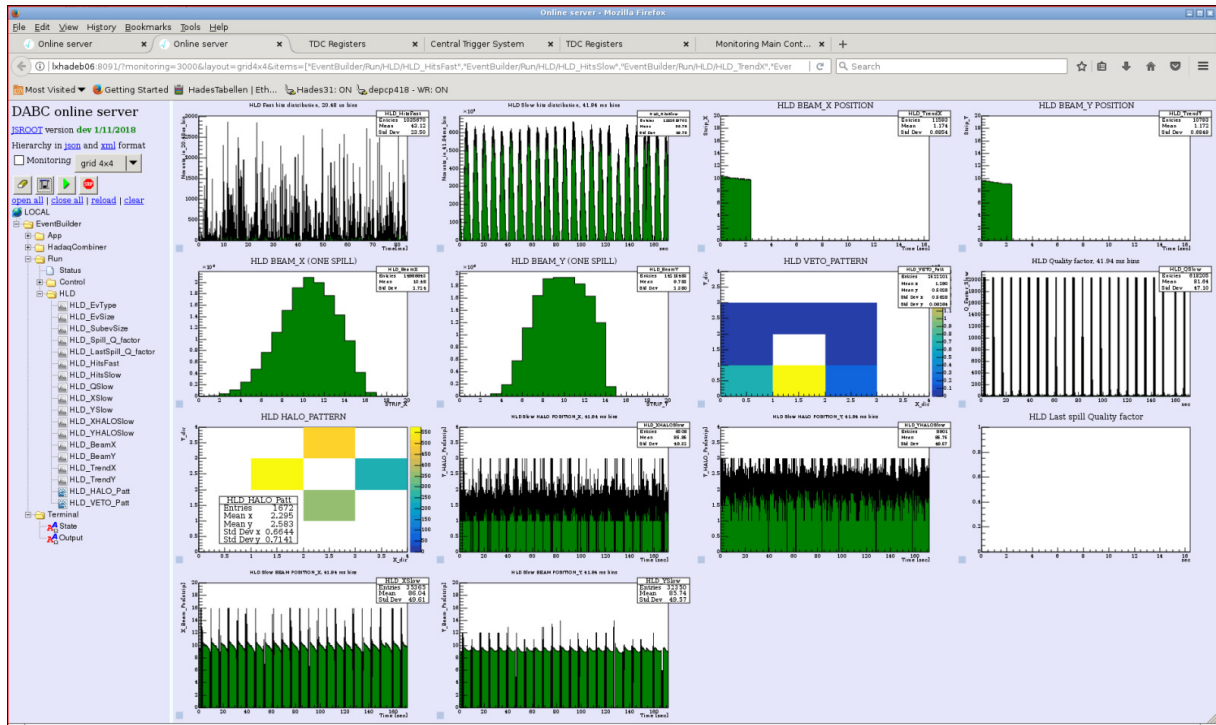


Figure 7.7.: Important beam properties (e.g. x - and y -beam-profile, macro- and micro-spill structure) can be displayed live in any web browser [18].

7.2.2 Beam profile and position measurement

The scCVD sensor, which metallization is segmented into 16 strips, allows a beam profile and position determination of the ion beam in front of the HADES target with a resolution of $300\ \mu\text{m}$. The HADES experiment typically requires a focused and stable beam on the target with a beam size of about $\sigma_{x,y} = 1\ \text{mm}$. In Fig. 7.8 the typical beam profile in x - and y -direction for an Ag (1.58A GeV) beam is shown. On average, a beam size of about $\sigma_x = 1.2\ \text{mm}$ in x -direction and about $\sigma_y = 0.8\ \text{mm}$ in y -direction have been achieved. During the beam-time, the diamond sensor has been moved in y -direction several times since radiation damage occurs over time which affects the time precision for the T0 determination. The movement of the sensor is shown in Fig. 7.9.

7.2.3 Spill profile, time structure and quality factor

During the HADES beam time in March 2019 the DABC based read-out system was used to monitor the quality of the beam. An $^{107}\text{Ag}^{45+}$ ion beam with an energy of 1.58A GeV has been delivered by the SIS100 accelerator via a so-called *slow extraction*. In order to ensure efficient data taking of the HADES experiment the macro spill profile is required to be almost flat, without spikes. Especially the HADES tracking system is limited to a maximal beam intensity of 10^6 particles/s [98]. Any rate above this

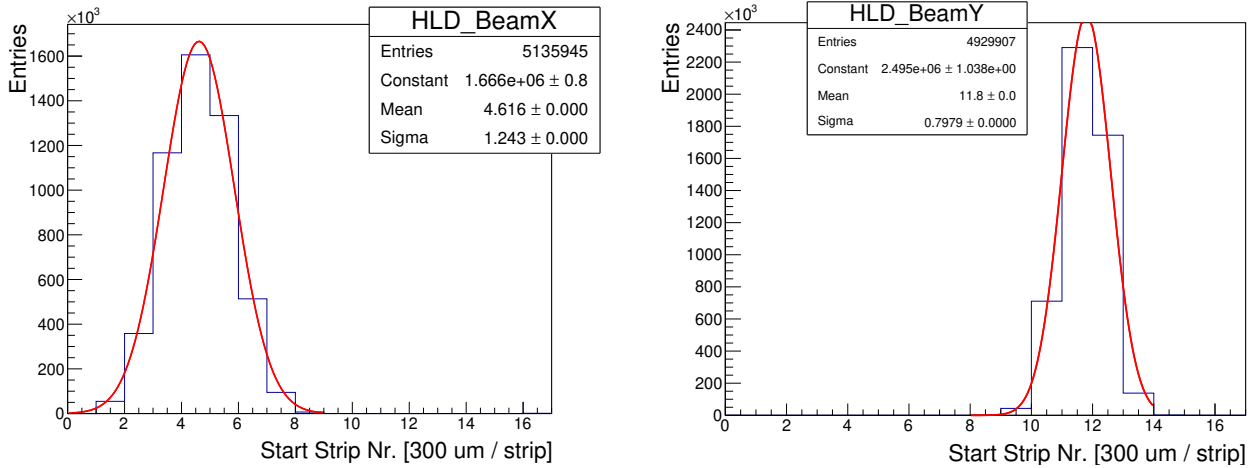


Figure 7.8.: Beam profile measurement in x -direction (left) and y -direction (right) of an $^{107}\text{Ag}^{45+}$ ion beam with an energy of 1.58 AGeV using a scCVD with a metallization segmented into sixteen stripes. Each bin corresponds to a width of 300 μm [18].

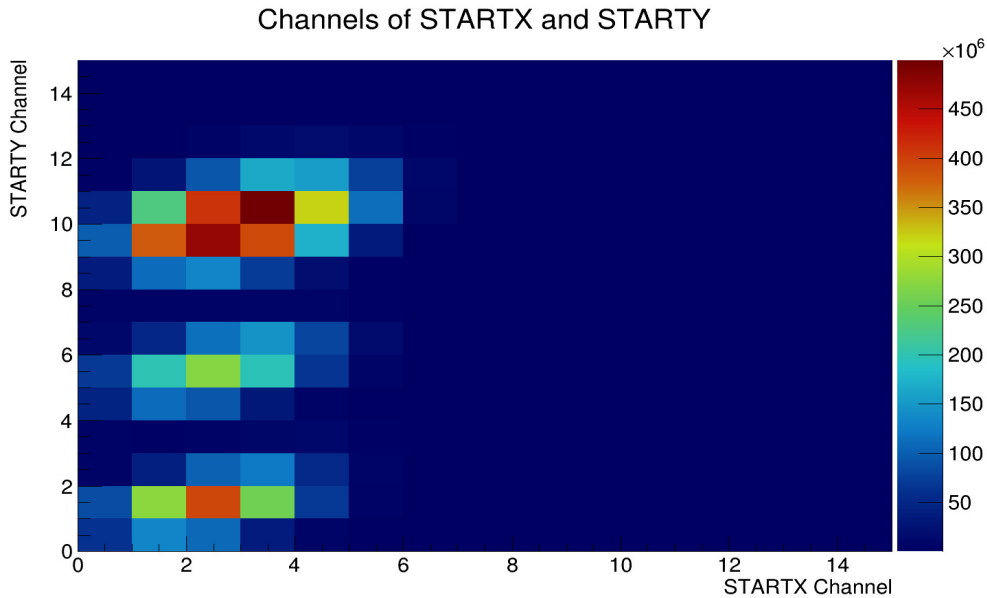


Figure 7.9.: Particle fluence on the HADES diamond detector during a four week beam time. The diamond sensor has been moved three times [97].

could potentially harm the drift chambers. In Fig. 7.10 (left) the typical macro spill structure for a spill duration of 18 s is shown, the corresponding micro spill structure is shown in Fig. 7.10 (right).

For the evaluation of the beam quality a *quality factor* or *Q-factor* has been introduced which represents the ratio between the peak and average event rates. The Q-factor is defined by [18]:

$$Q = \frac{N_{\max}(20 \mu\text{s})}{N_{\text{mean}}(40 \text{ms})}, \quad (7.7)$$

with the maximal number of hits in a 20 μs binning $N_{\max}(20 \mu\text{s})$ and the average number of hits in a 40 ms binning $N_{\text{mean}}(40 \text{ms})$. This factor should ideally be as close as possible to 1 throughout the complete spill duration. An example of the quality factor, for the corresponding spill which was shown

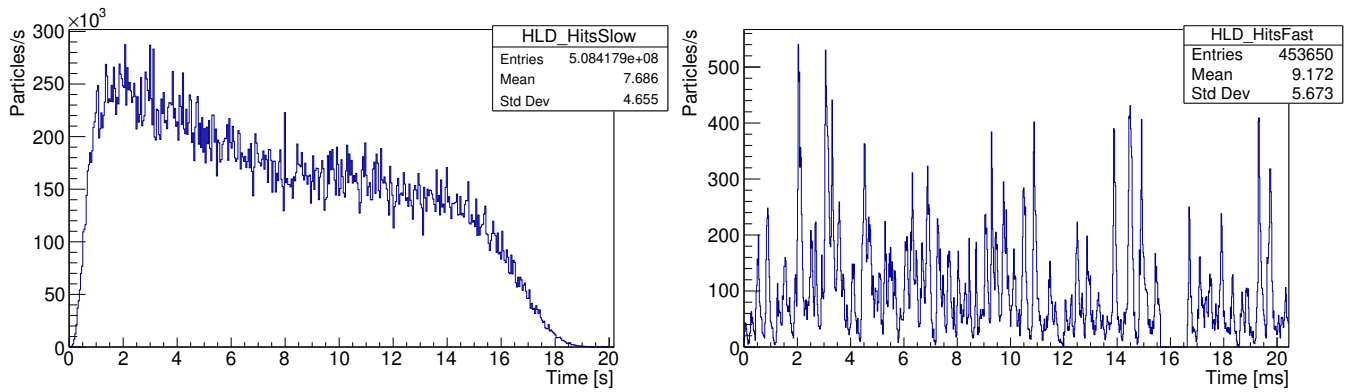


Figure 7.10.: **Left:** Macro-spill time structure measured by the scCVD diamond sensor in front of the HADES target. The ion particles are extracted from the SIS18 accelerator via a so-called *slow extraction*. A typical spill duration is about 18 s. The maximal average rate should not be above 10^6 particles/s. **Right:** The corresponding micro-spill time structure of the particle rates [18].

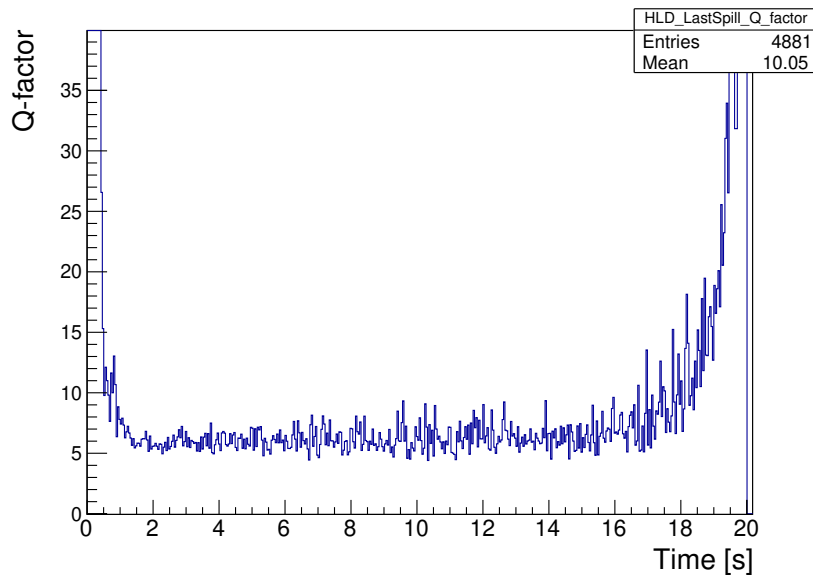


Figure 7.11.: Quality factor of the Ag beam which is defined by the ratio between the peak and average event rates [18].

in Fig. 7.10, is shown in Fig. 7.11. As one can see, especially during the beginning and the end of the extraction of the beam, larger deviations occur.

The beam monitoring system and the associated HADES DAQ infrastructure has been successfully used in order to improve the cycle-to-cycle feedback on the slow-extraction macro-spill structure [99, 100, 98] of the SIS18 accelerator. The system allowed to drive the relevant accelerator extraction parameters directly which improved the event data recording efficiency of HADES by about 15% on top of what has already been established by expert-driven manual fine-tuning.

7.2.4 Precision of the reaction time (T_0) reconstruction

During the beam time, a regular calibration of the T_0 detector is needed. Among other things, during the beam time, threshold and high voltage settings were modified and the y -position of the detector was changed. For a rough calibration the second diamond detector (*veto detector*) can be used. Thereby, the

distribution of time difference between coincident hits in the T0 detector and the veto channels can be used. A more precise method is based on the usage of negatively charged particles with a momentum above 300 MeV/c (which mainly consist of pions, see Fig. 1.11). Since their momentum and track length are measured by the spectrometer a theoretical flight time can be calculated. During one minute of beam almost 500 000 pions are measured in the HADES spectrometer which ensures enough data to perform a time calibration every minute. The calibration of the T0 detector is currently ongoing [27]. Currently the time precision is about $\sigma_{T0,start} = 150$ ps. However, it is assumed that further calibration will improve the precision. For example, a precision of 50 ps has been achieved with a similar detector in the HADES Au+Au beam time in 2012.

7.3 Research and development of Ultra-Fast Silicon Detectors for HADES

In Section 7.1 diamond detectors have been introduced. They have excellent properties for beam monitoring and timing applications. However, those detectors have two major disadvantages. On the one hand the available bulk size of scCVD diamond samples is only in the order of several millimeters. In order to cover larger areas mosaic detectors have to be used which are technically demanding to produce. On the other hand the samples are expensive. In addition, one of the main suppliers has currently delivery difficulties.

One of the concepts under development is the *Ultra-fast Silicon Detectors* (UFSD) technology [101, 102, 103, 104]. This new generation of position sensitive detectors is based on *Low-Gain Avalanche Detectors* (LGAD) design [105] and adds to the classical silicon detectors the ability to measure accurately time. Indeed, those detectors are optimized for timing applications for high radiation applications. Next-generation detectors of this technology, with improved radiation hardness, are in preparation [106]. A main development driver is the RD50 collaboration [107] at the *European Organization for Nuclear Research* (CERN). In the following the technology will be introduced. A prototype detector has been built for the needs of the HADES experiment. First results of its performance with an proton beam will be shown.

7.3.1 Working principle of Ultra-Fast Silicon Detectors

Ultra-Fast Silicon Detectors (UFSD) [101] are timing optimized *Low-Gain Avalanche Detectors* (LGAD) [105]. Those detectors are silicon detectors with an internal charge multiplication mechanism. The typical structure and the working principle of a LGAD is shown in Fig. 7.12. The sensors have an additional thin p+ doped layer ($\sim 50 \mu\text{m}$, $n_d \sim 10^{16}$ boron/cm²) added under the n implant. This configuration results in a strong electric field E in the avalanche region which generates signals 10 times larger than in standard silicon detectors. The technology allows building thin pixelated particle detectors for high precision timings applications. The fact that all advantages of Si detector technology remain, e.g. large area substrates, low cost and possible large scale production make them a competitor to diamond detectors. The main issue for their operation in high radiation environments is the decrease of gain with irradiation, due to effective acceptor removal in the gain layer. It has been shown [109] that at very high fluences the concentration of acceptors in the p+ implant is greatly reduced. In addition, acceptors are created in the bulk material which is then used for multiplication inside the sensor. The multiplication will then take place in the bulk material which shows even faster induced current rise times. This will result in even better timing properties. It has been shown [109] that the overall signal gain can be controlled by the bias voltage with expected time precision of 30 ps up to fluences of $6 \times 10^{15} \text{ cm}^{-2}$, which meets the requirements of the HADES experiment.

UFSD prototype detector

A first UFSD prototype detector [95] for possible timing applications in HADES has been built at GSI. The sensor (W15_1A and W3 types) is from a FBK (*Fondazione Bruno Kessler*, Trento, Italy) [106] production and has a thickness of 500 μm . The active avalanche region is 50 μm thick. The sensor covers an area

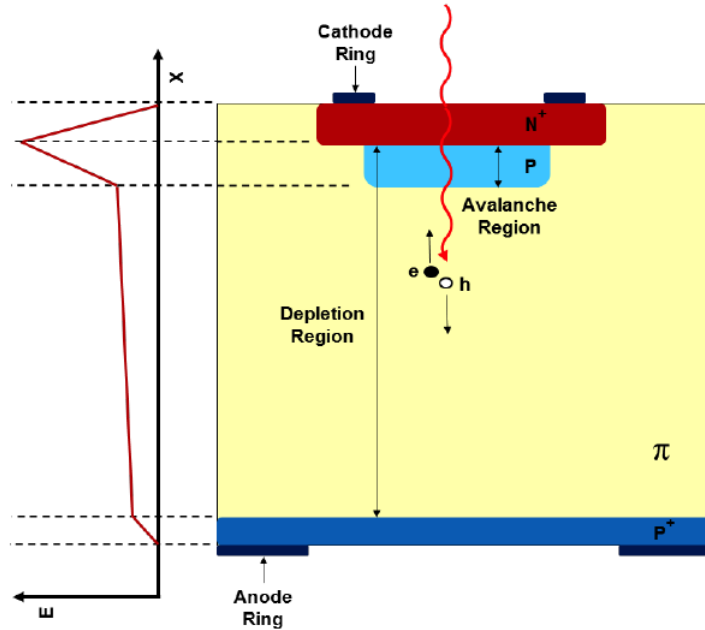


Figure 7.12.: Structure of a *Low-Gain Avalanche diode* (LGAD). The red area is a highly doped n-type layer. The moderately doped p-type multiplication layer is shown in blue. The resistive p-bulk is shown in yellow. This structure creates a large E -field in a small area resulting in a moderate charge multiplication with a gain of 10-50 without breakdown. (Taken from [108])

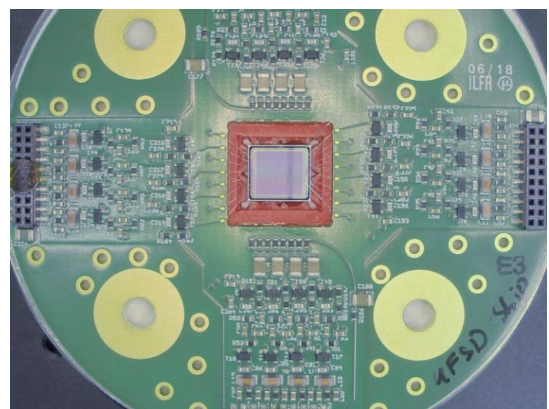
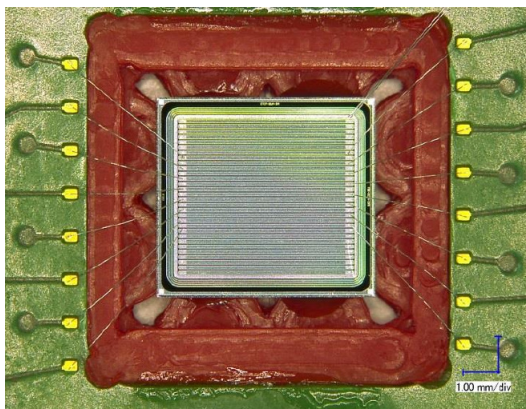


Figure 7.13.: **Left:** Close-up picture of the prototype UFSD sensor for HADES. The sensor covers an area of 5 mm × 4.5 mm. For testing purposes 16 stripes are bonded to a read-out PCB. **Right:** Read-out PCB with bonded UFSD detector. Two stages of transistor based amplifiers are located close to the sensor. (Taken from [95])

of 5 mm × 4.5 mm. The active regions are arranged in 30 parallel stripes with a pitch of 140 μm. The sensor, which is bonded to a read-out PCB, is shown in Fig. 7.13. Two amplification stages are installed close to the sensor. The read-out concept, which is shown in Fig. 7.14, is similar to the one of diamond detectors (see also Section 7.2.1). For testing purposes the stripes of the sensor are read out alternating by the NINO chip and the PaDiWa¹ [57] discriminator board. The performance of both systems is currently investigated and compared.

¹ In contrast to the PaDiWa-AMPS board (see section 3.3), the PaDiWa board, which is used here, implements 32 discriminator channels without signal integration functionality.

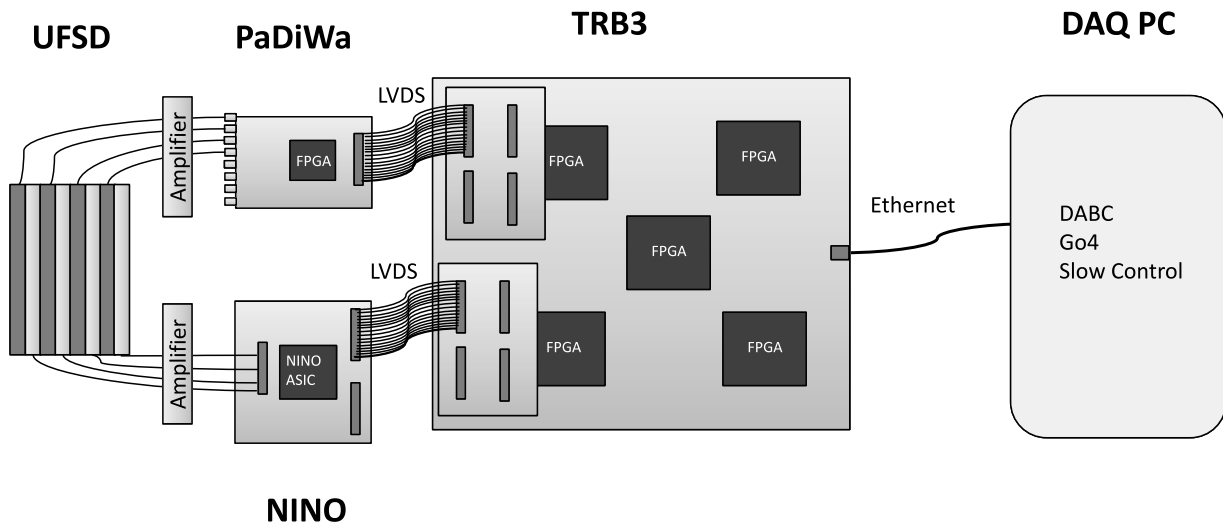


Figure 7.14.: Read-out scheme of the UFSD prototype detector. A NINO based read-out can be compared to the PaDiWa based read-out.

7.3.2 Performance study with proton beam at the COSY facility

A telescope set-up of two UFSD prototype detectors has been investigated [95] at the *Cooler Synchrotron (COSY)* at *Forschungszentrum Jülich* with a 2.9 GeV proton beam. The experimental set-up is shown in Fig. 7.15. Two UFSD prototypes have been aligned perpendicular to the beam z -axis. The strip orientation of the second sensor has been rotated by 90° in order to allow an evaluation of the time precision between the two sensors. A linear-stage allows a remote alignment of the telescope in x - and y -directions. The main goal was the evaluation of the time precision between the two sensors and their two discriminator systems. For that, two identical channels, which are read-out by the same system, are compared. Preliminary results [110], after calibration and time-walk corrections, are shown in Fig. 7.16. For the UFSD system which is read-out with the NINO discriminator a precision of $\sigma_{\text{NINO}} = 80 \text{ ps}/\sqrt{2} = 57 \text{ ps}$ can be archived. The PaDiWa discriminator delivers $\sigma_{\text{PaDiWa}} = 115 \text{ ps}/\sqrt{2} = 81 \text{ ps}$.

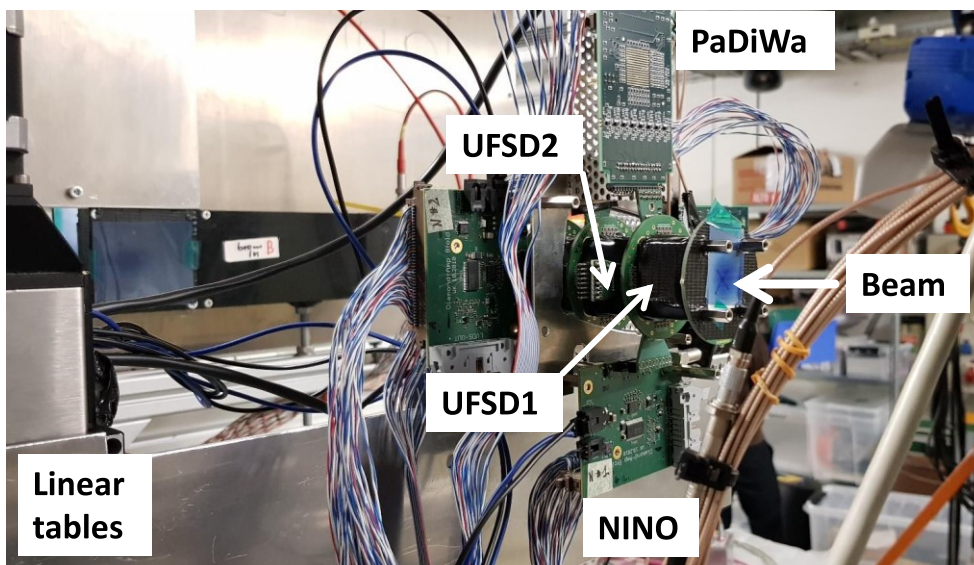


Figure 7.15.: A UFSD telescope set-up which has been tested with a minimum ionizing proton beam at the COSY facility in Jülich. The telescope consists of two UFSD sensors, where the strip orientation of the second sensor is rotated by 90° in order to allow an evaluation of the time precision between the two sensors.

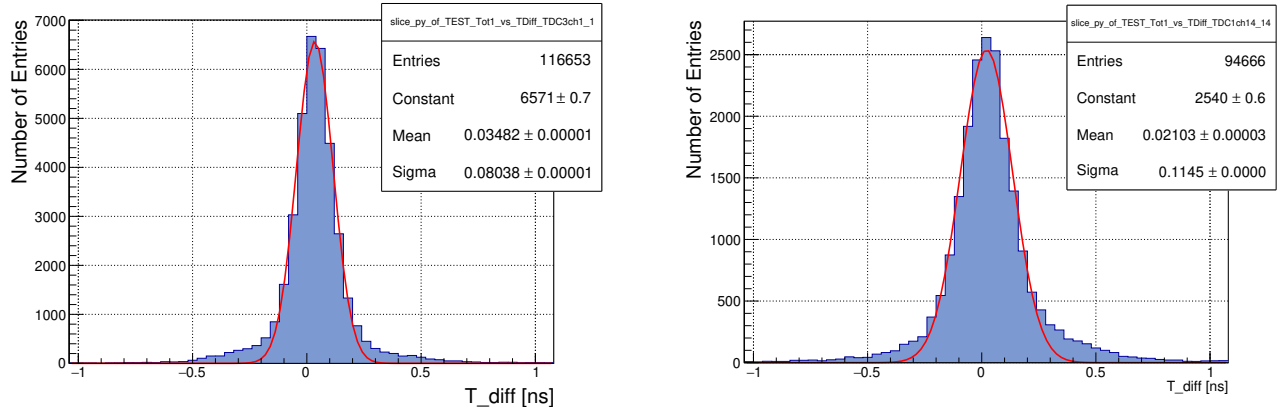


Figure 7.16.: **Left:** Time difference between first and second sensor using the NINO discriminator. A time precision of $\sigma_{\text{NINO}} = 80 \text{ ps}/\sqrt{2} = 57 \text{ ps}$ can be achieved. **Right:** Time difference between the firsts and the second sensor using the PaDiWa discriminator. $\sigma_{\text{PaDiWa}} = 115 \text{ ps}/\sqrt{2} = 81 \text{ ps}$ can be achieved [110].

The time precision achieved with the NINO chip is an excellent result for a system using state-of-the-art technology. The PaDiWa based read-out concept needs still further tuning. New read-out electronics is currently being developed. Furthermore, the next generation of UFSD sensors, with less inactive space between the strips, is being currently produced and will be available soon. An excellent platform for further investigation is provided by a new multi-purpose detector test set-up at the electron accelerator of TU Darmstadt, which will be introduced in the following Chapter 8.



8 Multi-purpose detector test set-up at the S-DALINAC

For research and development of new detectors for timing applications, a detector test stand has been installed at the electron accelerator of TU Darmstadt. Moreover it is planned to use it as a permanent multi-purpose set-up in order to allow a large variety of tests with an electron beam, e.g. beam and tracking detectors development tests or even radiation tests of read-out electronics.

In the following, the accelerator facility which can now be operated as an *Energy Recovery Linac* will be introduced. A panorama picture of the S-DALINAC main accelerator hall is shown in Fig. 8.1. Basic concepts of beam dynamics will be introduced which should facilitate the understanding of the physical concepts behind the needed beam transport simulations. Besides this, the design process of a new vacuum chamber for a dipole magnet will be shown. Finally, the installation, alignment and commissioning of the new beamline will be covered.



Figure 8.1.: Cylindrical panorama composite of the S-DALINAC main accelerator hall. On the right side one can see the helium vessels of the super-conducting main linear accelerator. On the left side three recirculation beamlines are visible. Dipole magnets are painted blue, quadrupole magnets are yellow and green. (Picture taken in April 2019)

8.1 S-DALINAC in Energy Recovery Linac mode

The *Superconducting-DARmstadt-electron-LINearACcellerator* (S-DALINAC) [111, 112, 113] is in operation at the Institute for Nuclear Physics of TU Darmstadt since 1991. During the last years it has been continuously optimized and upgraded. Recently, an additional recirculation beamline was installed, which allows to reach higher beam energies, and in addition, to operate the accelerator as an *Energy Recovery Linac* (ERL) [114]. An overview of the accelerator complex is illustrated in Fig. 8.3. Electrons can be generated by two different sources. First, by means of a thermionic gun, through glow emission from a tungsten wire and an electrostatic *continuous wave* (cw) pre-acceleration, beams with currents up to $60\mu\text{A}$ can be provided. In a second source, spin polarized electrons [115] can be produced via photon emission of a GaAs-cathode. With this source, a cw or pulsed operation is possible. The electrostatic pre-accelerated electrons are prepared by a *Chopper-Buncher-System* in order match the 3 GHz acceleration frequency which is used at the S-DALINAC and are focused into the capture section of the superconducting injector. The *injector* consists of one five-cell and two twenty-cell *superconducting radio-frequency* (SRF) cavities which are made of niobium. The cavities are mounted in a large helium vessel and operated at 2 K. The injector section allows to increase the beam energy up to 10 MeV. Without further acceleration the beam can be used for nuclear resonance fluorescence experiments at the DHIPS [116] set-up or the beam can be deflected to a diagnostic set-up. For a further acceleration the beam is deflected by 180° into the *main linac* which consists of eight twenty-cell SRF cavities. The beam energy is increased up to 30.6 MeV per linac pass. Three recirculations allow the beam to pass through the accelerator up to four times in order to achieve the maximum energy of 130 MeV. After acceleration, the beam can be extracted to the experimental area. The extraction beamline and the location of the main experiments is shown in Fig. 8.4. The beam quality can be optimized with the help of the *High-Energy-Scraper-System* [117]. The system reduces the energy spread of the beam, as well as the radiation background count rate which improves the conditions for all subsequent experiments. After

the passage of the high energy scraper-system the beam is guided to one of three experimental set-ups. Electron scattering experiments are conducted at the QCLAM [118] and LINTOTT [119] spectrometers. At the low-energy photon-tagger NEPTUN [120], the electron beam is used to generate *Bremsstrahlung* in order to investigate nucleons with photons. In front of the NEPTUN experiment, the multi-purpose detector test set-up is installed. The beam parameters at the new detector test set-up are summarized in Table 8.1.

Table 8.1.: Beam parameters of the S-DALINAC at the detector test set-up. (Values taken from [113, 121])

Beam energy	up to 130 MeV
Beam current	up to 20 μA (in main LINAC)
Beam emittance (RMS, normalized)	~ 1 mm/mrad
Operation mode	cw (3 GHz RF-acceleration)
Bunch length (RMS)	5 ps
Bunch charge (RMS)	up to 6.67 fC
Simulated beam size (1σ)	$\sim 100 \mu\text{m}$ - several mm

A recently installed beamline in the S-DALINAC allows an operation as an *Energy Recovery Linac* (ERL) [114]. This mode allows to reuse the energy of beam particles which have not been lost by interactions in an experiment. Those particles normally have to be dumped and consequently their energy is lost as thermal load inside the beam dump. The principle of an one-turn ERL operation is illustrated in Fig. 8.2. A first beam is injected and accelerated in the main linac. Electron bunches normally sit on the maximum of the RF-field. A *path-length adjustment system*, which is added to the newly installed second recirculation, allows to change the distance traveled by the beam in order to shift its phase by 180° . Nevertheless, the return loop is the place for an internal target not interfering too much with the beam like, e.g. a *Free Electron Laser* (FEL) undulator, a gas target or a beam-laser interaction point. The phase shifted beam is re-injected into the main linac as a second beam. The electron bunches now sit on the minimum of the RF-field and therefore the beam will be decelerated. The kinetic energy of the decelerated electrons is transferred back to the cavities fields and can be used for acceleration of the subsequent electrons.

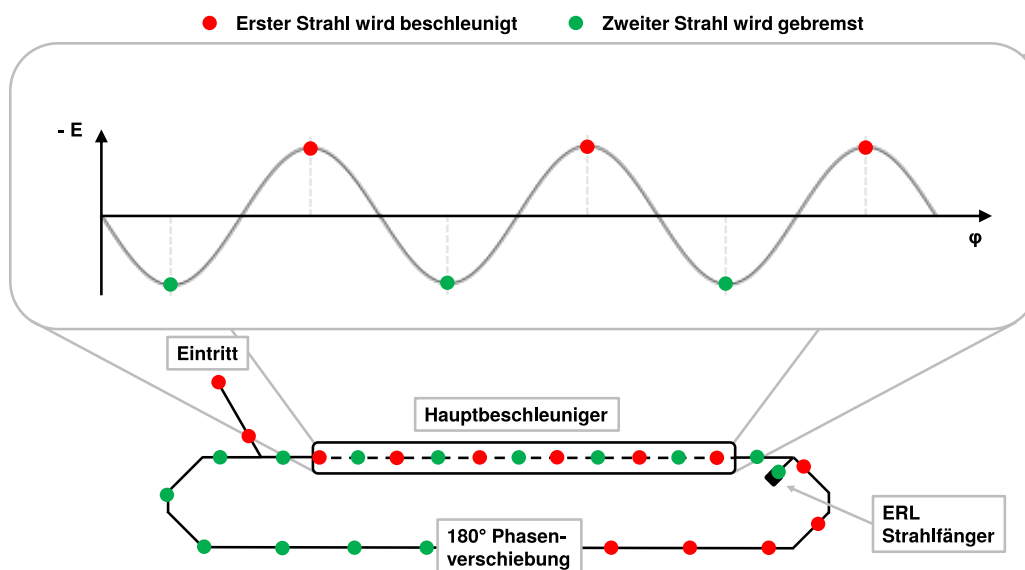


Figure 8.2.: Principle of a once recirculating ERL operation applied to the S-DALINAC. The first beam (red circles) is accelerated in the main accelerator while the second beam (green circles) is decelerated due to a phase shift of 180° . (Taken from [114])

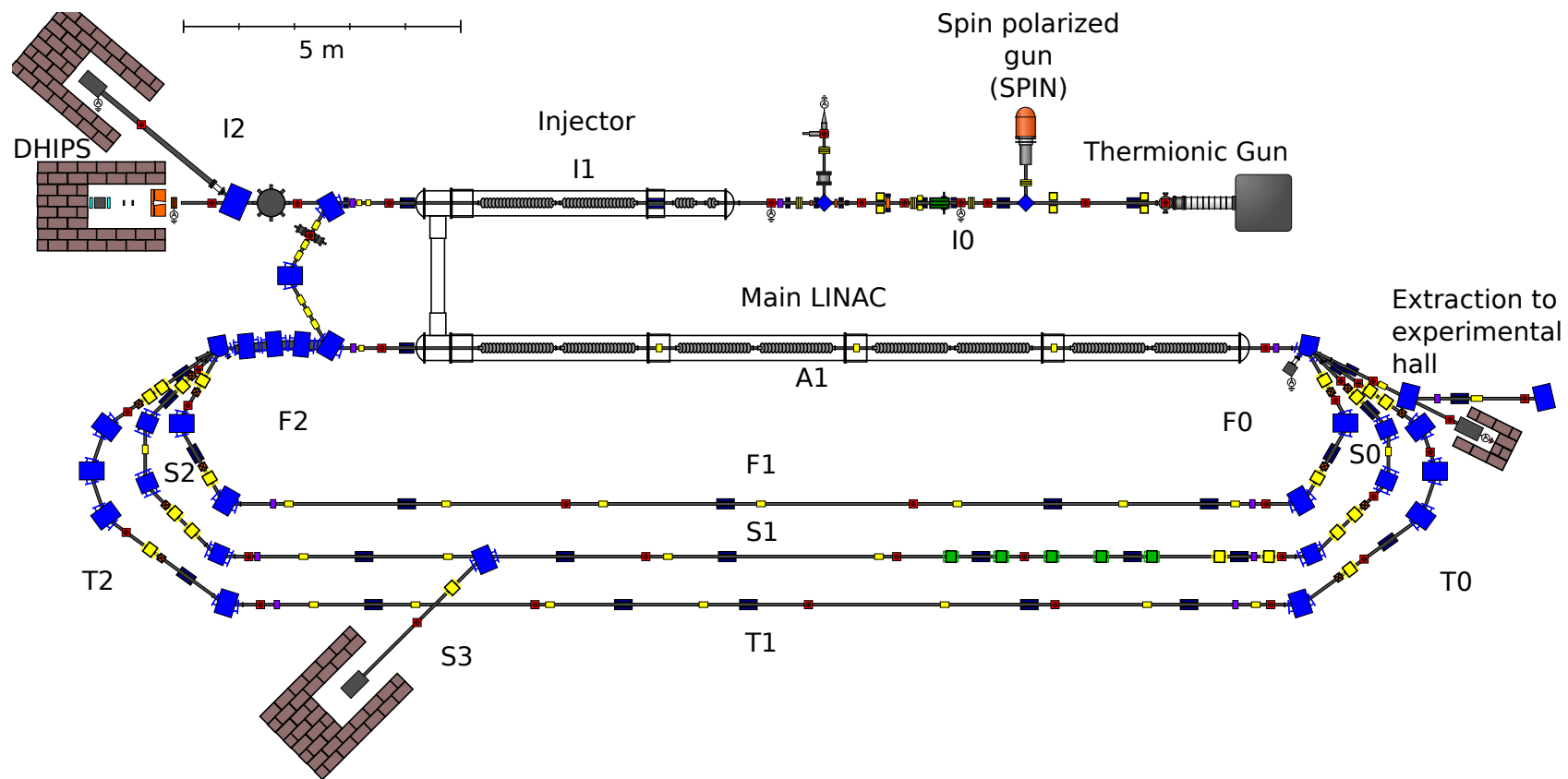


Figure 8.3.: Overview of the S-DALINAC accelerator complex. Electrons are produced by two different sources. The super-conduction *Injector* (I1) provides a beam energy of 10 MeV. The electron beam can be used for experiments at the DHIPS set-up or is guided to the *main LINAC* (A1) which allows to increase the energy up to 30.6 MeV. Three recirculation beamlines allow to achieve a total beam energy of 130 MeV.

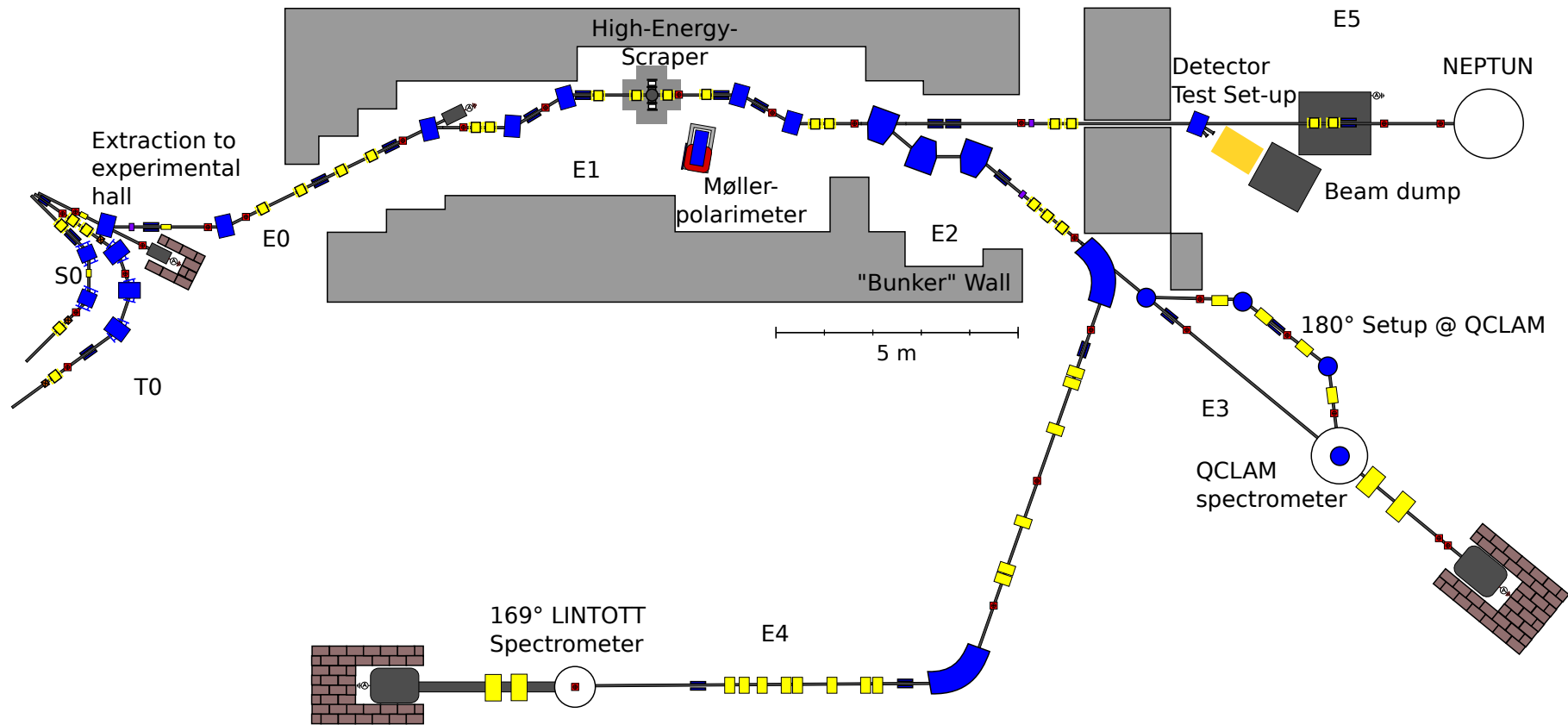


Figure 8.4.: Overview of the extraction beamline to the experiments. After the passage of a *High-Energy-Scraper-System* the electron beam is guided to either the QCLAM or LINTOTT spectrometers or the NEPTUN tagger. The *detector test set-up*, which has been installed in the context of this work, is located in front of the NEPTUN experiment. A dipole magnet allows an extraction of the electron beam to the detector test set-up. The yellow marked test-area, which is located between a dipole magnet and a beam dump, allows in future a large variety of detectors tests.

The S-DALINAC ERL is operated as an accelerator study so far. In August 2017 first ERL measurements [122] have been conducted successfully at the S-DALINAC, making it the first working ERL accelerator in Germany. The development of new beam diagnostic tools especially for the ERL operation is important. As shown in Fig. 8.2 electron bunches sit on the maxima and minima of the RF-field which is operated at 3 GHz. Therefore, bunches are separated by 167 ps. In Chapter 7, diamond and silicon based beam detector systems were introduced which can achieve a time precision below 100 ps. It is planned to use this technology for further beam diagnostic applications at the S-DALINAC in future.

8.2 Aspects of beam dynamics

The motion of a charged particle in an accelerator is determined by the *Lorentz force* which is the combination of electric and magnetic force on a point charge due to electromagnetic fields. A particle with a charge q moving with a velocity \vec{v} in an electric field E and a field with the magnetic flux density B experiences a force of:

$$\vec{F}_L = \vec{F}_E + \vec{F}_B = q(\vec{E} + \vec{v} \times \vec{B}). \quad (8.1)$$

For example an electron will be accelerated in the same linear orientation as the \vec{E} field, but will curve perpendicularly to both the instantaneous velocity vector \vec{v} and the magnetic flux density \vec{B} according to the *left-hand rule*¹. By comparing the magnitude of the electric force component \vec{F}_E with the magnetic force component \vec{F}_B , one obtains $\vec{E} \approx c\vec{B}$ for relativistic particles. This shows that for the same force resulting from a magnetic flux density of 1 T, which is technically feasible to produce, an electric field of $3 \times 10^8 \text{ V m}^{-1}$ would be required, which is technically challenging. Therefore, mainly magnets are used to deflect relativistic particles and electric fields are used mainly for acceleration. The two most common magnet types are the dipole magnet, which is used to deflect the beam on a circular orbit, and the quadrupole magnet, which is used to focus the beam.

In the following, both magnet types will be introduced. Afterwards, a short introduction into the description of a particle beam in an accelerator via the σ -matrix formalism will be given. In the end, important beam parameters like its profile and dispersion will be explained.

8.2.1 Dipole magnet

In particle accelerators, dipole magnets are used to realize bends of the particle trajectory. The field is usually generated by two coils which are wrapped around an iron yoke in order to reinforce the magnetic flux strength. The magnetic flux strength B can be calculated from the integral form of the *Ampere law*

$$\oint \vec{H} d\vec{l} = NI, \quad (8.2)$$

with $\vec{B} = \mu_r \vec{H}$. It follows for the *magnetic flux strength* in the homogeneous field of a dipole magnet

$$|\vec{B}| = \mu_0 \mu_r \cdot \frac{NI}{\mu_r l_1 + l_2}, \quad (8.3)$$

with the vacuum permeability μ_0 , the permeability of the yoke material μ_r , the electric current I , the coil winding number N , the gap-size of the yoke l_1 and the length of iron in the yoke l_r . Since in ferromagnetic material $\mu_{r,\text{yoke}} > 1000$ and $\mu_{r,\text{air}} \approx 1$ for air and vacuum in between the yoke, the equation can be simplified to

$$|\vec{B}| \approx \frac{NI\mu_0}{l_1}. \quad (8.4)$$

¹ The thumb is pointed in the direction of the motion \vec{v} of a negatively charged particle (e.g. electron). The first finger is pointed in the direction of the magnetic field \vec{B} (north to south). Then the orthogonal second finger will point in the direction of \vec{F}_L . Note: For positive particles the rules can be transferred to the right hand.

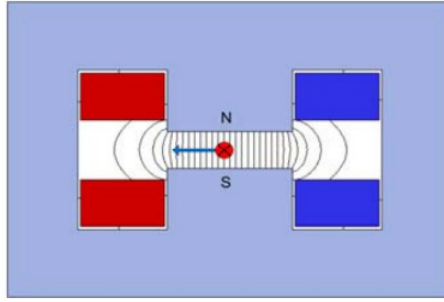


Figure 8.5.: Cross section view of a H-yoke dipole magnet. The magnetic field lines are orthogonal to the nominal beam direction. The blue arrow indicates the direction of the Lorentz force on a positive particle going into the image plane. (Taken from [123])

This holds, until saturation of the yoke material is reached. The use of iron dominated magnets is limited to approx. 1.5 T for that reason. Higher fields can be generated by *super-conducting magnets*, which will not be discussed here.

In Fig. 8.5 the dipole magnet cross section of a so-called *H-yoke* geometry is shown. In general the motion of a charged particle in a dipole magnet field will be circular in a plane perpendicular to the field and colinear to the direction of particle motion and free in the direction orthogonal to it. Thus, a particle injected into a dipole magnet will travel on a circular or helical trajectory. The *magnetic rigidity* BR can be calculated from the Lorentz force and the centripetal force

$$BR = \frac{p}{e}, \quad (8.5)$$

with the radius of curvature R for a particle of charge e and the fraction of particle momentum p perpendicular to B . From this one can deduce a useful formula which holds for an electron beam:

$$BR[\text{Tm}] \approx 3.3356p[\text{GeV}/c]. \quad (8.6)$$

As shown in Fig. 8.5, the magnetic flux density at the edges of the yokes becomes in-homogeneous. For beam dynamics calculations, an *effective length* (or *magnetic length*) is introduced in order to characterize the expansion of the field. For that, the real field is simplified by a field which has a constant value over the effective length. The boundary field of the magnet is approximated by instantaneous rising and falling edges. It describes the actual field distribution by an adjusted rectangular distribution of the length L_{eff} and the magnetic flux density B within the field is defined as a constant. In Fig. 8.6, the definition of the magnetic length is visualized. The effective length is defined in a way that the area beneath both areas is identical:

$$\int B ds = B_{\text{max}} \cdot L_{\text{eff}}. \quad (8.7)$$

A magnetic length can be defined for all magnet types and is therefore an important parameter for beam dynamics calculations.

The orientation of the orbit to the field edge of the dipole is determined by the entry and exit edge angle ψ_1 and ψ_2 . If the orbit is perpendicular to the entry and exit edge, one speaks of a sector magnet (edge angle $\psi = 0$). If the nominal path runs under a certain angle to the edges of the magnetic field, additional focusing or de-focusing effects occur in the horizontal and vertical plane. Focusing effects in a sector magnet and the definition of the edge angles are shown in Fig. 8.7.

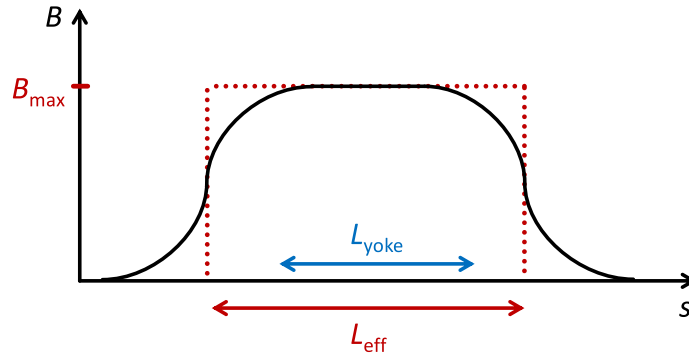


Figure 8.6.: The magnetic flux density of a magnet as a function of the location and the resulting effective length L_{eff} which is typically larger than the length of the yoke L_{yoke} .

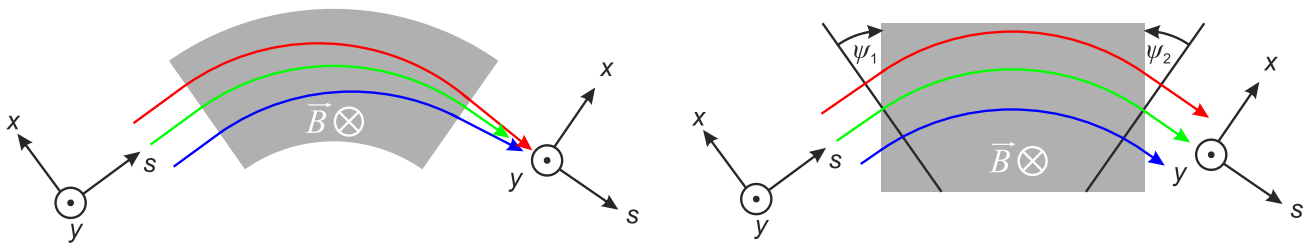


Figure 8.7.: **Left:** Focusing effects in a sector magnet for particles with the same momenta but different entry points. **Right:** Rectangular magnet and the definition of the edge angle ψ_1 and ψ_2 which are positive in this case. (Taken from [124])

8.2.2 Quadrupole magnet

In order to focus the particle beam in an accelerator, quadrupole magnets are used. They are made of a symmetric arrangement of four coils. A quadrupole magnet is always focusing in one plane while defocusing in the perpendicular plane. In Fig. 8.8, quadrupole focusing and defocusing effects are shown for a positively charged particle.

If the magnetic poles are formed hyperbolically and arranged with an angle of 45° to the horizontal and vertical planes, the components of the magnetic flux density in the plane transverse to the beam is given by

$$B_y = k \cdot x, B_x = k \cdot y, \quad (8.8)$$

with the field gradient k of the vertical component in the horizontal direction (or equivalently, the field gradient of the horizontal component in the vertical direction). The sign of k determines whether the quadrupole focuses ($k > 0$) or defocuses ($k < 0$) particles in the horizontal plane. The field gradient k can be calculated from a multipole expansion of the magnetic flux density [125]:

$$\frac{e}{p}B(x) = \frac{1}{R} + kx + \frac{1}{2!}mx^2 + \dots, \quad (8.9)$$

where the first term characterizes the *dipole*, the second term the *quadrupole* and the third term the *sextupole*, etc. It therefore follows for a pure quadrupole without any unwanted contributions from other multipole components

$$\frac{e}{p}B = kx. \quad (8.10)$$

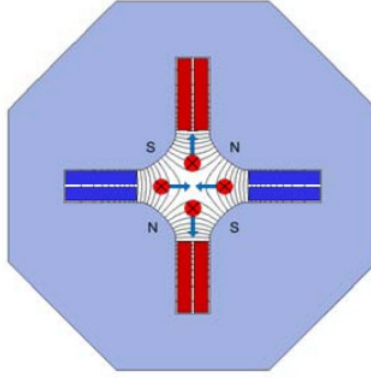


Figure 8.8.: Cross section view of a quadrupole magnet. The magnetic field lines are transverse to the nominal beam direction in the plane. The blue arrows indicate the direction of the Lorentz force on a positive particle going into the image plane. (Taken from [123])

For an electron beam one can deduce the following useful formula [114]:

$$k[\text{m}^2] \approx 0.2998 \frac{g[\text{T m}^{-1}]}{p[\text{GeV}]}, \quad (8.11)$$

where the gradient g can be calculated by

$$g = \frac{2\mu_0 NI}{r_0^2}, \quad (8.12)$$

with the winding number of the coils N , the current I , the radius of aperture r_0 and the vacuum permeability μ_0 .

Quadrupoles in the lattice¹ of an accelerator are typically of two types: so-called *F quadrupoles* (which are horizontally focusing but vertically defocusing) and *D quadrupoles* (which are vertically focusing but horizontally defocusing). If an F quadrupole and a D quadrupole are placed next to each other and the distance has been chosen correctly, the overall effect is focusing in both horizontal and vertical planes. This lattice is called an FODO cell and allows the transport of the beam over long distances. It consists of a focusing quadrupole F, a drift section with 0 fields, a defocusing quadrupole D and another length of drift section with 0 fields.

Dipole and quadrupole forces are constant or linearly dependent from the particles coordinates. Therefore, the dynamics in accelerators, which are built only from these magnets, can be described by the so-called *linear beam dynamics*, which will be presented in the next section. Non-linear forces like introduced by sextupoles or higher order magnets are not relevant for the work presented here.

8.2.3 Linear beam dynamics

In order to describe a particle trajectory in an accelerator, a moving coordinate system is introduced, where the origin is located always at the position of the reference particle and the z -axis is tangential to the reference path. Such a coordinate system is illustrated in Fig. 8.9. Usually, the individual trajectory of a beam particle is characterized with respect to the reference particle which travels on an assumed central trajectory.

¹ In accelerator physics, a magnetic lattice is a composition of electromagnets at given longitudinal positions.

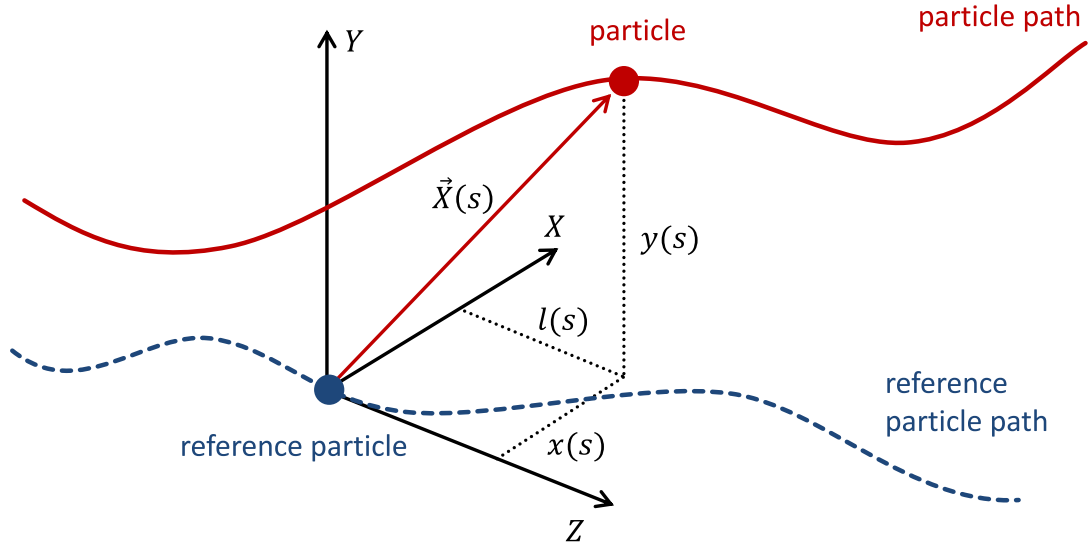


Figure 8.9.: Illustration of the moving coordinate system, where the coordinates of a particle on any path are described in relation to a reference particle on a reference path. In relation to the reference particle, the particle has the transverse coordinates $x(s)$ and $y(s)$ and the longitudinal coordinate $l(s)$.

The equations of motion of charged particles in an accelerator can be described by the *Hill's differential equations* [126]

$$x''(s) + \left(\frac{1}{R^2(s)} - k(s) \right) x(s) = \frac{1}{R(s)} \frac{\Delta p}{p_0}, \quad (8.13)$$

$$y''(s) + k(s)y(s) = 0, \quad (8.14)$$

where $R(s)$ is the bending radius, $k(s)$ the quadrupole strength and $\frac{\Delta p}{p_0}$ the relative momentum deviation to the reference particle. The solutions of the *Hill's differential equations* describe the transformation of the orbital vector by a magnetic beam guiding element and can be written in matrix form.

A full description of a beam particle in an accelerator can be represented by the six dimension vector \vec{r} , whose components are the positions, divergences and momentum of the particle with respect to the reference particle. This vector can be written in a single column matrix:

$$\vec{r} = \begin{pmatrix} x \\ x' \\ y \\ y' \\ l \\ \delta \end{pmatrix}, \quad (8.15)$$

where x and y are the horizontal and vertical displacement of the particle with respect to the reference particle on the assumed central trajectory, $x' = \frac{dx}{ds}$ and $y' = \frac{dy}{ds}$ are the particles divergences, l is the longitudinal distance and $\delta = \frac{\Delta p}{p_0}$ is the momentum deviation relative to the reference particle. For relativistic particles in an accelerator the longitudinal momentum is much larger than the transverse momenta, resulting in small divergence angles. This allows to describe transverse momenta by transverse angles, which hold as canonic coordinates. Electromagnetic influences can be described by 6×6 *transport*

matrices. In linear approximation the transformation of the particle vector \vec{r} in a magnetic lattice can be represented by a 6×6 -dimensional matrix T :

$$\vec{r}(s) = T(s)\vec{r}(0). \quad (8.16)$$

In linear beam optics, these matrices are reversible and it holds:

$$\det T = 1. \quad (8.17)$$

The matrix T has the following shape, if the horizontal and vertical components are decoupled, which is the case in a well aligned machine, and, if dipole deflection applies horizontally only, which is the case at S-DALINAC starting from injector on:

$$T = \begin{pmatrix} T_{11} & T_{12} & 0 & 0 & 0 & T_{16} \\ T_{21} & T_{22} & 0 & 0 & 0 & T_{26} \\ 0 & 0 & T_{33} & T_{34} & 0 & 0 \\ 0 & 0 & T_{43} & T_{44} & 0 & 0 \\ T_{51} & T_{52} & 0 & 0 & 1 & T_{56} \\ 0 & 0 & 0 & 0 & 0 & 1 \end{pmatrix}. \quad (8.18)$$

The traversing of several magnets and interspersing drift spaces can be described by Eq. 8.16, but T is now replaced by the product matrix $T(t) = T(n)...T(3)T(2)T(1)$ of the individual matrices of the system elements.

So far, the dynamics of individual beam particles have been considered. In accelerator and beam transport systems, the behavior of an individual particle is often of less concern than the behavior of a *bunch* of particles of which an individual particle is a member. One possibility is to describe this bunch of particles via a density distribution in the phase space. The particle ensemble can then be described by a 6×6 *beam matrix* σ . Those particles are represented in phase space by a 6-dimensional *phase space ellipsoid* which is shown in Fig. 8.10.

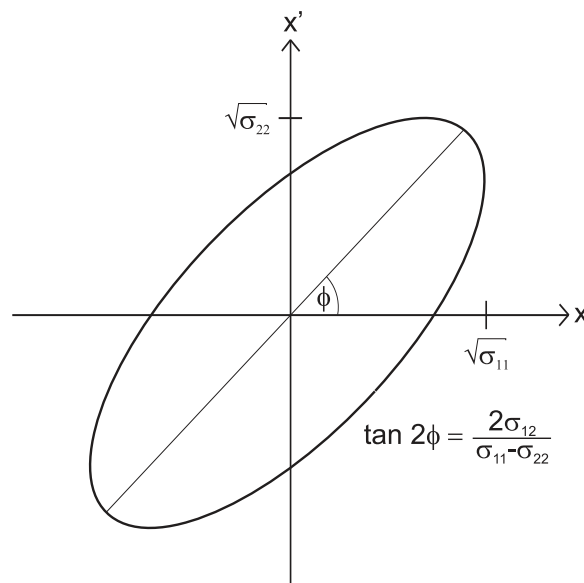


Figure 8.10.: Two dimension phase space ellipse in the x - x' -plane. The area which is enclosed by the ellipsoid is called the *emittance* ϵ_x . (Taken from [127])

For the transport of a bunch of particles, the calculations are analogous to that of a single particle. The σ -matrix corresponding to the transport matrices T is transformed via:

$$\sigma(s) = T(s)\sigma(0)T^T(s). \quad (8.19)$$

The transport matrices for a drift section T_{drift} , a dipole magnet T_{dipole} , a quadrupole magnet focusing in the x -plane $T_{\text{quad},x}$ and a quadrupole magnet focusing in the y -plane $T_{\text{quad},y}$ are given by [125]:

$$T_{\text{drift}} = \begin{pmatrix} 1 & L & 0 & 0 & 0 & 0 \\ 0 & 1 & 0 & 0 & 0 & 0 \\ 0 & 0 & 1 & L & 0 & 0 \\ 0 & 0 & 0 & 1 & 0 & 0 \\ 0 & 0 & 0 & 0 & 1 & 0 \\ 0 & 0 & 0 & 0 & 0 & 1 \end{pmatrix}, \quad (8.20)$$

$$T_{\text{dipol}} = \begin{pmatrix} \cos \frac{L_{\text{eff}}}{R} & R \sin \frac{L_{\text{eff}}}{R} & 0 & 0 & 0 & R(1 - \cos \frac{L_{\text{eff}}}{R}) \\ -\frac{1}{R} \sin \frac{L_{\text{eff}}}{R} & \cos \frac{L_{\text{eff}}}{R} & 0 & 0 & 0 & \sin \frac{L_{\text{eff}}}{R} \\ 0 & 0 & 1 & L_{\text{eff}} & 0 & 0 \\ 0 & 0 & 0 & 1 & 0 & 0 \\ -\sin \frac{L_{\text{eff}}}{R} & -R(1 - \cos \frac{L_{\text{eff}}}{R}) & 0 & 0 & 1 & \frac{L_{\text{eff}}}{\gamma_0^2} - R(\frac{L_{\text{eff}}}{R} - \sin \frac{L_{\text{eff}}}{R}) \\ 0 & 0 & 0 & 0 & 0 & 1 \end{pmatrix}, \quad (8.21)$$

$$T_{\text{quad},x} = \begin{pmatrix} \cos \Omega & \frac{1}{\sqrt{|k|}} \sin \Omega & 0 & 0 & 0 & 0 \\ -\sqrt{|k|} \sin \Omega & \cos \Omega & 0 & 0 & 0 & 0 \\ 0 & 0 & \cosh \Omega & \frac{1}{\sqrt{|k|}} \sinh \Omega & 0 & 0 \\ 0 & 0 & \sqrt{|k|} \sinh \Omega & \cosh \Omega & 0 & 0 \\ 0 & 0 & 0 & 0 & 1 & \frac{L_{\text{eff}}}{\gamma_0^2} \\ 0 & 0 & 0 & 0 & 0 & 1 \end{pmatrix}, \quad (8.22)$$

$$T_{\text{quad},y} = \begin{pmatrix} \cosh \Omega & \frac{1}{\sqrt{k}} \sinh \Omega & 0 & 0 & 0 & 0 \\ \sqrt{k} \sinh \Omega & \cosh \Omega & 0 & 0 & 0 & 0 \\ 0 & 0 & \cos \Omega & \frac{1}{\sqrt{k}} \sin \Omega & 0 & 0 \\ 0 & 0 & -\sqrt{k} \sin \Omega & \cos \Omega & 0 & 0 \\ 0 & 0 & 0 & 0 & 1 & \frac{L_{\text{eff}}}{\gamma_0^2} \\ 0 & 0 & 0 & 0 & 0 & 1 \end{pmatrix}, \quad (8.23)$$

with $\Omega = \sqrt{|k|}L_{\text{eff}}$, the length of the drift section L , the magnetic length L_{eff} and the Lorentz factor γ_0 .

The size of the physical space volume describes the expansion of the ensemble and can be represented by the *emittance* ϵ which is, graphically, the area enclosed by the phase space ellipsoid (see Fig. 8.10). It is an important beam quality parameter and can be calculated by:

$$\epsilon = \sqrt{\det \sigma}. \quad (8.24)$$

Often, beam transport simulation software is based on the σ -matrices approach which allows a resource-saving calculation of the beam dynamics for an accelerator.

8.2.4 Beam profile

An important parameter of a particle beam is its profile. For example, in x -direction the beam profile can be described by the one dimensional density distributions $\rho(x)$. Typically, the real density distribution can be approximated by a *Gaussian distribution* [126]:

$$\rho(x) = \frac{1}{\sqrt{2\pi}\sigma_x} \exp\left(-\frac{x^2}{2\sigma_x^2}\right). \quad (8.25)$$

In Fig. 8.11, the standard deviation σ_x ¹ of a *Gaussian* beam density distribution is shown. In this case the parameter is used to characterize the beam expansion. The matrix element σ_{11} (see also Fig. 8.10) is identified with the standard deviation σ_x ,

$$x_{max} = \sigma_x = \sqrt{\sigma_{11}}. \quad (8.26)$$

A beam profile can be approximated in the regime of $-\sigma_x \leq x \leq +\sigma_x$ using Eq. 8.25. Typically, the beam is surrounded by a so-called *beam halo*, which consists of a cloud of particles, with strong deviations from the reference particle. The particle distribution for $x > |3\sigma_x|$ can therefore differ from a *Gaussian* one significantly [126].

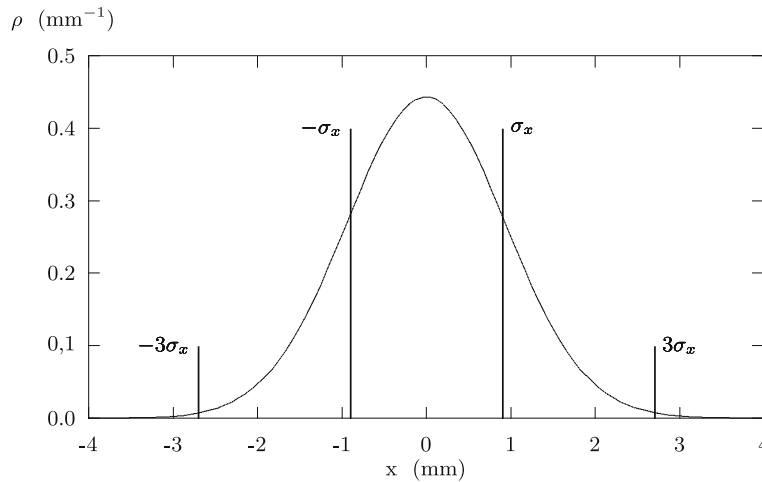


Figure 8.11.: *Gaussian* density distribution of a beam profile in x -direction. The value of σ_x is used in order to characterize the beam size. (Taken from [126])

8.2.5 Beam dispersion

Typically beam particles inside a bunch do not have exactly the same momenta. By a passage through a dipole magnet this momentum spread will lead to a dispersion of the beam. The trajectories of beam particles with lower momentum are deflected more than those of particles with higher momentum. This effect is schematically shown in Fig. 8.12. The *dispersion function* $D(s)$ can be calculated by [126]:

$$D(s) = \frac{\Delta x(s)}{\Delta p(s)/p_0}, \quad (8.27)$$

where $x(s)$ is the horizontal distance to the reference particle, $p(s)$ its momentum and $p(0)$ the momentum of the reference particle. The dispersion is given in the units of $1 \text{ mm}\%^{-1}$ which means the beam

¹ Note: The symbol σ is used two times, for the beam matrix and the standard deviation. One has to deduce the correct meaning from the context.

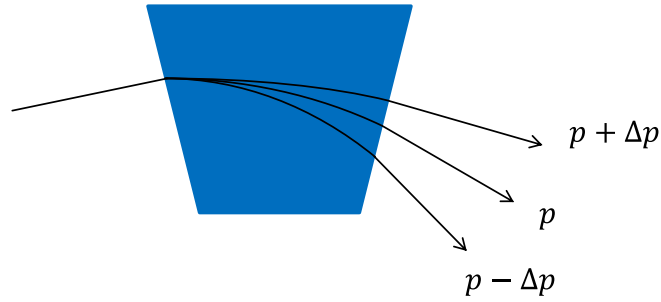


Figure 8.12.: Visualization of the transverse dispersion caused by a dipole magnet.

has accumulated a transverse distance of 1 mm from the reference trajectory due to a momentum offset of 1 % with respect to the reference particle. By choosing certain dipole and quadrupole settings, dispersion functions can be defined accordingly. In particular, so-called *achromatic settings* ($D = 0$, $D' = 0$) are chosen at S-DALINAC for all areas facing in long straight sections, like the linac or recirculations. On the other hand, at the position of scraper systems, D is maximized to enlarge energy definition.

8.3 Construction of a multi-purpose detector test set-up at the S-DALINAC

One goal of this work was constructing a multi-purpose detector test set-up [128, 129] in the E5 section of S-DALINAC, in between the high energy scraper system and the NEPTUN experiment (see Fig. 8.4). An additional pair of quadrupoles and a dipole magnet was installed into the beamline including a dedicated beam dump. Between dipole magnet and beam dump an area of about 2 m^2 can be used to locate detectors for tests with an electron beam. In Fig. 8.13, a technical drawing of the area is shown. The E5 beamline is divided by a concrete wall into two areas. Namely, the E5-"Bunker" area on its left side and the E5-"kleine Halle" area on its right side. It is obvious that the space constraints limit the positioning of new beamline elements. A major condition is, that the new detector set-up should not deteriorate the beam properties of the NEPTUN experiment which is located further downstream. On the contrary, in this work it has been shown that the focusing capability could even be improved. A further requirement was the flexibility of the detector test set-up. It should be possible to clear the area after the exit window including the beam dump within a short time in case the space is needed. The old separation dipole magnet of the twice recirculating S-DALINAC version had to be replaced by a new magnet in order to meet the requirements of the additional recirculation. Therefore, the old magnet

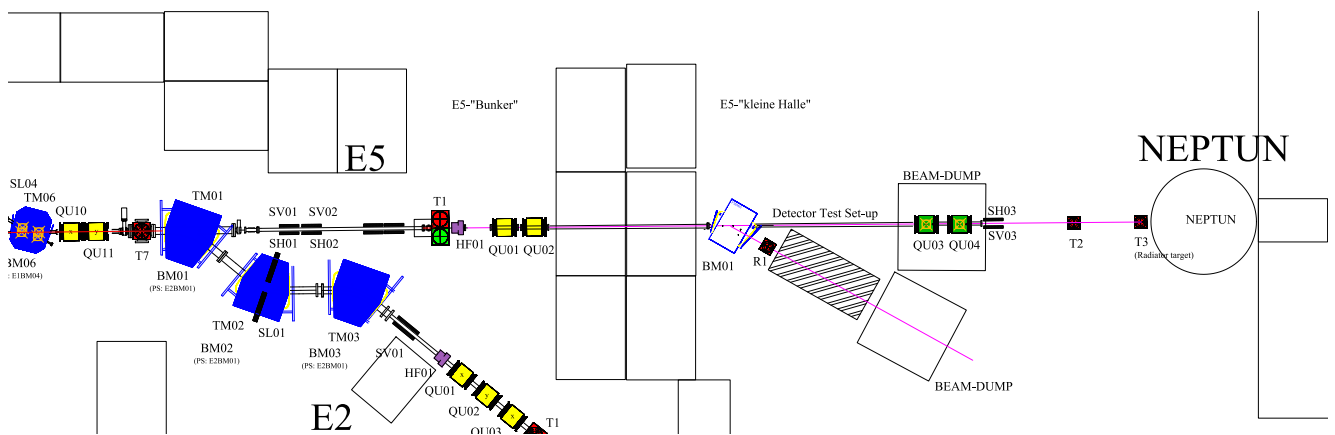


Figure 8.13.: Overview plan of the E5 section. An additional pair of quadrupoles (E5QU01, E5QU02) is installed in the E5-"Bunker" area. A dipole magnet (E5BM01) and a beam dump is installed in E5-"kleine Halle" in front of the NEPTUN experiment. Detector tests can take place in the gray shaded area between the dipole magnet and a beam dump.

has been reused as a deflecting magnet for the new test set-up. Furthermore, two spare quadrupoles have been available, which have been placed in front of the dipole in order to give more flexibility in focusing the beam on the detectors.

In the following, the design, installation and commissioning of the detector test set-up will be described. The results of beam transport simulations and the construction of a new vacuum chamber for the dipole magnet will be shown. Finally, the installation, alignment and the commissioning of the beam elements will be covered.

8.3.1 Beam transport simulations

The lattice from the extraction of the S-DALINAC to the NEPTUN experiment and to the detector test set-up was simulated [117] using the XBEAM software [130, 131]. The software is based on the σ matrices approach in order to allow a fast calculation of linear beam optics. A detailed description of the physical concepts can be found in Section 8.2.3. All following simulations have been carried out with electron beam energy of 130 MeV. For lower energies all fields need to be scaled down with the same factor (e.g. $E/130$ MeV). In Table 8.2 the simulation parameters are summarized. The lattice of beam elements has been modeled from the S-DALINAC extraction through the high energy scraper system up to the NEPTUN experiment. The simulations of the beam envelope must fulfill certain conditions. On the one hand, the beam envelope should fit the beam tube at every position which typically has a diameter of 30 mm at every point. Ideally, the beam envelope inside the beam pipe should be kept below 2 mm. On the other hand the beam envelope should be able to be focused at the position of the NEPTUN radiator foil and the detector test set-up.

Table 8.2.: Parameters used for the X-BEAM beam transport simulations.

Beam energy	130 MeV
Quadrupole effective magnetic length (green)	0.1959 m
Quadrupole effective magnetic length (yellow)	0.1958 m
Dipole effective magnetic length	0.1836 m
Dipole deflecting angle	34.56°
Dipole entrance angle	11.01°
Dipole exit angle	-4.25°

In the past, two pairs of quadrupoles, which are separated by a long distance of about 10 m, have been used to focus the beam on the NEPTUN radiator target [132]. In Fig. 8.14 the simulated beam envelope of the 1σ -regime is shown for the x - and y -directions for the original lattice configuration. In order to allow focusing of the beam at the position of the new detector set-up, two additional quadrupoles have been installed in between the two existing pairs. Now these two pairs of quadrupoles can be used to increase the focusing capability on the NEPTUN radiator as well. The simulation of the resulting lattice is shown in Fig. 8.15. The additional quadrupoles allow to improve the focusing capability for the NEPTUN experiment. On the entire route, the beam envelope $\sigma_{x,y}$ is below 0.2 mm. This also applies to the position of the dipole magnet, since the yoke and the vacuum chamber limit the beam pipe height constructional to 23 mm.

In Fig. 8.16, the simulated beam envelope from the main linac extraction to the detector test set-up is shown. The beam envelope should also be as small as possible at the test site. With the help of the two quadrupoles which are located in front of the dipole a minimum beam size of $\sigma_{x,y} = 0.1$ mm is expected to be realized.

The dipole magnet will cause a dispersion of the beam at the position of the test location. The expected transversal dispersion of about $5 \text{ mm} \%^{-1}$ is not crucial for detector tests, as $\Delta E/E$ is much smaller than 10^{-3} .

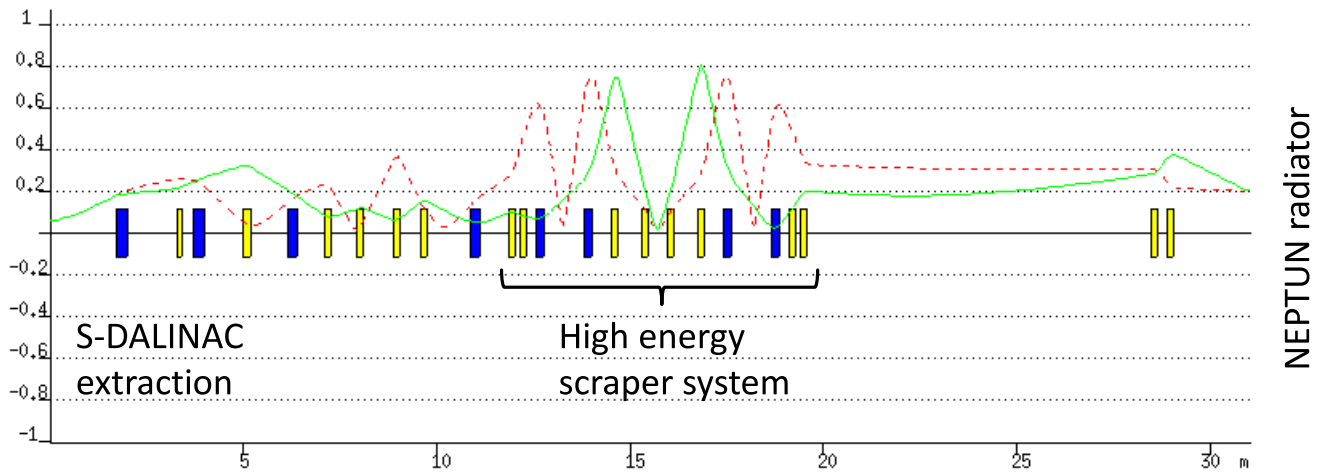


Figure 8.14.: Beam dynamics calculations for the NEPTUN beamline, from the main linac extraction to the NEPTUN radiator, using the original lattice. The dashed red line shows the 1σ beam envelope in x -direction, the solid green line in y -direction, both in mm. Dipole magnets are shown in blue, quadrupole magnets are shown in yellow.

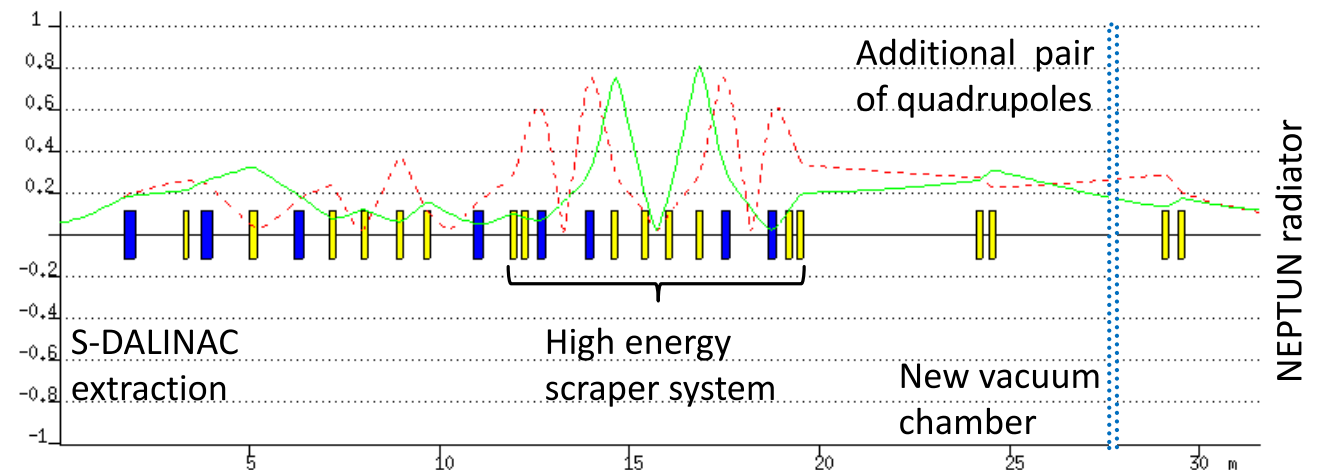


Figure 8.15.: Beam dynamics calculations for the NEPTUN beamline, from the main linac extraction to the NEPTUN radiator with an additional pair of quadrupoles. The dashed red line shows the 1σ beam envelope in x -direction, the solid green line in y -direction, both in mm. The vertical blue lines indicate the position of a new vacuum chamber which limits the beam tube height to 29 mm. The focusing properties for the NEPTUN experiment are significantly improved.

8.3.2 Dipole magnets, quadrupole magnets and power supplies

The separation dipole magnet of the twice recirculating version of the S-DALINAC is used to deflect the beam to the new detector test set-up. Important parameters are summarized in Table 8.3. A DANFYSIK SYSTEM 9000 power supply is available and can be used to power the dipole magnet. It can deliver a maximum voltage of 60 V with a current of 160 A. The dipole magnet was constructed with a maximum deflecting angle of 60° for 130 MeV electrons and a coil current of 182 A. Consequently, with 160 A, which can be provided by the power supply, a maximum bending angle of 52.7° can be realized.

A dedicated support structure has been designed and manufactured in order to allow an adjustment of the dipole magnet. The total weight of the dipole sits on three screws with embedded ball bearings which allow an adjustment of the height. The horizontal and vertical axes of the dipole magnet can be adjusted via adjustment screws which are mounted on the side and push the magnet in the desired

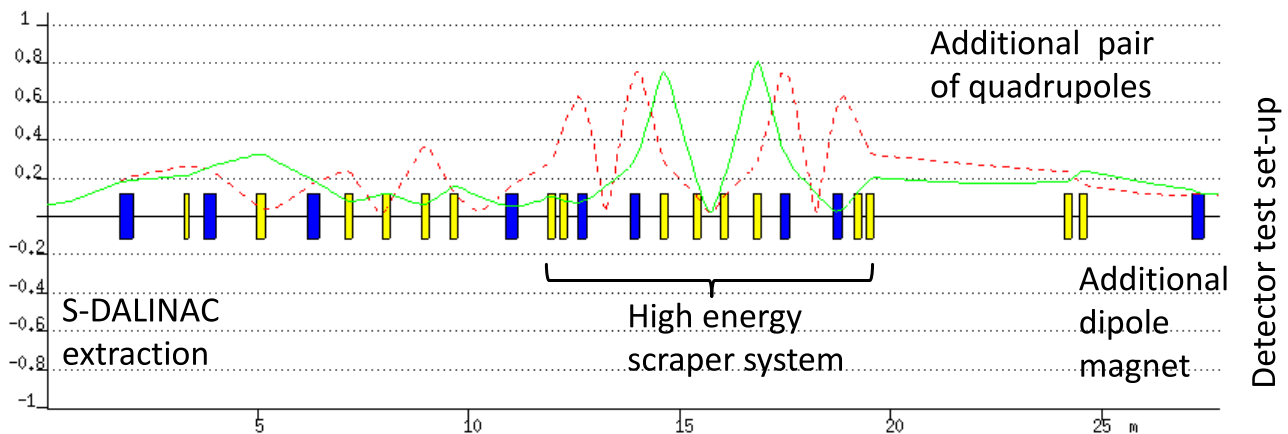


Figure 8.16.: Beam dynamics calculations from the main linac extraction to the detector test set-up. The beam is focused 15 cm downstream from the exit window. The dashed red line shows the 1σ beam envelope in x -direction, the solid green line in y -direction, both in mm. Dipole magnets are shown in blue, quadrupole magnets are shown in yellow.

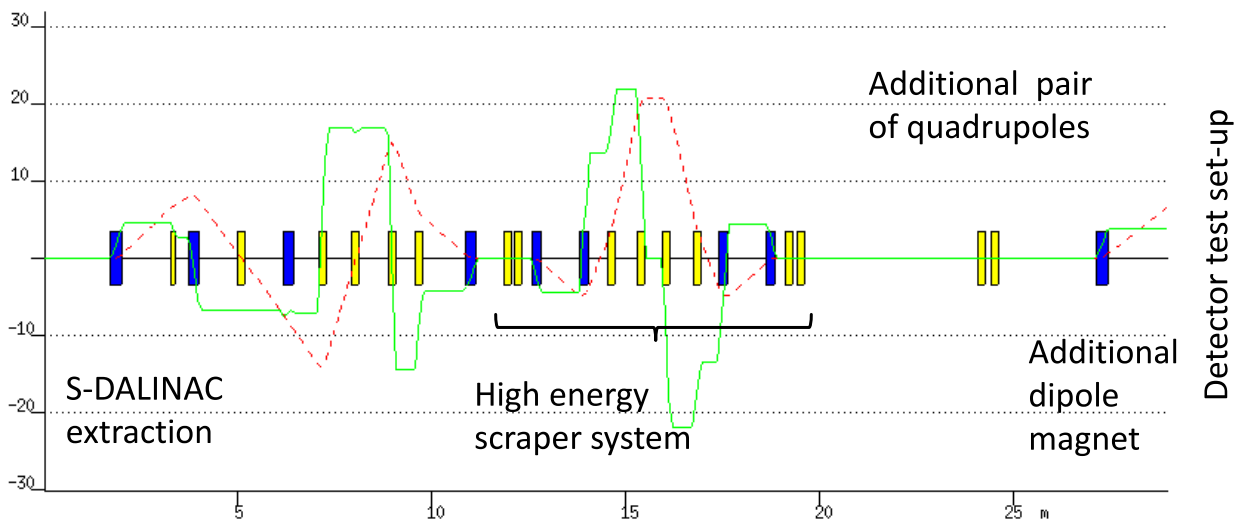


Figure 8.17.: Beam dynamics calculations of the beam dispersion from the main linac extraction to the detector test set-up. The dispersion $D(T_{16})$ is shown in red and is given in $\text{mm}\%^{-1}$. The angular dispersion, in $\text{mrad}\%^{-1}$, is shown in green.

direction. The schematic drawing of the complete support structure is shown in Fig. 8.18. The detailed technical drawings of all sub parts can be found in Appendix A.2-A.6.

8.3.3 Vacuum chamber

Initially it was planned to reuse the vacuum chamber of the twice recirculating S-DALINAC which was already mounted inside the dipole magnet. A photograph of this chamber is shown in Fig. 8.19. On closer inspection, it was found that the 0° -beamline, which should direct the beam to the NEPTUN experiment, only has an inner diameter of 15 mm. This could be problematic for the NEPTUN experiment because a beam halo, which could eventually hit the beam pipe, would significantly increase the signal to background noise ratio in the experiment. For this reason, a new chamber has been designed in order to maximize the aperture of the 0° -beamline.

In order to design a new vacuum chamber, the dipole magnet and the original chamber has been remodeled in CAD software [133, 134]. Necessary information of the dimensions has been taken from the

Table 8.3.: Physical parameters of the dipole magnet.

Naming convention	E5BM01
Pole gap	30 mm
Original deflecting angle	max. 60°
Original entrance angle	16.1°
Original exit angle	-18.6°
New deflecting angle	max. 49.8°
New entrance angle	11.0°
New exit angle (34.6°-beamline, $R = 304$ mm)	-4.3°
New exit angle (49.8°-beamline, $R = 400$ mm)	11.0°
Maximal voltage	12 V
Maximal current	190 A
Total weight	250 kg

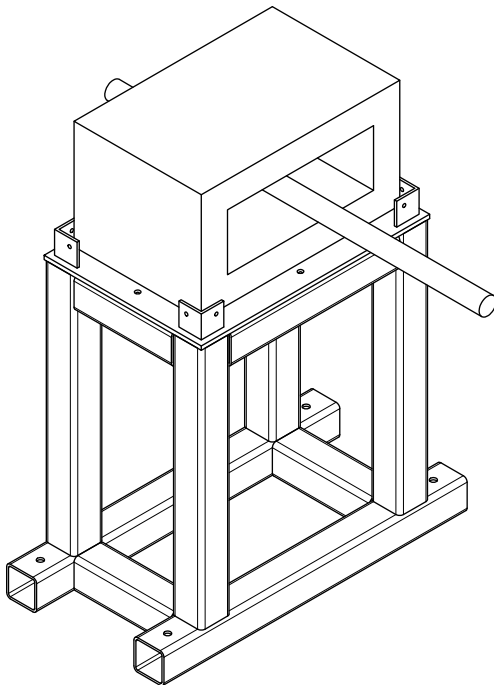


Figure 8.18.: Schematic drawing (left) and photograph (right) of the support structure for the dipole magnet. The construction allows an alignment of the dipole with the help of several adjustment screws. Detailed technical drawings of all sub parts can be found in Appendix A.2-A.6.

original technical drawings and missing ones have been measured. For the construction of new bending angles, the geometry of the magnetic field has to be known precisely. The CAD drawing in Fig. 8.20 (left) shows the yoke geometry, the magnetic field and the three beamlines for which the magnet was originally designed. The effective magnetic field was reconstructed from the original drawings. It is limited by two lines which are parallel to the yoke edges. By knowing the field geometry new bending angles have been defined. In order to maximize the beam tube diameter of the 0°-beamline, the new 0°-beamline had to be moved downwards 5 cm and rotated by about 5° with respect to the original 0°-beamline. The beamline which will be used for the detector test set-up has been for construction and space limitation reasons chosen to be 34.56° ($R = 400$ mm). An additional third beamline with a deflection angle of 49.81° ($R = 304$ mm) can be used in order to guide the beam to a second test area for possible future

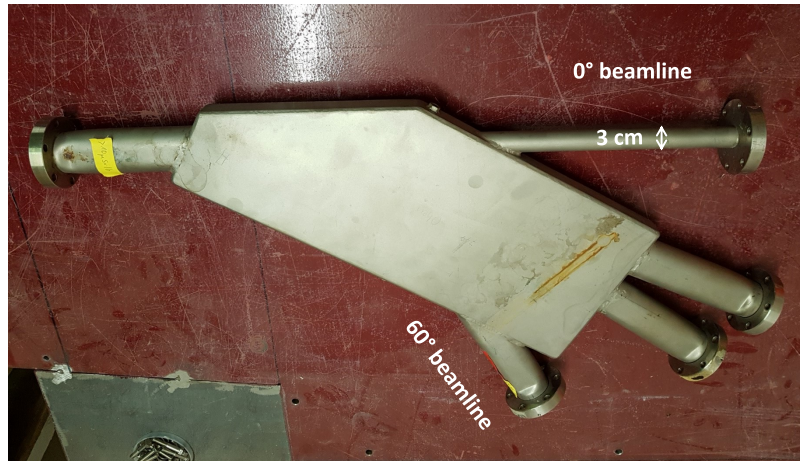


Figure 8.19.: Vacuum chamber of the twice recirculating S-DALINAC. The entrance beamline is visible on the right. The inner diameter of the exit-beamline which was dedicated to guide the beam to the NEPTUN experiment is only 15 mm.

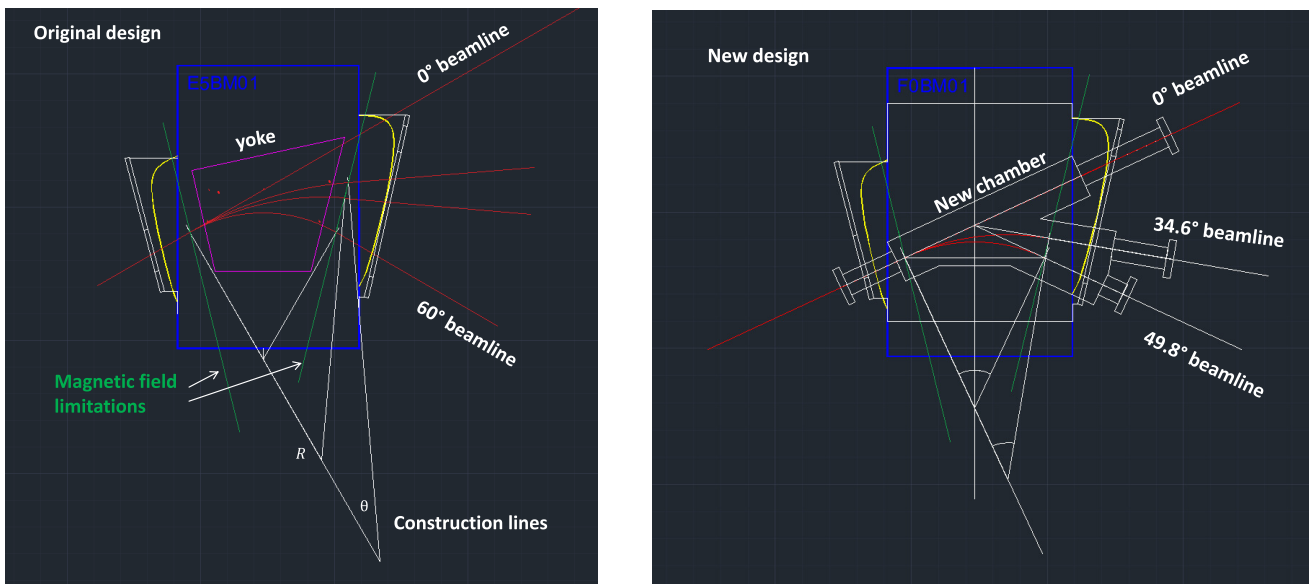


Figure 8.20.: **Left:** Reconstruction of the original deflecting angles in order to determine the magnetic field limitations, since they are essential in order to construct new deflection angles. **Right:** Construction of new deflection angles and design of a new vacuum chamber. More detailed drawings can be found in Appendix A.7-A.10.

applications. The final construction of the vacuum chamber is shown in Fig. 8.20 (right). More detailed technical drawings of the vacuum chamber can be found in Appendix A.7-A.10.

8.3.4 Exit window

The detector tests will take place in the space between the vacuum chamber and the beam dump. It should be possible to conduct tests under normal air pressure while the beam is extracted through a window and the detectors-under-test are placed behind it. This offers greatest flexibility on positioning and placing of *devices under test* (DUT). For that an exit window was made of aluminum with a thickness of 300 μm . It is installed instead of a gasket between two CF-40 flanges. A photography of the exit window is shown in Fig. 8.21, the corresponding technical drawing can be found in Appendix A.11.

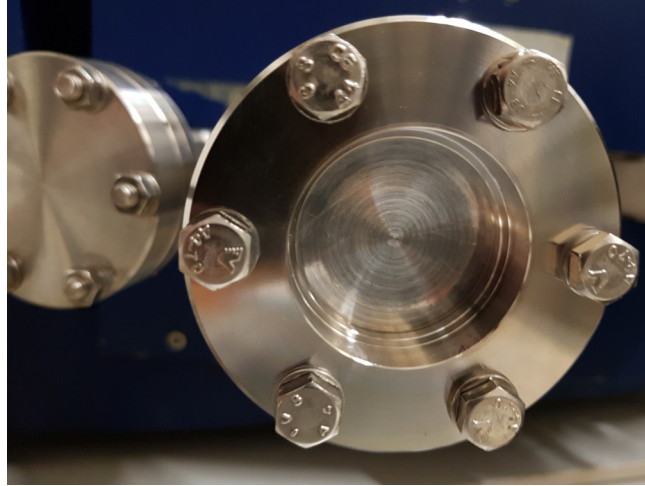


Figure 8.21.: Exit window made of aluminum with a thickness of $300\ \mu\text{m}$ which is installed instead of a gasket between two CF-40 flanges.

For most of the tests the beam size behind the exit window should be as small as possible. In Fig. 8.16 a minimum beam size of $\sigma_{x,y} = 0.1\ \text{mm}$ is visualized for a beam which is totally guided in vacuum. The beam extraction through an exit window and transport through air will cause an additional spreading of the beam.

A charged particle traversing a medium is deflected by many small-angle scatterings which are mainly caused due to Coulomb scattering with nuclei [6]. The deflection angle θ_{CS} of the beam can be calculated by [6]

$$\theta_{\text{CS}} = \frac{13.6\ \text{MeV}}{\beta c p} Z \sqrt{x/X_0} (1 + 0.038 \ln(x/X_0)), \quad (8.28)$$

where p , βc and Z are the momentum, velocity and charge number of the incident particle, the thickness of the scattering medium is given in radiation length x/X_0 . For an assumed electron beam momentum of $130\ \text{MeV}/c$ and an exit window thickness of $300\ \mu\text{m}$, which is assumed to be hit by the electron beam perpendicularly, a deflection angle of $\theta_{\text{CS},300\ \mu\text{m}} = 0.22^\circ = 3.8\ \text{mrad}$ can be calculated.

For detector tests a beam widening is not crucial since this allows to illuminate a larger area of the DUT with the beam. Nevertheless, for future experiments it is planned to exchange the exit window with a thinner one, e.g. a titanium foil with a thickness of about $35\ \mu\text{m}$.

8.3.5 Test set-up

Behind the exit window a total length of 1 m is available for any kind of detector tests. In Fig. 8.22 the test set-up is shown. It is possible to move the beam dump further downstream in order to gain more space. But for radiation safety reasons it must always be guaranteed that the beam will hit the entrance hole of the beam dump. For silicon and diamond detector tests, which were introduced in Chapter 7, a table will be mounted between exit window and beam dump. The *devices under test* (DUT) will be installed on linear-tables which can be operated remotely. This allows an alignment and the irradiation of different parts of the detector without touching the beam parameters. An example of such a set-up is shown in Fig. 8.23.

8.3.6 Beam dump

Behind the experimental area the electron beam has to be stopped in a controlled way. A beam dump, which was initially planned for [135, 136], is used for this purpose. The beam dump was originally designed in order to dump an $130\ \text{MeV}$ electron beam with a current of up to $20\ \mu\text{A}$, which results in a maximal dissipated heat load of $2.6\ \text{kW}$.



Figure 8.22.: Side (left) and top view (right) of the multi-purpose detector test set-up. Any kind of detectors can be placed between the dipole chamber exit window and the beam dump.

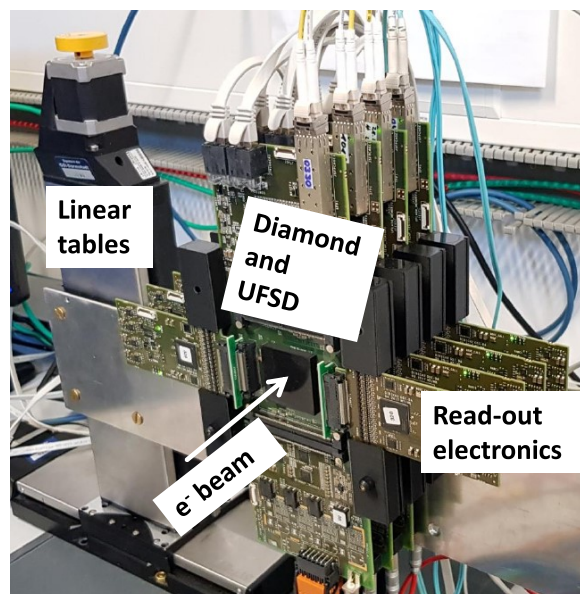


Figure 8.23.: Example set-up for silicon and diamond detector tests. The sensors are arranged in a telescope which is mounted on a linear-table. A remote control of the linear-stages allows an alignment and the irradiation of different parts off the detector without touching the beam parameters.

In Fig. 8.24 the structure of the beam dump is schematically shown. The beam dump consists of a cubic core of aluminum with an edge size of 30 cm. The core is surrounded by lead in order to shield high energetic gamma rays which are generated by *Bremstrahlung*. An outer layer of polyethylene is used to shield the detector test set-up and the NEPTUN experiment from neutrons. In order to keep back scattered electrons inside the beam dump a counter voltage of 200 V can be applied. Aluminum has the advantage that it is only slightly activated by the electron beam and has only a low neutron production rate at the used beam energies. In addition, the thermal conductivity of aluminum with $2.37 \text{ W cm}^{-1} \text{ K}^{-1}$ [137] is high, from which the heat dissipation will benefit. In addition, it is possible to cool the core with a water-cooling-system. The materials used are designed to withstand a maximal temperature of 200 °C. In [136] it has been estimated that due to the high weight of 2.8 t a temperature

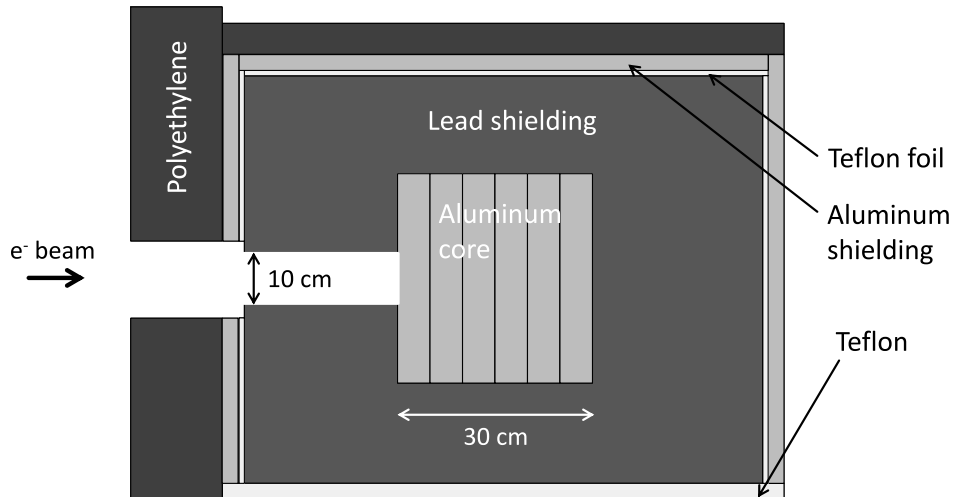


Figure 8.24.: Schematic view of the beam dump. The diameter of the entrance hole is 10 cm.

rise of 20 K is expected if the beam dump is irradiated by a 130 MeV electron beam with a current of $20 \mu\text{A}$ for 1 h.

For diamond or silicon based beam detector tests, beam currents of several nanoamperes are considered. Therefore, a water-cooling of the core is not needed. The diameter of the entrance hole is 100 mm. In the case the beam tests are planned in air, the beam will be widened due to the exit window (see also section 8.3.4), the air and the DUT material. Due to the low beam currents, however, the expansion does not need to be considered further. Nevertheless, for safety reasons, the beam dump should be located as close as possible behind the DUT. For experiments with higher beam currents, the beam expansion due to the exit window, the air and the DUT material must be examined in detail and the results have to be agreed with the *Radiation Safety Department* of the S-DALINAC. In the case beam tests will be performed in vacuum a beam size of $\sigma_{x,y} = 0.1 \text{ mm}$ (see Appendix A.4) is expected at the entrance of the beam tube, which is placed 125 cm behind the exit of the dipole magnet vacuum chamber.

8.4 Installation and alignment of beam elements

A precise alignment of the beam elements is important in order to ensure that the beam is always kept in the middle of the beam pipes. Especially the alignment precision of the vacuum chamber inside the dipole magnet should be below 1 mm. The alignment of the beam elements was done with the help of two *Bosch GLL 3-80* line-lasers. They can be operated in a self-leveling mode with a precision of 0.2 mm m^{-1} [138]. In the E5-"Bunker" area, alignment marks for the horizontal and vertical beam axis are available [139]. The alignment process of two quadrupoles, with the help of a line-laser and reference-marks, is shown in Fig. 8.25. The quadrupole magnets are mounted on support structures which allow an alignment in all three directions with the help of adjustment screws.

In order to allow a precise alignment of the vacuum chamber inside the dipole magnet the course of the 0° - and the 35° -beamlines have been marked on the upper side of the magnet. As shown in Appendix A.9, the same beam axes have been marked on the vacuum chamber by the manufacturer. The alignment of the chamber inside the magnet can be done with the help of two line-lasers. The alignment process is illustrated in Fig. 8.26. The coordinates of the reference beamlines, which are useful for an alignment, are shown in Appendix A.8.

For the alignment of the horizontal beam axis, a beam height reference mark in the E5-"Bunker" area was used [139]. The mark was transferred with the help of a line-laser to the E5-"kleine Halle" area. In order to minimize the leveling error of the line-laser, the device was rotated around its axis and the height for each rotation setting was marked on the wall. The mean value is marked by a circle. Several new height marks have been affixed in the E5-"kleine Halle" area. This height measurement is within 1 mm in agreement with a measurement carried out by a height gauge in 2016 [140]. The dipole magnet and

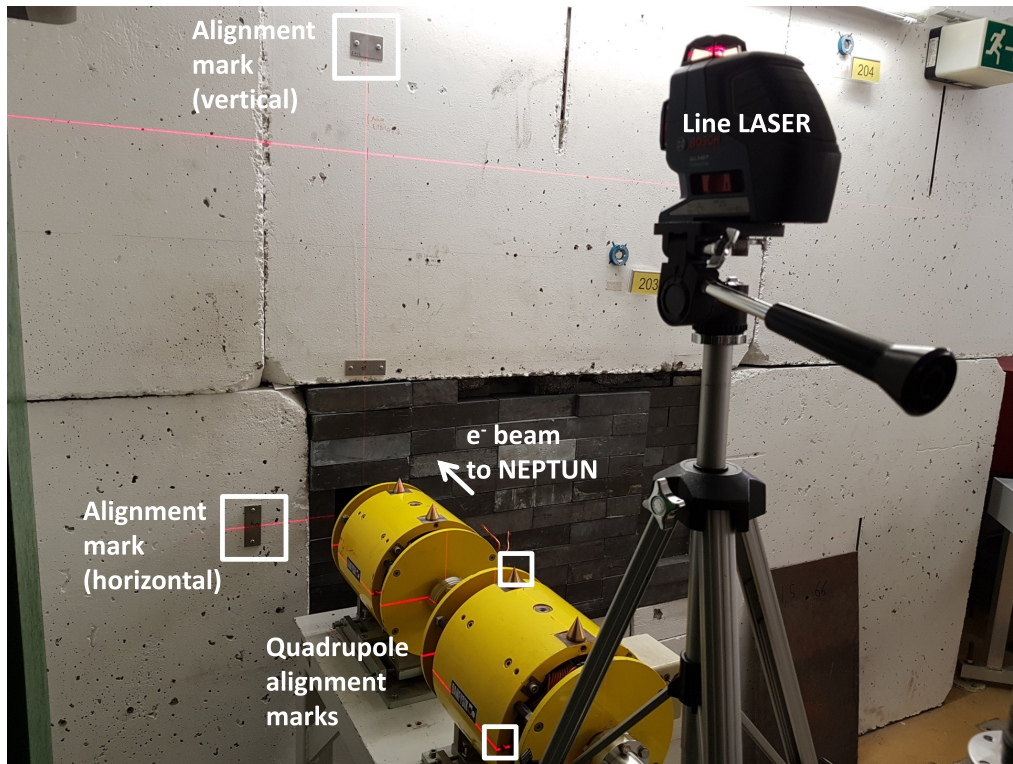


Figure 8.25.: Alignment of quadrupoles (E5QU1, E5QU2) in the E5-"kleine Halle" area with the help of a line-laser.

the two quadrupole magnets in the E5-"kleine Halle" have been adjusted with respect to the new laser marks. The height to the center of the beam pipe in the E5-"kleine Halle" area is about 94 cm.

The alignment of the vertical axis in the E5-"kleine Halle" was done with two alignment marks which have been prepared by the NEPTUN group [141]. The position of the marks are shown in Fig. 8.26.

8.5 Commissioning of the detector test set-up

Shortly before the completion of this work, the detector test set-up has been put into operation and a first electron beam was successfully extracted. The main task was to perform the function test of all beamline elements and the *machine safety system*. Another important part was the commissioning of the dipole magnet and the evaluation of the beam quality at the new detector test set-up and at the NEPTUN experiment.

The functionality of all beam elements was tested in so-called *dry runs*. For this, the magnets were operated without a beam in order to check the dipole magnet water-cooling system and the polarity of all installed magnets. Also, the correct operation of *fast closing safety valves* was checked which are important parts of the *machine safety system*.

For the commissioning of the beamlines several BeO targets are available. They can be moved pneumatically into the beam and monitored with the help of a CCD-camera. The overview map in Fig. 8.13 indicates the position of the targets. The E5T1 target is located in front of the new quadrupole doublet in the E5-"Bunker" area. The E5T2 target is located about 1.5 m in front of the NEPTUN radiator.

For the commissioning of the new beamline a BeO target (E5R1) with a diameter of 3 cm was mounted about 10 cm behind the exit window (see Fig. 8.27). The target was aligned with the help of a line-laser. A CCD-camera which is mounted in a lead brick can be used to observe the beam.

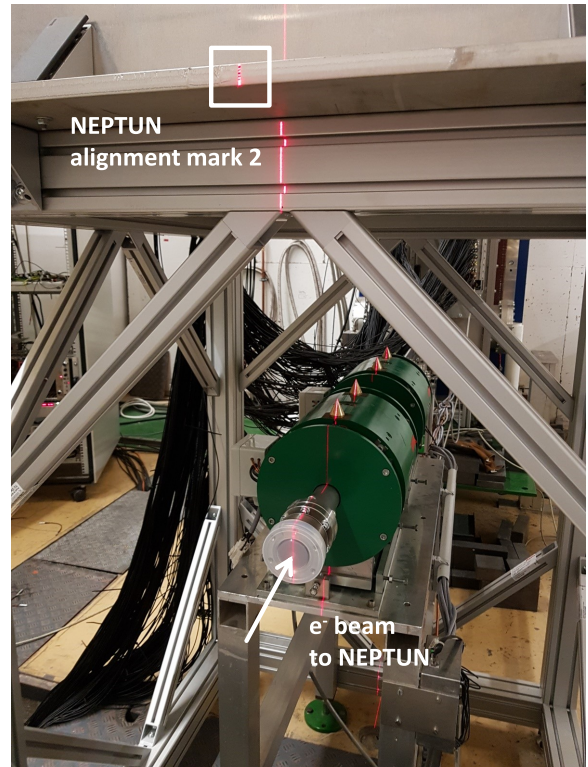
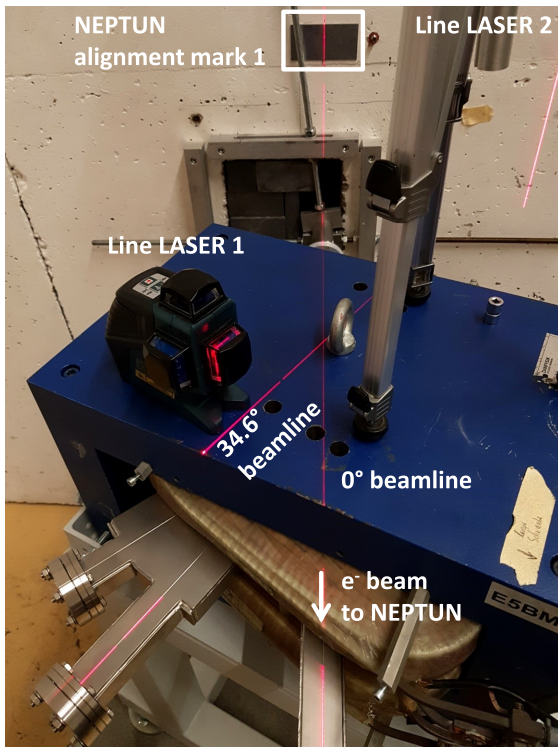


Figure 8.26.: Left: Vertical alignment of the vacuum chamber and dipole magnet (E5BM01) with the help of two line-lasers. Right: Vertical alignment of two quadrupoles (E5QU3, E5QU4) in the E5-"kleine Halle" area. Vertical alignment marks have been provided by the NEPTUN group.

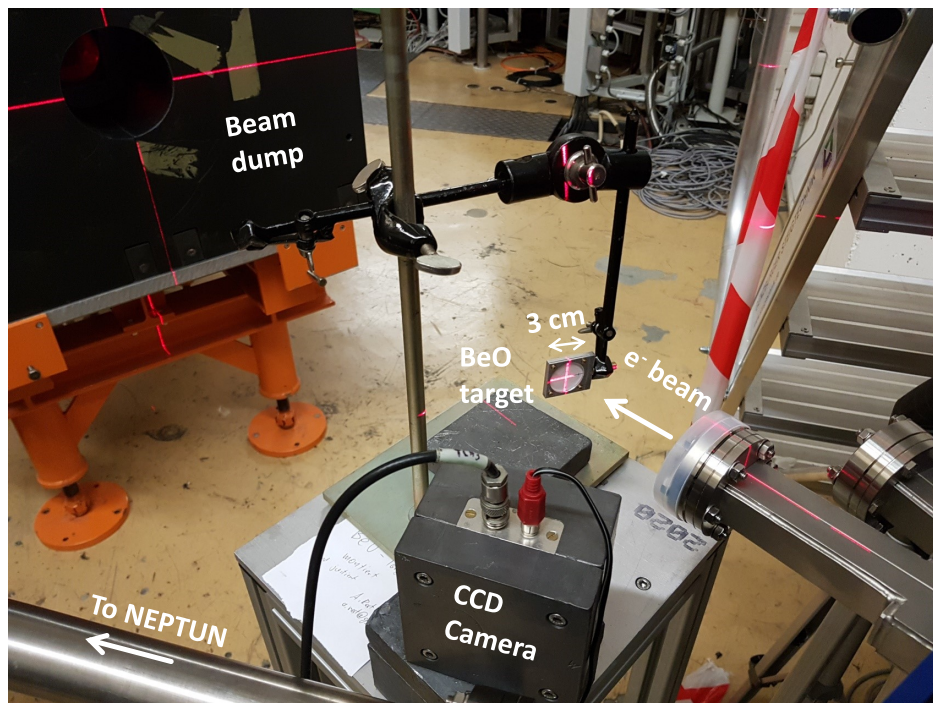


Figure 8.27.: Commissioning of the new detector test set-up. A BeO target (E5R1) with a diameter of 3 cm is mounted about 10 cm behind the exit window. Beam elements were aligned with the help of a line-laser.

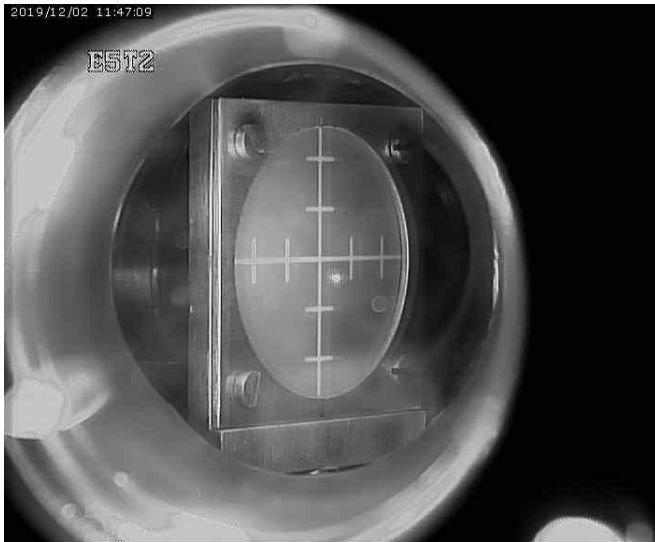


Figure 8.28.: **Left:** Camera picture of the E5T2 target which is located in front of the NEPTUN radiator. One tick is 5 mm, one pixel is 5/55 mm. **Right:** Beam spot on the same target without external illumination.

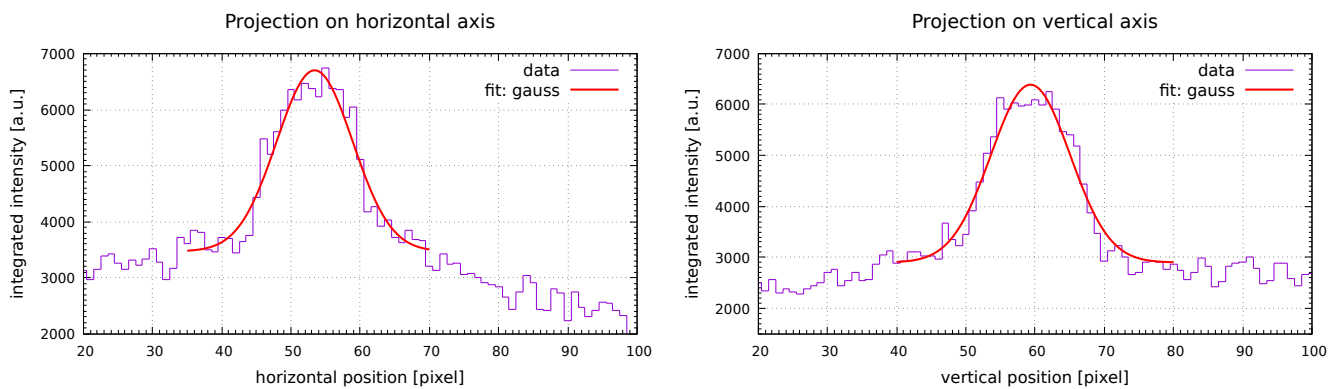


Figure 8.29.: **Left:** Projection of the E5T2 target picture, shown in Fig. 8.28 (right), on the horizontal axis. From a *Gaussian* fit a beam size of $\sigma_{\text{E5T2,horiz.}} = (5.50 \pm 0.23) \text{ pixel} = (0.50 \pm 0.02) \text{ mm}$ can be estimated. **Right:** Projection of the same picture on the vertical axis delivers a beam size of $\sigma_{\text{E5T2,vert.}} = (5.71 \pm 0.22) \text{ pixel} = (0.52 \pm 0.02) \text{ mm}$.

For the commissioning of the beamlines an electron beam with an energy of 30.5 MeV and a current of 100 nA¹ was focused on the E5T1 target. After this, the 0°-beamline towards the NEPTUN experiment was commissioned. The two new installed quadrupoles offer the operators more degrees of freedom during beam focusing and make it easier for them to adjust for a small beam size, which is requested by the NEPTUN experiment. The beam spot at the E5T2 target is shown in Fig. 8.28, the corresponding currents of the magnets are shown in Appendix A.3 (Table A.1). The beam spot has a nearly circular shape and especially without external illumination (see Fig. 8.28) no beam halo is visible.

With a focused beam on the E5T2 target, the new dipole magnet E5BM01 was switched on. The beam was focused on the E5R1 target which is shown in Fig. 8.30. The corresponding magnet currents are shown in Appendix A.3 (Table A.2).

The beam size on the E5T2 and E5R1 target has been evaluated by projecting the beam spot pictures Fig. 8.28 (right) and Fig. 8.30 (right) on the horizontal and vertical axis. The result is shown

¹ No current measurement was available at the time of commissioning. Since an energy scraper system is mounted in front of the new set-up the current is expected to be about a factor of a half lower.

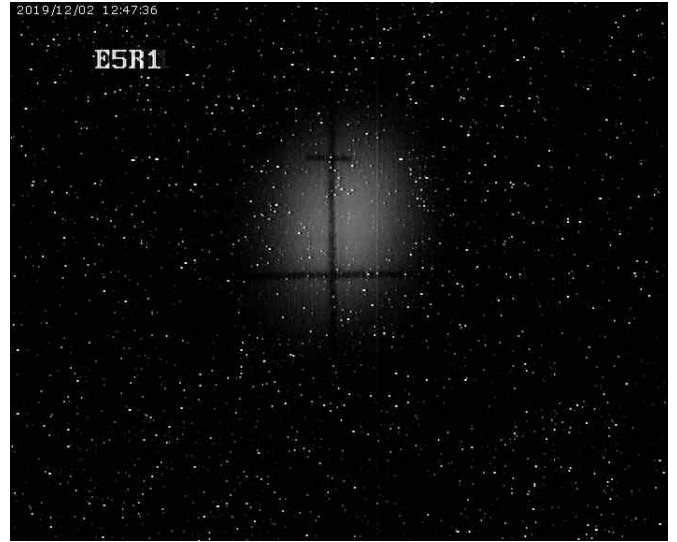
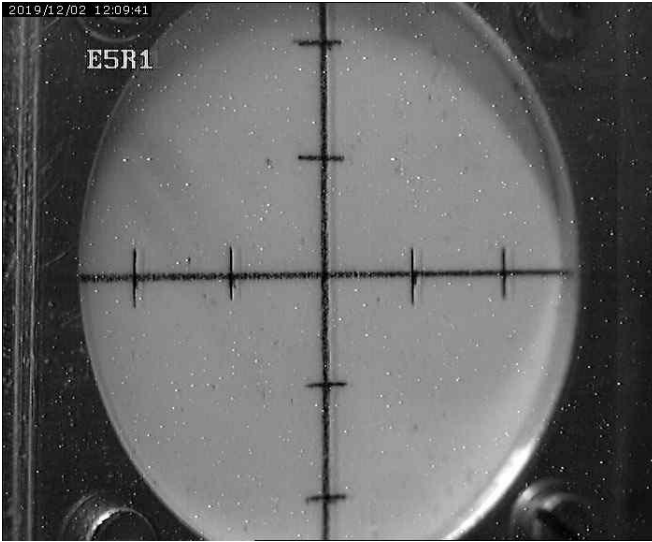


Figure 8.30.: **Left:** Camera picture of the E5R1 target which is located at the new detector test set-up in front of the beam dump. One tick is 5 mm, one pixel is 5/126 mm. **Right:** Beam spot on the target without external illumination.

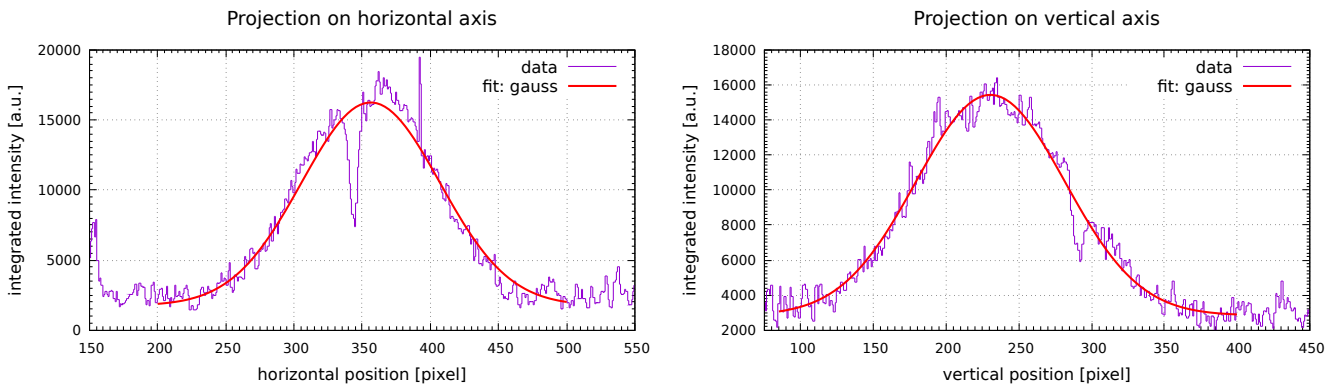


Figure 8.31.: **Left:** Projection of the E5R1 target picture, shown in Fig. 8.30 (right), on the horizontal axis. The spikes in the distribution are caused by the cross-hair on the target. From a *Gaussian* fit a beam size of $\sigma_{\text{E5R1,horiz.}} = (50.66 \pm 1.27) \text{ pixel} = (2.01 \pm 0.05) \text{ mm}$ can be estimated. **Right:** Projection of the same picture on the vertical axis delivers a beam size of $\sigma_{\text{E5R1,vert.}} = (51.19 \pm 0.72) \text{ pixel} = (2.03 \pm 0.03) \text{ mm}$.

in Fig. 8.29 and Fig. 8.31, respectively. By fitting the beam spot with a *Gaussian* distribution a beam size of $\sigma_{\text{E5T2,horiz.}} = (0.50 \pm 0.02) \text{ mm}$ and $\sigma_{\text{E5T2,vert.}} = (0.52 \pm 0.02) \text{ mm}$ can be estimated at the E5T2 target location. For the E5R1 target the beam size is $\sigma_{\text{E5R1,horiz.}} = (2.01 \pm 0.05) \text{ mm}$ and $\sigma_{\text{E5R1,vert.}} = (2.03 \pm 0.03) \text{ mm}$. At this point it must be noted that the beam spot appears, due to flare effects of the used BeO target material, slightly larger than it actually is.

For the NEPTUN experiment this work contributed to a significant improvement of the beam quality. During the commissioning it could be shown that the newly installed vacuum chamber of the dipole magnet did not create additional beam halo and therefore background radiation at the position of the NEPTUN experiment. Of great advantage are the two additional quadrupoles which offer the operators more freedom during beam focusing. Since the NEPTUN experiment was not ready for operation at the time of the commissioning, a detailed evaluation of the beam quality for the experiment was not possible. A further evaluation of the beam quality is planned for the next beam time in the beginning of 2020.

Through the commissioning it could be shown that it is possible to guide an electron beam to the new detector test area. Efforts were made to keep the beam spot as small as possible, but these were limited due to time constraints. Furthermore, the large beam spot, shown in Fig. 8.30, is mainly caused by the expansion of the beam in the exit window (see also section 8.3.4) and in air. For the planned detector tests this is not an obstacle, because it will allow a large illumination of the DUT. In order to reduce the expansion of the beam through the exit window, the installation of a thinner exit window is planned for future beam experiments. The exit window could be made for example from titanium were a thickness of approximately 35 μm is realizable. A new exit window is in planning and first detector tests, e.g. UFSD prototype detector tests, are planned for the beginning of 2020.

9 Summary and outlook

A major goal of this work was the design, installation and commissioning of new read-out electronics for the HADES ECAL detector. For that a *Charge-to-Digital-Converter* (QDC) and *Time-to-Digital-Converter* (TDC) based on a commercial *Field Programmable Gate Array* (FPGA) technology are used to read out 978 PMT signals of the ECAL. The charge measurement of the detector signals is based on a modified *Time-over-Threshold* (TOT) measuring method. In the context of this work the second generation of the PaDiWa-AMPS front-end board, for the TRB3 (*General Purpose Trigger and Readout Board* - generation 3), was designed, manufactured and tested in the laboratory. The requirements of the detector could be confirmed in laboratory measurements. The front-end achieves a time measurement precision of $\sigma_t = 16$ ps. The relative charge measurement precision for signal amplitudes above 1 V is below $\sigma_c = 0.5\%$.

The read-out electronics was installed in the ECAL detector and integrated into the HADES DAQ system. The system was commissioned with LASER signals and cosmic muons. A successful operation of the ECAL read-out system was shown during a four week physics production beam time with an 1.58A GeV Ag beam. The ECAL detector system is currently being calibrated, first results showed an energy resolution of $\frac{\sigma_E}{E} = \frac{6.6\%}{\sqrt{E[\text{GeV}]}}$ which is already close to the design value of $\frac{\sigma_E}{E} = \frac{5.5\%}{\sqrt{E[\text{GeV}]}}$. Besides this, the $\pi^0 \rightarrow \gamma\gamma$ decay could be successfully reconstructed.

Despite the successful usage of the read-out electronics during the production beam time, there is still room for improvements. One of the weak points of the read-out electronics is the limitation to a maximum rate of 100 kHz. This limitation can only be overcome by an active baseline restorer which requires a major change in the measurement method. The modular structure of the ECAL read-out system allows an easy exchange of individual parts in the read-out chain in a cost efficient way. A new front-end board with a novel charge measurement design is currently developed at *GSI Department for Electronics*. The used measurement technique implements a baseline restorer by default and could therefore be a potential successor of the PaDiWa-AMPS2 front-end board, which was addressed in this work. A first prototype is currently in production and first laboratory tests, in order to check the compatibility with ECAL signals, are planned for the beginning of 2020.

A read-out concept which is similar to ECAL is used to read-out diamond based beam detectors in the HADES experiment. Those detectors are used for the T0 determination of the *Time-of-Flight* measuring system, which is important for particle identification. Besides this, they are important for online beam monitoring purposes. The requirements for the time precision are in the order of 50 ps. Diamond detectors have been successfully used in HADES for years. Its radiation hardness and its time precision proved to be an advantage. Unfortunately, only small areas can be covered and the availability of artificial, detector grade diamond material is currently limited.

The new *Ultra-Fast Silicon Detector* (UFSD) technology has already been identified as a potential successor. A prototype detector was developed at GSI and tested with a proton beam. It could be shown that the requirements to the time-precision are almost met. A time precision of 56 ps, which was achieved with the NINO chip, is an excellent result for a system using state-of-the-art technology. The PaDiWa based read-out concept, which is currently adopted in order to read out UFSD sensors, needs still further tuning. New pre-amplifiers are currently being developed. Furthermore, the next generation of UFSD sensors, with less inactive space between the strips, is currently produced and will be available soon. It is planned to use this technology as a diagnostic instrument for *Energy Recovery Linac* operations of the electron accelerator S-DALINAC of TU Darmstadt.

In the context of this work a multi-purpose detector test set-up was constructed at the S-DALINAC. This set-up allows a large variety of detector tests using an electron beam with an energy up to 130 MeV and beam current up to 20 μA . Of special interest are research and development of UFSD prototype detectors, which have been presented in this work. These conditions are ideal to perform tests with a beam of minimum ionizing particles. The flexibility of the set-up and the available space allows the test

of many different systems in future. In the context of this work the necessary beam dynamic calculations were carried out. Furthermore, a new vacuum chamber for the dipole magnet was constructed with the goal of a maximized beam tube cross section. This will improve the signal-to-noise ratio in the NEPTUN experiment. The beamline of the test set-up was optimized to the spatial circumstances. The beam elements were installed and adjusted. The beamlines have been put successfully into operation shortly before the completion of this work. It could be shown that the focusing capabilities for the NEPTUN experiment are significantly improved. Besides this, the beamline of the new multi-purpose detector test set-up was successfully commissioned and is now ready for the first detector tests. A beam expansion which is mainly caused by the aluminum exit window will be eliminated in the future using a thinner metal foil. A titanium exit window is currently being planned. First detector tests are currently being planned and are scheduled in the next beam time of the S-DALINAC.

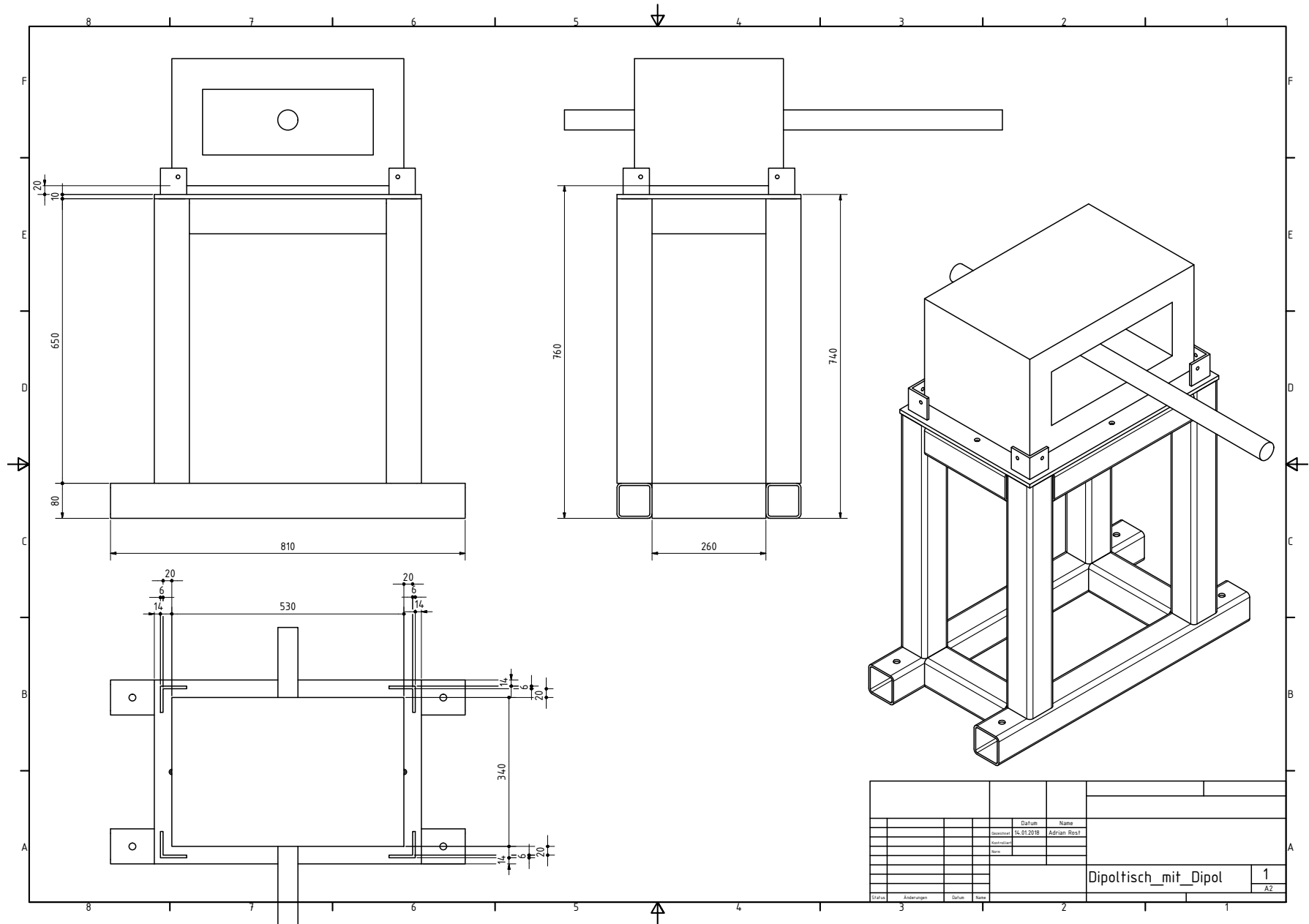


Figure A.2.: Fully assembled dipole magnet support structure at the S-DALINAC. The individual parts are shown in Appendix A.3 - A.6.

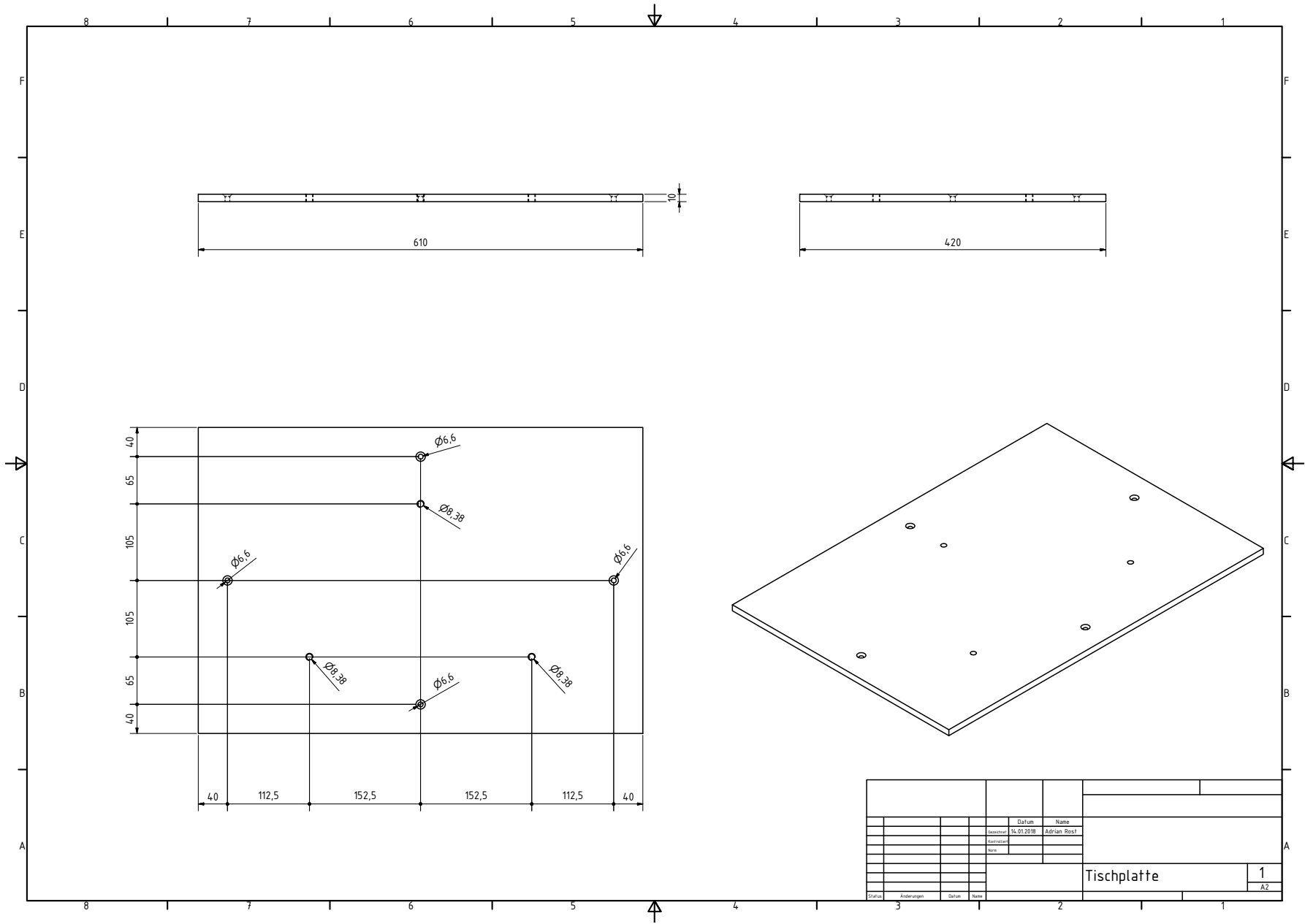


Figure A.4.: Top plate of the dipole magnet support structure at the S-DALINAC.

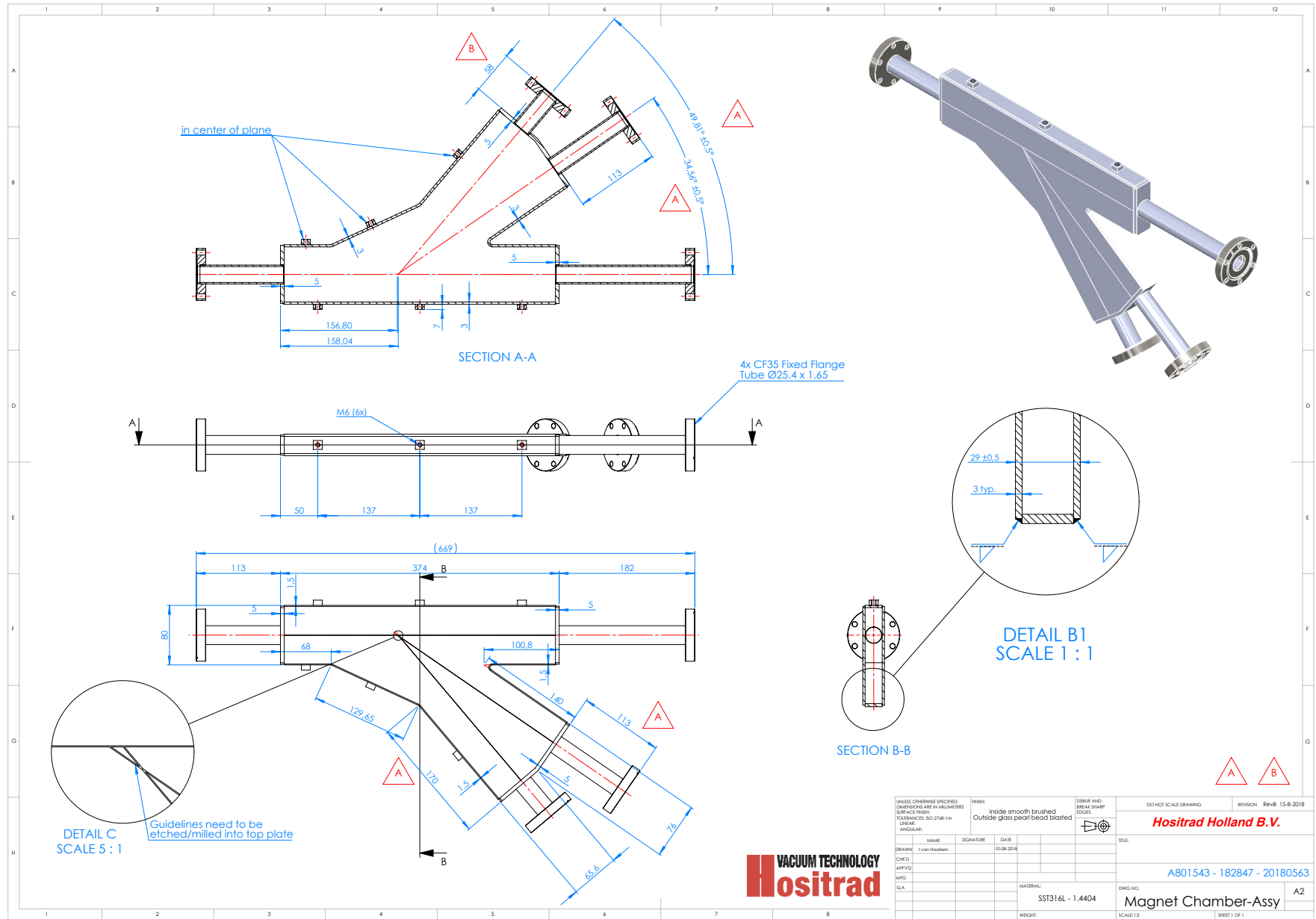


Figure A.9.: Vacuum chamber for the dipole magnet at the S-DALINAC. Note: The round beam pipes were replaced by rectangular ones in the final version (see A.7 and A.10). (Drawing taken from [142])

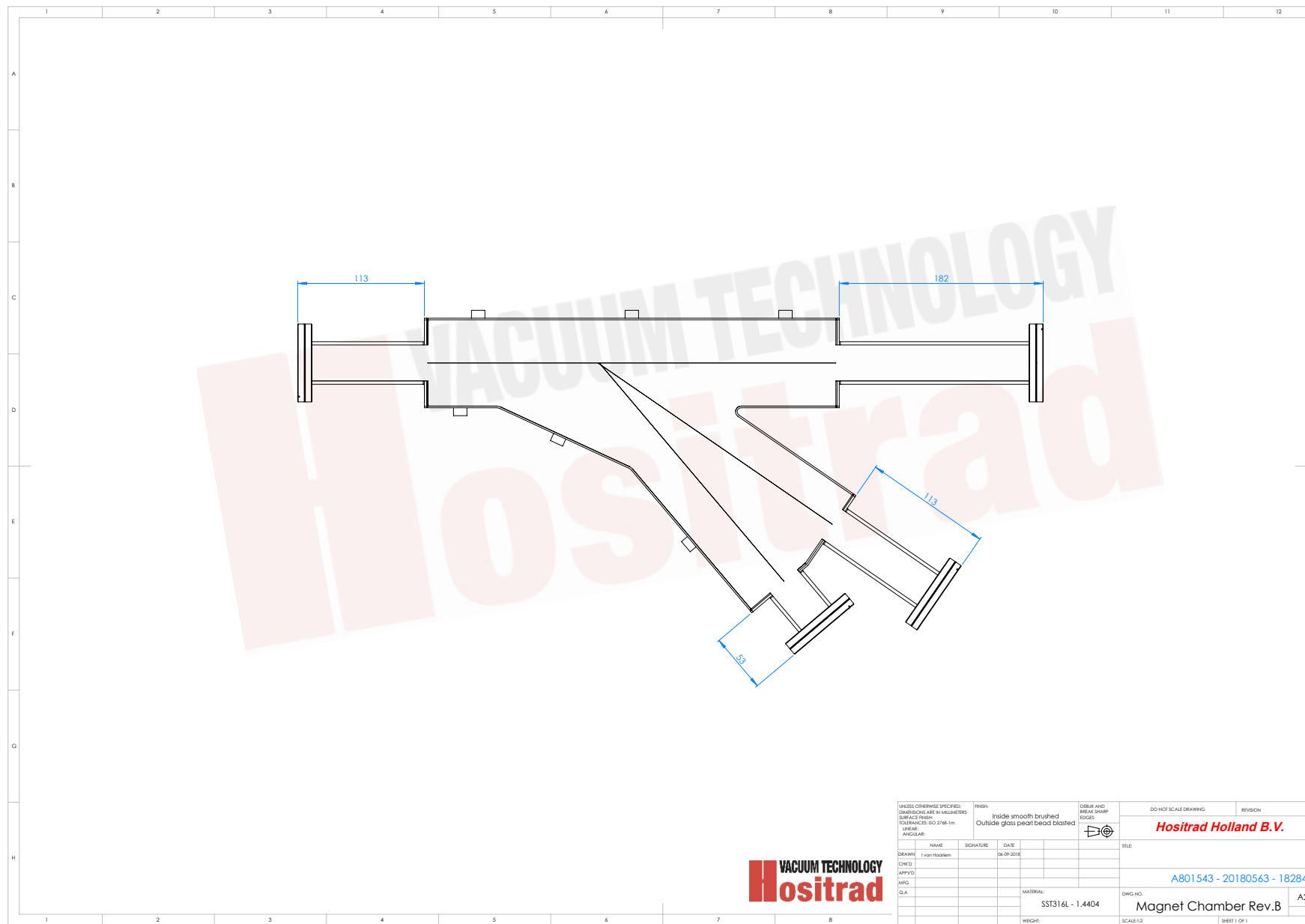


Figure A.10.: Vacuum chamber for the dipole magnet at the S-DALINAC. (Drawing taken from [142])

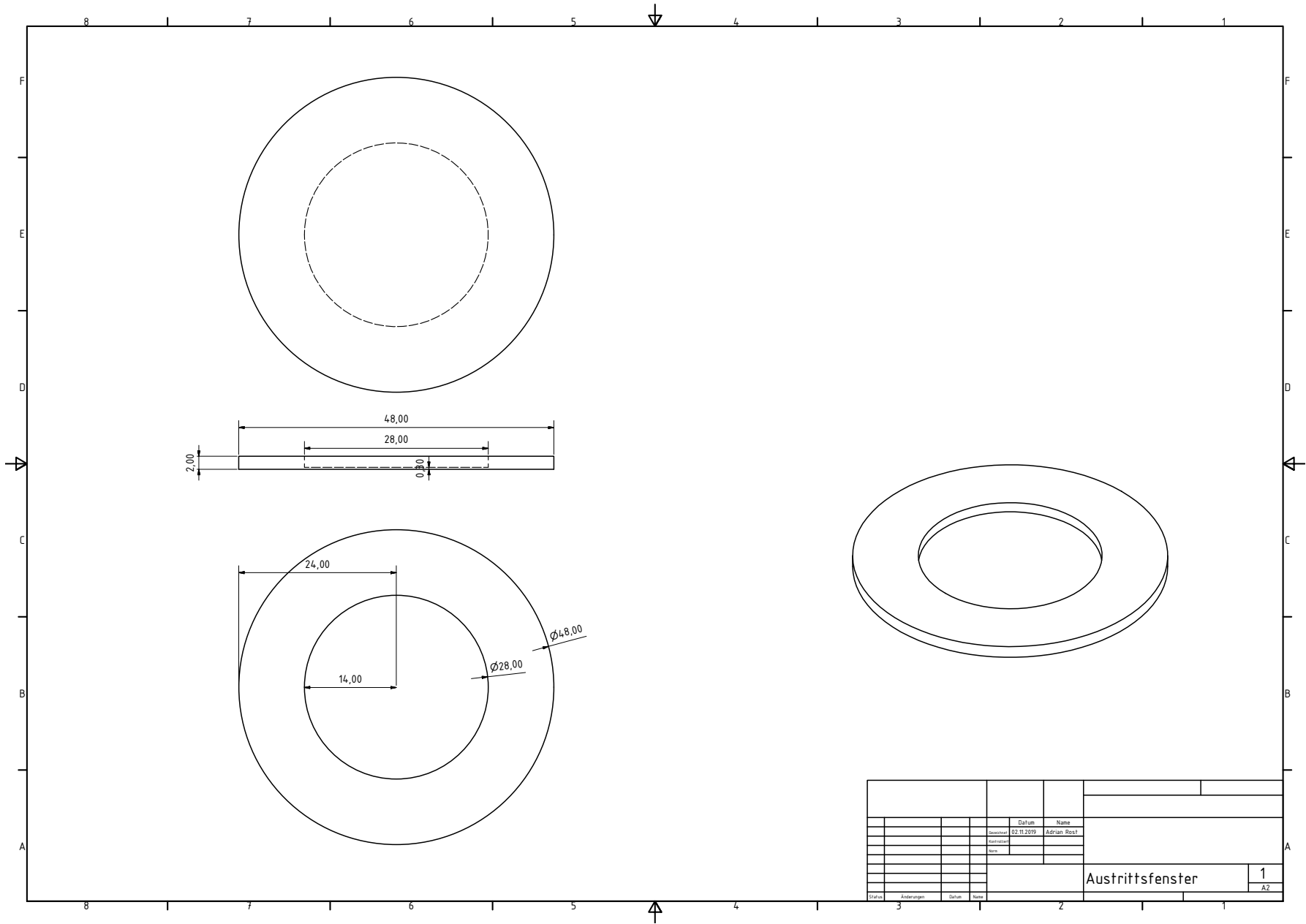


Figure A.11.: Aluminum exit window for a CF-40 flange which is installed instead of a gasket.

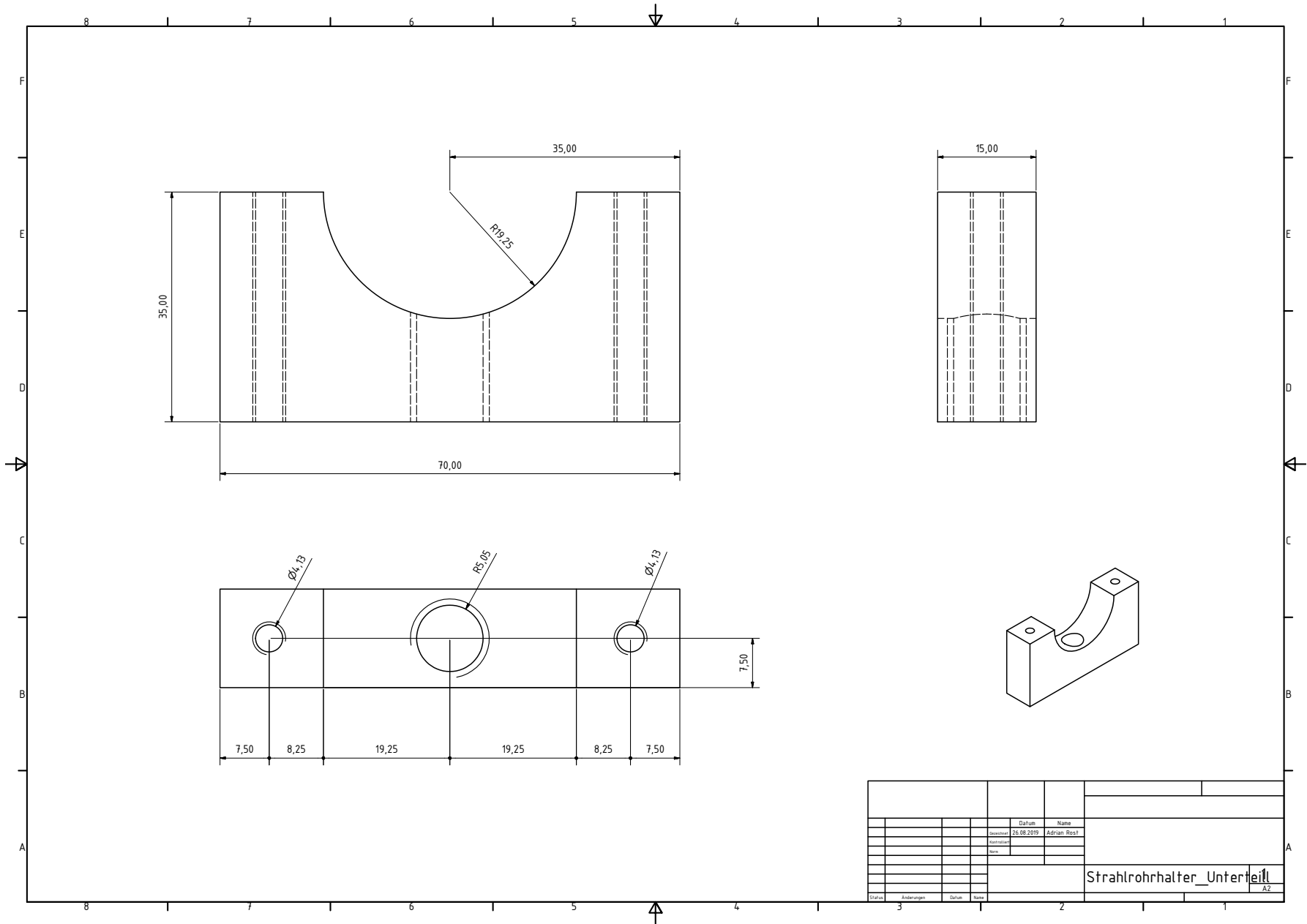


Figure A.13.: Lower part of a beam tube holder.

A.2 Schematics

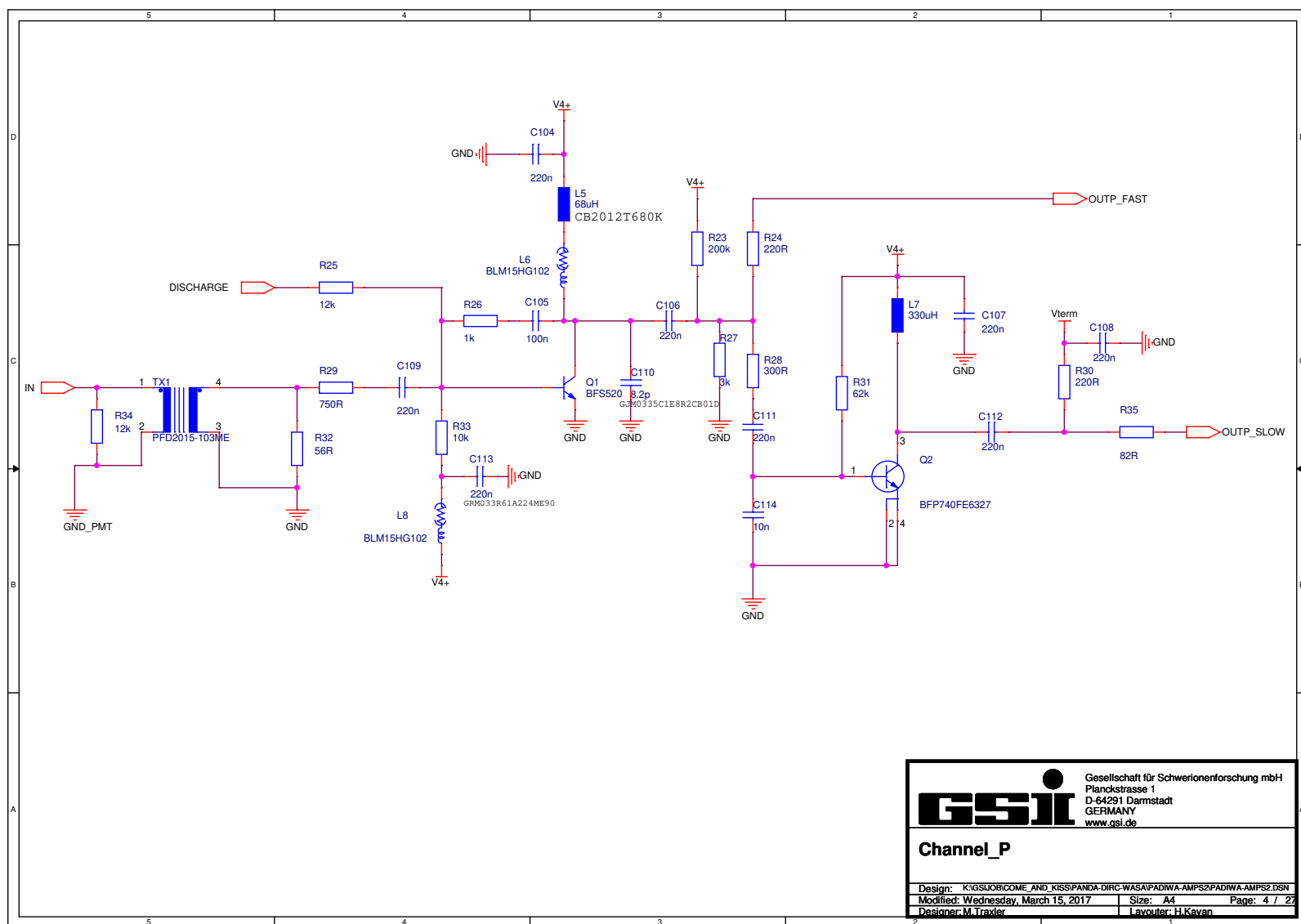
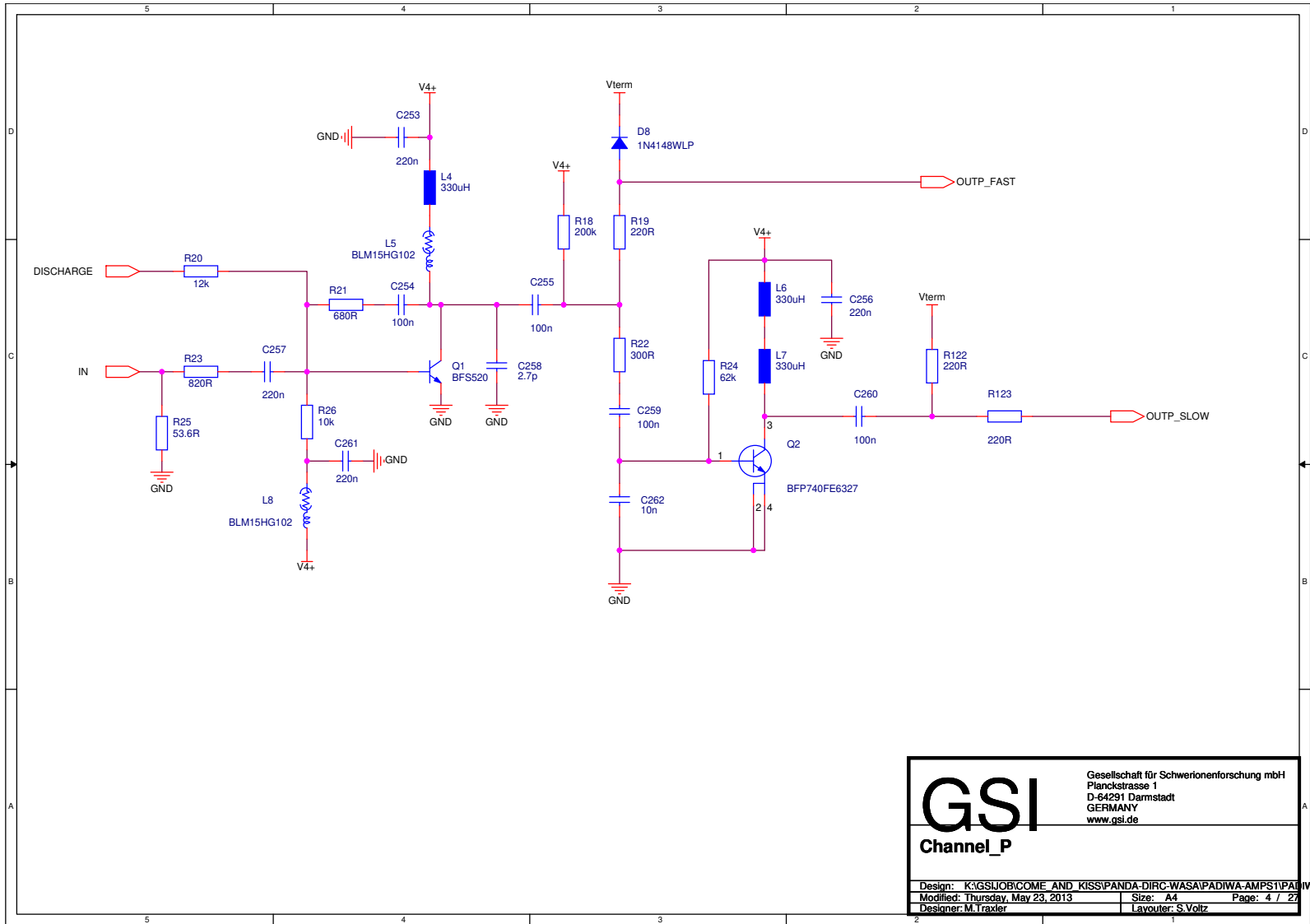


Figure A.14.: Schematics of the analog part of the first channel of the PaDiWa-AMPS2 front-end board. Note: The transistor BFSS20 is exchanged with the replacement type BFU55W.



GSI	Gesellschaft für Schwerionenforschung mbH Planckstrasse 1 D-64291 Darmstadt GERMANY www.gsi.de
	Channel_P
Design: K:\GSI\JOB\ICOME AND KISSIPANDA-DIRC-WASAIPADIWA-AMPS1\PAI	Size: A4
Modified: Thursday, May 23, 2013	Page: 4 / 23
Designer: M. Traxler	Layouter: S. Voltz

Figure A.15.: Schematics of the analog part of the first channel of the PaDiWa-AMPS1 front-end board.

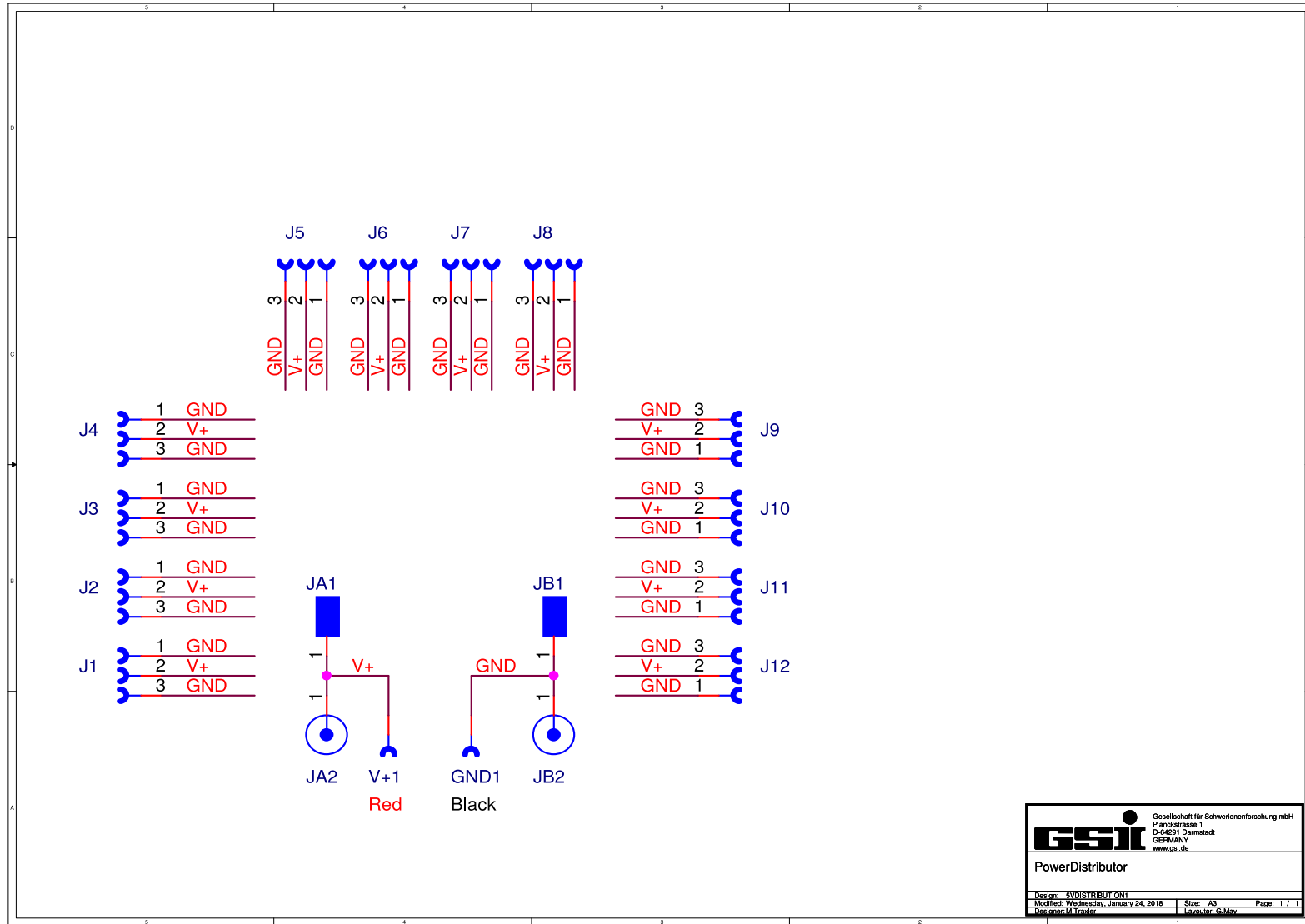


Figure A.16.: Schematics of the 5V-distribution board.

A.3 Magnet currents during the beam commissioning at S-DALINAC

Table A.1.: Settings of the magnet currents for beam focusing on the E5T2 target (see Fig.8.28) which is located in front of the NEPTUN radiator.

Magnet	Current
E5QU01	0.54 A
E5QU02	-0.46 A
E5BM01	0 A
E5QU02	1.07 A
E5QU02	-1.84 A

Table A.2.: Settings of the magnet currents for beam focusing on the E5R1 target (see Fig.8.30) of the new test set-up.

Magnet	Current
E5QU01	0.78 A
E5QU02	-0.191 A
E5BM01	70.53 A
E5QU02	0 A
E5QU02	0 A

A.4 Beam dynamic simulation to the beam dump in vacuum

In Fig. A.17 a simulation of the beam envelope in vacuum to the beam dump, which is located 125 cm away from the dipole chamber exit, is shown. A beam size of $\sigma_{x,y} = 0.1$ mm is expected, which will fit the beam dump entrance hole with a diameter of 10 cm.

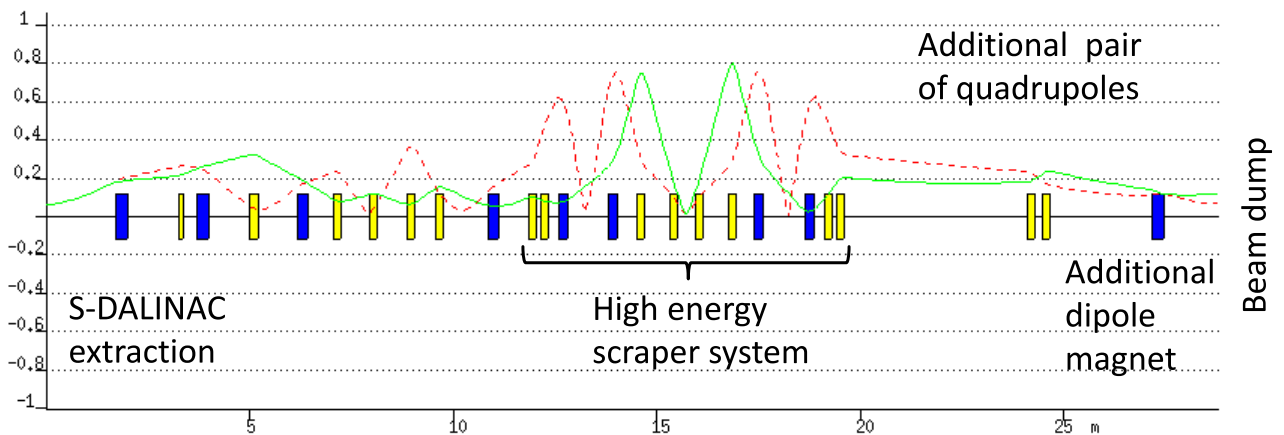


Figure A.17.: Beam dynamics calculations from the main linac extraction to the beam dump of the detector test set-up. Simulation parameters are the same as in Fig. 8.16 but now the beam is transported to a beam dump 125 cm downstream from the exit window. The dashed red line shows the 1σ beam envelope in x -direction, the solid green line in y -direction, both are given in mm.

A.5 PaDiWa-AMPS2 delay adjustment values

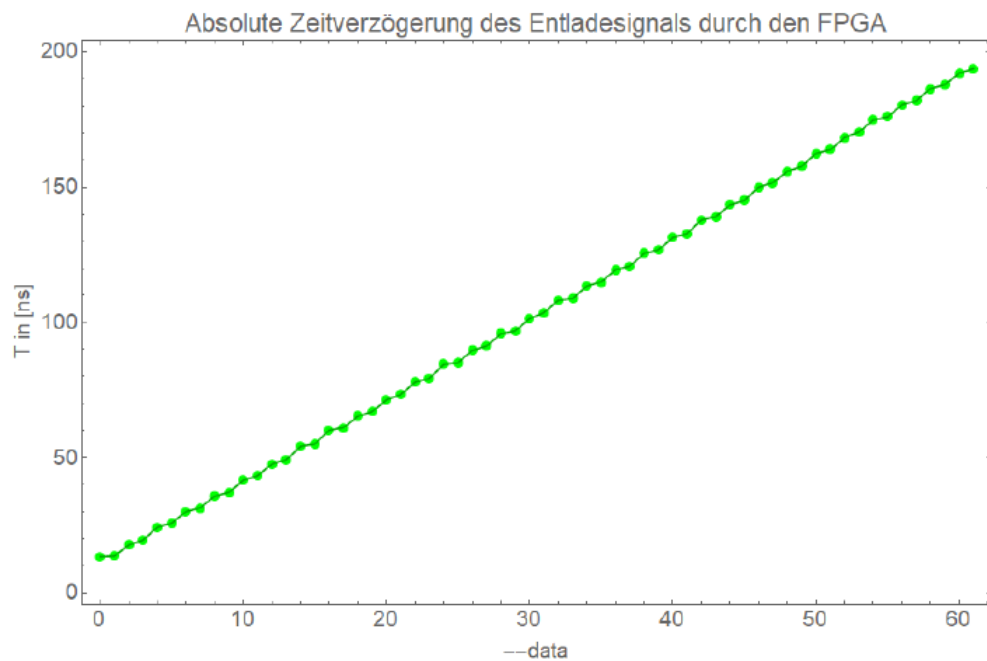


Figure A.18.: Time delay for the register value "-data". A delays between 10 ns and 200 ns with a step size of about 2 ns can be generated.

Bibliography

- [1] E. Rutherford, “LXXIX. The scattering of α and β particles by matter and the structure of the atom,” *The London, Edinburgh, and Dublin Philosophical Magazine and Journal of Science*, vol. 21, no. 125, pp. 669–688, 1911.
- [2] S. Witman, “Ten things you might not know about particle accelerators.” Website, 2020. Online available: <https://www.symmetrymagazine.org/article/april-2014/ten-things-you-might-not-know-about-particle-accelerators>; retrieved on 30 January 2020.
- [3] P. A. R. Ade *et al.*, “Planck 2015 results. XIII. Cosmological parameters,” *Astron. Astrophys.*, vol. 594, p. A13, 2016.
- [4] J. Steinheimer, A. Mukherjee, N. Wechselberger, M. Hanauske, S. Schramm, and H. Stöcker, “The Hot and Dense QCD Equation of State in Heavy Ion Collisions and Neutron Star Mergers,” *Springer Proc. Phys.*, vol. 208, pp. 191–198, 2018.
- [5] R. Rapp, “Fireball spectroscopy,” *Nature Phys.*, vol. 15, no. 10, pp. 990–991, 2019.
- [6] M. Tanabashi *et al.*, “Review of Particle Physics,” *Phys. Rev.*, vol. D98, no. 3, p. 030001, 2018.
- [7] P. Steinbrecher, “The QCD crossover at zero and non-zero baryon densities from Lattice QCD,” *Nucl. Phys.*, vol. A982, pp. 847–850, 2019.
- [8] A. Andronic, D. Blaschke, P. Braun-Munzinger, J. Cleymans, K. Fukushima, L. McLerran, H. Oeschler, R. Pisarski, K. Redlich, C. Sasaki, H. Satz, and J. Stachel, “Hadron production in ultra-relativistic nuclear collisions: Quarkyonic matter and a triple point in the phase diagram of QCD,” *Nuclear Physics A*, vol. 837, no. 1, pp. 65 – 86, 2010.
- [9] T. Galatyuk, “Future facilities for high μ_B physics,” *Nucl. Phys.*, vol. A982, pp. 163–169, 2019.
- [10] A. Andronic, P. Braun-Munzinger, K. Redlich, and J. Stachel, “Decoding the phase structure of QCD via particle production at high energy,” *Nature*, vol. 561, no. 7723, pp. 321–330, 2018.
- [11] H. J. Specht, “Thermal Dileptons from Hot and Dense Strongly Interacting Matter,” *AIP Conf. Proc.*, vol. 1322, no. 1, pp. 1–10, 2010.
- [12] J. Adamczewski-Musch *et al.*, “Probing dense baryon-rich matter with virtual photons,” *Nature Phys.*, vol. 15, no. 10, pp. 1040–1045, 2019.
- [13] G. Agakishiev *et al.*, “The High-Acceptance Dielectron Spectrometer HADES,” *Eur.Phys.J.*, vol. A41, pp. 243–277, 2009.
- [14] J. Adamczewski-Musch *et al.*, “A facility for pion-induced nuclear reaction studies with HADES,” *Eur. Phys. J.*, vol. A53, no. 9, p. 188, 2017.
- [15] P. Senger, “Exploring Cosmic Matter in the Laboratory - The Compressed Baryonic Matter Experiment at FAIR,” *Particles*, vol. 2, no. 4, pp. 499–510, 2019.
- [16] J. Adamczewski-Musch *et al.* [HADES collaboration], “Proposal for experiments at SIS18 during FAIR Phase-0,” Internal report, GSI Helmholtzzentrum für Schwerionenforschung GmbH, 2017.
- [17] J. Pietraszko, T. Galatyuk, V. Grilj, W. Koenig, S. Spataro, and M. Träger, “Radiation damage in single crystal CVD diamond material investigated with a high current relativistic ^{197}Au beam,” *Nucl. Instrum. Meth.*, vol. A763, pp. 1–5, 2014.

-
- [18] A. Rost, J. Adamczewski-Musch, T. Galatyuk, S. Linev, J. Pietraszko, and M. Traxler, “Beam Quality Monitoring System in the HADES Experiment at GSI Using CVD Diamond Material,” in *Proceedings, 7th International Beam Instrumentation Conference (IBIC 2018): Shanghai, Cina, September 9-13, 2018*, p. TUPC03, 2019.
- [19] C. Müntz *et al.*, “The HADES tracking system,” *Nucl. Instrum. Meth.*, vol. A535, pp. 242–246, 2004.
- [20] M. Wiebusch, *Towards new front-end electronics for the HADES drift chamber system*. PhD thesis, Johann Wolfgang Goethe-Universität, Frankfurt am Main, 2019.
- [21] C. Behnke, *Reconstruction of π^0 and η mesons via conversion in $197\text{Au}+197\text{Au}$ at $1.23\text{ GeV}/u$ with the HADES Spectrometer*. PhD thesis, Johann Wolfgang Goethe-Universität, Frankfurt am Main, 2016.
- [22] G. Konrakov, “Development of diamond detectors for HADES.” 6th ADAMAS Workshop, Croatian Academy of Sciences and Arts, Zagreb, 2017. Talk online available: http://www-adamas.gsi.de/ADAMAS06/talks/Kornakov_2017.pdf; retrieved on 19 December 2019.
- [23] C. Agodi *et al.*, “The time-of-flight wall for the HADES spectrometer,” *IEEE Trans. Nucl. Sci.*, vol. 45, pp. 665–669, 1998.
- [24] G. Kornakov *et al.*, “Time of flight measurement in heavy-ion collisions with the HADES RPC TOF wall,” *JINST*, vol. 9, no. 11, p. C11015, 2014.
- [25] G. Kornakov, “New Advances And Developments on the RPC TOF Wall Of The HADES Experiment at GSI,” PHD Thesis, Universidad de Santiago de Compostela, Santiago de Compostela, Spain, 2012.
- [26] HADES Collaboration, “HADES Wiki Page.” <https://hades-wiki.gsi.de/cgi-bin/view>, December 2019.
- [27] S. Spies *et al.*, “Diamond detectors in the HADES experiment.” 8th ADAMAS Workshop, GSI, Darmstadt, 2019. Talk online available: http://www-adamas.gsi.de/ADAMAS08/talks/Spies_ADAMAS2019.pdf; retrieved on 19 December 2019.
- [28] K. Zeitelhack *et al.*, “The HADES RICH detector,” *Nucl. Instrum. Meth.*, vol. A433, pp. 201–206, 1999.
- [29] J. Michel *et al.*, “Electronics for the RICH detectors of the HADES and CBM experiments,” *JINST*, vol. 12, no. 01, p. C01072, 2017.
- [30] C. Pauly *et al.*, “Upgrade of the HADES RICH photon detector with H12700 MAPMTs,” *Nucl. Instrum. Meth.*, vol. A876, pp. 164–167, 2017.
- [31] J. Förtsch, “Timing calibration and low level analysis of RICH.” XXXVII HADES Collaboration Meeting, Krakow, Poland, 2019. Talk online available: <https://indico.gsi.de/event/7791/session/8/contribution/30/material/slides/0.pdf>; retrieved on 19 December 2019.
- [32] W. Czyzycki, E. Epple, L. Fabbietti, M. Golubeva, F. Guber, *et al.*, “Electromagnetic Calorimeter for HADES,” 2011. arXiv:1109.5550.
- [33] O. Svoboda *et al.*, “Electromagnetic calorimeter for the HADES@FAIR experiment,” *JINST*, vol. 9, p. C05002, 2014.
- [34] A. Balanda *et al.*, “The HADES Pre-Shower detector,” *Nucl. Instrum. Meth.*, vol. A531, pp. 445–458, 2004.

-
- [35] J. Michel, M. Bohmer, I. Frohlich, G. Korcyl, L. Maier, M. Palka, J. Stroth, M. Traxler, and S. Yurevich, "The HADES DAQ system: Trigger and readout board network," *IEEE Trans. Nucl. Sci.*, vol. 58, pp. 1745–1750, 2011.
- [36] J. Michel, G. Korcyl, L. Maier, and M. Traxler, "In-beam experience with a highly granular DAQ and control network: TrbNet," *JINST*, vol. 8, p. C02034, 2013.
- [37] J. Michel, *Development and Implementation of a New Trigger and Data Acquisition System for the HADES Detector*. PhD thesis, Johann Wolfgang Goethe-Universität, Frankfurt am Main, 2012.
- [38] M. Penschuk, "Development and Implementation of a Central Trigger System for TrbNet-based systems," BSc Thesis, Johann Wolfgang Goethe-Universität, Frankfurt am Main, Germany, 2012.
- [39] J. Adamczewski-Musch, N. Kurz, and S. Linev, "Developments and applications of DAQ framework DABC v2," *Journal of Physics: Conference Series*, vol. 664, p. 082027, dec 2015.
- [40] GSI Helmholtzzentrum für Schwerionenforschung GmbH, "DABC web page." <http://dabc.gsi.de/>, December 2019.
- [41] T. Galatyuk, "Recent Results from HADES." 13th International Conference on Nucleus-Nucleus Collisions, Saitama, Japan, 2018. To appear in JPS Conf. Proc.
- [42] S. Harabasz, "Dileptons from AgAg 4.5A GeV." XXXV HADES Collaboration Meeting, GSI, Darmstadt, Germany, 2018. Talk online available: <https://indico.gsi.de/event/6723/session/4/contribution/32/material/slides/0.pptx>; retrieved on 19 December 2019.
- [43] D. Dittert, "Dilepton flow in Au and spectra from Ag." II HADES Physics Analysis Meeting, Seligenstadt, Germany, 2019. Talk online available: <https://indico.gsi.de/event/8841/session/12/contribution/60/material/slides/0.pdf>; retrieved on 19 December 2019.
- [44] C. Grupen, B. Shwartz, and H. Spieler, *Particle Detectors*. Cambridge Monographs on Particle Physics, Nuclear Physics and Cosmology, Cambridge University Press, 2008.
- [45] M. Tanabashi *et al.*, "Review of Particle Physics," *Phys. Rev.*, vol. D98, no. 3, p. 030001, 2018.
- [46] S. Menke, "The Electromagnetic Shower Simulator." <https://www.mpp.mpg.de/~menke/elss/description.shtml>, December 2019.
- [47] Hamamatsu Photonics K.K., "PHOTOMULTIPLIER TUBES - Basics and Applications (THIRD EDITION (Edition 3a))." https://www.hamamatsu.com/resources/pdf/etd/PMT_handbook_v3aE.pdf, December 2019.
- [48] O. Svoboda *et al.*, "Verification of Electromagnetic Calorimeter Concept for the HADES spectrometer," *J. Phys. Conf. Ser.*, vol. 599, no. 1, p. 012026, 2015.
- [49] P. Jeffreys, M. Akrawy, G. Arnison, J. Batley, K. W. Bell, *et al.*, "Development Studies for the Opal Endcap Electromagnetic Calorimeter Using Vacuum Photo Triode Instrumented Lead Glass," *Nucl.Instrum.Meth.*, vol. A290, p. 76, 1990.
- [50] OPAL Collaboration, "The OPAL detector at LEP," *Nuclear Instruments and Methods in Physics Research Section A: Accelerators, Spectrometers, Detectors and Associated Equipment*, vol. 305, no. 2, pp. 275 – 319, 1991.
- [51] T. C. Awes *et al.*, "The Midrapidity calorimeter for the relativistic heavy ion experiment WA80 at CERN," *Nucl. Instrum. Meth.*, vol. A279, pp. 479–502, 1989.

-
- [52] A. Rost, T. Galatyuk, W. Koenig, J. Michel, J. Pietraszko, P. Skott, and M. Traxler, "A flexible FPGA based QDC and TDC for the HADES and the CBM calorimeters," *JINST*, vol. 12, no. 02, p. C02047, 2017.
- [53] A. Neiser *et al.*, "TRB3: a 264 channel high precision TDC platform and its applications," *JINST*, vol. 8, p. C12043, 2013.
- [54] D. Ponikvar, "Wilkinson-type ADC with short conversion time and low clock frequency," *Nuclear Instruments and Methods in Physics Research Section A: Accelerators, Spectrometers, Detectors and Associated Equipment*, vol. 408, no. 2–3, pp. 523 – 529, 1998.
- [55] C. Ugur, S. Linev, J. Michel, T. Schweitzer, and M. Traxler, "A novel approach for pulse width measurements with a high precision (8 ps RMS) TDC in an FPGA," *JINST*, vol. 11, no. 01, p. C01046, 2016.
- [56] C. Ugur, W. Koenig, J. Michel, M. Palka, and M. Traxler, "Field programmable gate array based data digitisation with commercial elements," *Journal of Instrumentation*, vol. 8, no. 01, p. C01035, 2013.
- [57] GSI Helmholtzzentrum für Schwerionenforschung GmbH, "TRB3 web page." <http://trb.gsi.de/>, December 2019.
- [58] J. Kalisz, "Review of methods for time interval measurements with picosecond resolution," *Metrologia*, vol. 41, no. 1, p. 17, 2004.
- [59] J. Wu and Z. Shi, "The 10-ps wave union TDC: Improving FPGA TDC resolution beyond its cell delay," in *Proceedings, 2008 IEEE Nuclear Science Symposium, Medical Imaging Conference and 16th International Workshop on Room-Temperature Semiconductor X-Ray and Gamma-Ray Detectors (NSS/MIC 2008 / RTSD 2008)*, pp. 3440–3446, 2008.
- [60] J. Adamczewski-Musch, H. G. Essel, and S. Linev, "Online object monitoring with Go4 V4.4," *IEEE Trans. Nucl. Sci.*, vol. 58, pp. 1477–1481, 2011.
- [61] M. Hoek *et al.*, "The PANDA Barrel DIRC detector," *Nuclear Instruments and Methods in Physics Research Section A: Accelerators, Spectrometers, Detectors and Associated Equipment*, vol. 766, no. 0, pp. 9 – 13, 2014. RICH2013 Proceedings of the Eighth International Workshop on Ring Imaging Cherenkov Detectors Shonan, Kanagawa, Japan, December 2-6, 2013.
- [62] K. Fohl *et al.*, "The DIRC detectors of the PANDA experiment at FAIR," *Nucl. Instrum. Meth.*, vol. A595, pp. 88–91, 2008.
- [63] A. Rost, T. Galatyuk, W. Koenig, J. Michel, J. Pietraszko, P. Skott, and M. Traxler, "A flexible FPGA based QDC and TDC for the HADES and the CBM calorimeters," *Journal of Instrumentation*, vol. 12, pp. C02047–C02047, feb 2017.
- [64] A. Rost, "Test and Optimization of a flexible COME & KISS QDC and TDC for PMT, Si-PM and Diamond Detector Applications," Master's thesis, TU Darmstadt, 2016.
- [65] H. Kayan, "PaDiWa-AMPS2 layout design." private communication, March 2017.
- [66] L. W. Nagel and D. Pederson, "SPICE (Simulation Program with Integrated Circuit Emphasis)," Tech. Rep. UCB/ERL M382, EECS Department, University of California, Berkeley, Apr 1973.
- [67] Linear Technology Corporation, "Software: LTspice XVII." <https://www.analog.com/en/design-center/design-tools-and-calculators/ltspace-simulator.html>, December 2019.

-
- [68] A. Neiser, “Spice-padiwa-amps.” <https://github.com/neiser/spice-padiwa-amps>, December 2019.
- [69] R. Lalik, “Status and perspectives of hyperon production and electromagnetic decays with HADES at FAIR,” *J. Phys. Conf. Ser.*, vol. 1137, no. 1, p. 012057, 2019.
- [70] A. Lai, “Design of an FPGA-based calibration, monitoring and testing system for the HADES Electromagnetic Calorimeter,” Master’s thesis, TU Darmstadt, 2015.
- [71] J. Michel, J. Adamczewski-Musch, M. Böhmer, G. Korcyl, M. Palka, S. Yurevich and M. Traxler, “A Users Guide to the HADES DAQ System.” <http://trb.gsi.de/>, December 2019.
- [72] R. Brun and F. Rademakers, “ROOT: An object oriented data analysis framework,” *Nucl. Instrum. Meth.*, vol. A389, pp. 81–86, 1997.
- [73] G. M. Williams, “Optimization of eyesafe avalanche photodiode lidar for automobile safety and autonomous navigation systems,” *Optical Engineering*, vol. 56, no. 3, pp. 1 – 9, 2017.
- [74] F. Gonnella, V. Kozhuharov, and M. Raggi, “Time over threshold in the presence of noise,” *Nucl. Instrum. Meth.*, vol. A791, pp. 16–21, 2015.
- [75] H. Heggen and M. Traxler, “pQDC front-end board for the TRB platform.” private communication, January 2020.
- [76] M. Wiest, “Allgemeine Tests der ECAL-Ausleselektronik im HADES-Experiment,” Miniforschung, TU Darmstadt, 2018.
- [77] A. Weber, “TDC scaler and threshold monitoring script for RICH and ECAL.” private communication, February 2019.
- [78] J. Förtsch, “Automatic threshold script for RICH and ECAL.” private communication, August 2018.
- [79] Safibra, s.r.o. , “Optical monitoring system for the ECAL detector,” Internal HADES report, 2017.
- [80] A. Shabanov, “ECAL data quality check.” private communication, March 2019.
- [81] M. Traxler, “SLOW channel recovery script.” private communication, March 2019.
- [82] P. Chudoba, “Commissioning of the electromagnetic calorimeter ECAL of the HADES experiment.” FAIRness 2019, Genova, Italy, 2019. To appear in *Journal of Physics: Conference Series*.
- [83] J. Michel, “HADES run statistic.” private communication, March 2019.
- [84] S. Morozov, “Quarz hodoscope test.” private communication, March 2019.
- [85] A. Shabanov, “Calibration of the electromagnetic calorimeter ECAL of the HADES experiment.” FAIRness 2019, Genova, Italy, 2019. To appear in *Journal of Physics: Conference Series*.
- [86] A. Prozorov, “Work in progress: ECAL calibration and π^0 reconstruction.” private communication, January 2020.
- [87] S. Harabasz, “Characterizing baryon dominated matter with HADES measurements.” Quark Matter 2019 - The XXVIIIth International Conference on Ultra-relativistic Nucleus-Nucleus Collisions, Wuhan, China, 2019. Talk online available: https://indico.cern.ch/event/792436/contributions/3535624/attachments/1939659/3215570/SzymonHarabasz_HADES_QM2019_ver2.pptx; retrieved on 20 January 2020.

-
- [88] A. Gicquel, K. Hassouni, F. Silva, and J. Achard, “CVD diamond films: from growth to applications,” *Current Applied Physics*, vol. 1, no. 6, pp. 479 – 496, 2001.
- [89] M. Pomorski, *Electronic properties of single crystal CVD diamond and its suitability for particle detection in hadron physics experiments*. PhD thesis, Johann Wolfgang Goethe-Universität, Frankfurt am Main, 2009.
- [90] K. A. Olive *et al.*, “Particle Physics,” *Chin. Phys.*, vol. C38, p. 090001, 2014.
- [91] N. Minafra, H. Al Ghouli, R. Arcidiacono, N. Cartiglia, L. Forthomme, R. Mulargia, M. Obertino, and C. Royon, “Test of Ultra Fast Silicon Detectors for Picosecond Time Measurements with a New Multipurpose Read-Out Board,” *Nucl. Instrum. Meth.*, vol. A867, pp. 88–92, 2017.
- [92] W. Adam *et al.*, “The development of diamond tracking detectors for the LHC,” *Nucl. Instrum. Meth.*, vol. A514, pp. 79–86, 2003.
- [93] M. Hempel, *Development of a Novel Diamond Based Detector for Machine Induced Background and Luminosity Measurements*. PhD thesis, Brandenburg Tech. U., Hamburg, 2017.
- [94] J. Pietraszko, L. Fabbietti, and W. Koenig, “Diamonds as timing detectors for MIP: The HADES proton-beam monitor and start detectors,” *Nucl. Instrum. Meth.*, vol. A618, pp. 121–123, 2010.
- [95] J. Pietraszko, “Performance of UFSD Strip sensors for timing applications.” 8th ADAMAS Workshop, GSI, Darmstadt, Germany, 2019. Talk online available: http://www-adamas.gsi.de/ADAMAS08/talks/Pietraszko_ADAMAS2019.pdf; retrieved on 19 December 2019.
- [96] M. Despeisse, P. Jarron, F. Anghinolfi, S. Tiuraniemi, F. Osmic, P. Riedler, A. Kluge, and A. Ceccucci, “Low-power amplifier-discriminators for high time resolution detection,” *IEEE Trans. Nucl. Sci.*, vol. 56, pp. 375–381, 2009.
- [97] Marvin Kohls, “Particle fluence on the HADES diamond detector.” private communication, December 2019.
- [98] A. Rost, J. Adamczewski-Musch, T. Galatyuk, S. Linev, J. Pietraszko, M. Sapinski, and M. Traxler, “Performance of the CVD Diamond Based Beam Quality Monitoring System in the HADES Experiment at GSI*,” in *Proceedings, 10th International Particle Accelerator Conference (IPAC2019): Melbourne, Australia, May 19-24, 2019*, p. WEPGW019, 2019.
- [99] R. J. Steinhagen *et al.*, “HADES Slow-Extraction Control with a Cycle-to-Cycle Macro-Spill Feedback,” GSI-FAIR Scientific Report 2019 (in preparation), GSI Helmholtzzentrum für Schwerionenforschung GmbH, 2019.
- [100] R. Singh, P. Forck, and S. Sorge, “Smoothing of the slowly extracted coasting beam from a synchrotron,” 2019. arXiv:1904:09195.
- [101] N. Cartiglia *et al.*, “Design optimization of ultra-fast silicon detectors,” *Nucl. Instrum. Meth.*, vol. A796, pp. 141–148, 2015.
- [102] V. Sola *et al.*, “Ultra-Fast Silicon Detectors for 4D tracking,” *JINST*, vol. 12, no. 02, p. C02072, 2017.
- [103] H. F. W. Sadrozinski, A. Seiden, and N. Cartiglia, “4D tracking with ultra-fast silicon detectors,” *Rept. Prog. Phys.*, vol. 81, no. 2, p. 026101, 2018.
- [104] N. Cartiglia *et al.*, “Beam test results of a 16 ps timing system based on ultra-fast silicon detectors,” *Nucl. Instrum. Meth.*, vol. A850, pp. 83–88, 2017.

- [105] G. Pellegrini *et al.*, “Technology developments and first measurements of Low Gain Avalanche Detectors (LGAD) for high energy physics applications,” *Nucl. Instrum. Meth.*, vol. A765, pp. 12–16, 2014.
- [106] V. Sola *et al.*, “First FBK Production of 50 μ m Ultra-Fast Silicon Detectors,” *Nucl. Instrum. Meth.*, vol. A924, pp. 360–368, 2019.
- [107] S. Kuehn, “RD50 Collaboration overview: Development of new radiation hard detectors,” *Nucl. Instrum. Meth.*, vol. A824, pp. 422–425, 2016.
- [108] Z. Galloway, C. Gee, S. Mazza, H. Ohldag, R. Rodriguez, H.-W. Sadrozinski, B. Schumm, A. Seiden, W. Wyatt, and Y. Zhao, “Use of LGAD ultra-fast silicon detectors for time-resolved low-keV X-ray science,” *Nuclear Instruments and Methods in Physics Research Section A: Accelerators, Spectrometers, Detectors and Associated Equipment*, vol. 923, pp. 5 – 7, 2019.
- [109] G. Kramberger *et al.*, “Radiation Hardness of Thin Low Gain Avalanche Detectors,” *Nucl. Instrum. Meth.*, vol. A891, pp. 68–77, 2018.
- [110] W. Krüger, “Time precision investigations of UFSD for HADES,” Master Thesis (in preparation), TU Darmstadt.
- [111] J. Auerhammer, H. Genz, H. Graef, V. Huck, C. Luettge, A. Richter, T. Rietdorf, P. Schardt, E. Spamer, K. Rühl, *et al.*, “Latest of the superconducting Darmstadt Electron Accelerator S-DALINAC,” in *Proc. of SRF 1991*, pp. 110–120, 1991.
- [112] A. Richter *et al.*, “Operational Experience at the S-DALINAC,” in *Proc. of EPAC 1996*, vol. 96, pp. 110–114, IOP Publishing, 1996.
- [113] N. Pietralla, “The Institute of Nuclear Physics at the TU Darmstadt,” *Nuclear Physics News*, vol. 28, no. 2, pp. 4–11, 2018.
- [114] M. Arnold, *Auslegung, Planung und Aufbau einer dritten Rezirkulation mit ERL-Modus für den S-DALINAC*. PhD thesis, Technische Universität, Darmstadt, 2017.
- [115] Y. Fritzsche, *Aufbau und Inbetriebnahme einer Quelle polarisierter Elektronen am supraleitenden Darmstädter Elektronenlinearbeschleuniger S-DALINAC*. PhD thesis, Technische Universität, Darmstadt, 2011.
- [116] K. Sonnabend, D. Savran, J. Beller, M. Büssing, A. Constantinescu, M. Elvers, J. Endres, M. Fritzsche, J. Glorius, J. Hasper, *et al.*, “The Darmstadt High-Intensity Photon Setup (DHIPS) at the S-DALINAC,” *Nucl. Instr. Meth. Phys. Res. A*, vol. 640, no. 1, pp. 6–12, 2011.
- [117] L. Jürgensen, *Entwicklung und Aufbau eines Hochenergie-Elektronen-Scrapersystems für den S-DALINAC*. PhD thesis, Technische Universität, Darmstadt, 2018.
- [118] M. Knirsch, *Konzeption, Aufbau und Erprobung eines hochauflösenden QCLAM-Spektrometers mit großem Raumwinkel und hoher Impulsakzeptanz am Elektronenbeschleuniger S-DALINAC*. PhD thesis, TU Darmstadt, 1991.
- [119] D. Schüll, J. Foh, H.-D. Gräf, H. Miska, R. Schneider, E. Spamer, H. Theissen, O. Titze, and T. Walcher, “High resolution electron scattering facility at the Darmstadt linear accelerator (DALINAC): III. Detector system and performance of the electron scattering apparatus,” *Nucl. Instr. Meth. Phys. Res.*, vol. 153, no. 1, pp. 29–41, 1978.
- [120] D. Savran, K. Lindenberg, J. Glorius, B. Löher, S. Müller, N. Pietralla, L. Schnorrenberger, V. Simon, K. Sonnabend, C. Wälzlein, M. Elvers, J. Endres, J. Hasper, and A. Zilges, “The low-energy photon tagger NEPTUN,” *Nucl. Instr. Meth. Phys. Res. A*, vol. 613, no. 2, pp. 232–239, 2010.

-
- [121] J. Pforr, M. Arnold, T. Bahlo, F. Hug, and N. Pietralla, "Emittance measurements with optical transition radiation at the S-DALINAC," *Nuclear Instruments and Methods in Physics Research Section A: Accelerators, Spectrometers, Detectors and Associated Equipment*, vol. 959, p. 163540, 2020.
- [122] M. Arnold, J. Birkhan, J. Pforr, N. Pietralla, F. Schließmann, M. Steinhorst, and F. Hug, "First operation of the superconducting Darmstadt linear electron accelerator as an energy recovery linac," *Phys. Rev. Accel. Beams*, vol. 23, p. 020101, Feb 2020.
- [123] T. Zickler, "Basic design and engineering of normal-conducting, iron-dominated electromagnets," in *Proceedings, 2009 CAS-CERN Accelerator School: Specialised course on Magnets: Bruges, Belgium, June 16 - 25, 2009*, 2011.
- [124] F. Schließmann, "Untersuchungen zur nichtlinearen Strahldynamik und Optionen für Strahlführungsmodifikationen am S-DALINAC," Master's thesis, TU Darmstadt, 2017.
- [125] K. Wille, *Physik der Teilchenbeschleuniger und Synchrotronstrahlungsquellen*. Vieweg+Teubner Verlag, 2 ed., 1996.
- [126] F. Hinterberger, *Physik der Teilchenbeschleuniger und Ionenoptik*. Berlin Heidelberg: Springer-Verlag, 2 ed., 2008.
- [127] F. Hug, *Erhöhung der Energieschärfe des Elektronenstrahls am S-DALINAC durch nicht-isochrones Rezirkulieren*. PhD thesis, Technische Universität, Darmstadt, 2013.
- [128] A. Rost, T. Galatyuk, and J. Pietraszko, "Current Status of CVD Diamond Based Beam Detector Developments at the S-DALINAC," in *Proceedings, 6th International Beam Instrumentation Conference, IBIC2017*, p. TUPCC01, 2018.
- [129] A. Rost, T. Galatyuk, and J. Pietraszko, "Research and Development of Diamond Based Beam Monitoring and Diagnostics Systems at the S-DALINAC," in *Proceedings, 8th International Particle Accelerator Conference (IPAC 2017): Copenhagen, Denmark, May 14-19, 2017*, p. MOPAB038, 2017.
- [130] T. Winkler, "Entwurf, Bau und Erprobung eines energiedefinierenden Blendensystems für das magnetische 40°-Analysiersystem und Entwicklung eines Rechnerprogramms zur interaktiven graphischen Simulation des Strahltransports in 1. Ordnung für das magnetische Strahlführungssystem des S-DALINAC," Diploma Thesis, TH Darmstadt, Darmstadt, Germany, 1993.
- [131] IKP, TU Darmstadt, "Software: XBEAM 2.1," December 2019.
- [132] K. Lindenberg, *Development and Construction of the Low-Energy Photon Tagger NEPTUN*. PhD thesis, Technische Universität, Darmstadt, Darmstadt, March 2008.
- [133] Autodesk, "Software: AutoCAD 2017 (Student version)," December 2016.
- [134] Autodesk, "Software: Inventor Professional 2017 (Student version)," December 2016.
- [135] V. V. Morokhovskiy, *Untersuchung der parametrischen Röntgenstrahlung am S-DALINAC: spektrale Verteilung, Polarisation und Interferenz mit kohärenter Bremsstrahlung sowie Konstruktion, Bau und Test eines Strahlfängers*. PhD Thesis, TU Darmstadt, Darmstadt, Germany, 1998.
- [136] T. Bahlo, *Entwurf eines Møllerpolarimeters und Entwicklung einer aktiven Phasenstabilisierung für den Injektor des S-DALINAC*. PhD thesis, TU Darmstadt, Darmstadt, 2017.
- [137] D. Lide, *CRC Handbook of Chemistry and Physics, 84th Edition*. Taylor & Francis, 2003.

-
- [138] Robert Bosch GmbH, "Manual: GLL 3-80 Professional." Website, 2019. Online available: https://www.bosch-professional.com/binary/ocsmedia/optimized/full/o237517v21_160992A27S_201601.pdf; retrieved on 20 December 2019.
- [139] M. Lösler, M. Arnold, H. Bähr, C. Eschelbach, T. Bahlo, R. Grewe, F. Hug, L. Jürgensen, P. Winckmann, and N. Pietralla, "Hochpräzise erfassung von strahlführungselementen des elektronenlinearbeschleunigers s-dalinac," *zfv – Zeitschrift für Geodäsie*, vol. Geoinformation und Landmanagement, no. 140, p. 346, 2015.
- [140] L. Jürgensen, "Height gauge measurement." private communication, September 2019.
- [141] P. van Beek, "NEPTUN allignment marks." private communication, September 2019.
- [142] Hositrad Holland B.V, Netherlands, "Technical drawing." private communication, August 2018.



Danksagungen

An dieser Stelle möchte ich mich bei allen Personen herzlichst bedanken, die mich bei der Erstellung dieser Arbeit unterstützt haben.

Ich bedanke mich bei meiner *Doktormutter* **Tetyana Galatyuk**, für die Möglichkeit diese Arbeit in ihrer Arbeitsgruppe durchführen zu können. Während dieser Zeit genoss ich eine sehr gute Betreuung. Ich bedanke mich für die großen Freiheiten, die ich während der Arbeit an meiner Promotion genießen durfte. Die von mir getroffenen Entscheidungen wurden immer unterstützt und mit konstruktiven Hinweisen ergänzt. Vielen Dank auch für die Möglichkeit meinen aktuellen Forschungsstand auf nationalen und internationalen Konferenzen präsentieren zu können.

Ich bedanke mich bei meinem Zweitbetreuer **Florian Hug** für die Übernahme der Ko-Betreuung und die sehr wertvollen Kommentare und Diskussionen.

Mein Dank gilt auch meinem Mentor **Jerzy Pietraszko (Jurek)** für die Möglichkeit an der Entwicklung von High-Tech Diamant- und Siliziumdetektoren mitwirken zu können. Vielen Dank für die Unterstützung bei technischen und physikalischen Fragen.

Ich danke allen aktuellen und ehemaligen Mitglieder der **VIP-QM** Gruppe der TU Darmstadt: **Tetyana, Florian, Gosia, Szymon, Georgy, Dominique, Frederic, Fede** und die neue Generation **Max** und **Willy**. In unserer Arbeitsgruppe herrscht immer eine angenehme und wissenschaftlich sehr produktive Atmosphäre. Vielen Dank auch für die inspirierenden und philosophischen Nachtschichten bei Haxe und Bier in unserem Darmstädter Lieblingsbrauhaus.

I would like to thank all members of the **ECAL Group**. Especially I would like to thank **Pavel** who gave me great freedoms during the realization of the read-out electronics for ECAL. In the event of any problems, with his professional and relaxed way, he contributed a lot to find a solution. Many thanks to **Petr** with whom I was allowed to spend hundreds of hours in the ECAL main-frame, but also enjoyed the nightlife in Darmstadt and at several conferences. Many thanks also to **Lukas, Sasha** and **Ondrej** and the rest of the Prague technical team for the help to transport several tons of lead glass. I would also like to thank all students and doctors who helped me with the installation and wiring of the ECAL electronics. My thanks also go to my Russian colleagues for their support in evaluating the electronics.

Ich bedanke mich bei der **GSI Elektronik Abteilung** für die großartige Arbeit und Unterstützung während des Designs und der Herstellung der PaDiWa-AMPS2 Elektronik. Ein großer Dank gilt **Michael Traxler** welcher mich bei meinen Vorhaben und der Verwirklichung meiner Ideen immer voll unterstützte. Ich bedanke mich für die nützlichen Diskussionen. Sehr aufbauend war sein Lob aber vor allen Dingen auch seine konstruktive Kritik. Mein Dank gilt auch den Layoutern und den Damen aus der Fertigung. Außerdem bedanke ich mich für die großartige Unterstützung und Hilfeleistung von **Jörn, Sergej** bei DAQ-Software Problemen und **Peter** für die Hilfe bei Angelegenheiten im Kontrollsystem.

Große Unterstützung erhielt ich auch von **Jan**. Ich bedanke mich für die FPGA „Programmiercrashkurse“ und den DAQ Support und die sehr produktiven „Hardware-Sessions“ in seinem Labor an der Goethe Universität Frankfurt. Ein Dankeschön gilt auch **Ingo** für die Hilfe bei der FPGA-Programmierung.

Ich danke dem **HADES Technik Team** für die Unterstützung bei technischen Angelegenheiten. Ganz besonders danke ich **Erwin, Torsten** und **Max** welche mich bei technischen Fragen und Aufgaben immer

zuverlässig und schnell beiseite standen.

Ein Dank gilt auch **Wolfgang** für die Einführung in die Elektronikentwicklung und Diamantdetektoren während meiner Master-Zeit.

Ich bedanke mich bei der RICH Gruppe für die sehr gute Kollaboration während der Inbetriebnahme von ECAL und RICH. Einen großer Dank geht dabei an **Adrian** und **Jörg**.

Ich danke dem MDC Team, vor allem **Christian Wendisch** und **Michael Wiebusch** für die Kollaboration im Detektorlabor mit großartiger gegenseitiger Unterstützung.

Ich danke dem **Jeden-Tag-pünktlich-um-12-Uhr-Mittagessen Team** für die interessanten physikalischen und nichtphysikalischen Diskussionen während dem Mittagessen und der Kaffeepause.

Besonders danke ich **Jochen** welcher wieder meine Lust zum Gitarrenspiel erweckt hat.

It is an honor for me to be part of the **HADES Collaboration**.

Ich bedanke mich bei allen Mitgliedern der **Beschleunigergruppe** der TU Darmstadt für die Unterstützung bei der Realisierung meines Testplatzes am S-DALINAC. Hervorzuheben sind hier **Michaela, Lars, Felix, Jonas, Simon, Thore, Ruben, Jan, Jonny, Manu, Manuel** und **Marco** welche mich bei technischen und physikalischen Fragen beraten aber auch tatkräftig mit angepackt haben. Großer Dank gilt auch der **Beschleunigerbetriebsgruppe**, der **Mechanischen Werkstatt**, dem **Strahlenschutz** und der **NEPTUN Gruppe**.

Ich danke den super kompetenten Damen aus dem **IKP Sekretariat** der TU Darmstadt. Ich danke **Carina** für die großartige Unterstützung im administrativen Bereich. An dieser Stelle danke ich auch **Annette** vom **HADES/CBM Sekretariat** an der GSI.

Ich danke allen Mitgliedern von **GRK 2128 AccelencE** für die professionelle wissenschaftliche aber auch freundschaftliche Zeit während meiner Promotion. Vielen Dank an **HGS-HIRe for FAIR** für die finanzielle Unterstützung und die Möglichkeit mein Wissen und meine Fertigkeiten in Softskill-Kursen und Powerweeks erweitern zu können.

Zuletzt bedanke ich mich bei meiner **Familie** ohne die diese Arbeit nicht zustande gekommen wäre. Großer Dank gilt meinen **Eltern, Großeltern**, meiner **Schwester**, meinen **Tanten** und **Onkeln** welche mir moralisch aber auch finanziell immer beiseite stehen. Ein Dankeschön gilt auch allen meinen **Freunden** welche immer für mich da sind. Zuletzt geht ein Dankeschön an **Marc** für die Hilfe bei der Beseitigung sämtlicher Rechtschreibfehler.

This work has been supported by BMBF under ErUM-FSP C.B.M. and by DFG under GRK 2128 AccelencE.

Curriculum vitae

Personal information

Name: Adrian Rost

Date of birth: 06 March 1988

City of birth: Frankfurt am Main, Germany

Education

Since 05/2016 PhD in Physics
Technische Universität Darmstadt

10/2013 - 04/2016 Master of Science in Physics
Technische Universität Darmstadt

10/2008 - 09/2013 Bachelor of Science in Physics
Technische Universität Darmstadt

06/2008 - 06/2000 Abitur (A-levels)
Otto-Hahn-Schule, Hanau
Main subjects: Physics and Chemistry

Supervision experience

Physikalisches Grundpraktikum (2012-2019)
Miniforschung (2016)
Pupil internships at GSI (2015, 2016)

Additional experience

"HGS-HIRe for FAIR" Training:
Basic Soft Skills Course III: Leadership and Career Development (2019)
Basic Soft Skills Course II: Leading Teams in a Research Environment (2018)
Basic Soft Skills Course I: Making an Impact as an Effective Researcher (2017)
Power Week: Detectors and Read-Out Electronics (2017)

Invited talks

Technical Seminar of the PRISMA Detector Laboratory in January 2019, JGU Mainz, "The TRB3 Read-out Platform - from Calorimeter Read-out to Online Beam Monitoring".

Awards

Giersch Excellence Award 2016

Important publications

A. Rost et al., "Performance of the CVD Diamond Based Beam Quality Monitoring System in the HADES Experiment at GSI*", in Proc. IPAC'19, Melbourne, Australia, May 2019, pp. 2507-2509.

A. Rost et al., “Beam Quality Monitoring System in the HADES Experiment at GSI Using CVD Diamond Material*”, in Proc. IBIC’18, Shanghai, China, Sep. 2018, pp. 300-302.

A. Rost et al. “The PaDiWa-AMPS2 TDC and QDC front-end electronics for the HADES Electromagnetic Calorimeter”, GSI-FAIR Scientific Report 2017, GSI Helmholtzzentrum für Schwerionenforschung GmbH, Darmstadt, Germany, 2018.

A. Rost et al., “Current Status of CVD Diamond Based Beam Detector Developments at the S-DALINAC”, in Proc. IBIC’17, Grand Rapids, MI, USA, Aug. 2017, pp. 150-152.

A. Rost et al., “Research and Development of Diamond Based Beam Monitoring and Diagnostics Systems at the S-DALINAC”, in Proc. IPAC’17, Copenhagen, Denmark, May 2017.

A. Rost et al. “A flexible FPGA based QDC and TDC for the HADES and the CBM calorimeters”, JINST 12 (2017) C02047.